



International Committee for Future Accelerators

Sponsored by the Particles and Fields Commission of IUPAP

Beam Dynamics Newsletter

No. 72

**Issue Editors:
M. Benedikt and F. Zimmermann**

**Editor in Chief:
Y. H. Chin**

December 2017

Contents

1	FOREWARD	9
1.1	From the Chair.....	9
1.2	From the Editors.....	9
2	FUTURE ENERGY-FRONTIER CIRCULAR COLLIDERS	11
2.1	Highlights from SuperKEKB Commissioning Phase 1 and Plan for Phase 2. 11	
2.1.1	Introduction.....	11
2.1.2	Highlights from SuperKEKB Commissioning Phase 1.....	11
2.1.3	Commissioning Plan for Phase 2.....	15
2.1.4	References.....	19
2.2	FCC-ee Optics Design.....	19
2.2.1	Introduction.....	20
2.2.2	Optimization of machine parameters.....	20
2.2.3	Changes in optics since FCC Week 2017.....	22
2.2.4	Dynamic Aperture.....	23
2.2.5	Acknowledgement.....	25
2.2.6	References.....	25
2.3	A novel e+e- beam-beam instability.....	25
2.3.1	Introduction.....	25
2.3.2	Cross wake force induced by beam-beam interaction.....	26
2.3.3	Mode coupling theory for localized wake force.....	28
2.3.4	Summary.....	29
2.3.5	References.....	30
2.4	FCC-ee Parameter Optimization.....	30
2.4.1	Introduction.....	30
2.4.2	Luminosity Optimization at the Top Energy.....	31
2.4.3	Beam-Beam Interaction at Low Energies.....	33
2.4.4	Conclusion.....	40
2.4.5	Acknowledgements.....	41
2.4.6	References.....	41
2.5	Strategy, Site Selection Process and CE Studies for CEPC-SppC.....	42
2.5.1	CEPC-SppC Strategy and Status.....	42
2.5.2	CEPC-SppC Site Selection Process and Status.....	47
2.5.3	Civil Engineering Studies.....	48

2.5.4	Conclusions	48
2.5.5	Acknowledgments	48
2.5.6	References.....	48
2.6	CEPC Design Highlights	49
2.6.1	Introduction.....	49
2.6.2	Main parameters	49
2.6.3	Geometry of CEPC	50
2.6.4	The design of interaction region	51
2.6.5	Lattice of the collider ring	53
2.6.6	Dynamic aperture.....	54
2.6.7	Summary.....	55
2.7	Collective effects in CEPC	55
2.7.1	Introduction.....	55
2.7.2	Impedance studies.....	55
2.7.3	Impedance-driven instabilities.....	57
2.7.4	Electron cloud.....	59
2.7.5	Beam ion instabilities	59
2.7.6	Summary.....	60
2.7.7	References.....	61
2.8	Some critical collective effects for the FCC-ee collider	61
2.8.1	Introduction.....	61
2.8.2	Wake fields and impedances	62
2.8.3	Electron cloud.....	66
2.8.4	References.....	68
2.9	Interaction Region for the FCC-ee Design	70
2.9.1	Introduction.....	70
2.9.2	Present IR design	70
2.9.3	SR backgrounds from the last bend magnet before the IR	74
2.9.4	SR backgrounds from the final focus quadrupoles.....	76
2.9.5	Other beam related backgrounds	76
2.9.6	Conclusion	77
2.9.7	Acknowledgements.....	77
2.9.8	References.....	77
2.10	HOM mitigation for FCC-ee.....	78
2.10.1	Introduction.....	78
2.10.2	HOM excitation	78

2.10.3	Summary with recommendations on the beam pipe geometry.	81
2.10.4	References	82
2.11	Final twin quadrupole design for the FCC-ee based on the canted cosine theta concept.....	82
2.11.1	Introduction	82
2.11.2	Edges Correction	84
2.11.3	Crosstalk compensation.....	86
2.11.4	Conclusions	88
2.11.5	Acknowledgements	88
2.11.6	References	88
2.12	Proposed RF Staging Scenario for FCC-ee	89
2.12.1	Introduction	89
2.12.2	Operation model	89
2.12.3	RF configurations	90
2.12.4	Cavity material options	90
2.12.5	Beam-cavity interaction and beam dynamic issues.....	91
2.12.6	A flavor of other R&D challenges	91
2.12.7	Installation and staging plan.....	92
2.12.8	The booster ring.....	94
2.12.9	Summary	94
2.12.10	Acknowledgments	95
2.12.11	References	95
2.13	Lessons from the LHC and Technology Advances for HL-LHC.....	96
2.13.1	Introduction	96
2.13.2	Lessons from the LHC	96
2.13.3	Novel Technologies for the HL-LHC	98
2.13.4	Outlook.....	99
2.13.5	References	99
2.14	FCC-hh Design Highlights	99
2.14.1	Introduction	99
2.14.2	Layout and Key Parameters	100
2.14.3	Energy considerations	100
2.14.4	Injector considerations	101
2.14.5	Luminosity Considerations.....	102
2.14.6	Key Design Components.....	104
2.14.7	Ion Operation.....	107

2.14.8	Conclusion	107
2.14.9	Acknowledgements.....	107
2.14.10	General References.....	107
2.14.11	Specific References	107
2.15	R&D towards 16 T Nb ₃ Sn dipole magnets	110
2.15.1	Introduction.....	110
2.15.2	R&D directions.....	110
2.15.3	Overview of development programs towards 16 T Nb ₃ Sn magnets.....	110
2.15.4	Conclusion	112
2.15.5	References.....	112
2.16	Faster Magnet Ramps for Using the LHC as FCC Injector	113
2.16.1	Introduction and motivation	113
2.16.2	The present situation.....	113
2.16.3	Constraints for faster ramps.....	115
2.16.4	Options for faster ramps up	118
2.16.5	Options for faster ramps down	119
2.16.6	Conclusions	120
2.16.7	Acknowledgements.....	121
2.16.8	References.....	121
2.17	Update on the SPPC design	121
2.17.1	1 Introduction.....	121
2.17.2	Lattice	123
2.17.3	Luminosity and leveling	124
2.17.4	Collimation	125
2.17.5	High-field superconducting magnets.....	126
2.17.6	Vacuum and beam screen	127
2.17.7	Injector chain	128
2.17.8	Summary.....	128
2.17.9	Acknowledgements.....	128
2.17.10	References:	129
2.18	Development of Fe-based HTS Wire and Conceptual Design Study of the Magnet for Future High Energy Accelerators	130
2.18.1	Introduction.....	130
2.18.2	Development of Advanced IBS HTS Wire	131
2.18.3	Conceptual Design Study of the Dipole Magnet for Future High Energy Accelerators	134

2.18.4	References	137
2.19	HE-LHC Overview, Parameters and Challenges.....	138
2.19.1	Introduction	138
2.19.2	Design Targets and Constraints.....	138
2.19.3	Baseline Parameters	139
2.19.4	Challenges	140
2.19.5	References	141
2.20	HE-LHC Optics Development.....	141
2.20.1	Introduction	142
2.20.2	Lattice Design.....	142
2.20.3	Dynamic Aperture	146
2.20.4	Realistic Injection Lattice Model	149
2.20.5	Conclusion.....	150
2.20.6	References	150
2.21	Single-beam transverse collective effects for HE-LHC	151
2.21.1	Introduction	151
2.21.2	Space Charge effects	152
2.21.3	Beam impedance and stability scalings from FCC-hh and HL-LHC...	154
2.21.4	Impedance model	157
2.21.5	Elements contributions to impedance.....	160
2.21.6	Beam stability and Landau damping.....	161
2.21.7	Conclusion.....	173
2.21.8	Acknowledgements	173
2.21.9	References	173
3	WORKSHOP AND CONFERENCE REPORTS	175
3.1	ICFA Mini-Workshop on Impedances and Beam Instabilities in Particle Accelerators 2017.....	175
3.2	LHeC/FCC-eh Workshop at CERN, September 2017	179
3.2.1	References	181
3.3	300 Scientists Discussed Novel Accelerators at the 3 rd European Advanced Accelerator Concept Workshop	181
3.4	The ICFA mini-workshop Space Charge 2017	183
3.5	The 2 nd Workshop on Slow Extraction, 9-11 November 2017.....	185
4	RECENT DOCTORAL THESES.....	188
4.1	Beam Diagnostics and Dynamics in Nonlinear Fields	188

4.2	Luminosity Performance Limitations due to the Beam- Beam Interaction in the Large Hadron Collider	189
4.3	Applications of Neural Networks to Modeling and Control of Particle Accelerators	189
5	FORTHCOMING BEAM DYNAMICS EVENTS	190
5.1	7th Low Emittance Rings Workshop, 15-17 January 2018	190
5.2	ARIES Topical Workshop on "Emittance Measurements for Light Sources and FELs", 29-30 January 2018	191
5.3	ICFA Mini-Workshop on Beam-Beam Effects in Circular Colliders, 5-7 February 2018.....	191
5.4	TIARA, ARIES and AMICI joint Accelerator-Industry Co-innovation Workshop.....	192
5.5	ICFA Mini-Workshop on Machine Learning Applications in Accelerator Physics, February 28 - March 2, 2018.....	192
5.6	ARIES APEC Topical Workshop on Ion Sources and Low Energy Beam Transport into RF Linacs, February 28 - March 2, 2018.....	193
5.7	60th ICFA Advanced Beam Dynamics Workshop on Future Light Sources, FLS2018, March 4-9, 2018, SINAP	194
5.8	ARIES-APEC Pulse Power for Kicker Systems (PULPOKS) Workshop, 12-13 March 2018, CERN	194
5.9	ALEGRO 2018 workshop, Oxford, 26-29 March 2018	195
5.10	Future Circular Collider Week 2018, 9-13 April 2018.....	195
5.11	9th International Particle Accelerator Conference (IPAC'18), in Vancouver, from April 29 to May 4, 2018.....	196
5.12	E-CLOUD'18, 3-7 June 2018	196
5.13	2018 LHeC/FCC-eh/PERLE Workshop.....	197
5.14	High-Brightness Hadron Beams 2018 (HB2018).....	198
5.15	29 th Linear Accelerator Conference (LINAC18).....	198
6	ANNOUNCEMENTS OF THE BEAM DYNAMICS PANEL	199
6.1	ICFA Beam Dynamics Newsletter	199
6.1.1	Aim of the Newsletter	199
6.1.2	Categories of Articles	199
6.1.3	How to Prepare a Manuscript.....	199
6.1.4	Distribution	200
6.1.5	Regular Correspondents.....	200
6.2	ICFA Beam Dynamics Panel Members	202

1 Foreword

1.1 From the Chair

Yong Ho Chin, KEK
Mail to: yongho.chin@kek.jp

Next year, we will have two important ICFA Advanced Beam Dynamics Workshops:

1. The 60th ICFA Advanced Beam Dynamics Workshop on Future Light Sources (FLS2018), March 4-9, 2018, at SINAP, China. <http://indico.sinap.ac.cn/event/4/>
2. The 61st ICFA Advanced Beam Dynamics Workshop on High-Intensity and High- Brightness Hadron Beams (HB2018), June 17-22, 2018, in Daejeon, Korea. <http://hb2018.ibs.re.kr>

FLS2018 is a kind of “reboot” from the previous FLS workshop series with the new concept and structure. FLS2018 will bring together worldwide scientists to exchange ideas and best practices about accelerator based light sources, their new development trend and related key technologies. The workshop program will consist of plenary talks and working group sessions. The working groups will include Linac-based light sources, Ring-based light sources, Compact light sources, and Key technologies.

The preparation of the both workshop is under way very well and the next year will be a very productive year for the ICFA Beam Dynamic Panel activities.

During the ICFA seminar in Ottawa in November, ICFA issued the ICFA Statement on the ILC Operating at 250 GeV as a Higgs Boson Factory. The next year will be a very crucial year for ILC.

The editors of this issue are Drs. Michael Benedikt and Frank Zimmermann, senior scientists at CERN and the leaders of FCC activities. The theme is “Future Energy-Frontier Circular Colliders”. It includes also the present SuperKEKB activity report. They collected a large amount of well-written review articles, and they provide very good and comprehensive reviews of the present and future circular colliders. I want to thank Michael and Frank for editing a valuable and formidable newsletter of high quality for the accelerator community.

1.2 From the Editor

Michael Benedikt and Frank Zimmermann, CERN, Geneva, Switzerland
Mail to: Michael.Benedikt@cern.ch , Frank.Zimmermann@cern.ch

In this second decade of the 21st century, we are witnessing a truly exciting period for high-energy accelerators. While the Large Hadron Collider (LHC) at CERN is, by now, well into its run no. 2 and has recently been setting new luminosity world records, the SuperKEKB B factory at KEK is being commissioned with beam in Japan. At the same

time, several ambitious plans for future frontier facilities are being developed: the Future Circular Collider study at CERN and the Chinese Electron Positron Collider / Super Proton Proton Collider at IHEP Beijing both aim at frontier electron-positron and proton-proton collisions in new tunnels of about 100 km circumference. Both studies will finalize Conceptual Design Reports within the coming year.

Some time ago, the former Chair of the ICFA Beam Dynamics Panel, Weiren Chou, who also happens to be one of the leaders of the CEPC/SPPC design study, had invited us to serve as editors for an ICFA Newsletter issue devoted to Future Energy-Frontier Circular Colliders – A challenge which we happily accepted. Recently, the new Chair of the ICFA Beam Dynamics Panel, Yong Ho Chin, reminded us of our earlier commitment and renewed the invitation.

This issue of the ICFA Newsletter first reports from the existing SuperKEKB and LHC, including their future plans, and then reviews key challenges in accelerator physics, key technologies, technical infrastructure and civil engineering for the proposed 100 km lepton and hadron colliders FCC-ee, CEPC, FCC-hh, and SPPC. The compilation is completed by a few articles on the High Energy LHC, a proposed 27 TeV hadron collider in the existing 27 km tunnel at CERN, which could be realized by using the 16 Tesla magnet technology developed for the FCC hadron collider.

We hope that the readers will enjoy, and benefit from, the following collection of articles covering a wide area of topics, such as primary parameter choices, beam optics, collective effects, machine-detector interface, radiofrequency systems, magnet technology, civil engineering studies and site selection process.

2 Future Energy-Frontier Circular Colliders

2.1 Highlights from SuperKEKB Commissioning Phase 1 and Plan for Phase 2

Yoshihiro Funakoshi and Yuki Yoshi Ohnishi
 Mail to: yoshihiro.funakoshi@kek.jp, yuki.yoshi.ohnishi@kek.jp,
 KEK, 1-1 Oho, Tsukuba, Ibaraki 305-0801, Japan

2.1.1 Introduction

The purpose of SuperKEKB is to search a new physics beyond the standard model of the particle physics in the B meson regime. SuperKEKB consists of an injector linac, a damping ring for the positron beam and two main rings: *i.e.* the low energy ring (LER) for positrons and the high energy ring (HER) for electrons, and the physics detector named Belle II. The beam energies of LER and HER are 4GeV and 7GeV, respectively. The design beam currents of LER and HER are 3.6A and 2.6A, respectively. The design luminosity is $8 \times 10^{35} \text{ cm}^{-2}\text{s}^{-1}$. More details of SuperKEKB are described elsewhere [1].

The beam commissioning of SuperKEKB will proceed in three steps; *i.e.* Phase 1, 2 and 3. The Phase 1 commissioning has been already done for 5 months in 2016. In Phase 1, the superconducting final focus doublets and other correction coils (called QCS as a whole) and Belle II were not installed and no beam collision was performed. The commissioning of the damping ring, which is newly introduced for SuperKEKB, will start in December 2017. The Phase 2 commissioning of the main rings will start in middle of February 2018 and continue for about 5 months. In Phase 2, the QCS magnets and the main part of the Belle II detector will be installed. But the vertex detector will not be installed in Phase 2. This is based on an idea that the vertex detector, which is very sensitive to the beam background, should be installed after sufficient beam tuning with the QCS magnets. From the viewpoint of the accelerator tuning, we can make machine tuning on condition that hardware components are fully installed except for the beam background tuning to the vertex detector. The target luminosity in Phase 2 is $1 \times 10^{34} \text{ cm}^{-2} \text{ s}^{-1}$. The Phase 3 commissioning will start in autumn 2018. In this phase, the vertex detector will be installed and we will continue beam tuning aiming at the design luminosity in parallel with the physics experiment.

2.1.2 Highlights from SuperKEKB Commissioning Phase 1

2.1.2.1 Missions of Phase 1 commissioning

After 5 years of upgrade work from KEKB, the Phase 1 beam commissioning of SuperKEKB started on Feb. 1st 2016 and finished at the end of June 2016. Missions of the commissioning in Phase 1 were startup of each hardware component, establishment of beam operation software tools, preparation of installation of Belle II detector, an optics study and tuning without QCS and the detector solenoid magnet and other machine studies. As for preparation for installation of the Belle II detector, vacuum scrubbing was of essential importance. The Belle II group required 1 month vacuum scrubbing with the beam current of 0.5-1 A, which corresponds to the beam dose of 360-720 Ah. In addition, the study on the beam background to the detector was also important by using a test

detector named Beast. As for the optics study, Phase 1 provided us with a unique opportunity to conduct a study without the detector solenoid nor QCS. The low emittance tuning was an important item.

2.1.2.2 *History of Phase 1 beam commissioning*

Figure 1 shows the history of Phase 1 commissioning. In the figure, the red, violet and cyan dots show the beam currents, averaged vacuum pressure and the beam lifetime, respectively. The commissioning started on Feb. 1st. The beam currents increased gradually and the maximum beam currents of LER and HER in Phase 1 were 1010 mA and 870 mA, respectively. In the latter half of June, we had to decrease the HER beam current due to a trouble of a stripline kicker of the transverse bunch-by-bunch feedback. In LER, 98 % of vacuum chambers of KEKB were replaced with new ones. In arc sections, ante-chambers with TiN coating to suppress the effects of the electron clouds and mitigate the issues of heating by the synchrotron radiation were adopted. In HER, the most of the vacuum chambers in arc sections are reused from KEKB. About 18 % of vacuum chambers in the whole ring were replaced with new ones in HER. Vacuum scrubbing proceeded smoothly as is seen in Fig. 1. The averaged vacuum pressures of LER and HER were 4.7×10^{-7} Pa with the beam current of 1.01 A on June 17th and 5.7×10^{-8} Pa with the beam current of 0.87 A on June 22nd, respectively. The corresponding beam lifetime of those times of LER and HER were about 60 min. and 200 min. The main processes to determine the beam lifetime are the Touschek effect and the scattering from the residual gas particles. The cumulative dose of the beam currents in Phase 1 of LER and HER are 776 Ah and 662 Ah and we have met the requirement from the Belle II group. More details on the commissioning of the vacuum system are written elsewhere [2].

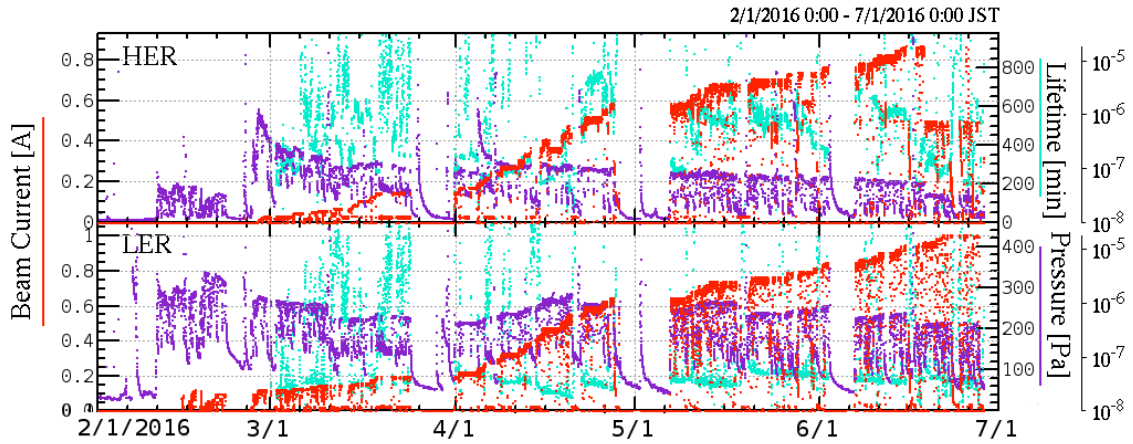


Figure 1: History of SuperKEKB operation in Phase 1.

2.1.2.3 *Vertical beam size blowup in LER*

In LER of KEKB, the electron clouds caused the vertical beam size blowup and gave a serious limit to the luminosity, although various efforts were devoted to suppress it throughout the beam operation period of KEKB. Based on the experiences at KEKB, we made more fundamental countermeasures for the problem. The vacuum chambers newly fabricated are antechambers with the TiN coating. In the wiggler section, the chambers have clearing electrodes. The vacuum

chambers of the bending magnets have the grooved structure. In addition to those countermeasures which were already made, we plan to install solenoid magnets in the drift section which were not installed before in Phase 1. In Phase 1, we observed a vertical beam size blowup as shown in Fig. 2(a). In the graph, the vertical beam size with an emittance control knob is also shown. This knob can create vertical dispersions all around the ring and control the vertical emittance. In the vacuum scrubbing operation, we intentionally enlarge the beam size to increase the beam lifetime mainly from the Touschek effect. In both cases, the vertical beam size started to increase at around 500 mA and showed serious blowup at higher beam currents with a filling pattern used for the vacuum scrubbing (1576 bunches in total, 3.06 RF bucket spacing in average). In addition to this problem, a nonlinear vacuum pressure rise against the beam current was also observed in LER. The aluminum bellows chambers were suspected of inducing those phenomena. TiN coating is applied to the other vacuum chambers in LER. But no TiN coating is applied to the bellows chamber. During a short operation break in the beginning of June, permanent solenoid-like magnets, whose typical magnetic field is ~ 100 Gauss were installed at all of ~ 800 such aluminum bellows chambers. By installing the permanent solenoid magnets, both problems were mitigated. As shown in Fig. 2(b), the blowup was almost suppressed up to 800 mA with the same filling pattern except for the slow blowup which we haven't understood yet. To study the blowup in more details, we conducted a machine study with shorter bunch spacing a part of which is shown in Fig. 2(a). The details of this study are described elsewhere [3]. It turned out that the vertical beam blowup is still serious with the shorter bunch spacing. During the period between Phase 1 and Phase 2, all of the drift space other than the bellows chambers were covered with the permanent solenoid magnets to suppress the blowup.

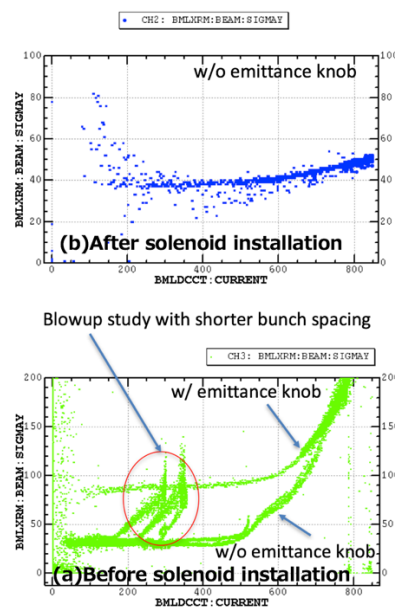


Figure 2: Vertical beam size as function of beam current in LER. (a) before solenoid installation, (b) after solenoid installation.

2.1.2.4 Optics corrections and low emittance tuning

Details of the optics correction are described elsewhere [4]. In this paper, only some highlights on the low emittance tuning in Phase 1 are described. The X-Y coupling correction and dispersion correction are important to get a low vertical emittance. While the corrections in HER went well, we encountered a difficulty in the LER. The obstacle of the corrections was leakage magnetic field from the Lambertson septum magnet whose main component is skew-Q. The Lambertson magnet is a part of the beam abort system. To cope with this problem, we took two measures. First, we activated skew-Q coils wound at a focusing sextupole magnet downstream of the septum magnet. Second, we installed a permanent skew-Q magnet upstream of the septum magnet. The picture and drawing of the permanent skew-Q magnet is shown in Fig. 3. With the two countermeasures, both the X-Y coupling and the residual vertical dispersion were improved. Figure 4 shows results of measurements of the X-Y coupling before taking the countermeasures and after them. In the measurement, vertical leakage orbits created by 6 independent horizontal steering kicks were observed. In the graph, such 6 vertical leakage orbits are shown as a function of the ring position where $s = 0$ corresponds to the interaction point (IP). The horizontal steering kicks were $200\mu\text{rad}$ and the horizontal orbit amplitude was about 2-3 mm in its peaks. As for correctors for the X-Y coupling, we employ skew-Q windings on sextupole magnets. Around $s = -1300\text{m}$, there remains some large X-Y coupling. At the location of $s = \sim 1400\text{m}$, the Lambertson DC septum magnet is located. As a result of the two countermeasures, the residual X-Y coupling at around the Lambertson septum almost vanished. Similarly, the vertical dispersion was much improved by the countermeasures.

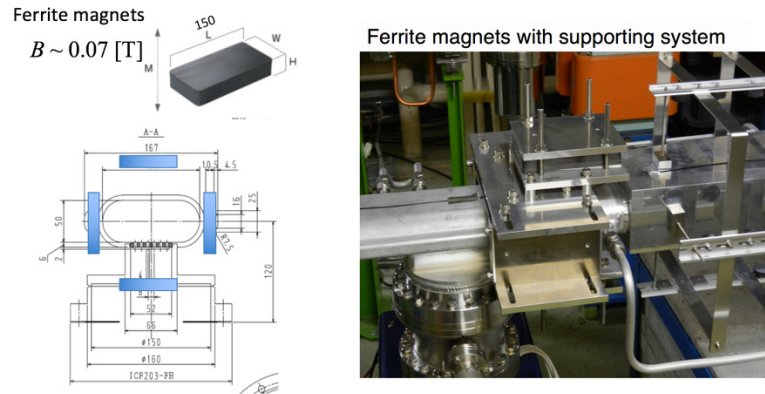


Figure 3: Picture and drawing of permanent skew-Q magnet

Table 1 shows the reaching point of the optics corrections in Phase 1 together with typical values of KEKB LER. The dispersions and the beta-beats in the list are r.m.s values of the deviations from the design measured at the BPMs around the rings. As seen in the table, the beta-beats are already smaller than the typical values of KEKB, although the distance of the horizontal betatron tunes from the half integer is longer than KEKB. From the measured vertical dispersion and the X-Y coupling, the vertical emittances of LER and HER are estimated as $\sim 6.8\text{ pm}$ and $\sim 8.0\text{ pm}$, respectively. In LER, the vertical emittance is calculated from the beam size measurement using the X-ray monitor as $\sim 10\text{ pm}$ and is more or less consistent with the optics measurement. On the other hand, the vertical emittance from a measurement by using the X-ray monitor in HER was $\sim 200\text{ pm}$

and there was a large discrepancy between the estimation from the optics measurement and the measurement by using the X-ray monitor. We took this issue seriously and investigated it in detail. First, we tried the calibration of the X-ray monitor by using the emittance control knob. Second, we measured the beam size with changing the vertical beta function at the source point of the X-ray monitor. As for the calibration, the calibration constant was determined to be 1.18, which means that the measured size is larger than the true beam size by a factor 1.18. From the measurement by changing the beta function at the source point, it turned out that the measured beam size of the X-ray monitor includes a large offset. The measured value is about $\sim 40\mu\text{m}$ and the offset value is more than $30\mu\text{m}$. Here, the measured size is assumed to be the square root of the square-sum of the true beam size and the offset value. This large offset was also supported by an independent analysis using a data on the beam size dependence of the Touschek beam lifetime. The origin of this large offset has not been understood. Even with this large offset and the calibration factor, an estimated vertical emittance in HER is about 40 pm and is still much larger than the estimation from the optics measurement. We will continue the investigation on this problem in Phase 2 commissioning.

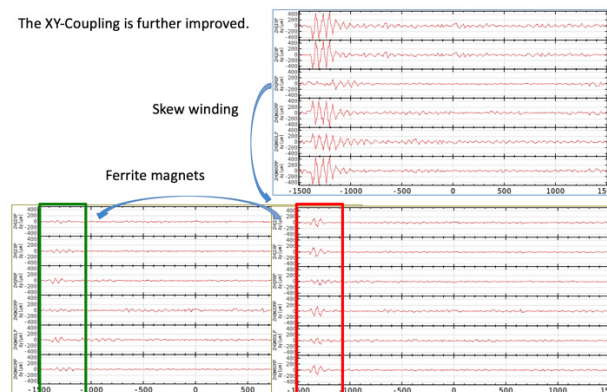


Figure 4: Improvement of X-Y coupling with two countermeasures at LER

Table 1: Reaching point of optics corrections in Phase 1.

	LER	HER	LER KEKB	Units
X-Y coupling ^{*)}	0.9	0.6		%
$\Delta\eta_x$ r.m.s	8	11	10	mm
$\Delta\eta_y$ r.m.s	2	2	8	mm
$\Delta\beta_x/\beta_x$ r.m.s.	3	3	6	%
$\Delta\beta_y/\beta_y$ r.m.s.	3	3	6	%

*) Ratio between the average of r.m.s. values of 6 vertical leakage orbits and that for the horizontal orbits.

2.1.3 Commissioning Plan for Phase 2

A verification of the nano-beam scheme is one of the targets for the commissioning in Phase 2 at SuperKEKB [5]. The nano-beam scheme adopts low emittance optics with a large Piwinski angle [6]. The specific luminosity is expected to be larger than 4×10^{31}

$\text{cm}^{-2}\text{s}^{-1}/\text{mA}^2$ with the beam-beam parameter of about 0.05. On the other hand, a study of the beam background for the Belle II detector is very important before the installation of the pixel vertex detector (PXD) that is used in Phase 3 as the most inner detector.

The luminosity for the nano-beam scheme is described by

$$L = \frac{N_+ N_- n_b f_0}{4\pi \sigma_{x,eff}^* \sigma_y^*} R_L = \frac{N_+ N_- n_b f_0}{4\pi (\sigma_z \phi_x) \sqrt{\varepsilon_y \beta_y^*}} R_L,$$

where the N_+ and N_- are the number of particles per bunch for positrons and electrons, respectively, n_b is the number of bunches, f_0 is the revolution frequency, σ_x^* and σ_y^* are the beam size at the IP in the horizontal and vertical direction, the suffix of *eff* means an effective value, ε_y is the vertical emittance, β_y^* is the beta function at the IP, σ_z is the bunch length, ϕ_x is the half crossing angle, and R_L is the luminosity reduction factor. Then, the specific luminosity can be defined by

$$L_{sp} = \frac{L}{I_+ I_- n_b} = \frac{1}{4\pi e^2 f_0 \sigma_{x,eff}^* \sigma_y^*} \frac{R_L}{I_- \beta_y^*} \propto \frac{\xi_{y+}}{I_- \beta_y^*},$$

where I_+ and I_- are the bunch beam currents. The beam-beam parameter in the case of the nano-beam scheme can be expressed by

$$\xi_{y+} = \frac{r_e \beta_y^*}{2\pi \gamma_+ \sigma_y^* (\sigma_{x,eff}^* + \sigma_x^*)} \frac{N_-}{R_{\xi y}} \simeq \frac{r_e}{2\pi \gamma_+ \sigma_z \phi_x} \frac{N_-}{\sqrt{\varepsilon_y}} \sqrt{\beta_y^*} R_{\xi y},$$

where $R_{\xi y}$ is another reduction factor. Alternatively, the luminosity formula is written by

$$L = \frac{\gamma_+}{2er_e} \left(1 + \frac{\sigma_y^*}{\sigma_{x,eff}^*}\right) \frac{n_b I_+ \xi_{y+}}{\beta_y^*} \frac{R_L}{R_{\xi y}} \propto \frac{N_+ N_-}{\sigma_z \phi_x \sqrt{\varepsilon_y \beta_y^*}}$$

These formulae tell us that the luminosity can be large with keeping the beam-beam parameter constant when the both the vertical beta function at the IP and the vertical emittance can be small by the same ratio. The Piwinski angle implies how much we can squeeze the vertical beta function and SuperKEKB realizes the large Piwinski angle, Φ , more than 10-20, where

$$\Phi = \frac{\sigma_z}{\sigma_x^*} \tan \phi_x.$$

The hourglass effect in the nano-beam scheme determines a possible beta function at the IP. The vertical beta function at the IP can be squeezed to be

$$\beta_y^* > \frac{\sigma_z}{\Phi}.$$

In order to make a larger Piwinski angle, the small horizontal emittance is necessary, however, the horizontal beam-beam parameter is not affected in the nano-beam scheme. The machine parameters in Phase 2 are shown in Table 2.

There are several sub phases in Phase 2. We will start big beta functions at the IP, for instance, 81 mm in the vertical direction, in the first commissioning in order to find a closed orbit with the final focus system (QCS) [7]. This sub phase is called Phase 2.0. The hardware and software are checked and measurements and corrections of the beam optics with QCS are performed during Phase 2.0. The vacuum scrubbing in the vicinity of the IP will be done before the beam collision. The dithering system is also prepared and tested in this phase. Then, the beta functions are squeezed down to be 6 mm that is the same value of the bunch length, if necessary in Phase 2.1. In Phase 2.2, the vertical beta function is squeezed to be about 2 mm to test the nano-beam scheme. The first collision that means a measurement of beam-beam deflection will be performed during

this phase. Once we can perform Phase 2.2 successfully, we can squeeze the beta functions at the IP adiabatically. The local chromaticity corrections should be worked and several quadrupole magnets located in the matching sections near the arc sections are used to squeeze the beta functions without any modifications both of the final focus system and the local chromaticity corrections. Further beta squeezing in the vertical direction down to 1 mm will be done in Phase 2.4. The beta squeezing to the final value of 0.3 mm in the vertical direction will be tested between Phase 2.3 and Phase 2.4. We have a plan to squeeze the vertical beta function down to about 0.1 mm to study a possibility of future linear colliders, ILC and CLIC, if possible [8].

Table 2: Machine parameters in Phase 2 and comparisons with those of KEKB and Phase 3 final parameters. The left column is values in the LER and those of the HER in the right.

Parameter LER / HER	KEKB (2006)	Phase 2.2	Phase 2.3	Phase 2.4	Phase 3 (final)
β_x^* [mm]	590 / 560	256 / 200	128 / 100	128 / 100	32 / 25
β_y^* [mm]	6.5 / 5.0	2.16 / 2.40	2.16 / 2.40	1.08 / 1.20	0.27 / 0.3
ε_x [nm]	18 / 24	2.1 / 4.6	2.1 / 4.6	2.1 / 4.6	3.2 / 4.6
$\varepsilon_y/\varepsilon_x$ [%]	3 / 2.5	5.0	1.4	0.7	0.27 / 0.28
σ_x^* [μm]	103 / 116	23.2 / 30.3	16.4 / 21.4	16.4 / 21.4	10.1 / 10.7
σ_y^* [nm]	1900 / 1900	476 / 743	252 / 393	126 / 197	48 / 62
σ_z [mm]	7 / 7	6 / 5	6 / 5	6 / 5	6 / 5
ϕ_x [mrad]	11	41.5	41.5	41.5	41.5
Φ (Piwinski)	0.75 / 0.66	10.7 / 8.2	15.2 / 9.7	15.2 / 9.7	24.7 / 19.4
I [A]	1.66 / 1.34	1.0 / 0.8	1.0 / 0.8	1.0 / 0.8	3.6 / 2.6
(n_b)	(1388)	(1576)	(1576)	(1576)	(2500)
ξ_x	0.117 / 0.070	0.005 / 0.002	0.005 / 0.002	0.005 / 0.002	0.0028 / 0.0012
ξ_y	0.105 / 0.056	0.026 / 0.026	0.048 / 0.050	0.050 / 0.050	0.0881 / 0.0807
L_{sp} [$\text{cm}^{-2}\text{s}^{-1}/\text{mA}^2$]	1.06×10^{31}	1.97×10^{31}	3.94×10^{31}	7.88×10^{31}	2.14×10^{32}
L [$\text{cm}^{-2}\text{s}^{-1}$]	1.71×10^{34}	10^{34}	2×10^{34}	4×10^{34}	8×10^{35}

The specific luminosity as a function of the number of bunches multiplies the bunch current products is show in Fig. 5. We will start small beam currents with small number of bunches to keep bunch currents as much as possible. The nominal bunch current is 0.64 mA in the LER and 0.51 mA in the HER. When we will reach the specific luminosity of $2 \times 10^{31} \text{ cm}^{-2}\text{s}^{-1}/\text{mA}^2$, we will increase the number of bunches up to 1576 that corresponds to 3-bucket spacing similar to that of Phase 1. The total beam current of 1 A in the LER and 0.8 A in the HER achieves $10^{34} \text{ cm}^{-2}\text{s}^{-1}$ luminosity with 5 % emittance ratio. If we can improve the emittance ratio down to 1.4 %, the specific luminosity becomes approximately $4 \times 10^{31} \text{ cm}^{-2}\text{s}^{-1}/\text{mA}^2$ and $2 \times 10^{34} \text{ cm}^{-2}\text{s}^{-1}$ can be achieved which is almost the same luminosity of KEKB world record [9].

The dynamic aperture of the LER and HER are considered in Phase 2. In the case of Phase 2.3, Touschek lifetime is expected to be 60 min in the LER and 189 min in the HER without considering machine errors and beam-beam interactions. The machine error reduces the dynamic aperture about 10-20 % and the effect of the beam-beam interaction will be less than 10 %. Consequently, we assume the total lifetime of 40 min in the LER and 150 min in the HER during Phase 2.

Table 3 shows the requirements of linac beams during Phase 2. Since the dynamic aperture for the injected beam will be much smaller than that of Phase 1, the small emittance is necessary for the injected beam. In order to satisfy the requirements, the RF gun [10] is utilized for the electron beam and the positron beam are captured by the flux concentrator [11] and the huge emittance is reduced by using the 1.1 GeV damping ring [12] which locates an intermediate of the injector linac.

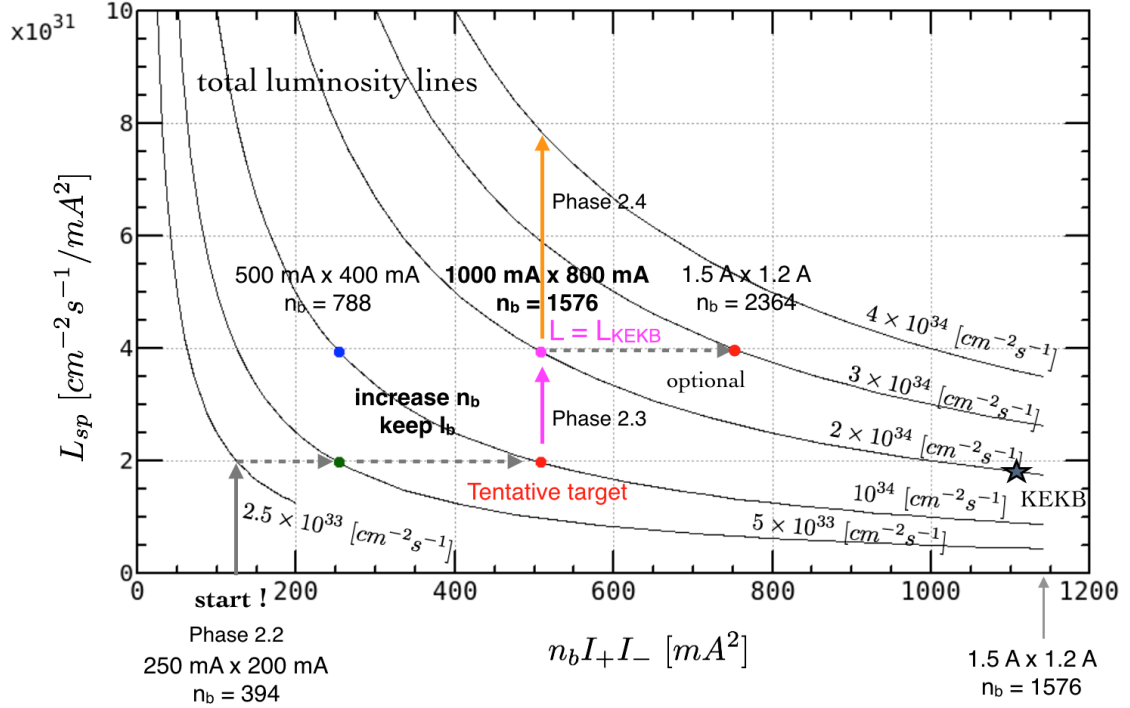


Figure 5: Travel guide for Phase 2. Specific luminosity as a function of number of bunches multiplies bunch current products. The curved line indicates total luminosity.

The commissioning of Phase 2 will be start mid of February 2018 and continue until mid of July 2018 for about five months. We expect that it will take one month at least for each sub phase. Several machine studies are planed with the physics run and the luminosity tuning. The vertical emittance is one of the most important parameters to improve the luminosity. Permanent solenoid-type magnets are installed in the LER as one of the countermeasures for the electron cloud effect during the long shutdown between Phase 1 and Phase 2. New type collimators are also installed in the both of LER and HER in the straight section near the IP to control beam backgrounds for the Belle II detector. We try to verify the nano-beam scheme and to get knowledge the beam background due to Touschek effects, beam-gas scatterings, and injection errors during Phase 2.

Table 3: Requirements for linac in Phase 2. The area of 95.4 % occupied by particles defines 2σ . The emittance is derived from the σ . The energy acceptance is defined by $3\sigma_\delta$.

<i>Parameter</i>	<i>Positron (LER)</i>	<i>Electron (HER)</i>	<i>Unit</i>
Beam energy	4	7	GeV
Normalized emittance, $\gamma\beta\epsilon_x / \gamma\beta\epsilon_y$	200 / 40	150 / 150	μm
Energy spread, σ_δ	0.16	0.10	%

Bunch charge at injection point	0.5	1.0	nC
---------------------------------	-----	-----	----

2.1.4 References

1. T. Abe et al., Technical Design Report of SuperKEKB, in preparation and to be published as a KEK report. A preliminary version is seen in <https://kds.kek.jp/indico/event/15914/>.
2. Y. Suetsugu, H. Hisamatsu, T. Ishibashi, K. Kanazawa, K. Shibata, M. Shirai, S. Terui, “First Commissioning of the SuperKEKB Vacuum System”, proceedings of the IPAC’ 16, Buson, Korea, TUP105 (2016).
3. H. Fukuma K. Ohmi, Y. Suetsugu, M. Tobiyama, “ELECTRON CLOUD AT SuperKEKB”, proceedings of eeFACT2016, Daresbury, UK.
4. Y. Ohnishi, Y. Funakoshi, H. Koiso, A. Morita, K. Oide, H. Sugimoto, “Optics Correction and Low Emittance Tuning at the Phase 1 commissioning of SuperKEKB”, proceedings of eeFACT2016, Daresbury, UK.
5. Y. Ohnishi et al., Prog. Theor. Exp. Phys., 2013 03A011 (2013).
6. “SuperB Conceptual Design Report”, INFN/AE-07/2, SLAC-R-856, LAL 07-15, March 2007.
7. N. Ohuchi et al., “Design of the Superconducting Magnet System for the SuperKEKB Interaction Region”, in Proceedings of NAPAC ’13, Pasadena, September 2013, WEODA1, pp. 759-961.
8. P. Thrane et al, CLIC-Note-1077, (2017).
9. T. Abe et al., Prog. Theor. Exp. Phys. 2013 03A001 (2013).
10. X. Zhou et al., “Developing an Yb/Nd Doped Hybrid Solid Laser of RF Gun for SuperKEKB Phase II Commissioning”, in Proceedings of IPAC ’17, Copenhagen, Denmark, May 2017, THPVA047, pp. 4540-4543.
11. T. Kamitani et al., “SuperKEKB Positron Source Construction Status”, in Proceedings of IPAC ’14, Dresden, Germany, MOPRI004, pp. 579-581.
12. M. Kikuchi, Nucl. Inst. Meth. A556, pp. 13-19 (2006), M. Kikuchi et al., “Design of Position Damping Ring for SuperKEKB”, in Proceedings of IPAC ’10, Kyoto, Japan, TUPEB054, pp. 1641-1643.

2.2 FCC-ee Optics Design

Katsunobu Oide
 Mail to: Katsunobu.Oide@kek.jp
 KEK, 1-1 Oho, Tsukuba, Ibaraki 305-0801, Japan

2.2.1 Introduction

The FCC-ee is a double-ring e^+e^- collider to be installed in a common tunnel of ~ 100 km circumference, as a potential first step before the FCC-hh hadron collider. The beam energy covers at least from the Z -pole (45.6 GeV) to $t\bar{t}$ (182.5 GeV) threshold. The design restricts the total synchrotron radiation (SR) power at 100 MW, thus the stored current per beam varies from 1.4 A at Z to 5.9 mA at $t\bar{t}$.

An update has been performed on the “baseline” beam optics[1] for the FCC-ee double-ring e^+e^- collider. The major changes are: (a) Mitigation of the coherent beam-beam instability[2,3] at Z by squeezing β_x^* down to 15 cm and changing the arc phase advance to $60^\circ/60^\circ$ at Z [4]. (b) Application of the twin aperture quadrupole scheme[5] to save the power consumption of quadrupole magnets. (c) Fitted to a modified layout of the FCC-hh collider[6]. The changes have been described at the IPAC’17 as well as FCC Week 2017[7,8].

Further changes have been made on the design until Nov. 2017: (d) Mitigation of the coherent beam-beam effect has been extended to W^\pm , and Zh . Parameters are re-optimized taking the 3D-flipflop effect and a “bootstrap” method has been developed to reach the maximum luminosity without causing the flipflop[4]. (e) Increased the beam energy at $t\bar{t}$ from 175 to 182.5 GeV considering the optimal measurements of the electroweak coupling[9]. (e) Filled dipoles to eliminate drift spaces in the arc as much as possible to improve the packing factor of dipoles. (f) The momentum acceptance due to DA has been effectively increased by “asymmetry acceptance” scheme at $t\bar{t}$. (g) Placed special sections for inverse Compton spectrometers[10] in the inner ring of the intermediated straight sections B and H.

The main characteristics of the optics design have been preserved: 45 to 182.5 GeV beam energy, 100 km circumference with two interaction points (IPs) per ring, horizontal crossing angle of 30 mrad at the IP, and the crab-waist scheme with local chromaticity correction system. The arc lattice has non-interleaved sextupole scheme with hundreds of independent families for both phase advances. A so-called “tapering” of all magnets is applied, which scales all fields of magnets except the solenoids with the local beam energy determined by the SR. An asymmetric layout near the interaction region suppresses the critical energy of SR incoming to the detector at the IP below 100 keV. Sufficient transverse/longitudinal dynamic apertures (DAs) have been obtained to assure adequate beam lifetime with beamstrahlung and top-up injection[11].

2.2.2 Optimization of machine parameters

The basic machine parameters have been chosen to maximize the luminosity under given constraints such as the circumference, layout, synchrotron radiation power, beam instabilities, and the capacity of the injector. The key physics is the beam-beam effects including beamstrahlung and coherent synchrotron-betatron resonance at each energy. The procedure of the optimization is described in Ref. [4] of this newsletter. The 6D dynamic aperture of the collider ring gives a definite boundary for the optimization.

Table 1 lists parameters related to beam optics, as the result of the optimization. The lattice for each energy has been constructed, and the dynamic aperture has been optimized at each energy to satisfy the requirements.

Table 1: Machine parameters of the beam optics of FCC-ee for each energy. More parameters are shown in Ref.~[1]. These parameters take the radiation loss along the ring with tapering into account.

	Z	W^\pm	Zh	$t\bar{t}$
Beam Energy [GeV]	45.6	80	120	182.5
Circumference [km]	97.756			
Arc phase adv. [deg]	60/60	90/90		
Mom. compaction [10^{-5}]	1.48	0.73		
β_x^* [m]	0.15	0.2	0.3	1
β_y^* [mm]	0.8	1	1	2
Hor. emittance ε_x [nm]	0.27	0.28	0.63	1.43
Ver. emittance ε_y [pm]	1.0	1.0	1.3	2.9
Hor. tune ν_x	269.138	389.154	389.129	389.104
Ver. tune ν_y	269.220	389.220	389.199	389.176
Long. tune ν_z	-0.0248	-0.0229	-0.0357	-0.0672
Bunch length σ_z (SR/BS) [mm]	3.5/12.1	3.3/7.65	3.15/4.9	2.45/3.3
Mom. spread σ_δ (SR/BS) [10^{-3}]	0.38/1.32	0.66/1.53	0.99/1.51	1.53/1.95
SR loss / turn U_0 [GeV]	0.036	0.334	1.69	9.05
RF frequency [MHz]	400 ^a			
RF voltage [GV]	0.096	0.43	1.96	10.6
RF bucket height [%]	1.9	1.9	2.3	4.7
Mom. acceptance by DA [%]	± 1.3	± 1.3	± 1.5	+2.4 -2.8
Crossing angle at IP [mrad]	30			
Crab waist strength [%]	97	90	85	50
# of turns for DA survey	2550	475	145	45

^aA mixture with 800 MHz is an option for $t\bar{t}$.

The lattice is basically common for all energies. The phase advance in the arc cell and β^* at the IP are changed only by strengths of quadrupoles. The RF cavities are common for two beams at $t\bar{t}$ and separated at lower energies, thus some re-arrangement of the RF section will be necessary. The detector solenoid, which is kept constant at 2 T for all energies, is currently removed from the lattice, since the effects on the optics and DA is minimized by a local compensation by counter solenoids.

The most significant change in the optics is to make the arc lattice compatible to both phase advances with non-interleaved sextupole scheme, and smaller $\beta^*_{x,y}$ at lower energies.

2.2.3 Changes in optics since FCC Week 2017

Let us describe several changes in the beam optics made after May 2017.

2.2.3.1 *Further reduction of β^* at the IP at Z, W^\pm , and Zh*

The $\beta^{*x,y}$ were (0.5 m, 1 mm) at Z, W^\pm , and Zh energies in the baseline in 2016, then was squeezed to (0.15 m, 1 mm) at Z by May 2017 to mitigate the coherent beam-beam effect. Further squeezes have been performed at Z, W^\pm , and Zh as shown in Table 1 since May as the result of maximizing the luminosity at each energy. The splitting final quadrupoles with variable polarities helped the squeeze by suppressing the chromaticity. The resulting momentum acceptance by DA has shrunk by the squeeze from the previous value $\pm 2\%$ to those shown in Table 1, but they are still acceptable considering the lifetime due to beamstrahlung.

2.2.3.2 *Increasing the beam energy at ttbar*

Although the beam energy at ttbar has been increased from 175 GeV to 182.5 GeV, the critical energy of SR from the upstream dipoles have been even reduced from 100 keV to 90 keV. This was made possible by a small rearrangement of the beam line in the interaction region. Thus if we allow 100 keV, there is a possibility to make the system more compact.

2.2.3.3 *A better packing factor of dipoles in the arc*

The phase advance per a FODO cell in the arc changes from $60^\circ/60^\circ$ at Z to $90^\circ/90^\circ$ at higher energies. As we have chosen the non-interleaved sextupole scheme for all energies, the location of the sextupoles depends on the phase advance. The sextupole for Z can be thinner than for other energies because of the energy. Then there are three types of the spacings between a quadrupole and the next dipole: a thick sextupole, a thin sextupole, no sextupole. If we want to fill the drift spaces as much as possible, then we need three lengths of the dipole magnets, which are 21.84 m, 23.54 m, 24.44 m in this case. Then the beam optics, especially the horizontal dispersion is no longer periodic in a FODO cell, but requires 35 FODOs. Actually $\beta_{x,y}$ are still almost periodic in a FODO, since the focusing of the dipoles are weak. While the deviation from a simple FODO brings a variation of the dispersion by about 10%, whose effect on the DA and other performance is small.

2.2.3.4 *Asymmetric momentum acceptance at ttbar*

The purpose of a wide momentum acceptance is to capture the particles which emitted a beamstrahlung photon at the IP. Since the primary energy change is always negative, the momentum acceptance can be wider in the negative side and somewhat narrower in the positive side. The acceptance in the positive side can be determined by the damping and the diffusion during a half cycle of the synchrotron motion as:

$$A_+ \approx -A_- \exp(-\alpha_z/2\nu_s) + 3\sigma_{\delta,BS} \sqrt{1 - \exp(-\alpha_z/\nu_s)}$$

where α_z , ν_s , $\sigma_{\delta,BS}$ are the longitudinal damping rate, synchrotron tune, and the equilibrium momentum spread including the beamstrahlung. We have set the size of the diffusion to be 3σ . At ttbar if we use $A_- = -2.8\%$, obtain $A_+ = +2.4\%$, which are shown in Table 1. The

optimization of the DA at ttbar has been done for such an asymmetric momentum acceptance. Since the effect at lower energies are weak, a symmetric acceptance has been applied.

2.2.3.5 *Spaces for inverse Compton spectrometer*

An inverse Compton spectrometer, proposed by N. Muchnoi[10], is a good candidate of devices for beam-energy calibration and a measurement of beam polarization. It hit the beam right before a dipole magnet and observed the scattered electrons and photons after the dipole. Such a location is available in the entrance of the inner ring at the intermediate straight section B and H, utilizing the dispersion suppressor dipole. For a precise measurement, the magnetic field between the dipole and the detector must be as simple as possible. Therefore we reconstructed the optics in that section to remove quadrupoles after the dipole for 100 m.

2.2.4 **Dynamic Aperture**

The resulting DA at each energy looks acceptable. The method is basically same as described in Ref. [1]. It includes synchrotron motion, synchrotron radiation damping in dipoles and quadrupoles, tapering, fringe field, and kinematical terms of all elements. The effects of the radiation fluctuation was evaluated separately. The DA has been optimized at each energy with a simplex method by varying all sextuple families, which are 212 and 296, at Z and higher energies, respectively. The resulting DAs for the ideal machines, shown in Fig. 1, look sufficient for the beamstrahlung and a top-up injection. The effects with machine errors, misalignments, beam-beam, and injection have been under study.

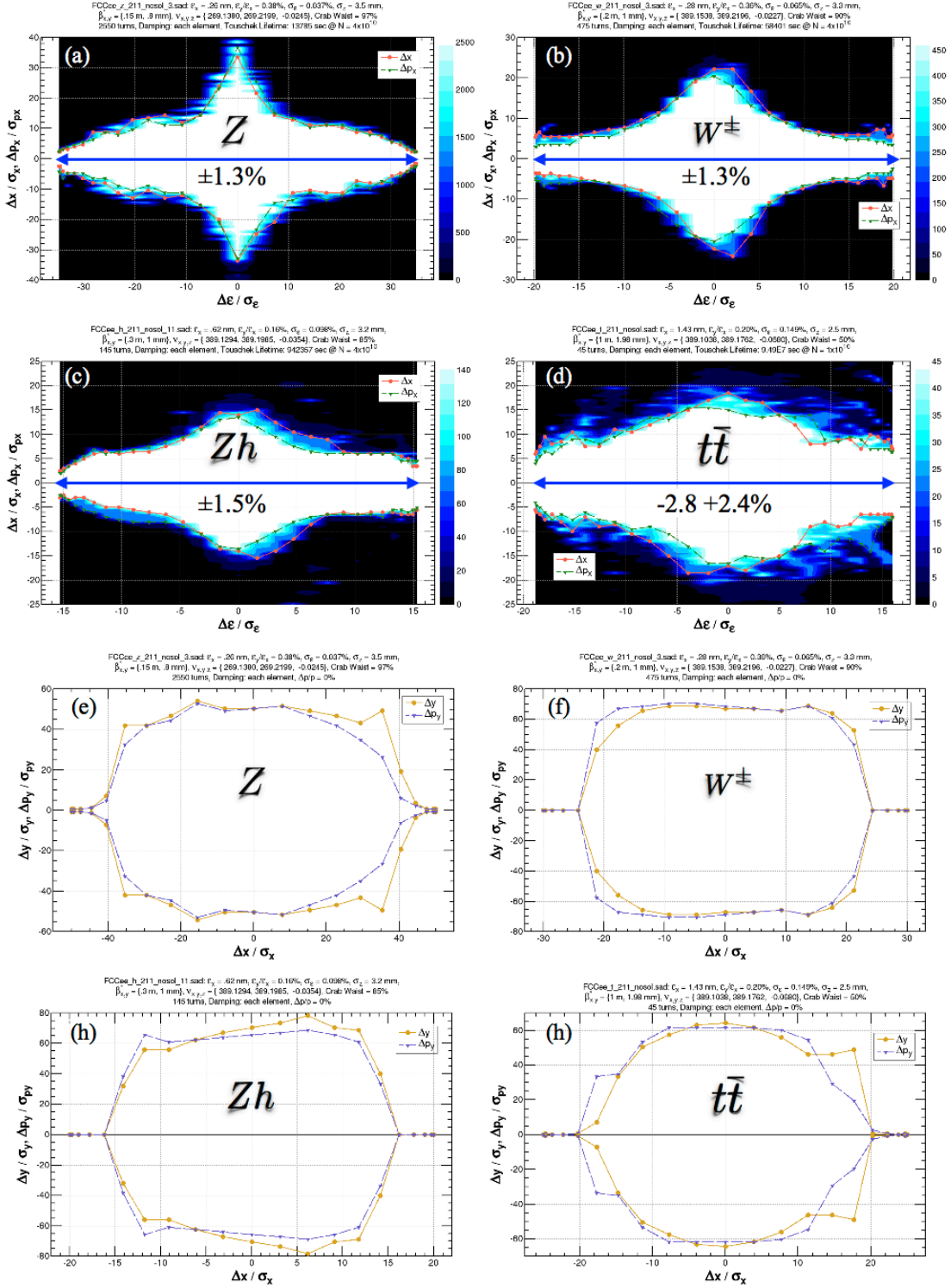


Fig. 1: The dynamic aperture of the FCC-ee collider ring at (a,e) Z , (b,f) W^\pm , (c,g) Zh , (d,h) $t\bar{t}$ energies. Plots (a,b,c,d) show the longitudinal acceptance, where J_y/J_x is chosen to the emittance ratio of Table 1. Plots (e,f,g,h) show the transverse acceptance at the design momentum. Tracking is done for the number of turns shown in Table 1, which corresponds to the 2 times the longitudinal damping time.

2.2.5 Acknowledgement

The author thank D. Shatilov for optimization of the luminosity. He also thank M. Benedikt, A. Blondel, A. Bogomyagkov, D. El Khechen, P. Janot, M. Koratzinos, E. Levichev, D. Zhou, and F. Zimmermann as well as all of FCC-ee team for various helps and suggestions.

2.2.6 References

1. K. Oide, *et al.*, “Design of Beam Optics for the FCC-ee Collider Ring”, *Phys.Rev.Accel.Beams* 19 (2016) no.11, 111005.
2. K. Ohmi, presentation at FCC Week 2016, May 11-15, Rome, Italy (2016).
3. K. Ohmi, *et al.*, “Coherent Beam-Beam Instability in Collisions with a Large Crossing Angle”, *Phys.Rev.Lett.* 119 (2017) no.13, 134801.
4. D. Shatilov, “FCC-ee Parameters Optimization”, in this newsletter (2017).
5. A. Milanese, “Efficient twin aperture magnets for the future circular e+/e-collider”, *Phys.Rev.Accel.Beams* 19 (2016) no.11, 112401.
6. D. Schulte, “FCC-hh Design Highlights” in this newsletter (2017).
7. K. Oide, *et al.*, “Progress in the Design of Beam Optics for FCC-ee Collider Ring”, IPAC’17, May 15-19, Copenhagen, Denmark (2017), TUOCB1.
8. K. Oide, presentation at FCC Week 2017, May 29-June 2, Berlin, Germany (2017).
9. e.g., P. Azzi, presentation at FCC Week 2017, May 29-June 2, Berlin, Germany (2017).
10. N. Muchnoi, presentation at FCC-ee Polarization Workshop, Oct. 17-28, CERN, Geneva. Switzerland (2017).
11. M. Aiba, *et al.*, “Top-up injection schemes for future circular lepton collider”, *Nucl.Instrum.Meth.* A880 (2018) 98-106.
12. <http://acc-physics.kek.jp/SAD/index.html>, <https://github.com/KatsOide/SAD>.
- 13.

2.3 A novel e+e- beam-beam instability

Kazuhito Ohmi
KEK, 1-1 Oho, Tsukuba, 305-0801, Japan
Mail to: kazuhito.ohmi@kek.jp

2.3.1 Introduction

Recently strong-strong beam-beam simulations have shown a strong coherent head-tail instability in collisions with a large crossing angle [1,2]. A cross wake force, which gives correlation between dipole moment densities of two beams, is introduced to explain the instability [2]. The cross wake force is regarded as ordinary wake force, when coherent head-tail beam-beam mode is limited to σ or π mode. Mode coupling due to the wake force is analyzed.

Collision scheme with a large crossing angle is being very popular in design of electron positron collision accelerator. In SuperKEKB project, a collision with a large crossing angle is performed to improvement luminosity. Future collision accelerator,

FCC is also designed with large crossing angle. The instability may affect all collider designs based on the crab waist scheme.

2.3.2 Cross wake force induced by beam-beam interaction

2.3.2.1 Cross wake force

Conventional transverse wake force characterize a transverse kick at z for dipole moment at z' . The momentum kick is expressed by

$$\Delta p_x = - \int_{-\infty}^{\infty} W(z - z') \rho_x(z') dz' \quad (1)$$

Causality gives limitation for $z' > z$: i.e. a dipole moment at head-part gives kick at tail part.

For collision with a crossing angle, dipole moment of e^+ beam at z' induces a transverse momentum kick in the other e^- beam at z . We represent the momentum kick using a cross wake. The cross-wake force mediates the correlation between two colliding bunches.

$$\Delta p_x^{(\mp)} = - \int_{-\infty}^{\infty} W^{(\mp)}(z - z') \rho_x^{(\pm)}(z') dz' \quad (2)$$

The cross wake force is represented by the Bassetti-Erskine formula with asymptotic form $F_x \sim 2/x$ [2],

$$W^{(\mp)}(z - z') = - \frac{N^{(\pm)} r_e}{\gamma^{(\mp)}} \frac{\partial F_x}{\partial x} \Big|_{x=(z-z')\theta_c} \quad (3)$$

Above, $\rho_x^{(\pm)}(z)$ is the longitudinal density distribution of the horizontal dipole moment of e^+ beam. An example of the wake force (FCC-ee-Z(HiLumi)) is shown in Figure 1. The parameters are summarized in Ref.[2]

The minimum cross wake is $W^{(\mp)}(0) \approx N^{(\pm)} r_e / \gamma^{(\mp)} \sigma_x^2$ at $z=0$, where $\sigma_x^2 = (\sigma_{x,+}^2 + \sigma_{x,-}^2)/2$. $W=0$ at $z \approx \pm 1.8\sigma_x/\theta_c = 1.8\sigma_z/\theta_p$, where $\theta_p = \theta_c \sigma_z/\sigma_x$ is Piwinski angle. Maximum is $W \approx 0.28 |W(0)|$ at $z \approx \pm 3.1\sigma_x/\theta_c = 3.1\sigma_z/\theta_p$. Frequency of the wake is evaluated as $\omega = 2\pi c/\lambda = c\theta_p/\sigma_z$, since the wave length $\lambda = 6.2\sigma_z/\theta_p$. Oscillation inside of the bunch is $\omega\sigma_z/c = \theta_p$.

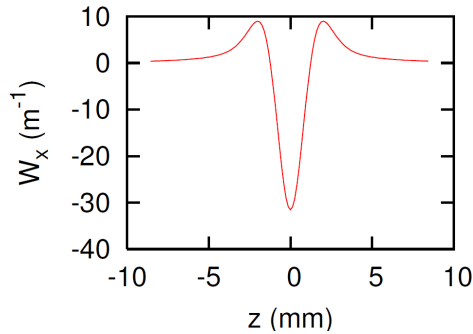


Figure 1: Cross wake force for FCC-ee-Z (HiLumi) [2].

2.3.2.2 σ and π mode

The cross wake force is treated as a usual single bunch wake by assuming a relation between the distributions of e+ and e- bunches. We consider the σ mode, in which dipole moments are equal, $\rho_x^{(+)}(z)=\rho_x^{(-)}(z)$, and the π mode, in which they are opposite $\rho_x^{(+)}(z)=-\rho_x^{(-)}(z)$. Eq.(2) then reduces to the usual formula for the wake force of a single bunch,

$$\Delta p_x = \mp \int_{-\infty}^{\infty} W(z - z') \rho_x(z') dz', \quad (4)$$

where the $-/+$ sign is chosen for σ/π mode, respectively.

Impedance is given by Fourier transformation of the Wake force,

$$Z(\omega) = i \int_{-\infty}^{\infty} W(z) e^{-i\omega z/c} \frac{dz}{c}.$$

Figure 2 shows the impedance for the wake in Fig.1. The wake force is symmetric for z , thus the real part of the impedance, which is given by sin transformation, is zero. The wake force is a large negative peak at $z=0$. The imaginary part, which is given by cos transformation, is negative.

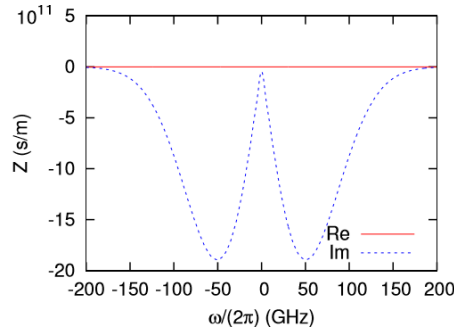


Figure 2: Impedance of the wake force for FCC-ee-Z in Fig.1 [1].

2.3.2.3 Conventional mode coupling theory

In the usual instability theory, the dipole moment is expanded by azimuthal and radial modes, and stability of each mode is discussed. The dipole moment in the longitudinal phase space is expanded by azimuthal modes using Fourier transformation for the synchrotron phase.

$$x(J, \phi) = \sum_{l=-\infty}^{\infty} x_l(J) e^{il\phi}, \quad (5)$$

where $\rho_x(z) = \int x(z, \delta) \psi_0(J) d\delta$ for the density distribution $\psi_0(J) = \exp(-\frac{J}{\varepsilon_z}) / (2\pi\varepsilon)$.

For the radial modes, each Fourier component is expanded using Laguerre polynomial ($L_k^{(l)}$).

$$x_l(J) = \sum_{k=0}^{\infty} x_{lk} \sqrt{k! (|l| + k)!} \hat{f}^{\frac{|l|}{2}} L_k^{(l)}(\hat{f}), \quad (6)$$

where $\hat{f} = J/\varepsilon_z$.

Each component oscillates for revolutions as

$$x_{lk} = a_{lk} e^{-i\mu s/c}.$$

Tune of each mode ($\mu=2\pi\nu$) is expressed by [3]

$$(\mu - \mu_x - l\mu_s)\delta_{ll'}\delta_{kk'} = M_{lkl'k'}. \quad (7)$$

The matrix M is expressed by

$$M_{lkl'k'} = \pm \frac{\beta_x}{2} i^{l-l'-1} \int_{-\infty}^{\infty} d\omega Z(\omega) g_{lk}(\omega) g_{l'k'}(\omega), \quad (8)$$

where

$$g_{lk}(\omega) = \frac{1}{\sqrt{2\pi k! (|l| + k)!}} \left(\frac{\omega \sigma_z}{\sqrt{2c}} \right)^{|l|+2k} e^{-\left(\frac{\omega \sigma_z}{\sqrt{2c}}\right)^2}.$$

The +/- sign is chosen for σ/π mode, respectively. The summation for every revolution harmonics is replaced by integration for ω , since the impedance is broadband.

The matrix element is evaluated by integration of impedance and bunch spectra of coupled two modes. We take notice that the impedance is symmetric. The integral for two modes with different parity in l, l' is 0. For same parity of l, l' , the matrix element is kept for exchange of l to l' and k to k' : that is, the matrix in Eq.(8) is symmetric. Eigenvalues for real symmetric matrix are real. Therefore the eigen-tunes are real: that is, the wake force/impedance causes tune shift, but does not cause instability.

2.3.3 Mode coupling theory for localized wake force

The wake force studying here is induced by the beam-beam interaction. It is localized at the interaction point. Localized linear force gives not only tune shift but also distortion of beta and linear resonances. The situation is the same for wake force, not only tune shift but also beta of modes are distorted by the wake force. Eigen state, in which the momentum kick is expressed by Eq (4), is analyzed.

We consider transfer matrix for the dipole moment (x_{kl}, p_{kl}), where $p(J, \phi)$ is expanded the same way as $x(J, \phi)$. Revolution matrix M_0 for the dipole moment (5) is expressed by

$$M_0 = e^{i\mu_s} \delta_{ll'} \delta_{kk'} \begin{pmatrix} \cos \mu_x & \sin \mu_x \\ -\sin \mu_x & \cos \mu_x \end{pmatrix}. \quad (9)$$

The transformation for the momentum kick due to the wake force in Eq.(4) is expressed by

$$M_W = \begin{pmatrix} 1 & 0 \\ -2 M_{lkl'k'} & 1 \end{pmatrix}, \quad (10)$$

where $M_{lkl'k'}$ is given in Eq. (8).

Stability of the colliding bunches is discussed by eigenvalues/vectors of the matrix product $M_W M_0$, which is a complex matrix. The size of matrices is $2 \times (2L_{\max}+1) \times n_k$. Here we show results for $L_{\max}=8$ and $n_k=20$: that is, the size of the matrix is 680^2 . Tune is $\nu_x=0.54$ and $\nu_s=0.018$.

Eigenvalues (λ 's) are plotted in Figure 3, where the growth rate per revolution and tune are given by $\log|\lambda|$ and $\tan^{-1}(\text{Im } \lambda / \text{Re } \lambda) / (2\pi)$, respectively. Figure shows the growth rate for σ/π modes. All of the π modes are stable. Pairs of growth and damping modes are seen in the σ modes. The unstable tunes are $0.5 + m\nu_s$, $m < 7$. The most unstable mode is at $\nu=0.5$. In ref [2], the dipole mode discretized in the longitudinal phase space was treated as base vector of eigenvalue problem. The unstable tunes were $m < 15$. The difference is due to the modes are terminated at $L_{\max}=8$ here. Dominant modes and the

growth rates are the same as those in Ref.[2]. The termination does not miss essentials of the physics.

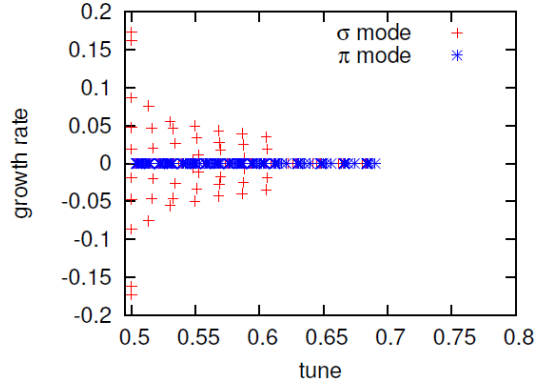


Figure 3: Eigenvalues of the beam-beam colliding system for FCC-ee-Z.

Eigen-tune as function of wake force strength illustrates mode coupling. Figure 4 shows eigenvalues, tune and growth rate, of σ modes for FCC-ee-Z parameter, where $v_x=0.54$ and $v_s=0.018$. W_0 is the design wake strength. Lines start from $v=v_x +lv_s$ at $W=0$. The matrices M_W and M_0 are symplectic, thus the eigenvalues should be $\exp(\pm i\mu)$. A pair of growth rates appears as $\pm \text{Im}v$. For $v < 0.5$, v , which is wrapped, results $v=1-(v_x+lv_s)$ for $l \leq -3$. For $l=-3,-4,-5$, v is 0.514, 0.532, 0.55, respectively, at $W=0$. An instability appears, when $l=-2$, $v=0.504$ mode approaches to 0.5 at ($W \sim 0.1W_0$). At the similar W , $l=-1,-3$ and $l=0,-4$ modes merge and imaginary tune appears. Mode coupling occurs between modes with the same parity, since the impedance is pure imaginary and symmetric for ω , Increasing the wake strength, modes $l=1,-5$ and $l=2,-6\dots$ are coupled. Diagonal components of Eq.(8) show that the tune shift is smaller for larger $|l|$. The threshold is higher when sum of two $|l|$'s is larger. The finite growth rate appears at the wake strength, where modes couples.

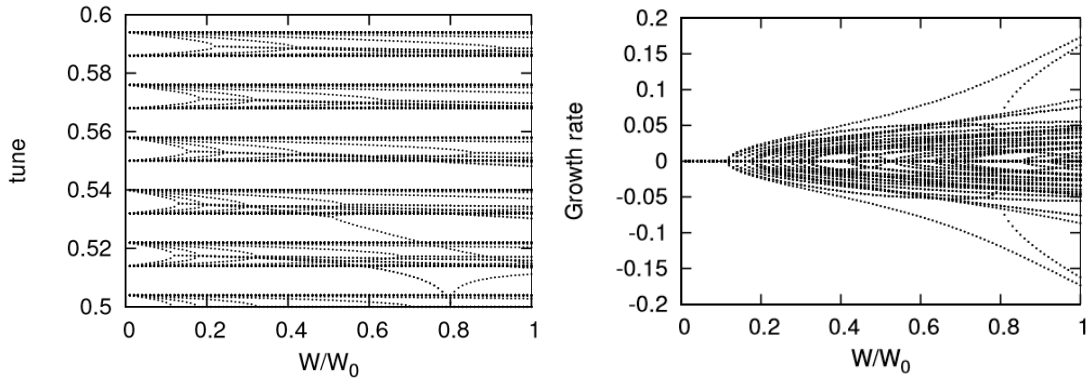


Figure 4: Tune and growth rate as function of wake field strength.

2.3.4 Summary

In collisions with a large crossing angle, correlation of dipole moments density of two beam is represented by the cross wake force. When the beam-beam mode is assumed σ/π modes, in which $\rho_x^{(+)}(z) = \pm \rho_x^{(-)}(z)$, the cross wake is regarded as an ordinary wake force. The wake force, which is induced by beam-beam interaction, is localized at IP. Mode

coupling theory with the localized wake force showed a strong head-tail instability, which has been seen in strong-strong beam-beam simulations.

2.3.5 References

1. K. Ohmi, proceedings of IPAC2016.
2. K. Ohmi, N. Kuroo, K. Oide, D. Zhou, F. Zimmermann, “Coherent beam-beam instability in collisions with a large crossing angle”, Phys. Rev. Lett., 119, 134801 (2017).
3. A. W. Chao, “Physics of Collective Beam Instabilities in High Energy Accelerators”, Wiley-Interscience Publication, New York, 1993).

2.4 FCC-ee Parameter Optimization

Dmitry Shatilov

Mail to: Shatilov@inp.nsk.su

BINP, Novosibirsk 630090, Russia

2.4.1 Introduction

FCC-ee is a double-ring e^+e^- collider which will work in the wide energy range from Z-pole (45.6 GeV) to $t\bar{t}$ (up to 185 GeV). At such high energies, beam-beam effects can get an extra dimension due to beamstrahlung (BS) – radiation in the field of the oncoming bunch [1, 2]. FCC-ee apparently will be the first collider where BS plays a significant role in the beam dynamics. For this to happen, two conditions must be fulfilled: high energy and high charge density in the bunches. For example, the energy in LEP was large enough, but the charge density too small, so the effect was negligible. BS increases the energy spread (and hence the bunch length) and creates long non-Gaussian tails in the energy distribution, that can limit the beam lifetime due to a possible ingress of particles beyond the energy acceptance.

Next, we will only consider the optimization process associated with the beam-beam effects. The actual table of parameters can be found in [3]. The collider has a two-fold symmetry and two IPs with a horizontal crossing angle and crab waist collision scheme [4, 5]. The luminosity per IP for flat beams ($\sigma_y \ll \sigma_x$) can be written as:

$$L = \frac{\gamma}{2e r_e} \cdot \frac{I_{tot} \xi_y}{\beta_y^*} \cdot R_{hg}, \quad (1)$$

where I_{tot} is the total beam current which in our case is determined by the synchrotron radiation power 50 MW. Therefore L can be increased only by making ξ_y larger and β_y^* smaller while keeping R_{hg} reasonably large. We assume that ξ_y can be easily controlled by N_p (number of particles per bunch), that implies adjusting the number of bunches N_b to keep I_{tot} unchanged.

The hour-glass factor R_{hg} depends on L_i/β_y^* ratio, where L_i is the length of interaction area which in turn depends on σ_z and Piwinski angle ϕ :

$$\phi = \frac{\sigma_z}{\sigma_x} \operatorname{tg}\left(\frac{\theta}{2}\right), \quad (2)$$

$$L_i = \frac{\sigma_z}{\sqrt{1+\phi^2}} \Rightarrow \frac{2\sigma_x}{\theta}. \quad (3)$$

Here θ is the full crossing angle, and expressions after arrow correspond to $\phi \gg 1$ and $\theta \ll 1$, see Fig. 1.

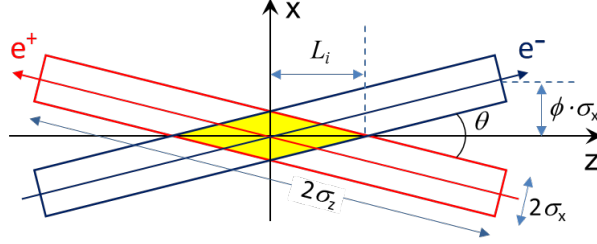


Figure 1: Collision scheme with large Piwinski angle.

The beam-beam parameters for $\sigma_y \ll \sigma_x$ and $\theta \neq 0$ become [6]:

$$\begin{aligned} \xi_x &= \frac{N_p r_e}{2\pi\gamma} \cdot \frac{\beta_x^*}{\sigma_x^2(1+\phi^2)} \Rightarrow \frac{N_p r_e}{\pi\gamma} \cdot \frac{2\beta_x^*}{(\sigma_z\theta)^2} \\ \xi_y &= \frac{N_p r_e}{2\pi\gamma} \cdot \frac{\beta_y^*}{\sigma_x\sigma_y\sqrt{1+\phi^2}} \Rightarrow \frac{N_p r_e}{\pi\gamma} \cdot \frac{1}{\sigma_z\theta} \sqrt{\frac{\beta_y^*}{\varepsilon_y}} \end{aligned} \quad (4)$$

In particular, $\xi_x \propto 1/\varepsilon_x$ (in head-on collision) transforms to $\xi_x \propto \beta_x^*/\sigma_z^2$ when $\phi \gg 1$, and ξ_y dependence on σ_x vanishes. Further, because of the symmetry, we consider a model with one IP (that is a half ring of the real collider).

2.4.2 Luminosity Optimization at the Top Energy

At 175÷185 GeV the beam lifetime is determined mainly by single high-energy BS photons [2], that imposes another limitation on the luminosity. For the beamstrahlung lifetime we have [7]:

$$\tau_{BS} \propto \exp\left(\frac{2\alpha\eta\rho}{3r_e\gamma^2}\right) \cdot \frac{\rho\sqrt{\eta\rho}}{L_i\gamma^2}, \quad (5)$$

where α is a fine structure constant, η is the energy acceptance (which should be maximized), and ρ is the bending radius of particle's trajectory in the field of oncoming bunch. Evidently, ρ is inversely proportional to the absolute value of transverse electromagnetic force acting on the particle. Its dependence on the transverse coordinates for flat beams is shown in Fig. 2. The lifetime is determined by the minimum values of ρ which correspond to the particles with $|x| < \sigma_x/2$ and $|y| > 2\sigma_y$. However, during collision particles traverse the opposite bunch horizontally because of the crossing angle. This means that the maximum force depends mainly on the vertical coordinate, and ρ is inversely proportional to the surface charge density in the horizontal plane:

$$\frac{1}{\rho} \propto \frac{N_p}{\gamma\sigma_x\sigma_z} \propto \frac{\xi_y}{L_i} \sqrt{\frac{\varepsilon_y}{\beta_y^*}} \propto L \sqrt{\frac{\varepsilon_y}{\beta_y^*}}. \quad (6)$$

These relations are valid for both head-on and crossing angle collisions; the last transformation is based on (1) and assumption that $L_i \approx \beta_y^*$.

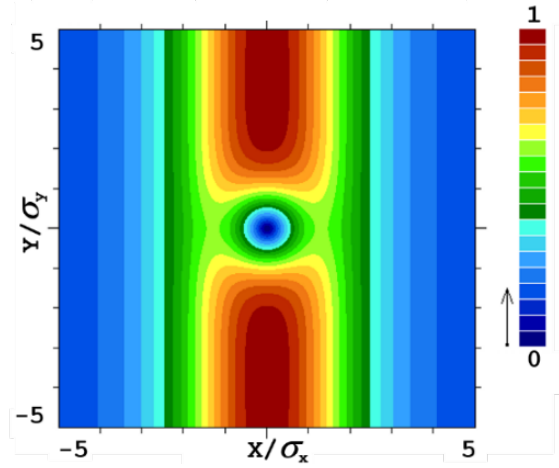


Figure 2: Absolute value of transverse force for flat beams, in relative units.

Our goal is to increase L while keeping the lifetime (and therefore ρ) large enough. It follows that ε_y (i.e. both the betatron coupling and ε_x) should be minimized, and β_y^* should be *increased*. For example, increase in β_y^* (together with L_i) by a factor of k may result in the luminosity gain by $k^{1/2}$ with ρ unchanged. In fact, as is seen from (5), τ_{BS} is inversely proportional to L_i provided that $\rho = const$. Therefore, to keep $\tau_{BS} = const$ when L_i is increased, we need to slightly increase ρ . However, τ_{BS} dependence on L_i is much weaker than the dependence on ρ (because the argument of exp is $\gg 1$), so the gain in luminosity will be “almost” $k^{1/2}$. All these manipulations mean an increase in σ_x and N_p , but other than that, ξ_y will also rise by $k^{3/2}$. Consequently, we may perform such optimization only as long as ξ_y remains below the beam-beam limit.

This can be formulated in a different way. If there are multiple limiting factors, the maximum performance is achieved when all limits are reached simultaneously. In our case it means that β_y^* (together with L_i) should be adjusted in such a way that both τ_{BS} and ξ_y achieve their limits. This implies that if the balance shifts towards “limit by the BS lifetime” (e.g. decrease in η or increase in γ , ε_y), the luminosity optimization will require

some increase in L_i (together with β_y^*), and vice versa. But we should not forget that the condition $L_i \approx \beta_y^*$ is not very strict.

If the bunch population is less than the nominal value, BS for the counter (strong) bunch weakens and its length decreases accordingly. Therefore, BS for the weak bunch becomes stronger and its lifetime decreases. Top-up injection can provide an asymmetry within $\pm 3\%$, while the lifetime should be ≥ 15 minutes. For safety margins, we chose the nominal N_p to get a lifetime of ~ 25 minutes for $N_p^w = 0.97 \cdot N_p$ and $N_p^s = 1.03 \cdot N_p$. Hereinafter the superscripts w and s mark the weak and the strong beams, respectively.

To find the optimum beta-functions we tested several options, and assume for now that η does not depend on β^* . The results for 182.5 GeV are presented in Table 1. As we see, a decrease in β_x^* requires smaller N_p in order to keep the lifetime unchanged. Accordingly increase in β_x^* helps to rise up the luminosity. Comparing the last two columns, note that the luminosity increases by only 10% when β_y^* halves; the reason is the hour-glass which is just optimal for the rightmost column. Then, taking into account that in fact dynamic aperture and energy acceptance are larger for relaxed β^* , the values in last column ($\beta_x^* = 100$ cm, $\beta_y^* = 2$ mm) should be considered closest to the optimal.

Table 1: Luminosity at 182.5 GeV for different β^* .

<i>Parameter</i>	$\beta_x^* = 50$ cm		$\beta_x^* = 100$ cm	
$\varepsilon_x / \varepsilon_y$ [pm]	1450 / 2.9			
σ_z (SR / BS) [mm]	2.5 / 3.3			
η	0.025			
Asymmetry	$\pm 3\%$			
τ_{BS} [min]	~ 25			
ϕ (with BS)	1.84		1.3	
L_i [mm]	1.6		2.0	
N_p [10^{11}]	2.1		2.8	
N_b	52		39	
β_y^* [mm]	1	2	1	2
L [10^{34} cm $^{-2}$ c $^{-1}$]	1.5	1.3	1.65	1.5

2.4.3 Beam-Beam Interaction at Low Energies

When energy decreases, the lifetime limitation due to BS weakens. This is easy to understand from the following considerations. Assuming that the lattice is not changed, emittances drop quadratically and σ_x, L_i – linearly with energy. If we keep ξ_y and β_y^* unchanged then, as follows from (6) and (5), ρ remains constant and τ_{BS} grows significantly because its dependence on γ is very strong. Hence at low energies we may allow some reduction of η , and for higher luminosity we need to decrease β_y^* and ρ . Consequently, since the bending radius in dipoles remains unchanged, the relative contribution of BS to the energy spread grows and the bunch lengthening becomes larger. For example, σ_z increases due to BS almost 3.5 times at 45.6 GeV and only 1.3 times at 182.5 GeV. Why then we do not see this effect in low energy colliders? Because they have much higher magnetic field in the dipoles or, which is the same, much smaller bending radius in the arcs.

Reduction of β_y^* has also limitations related to its maximum value in the nearest to IP quadrupole QD0: β_y^{\max} depends on L^* (distance from IP to the quad's edge) and its strength. If QD0 is divided longitudinally into several sections, as shown in Fig. 3, then at low energy we can use only the first section – with larger gradient. This moves the azimuth of β_y^{\max} towards IP and helps to reduce β_y^* . In addition, the following sections can be turned in the opposite polarity and used as QF1.

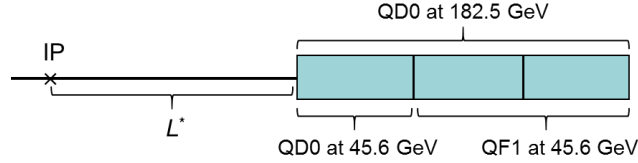


Figure 3: Longitudinal slicing of QD0.

Next we will consider the beam-beam effects at 45.6 GeV, where $\beta_y^* = 0.8$ mm can be obtained [3]. Decreasing σ_x and increasing σ_z leads to $\phi \gg 1$, so we can take full advantage of crab waist collision scheme. On the other hand, in collisions with $\phi \gg 1$ new phenomena were recently discovered in simulations: 3D flip-flop [8] and coherent X-Z instability [9, 10]. It is these effects that now limit the collider performance, and further optimization was aimed at finding such parameters with high luminosity at which these instabilities do not arise.

2.4.3.1 3D Flip-flop

Flip-flop instability is a well-known effect. For flat beams, where the perturbations occur mainly in the vertical direction, the same applies to flip-flop: it is actually 1D. In FCC-ee we have another kind of flip-flop, which is essentially 3D; beamstrahlung makes the difference. The threshold depends on asymmetry in population of colliding bunches, which causes a positive feedback in the following chain:

- 1) Asymmetry in the bunch currents leads to asymmetry in the bunch lengths (due to beamstrahlung).
- 2) In collisions with $\phi \gg 1$, asymmetry in the bunch lengths enhances synchrotron modulation of the horizontal kick for a longer bunch, thus amplifying synchro-betatron resonances. In addition, ξ_x^w grows quadratically and ξ_y^w – linearly with decrease of σ_z^s , so the footprint expands and can cross more resonances. All this leads to increase in both emittances of the weak bunch (but mainly ε_x^w).
- 3) An increase in ε_x^w has two important consequences: a) weakening of BS for a strong bunch, which makes it shorter, and b) growth of ε_y^w due to the betatron coupling, which leads to asymmetry in the vertical beam sizes.
- 4) As follows from Fig. 2, the greatest BS is experienced by the particles with the vertical coordinates $|y^w| > 2\sigma_y^s$. When $\sigma_z^w > \sigma_z^s$, the number of particles in the weak bunch experiencing strong BS increases while the number of such particles in the strong bunch decreases. Thus, asymmetry in the vertical beam sizes leads to further increase of asymmetry in the bunch lengths.
- 5) Now we go back to point 2, and the loop is closed.

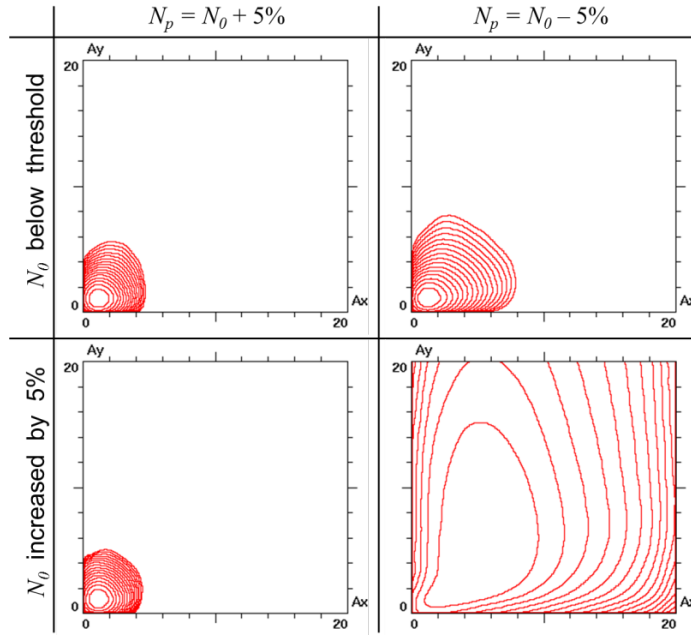


Figure 4: Example of 3D flip-flop. Density contour plots ($\sqrt{6}$ between successive lines) in the space of normalized betatron amplitudes are shown for stable (top) and unstable (bottom) cases.

In the end, we can get very strong blowups in all three directions, an example is shown in Fig. 4. Here asymmetry in the bunch currents is $\pm 5\%$. The top row corresponds to stable situation, though some acceptable blowup of the weak bunch is seen. In the bottom row asymmetry is the same, but N_p increased by 5%. As a result the strong bunch shrank to unperturbed sizes (as without beam-beam), while the weak bunch became swollen in all three dimensions. Hence, this instability can limit the maximum allowable N_p , and consequently the luminosity.

2.4.3.2 *Coherent X-Z instability*

This instability develops in the horizontal plane and it is manifested by wriggle of the bunch shape. If we imagine that the bunch is sliced longitudinally in many pieces, the amplitudes of X-displacement of the slices depend on their Z-coordinates and vary on every turn. In Fig. 5 we can see ε_x evolution with time and coordinates of centers of slices at different turns. Red line corresponds to unperturbed state, green – to oblique part of the curve on the right, and blue – to the final stage with ε_x blown up.

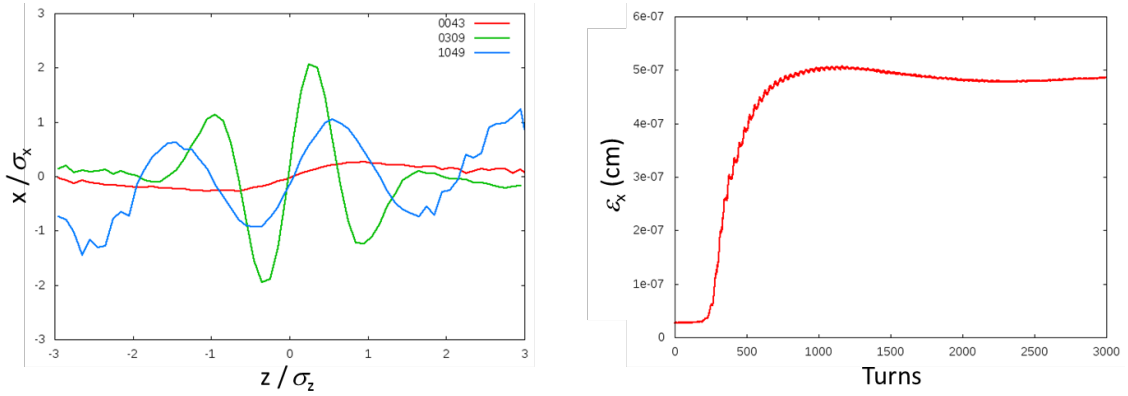


Figure 5: Example of coherent X-Z instability: the bunch shape at 43, 309 and 1049 turns (left) and evolution of the horizontal emittance (right).

The wiggles disrupt the operation of crab waist scheme, but the main damage is associated with a multiple increase in the horizontal emittance. In collision schemes with $\phi \gg 1$, an increase in ϵ_x itself does not have a noticeable impact on luminosity. However, this leads to a proportional increase in ϵ_y due to the betatron coupling, so eventually the luminosity will decrease several times. The instability does not cause dipole oscillations and therefore cannot be suppressed by feedback. We need to look for conditions under which it does not arise.

2.4.3.3 *Parameters optimization at Z*

Both instabilities are associated with the growth of ϵ_x , therefore we have to reduce β_x^* which means a decrease in both the normalized horizontal kick and ξ_x . One of the features of FCC-ee IR design is the absence of local horizontal chromaticity correction sections. Because of this, β_x^* cannot be made too small, and attempts to do this lead to a decrease in the energy acceptance. Nevertheless, β_x^* can be reduced to 15 cm while obtaining a sufficient $\eta = 1.3\%$ [3]. Longitudinal slicing of QD0 and the use of its part as QF1 (see Fig. 3) helps to achieve this. However, this is not enough to suppress the instabilities.

The next step is to reduce ξ_x with a given β_x^* . In fact ξ_x is important not itself, but in comparison with ν_s . As we shall see later, the greatest danger arises from synchro-betatron resonances $2\nu_x - 2m \cdot \nu_s = 1$, the distance between them is just ν_s . Our task is to make ξ_x noticeably smaller than ν_s , then we can put the working point and the whole footprint between resonances. Herewith, by decreasing ξ_x we should preserve the luminosity, i.e. ξ_y . In assumption that $\beta_{x,y}^*$ and ϵ_y were already minimized and therefore are not free parameters, from (4) it follows that the only way to reduce ξ_x/ξ_y ratio is to increase the bunch length. The requirement of keeping ξ_y unchanged means that N_p/σ_z is constant, therefore ξ_x decreases by the same factor that σ_z grows (not quadratically as it may seem). However, if we simply reduce RF voltage, ν_s also decreases and the ratio ξ_x/ν_s does not change. We will return to lowering U_{RF} later, but now consider another way of the bunch lengthening: an increase in the momentum compaction factor α_p [11].

An advantage is that ν_s grows together (and by the same factor) with σ_z and $1/\xi_x$. In addition, larger α_p increases the threshold of microwave instability to an acceptable level. The main drawback of this approach is that ϵ_x also grows in the power of 3/2 with respect to α_p . As we already said, ϵ_x is not so important by itself, but ϵ_y should be small and it is

usually proportional to ε_x , though at low energy some contribution to ε_y (0.2÷0.3 pm) comes from the detector solenoids. Besides, when the natural emittance is very small, various weak effects (feedback noises, etc.) become noticeable. For these and some other reasons, the lower limit for ε_y was set to 1 pm. Since the natural emittance at 45.6 GeV in the nominal lattice with small α_p is less than 90 pm, even its threefold increase still allows to obtain $\varepsilon_y = 1$ pm with adopted for FCC-ee betatron coupling 0.2%. Thus we switched to a lattice where doubling of α_p is achieved by reducing the phase advance per FODO cell in the arcs from 90°/90° to 60°/60° [3, 12]. At higher energies (80, 120 GeV), where instabilities are also present, this approach no longer has an advantage, due to an unacceptable increase in ε_y .

To select the working point, we performed a scan of betatron tunes in a simplified model: linear lattice without explicit betatron coupling. The beam-beam effects were implemented in a weak-strong approximation, so there are no coherent instabilities. The results are presented in Fig. 6.

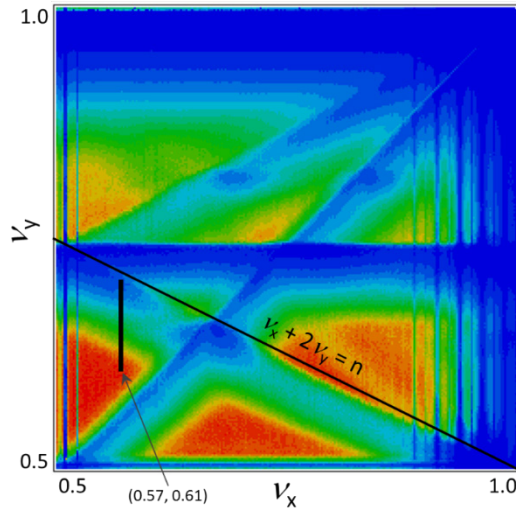


Figure 6: Luminosity as a function of betatron tunes. The color scale from zero (blue) to $2.3 \cdot 10^{36} \text{ cm}^{-2} \text{ c}^{-1}$ (red). The black narrow rectangle shows the footprint at (0.57, 0.61).

Since $\xi_x \ll \xi_y$, the footprint looks like a narrow vertical strip, bottom edge resting on the working point. Particles with small vertical betatron amplitudes have maximum tune shifts and are in the upper part of the footprint, so the resonances in Fig. 6 seem to be shifted down. The good region is reduced to a red triangle bounded by the main coupling resonance $\nu_x = \nu_y$, sextupole resonance $\nu_x + 2\nu_y = n$, and half-integer resonance $2\nu_x = 1$ with its synchrotron satellites. All other higher-order coupling resonances are suppressed by crab waist, and therefore are not visible. From this plot it is also clear that moving the working point to the right we should increase ν_y to keep the distance to the main coupling resonance. Both these actions lead to a decrease in the distance between the upper edge of the footprint and the resonance $\nu_x + 2\nu_y = n$. Thus, if we want to have large ξ_y , the range of permissible ν_x is bounded to the right by the values 0.57÷0.58.

Then we performed a scan of ν_x in a quasi-strong-strong model, in which coherent instabilities and flip-flop can be observed. The results are presented in Figures 7 and 8, where the synchro-betatron resonances are clearly seen. As the order of resonances increases their strength weakens, but we cannot move the working point too far to the right. Accordingly, for $U_{\text{RF}} = 250 \text{ MV}$ there are no regions free from coherent instability

in the working range of ν_x . And here we are helped by the reduction of U_{RF} , thereby decreasing ν_s (while ξ_x/ν_s not changed) and increasing the order of resonances located in the region of interest. In the end, we can now find good working points. Note that N_p for the green lines in Figs. 7 and 8 was adjusted to get the same ξ_y as for the red line.

Here it is appropriate to recall the semi-analytical scaling law obtained from other considerations for the threshold bunch intensity [12]:

$$N_{th} \propto \frac{\alpha_p \sigma_\delta \sigma_z}{\beta_x^*}, \quad (7)$$

where σ_δ is the energy spread. In respect that $\alpha_p \sigma_\delta \propto \nu_s \sigma_z$ and $\xi_x \propto N_p \beta_x^* / \sigma_z^2$, this is nothing else than a condition on the ratio ξ_x / ν_s . We obtained a similar relation from the simple requirement to "squeeze" the footprint in between synchro-betatron resonances.

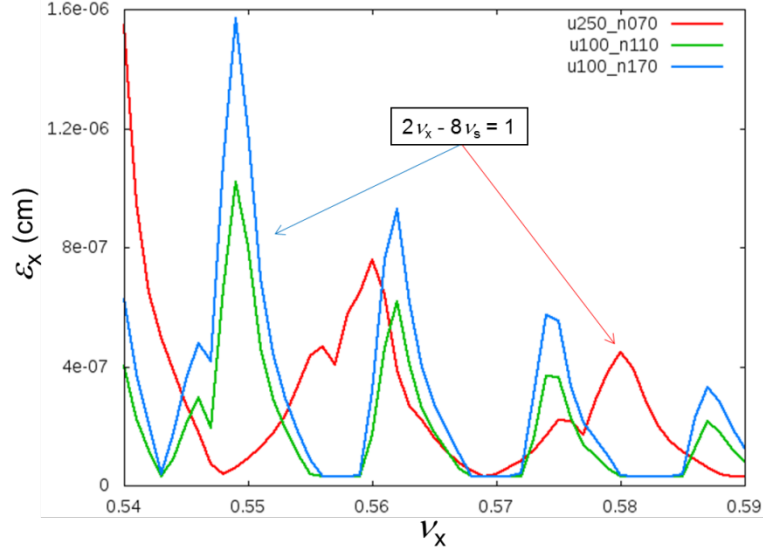


Figure 7: Growth of ε_x due to coherent X-Z instability, as a function of ν_x . Red line corresponds to $U_{RF} = 250$ MV, $N_p = 7 \cdot 10^{10}$, green and blue lines – $U_{RF} = 100$ MV, $N_p = 1.1 \cdot 10^{11}$ and $1.7 \cdot 10^{11}$.

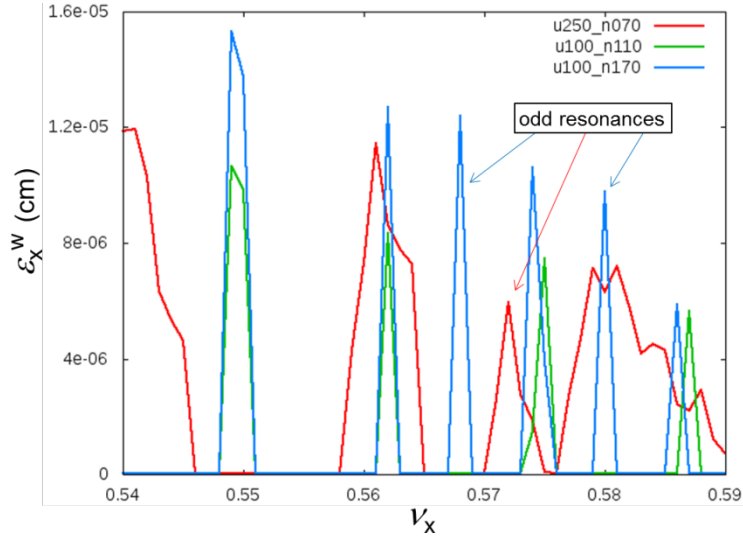


Figure 8: Growth of ξ_x^w due to 3D flip-flop, as a function of ν_x . The colors are the same as in Fig. 7. Asymmetry in the bunch currents is $\pm 5\%$ for red and green lines, $\pm 3\%$ for blue line.

However, as for the threshold, it is not so simple. Indeed, as N_p increases, σ_z will also grow. In our range of parameters, where σ_z is defined mainly by BS, it scales as $\sigma_z^2 \propto N_p$. The rationale for this dependence is not so obvious, and we will not go into this, but in the simulation it was confirmed with good accuracy. As a result, it turns out that ξ_x does not depend on N_p . Thus if we stay in a good area, N_p can be increased – and there is simply no threshold. This is clearly seen in Fig. 7 comparing the green and blue lines, which differ only in N_p . The reverse side of this coin is that if we have instability, then getting rid of it simply by reducing N_p will be quite difficult. To do this, it is necessary to descend to the region where the dependence $\sigma_z^2 \propto N_p$ is violated, which means a decrease in the luminosity several times.

Then if we stay at a good point, what limits us? First, the increase in the energy spread (due to BS), which becomes comparable with that on the top energy. The non-Gaussian tails of the energy distribution are now not so long, but η has almost halved – as a result of a significant decrease in β_x^* and damping decrements. Consequently, as N_p grows, we will encounter a lifetime limitation by the energy acceptance. Secondly, by increasing ν_x (and correspondingly ν_y) we reduced the allowable ξ_y and approach the ordinary beam-beam limit. This is particularly evident in Fig. 8, where the asymmetry causes an additional increase in ξ_y^w which reinforces the flip-flop. And we see how additional odd resonances appear to the right – where the top of footprint approaches $\nu_x + 2\nu_y = n$. It means that minimizing asymmetry in the currents of colliding bunches again becomes critical.

In the end we can get high luminosity, but bunches will lengthen ~ 3.5 times because of BS. If we bring into collision so large currents with the “nominal” σ_z (energy spread created only by SR), the beam-beam parameters will be far above the limits and the beams will be blown up and killed on the transverse aperture, before they are stabilized by BS. To avoid this, we must gradually increase the bunch current during collision, so we come to bootstrapping. An example is presented in Fig. 9. We start with approximately one quarter of the final bunch population, then adding small portions to e^+ and e^- beams by turns. In fact, the injection cycle will last about 2 minutes, but in simulations it was reduced to ~ 2 damping times (10000 turns in “half-ring” collider).

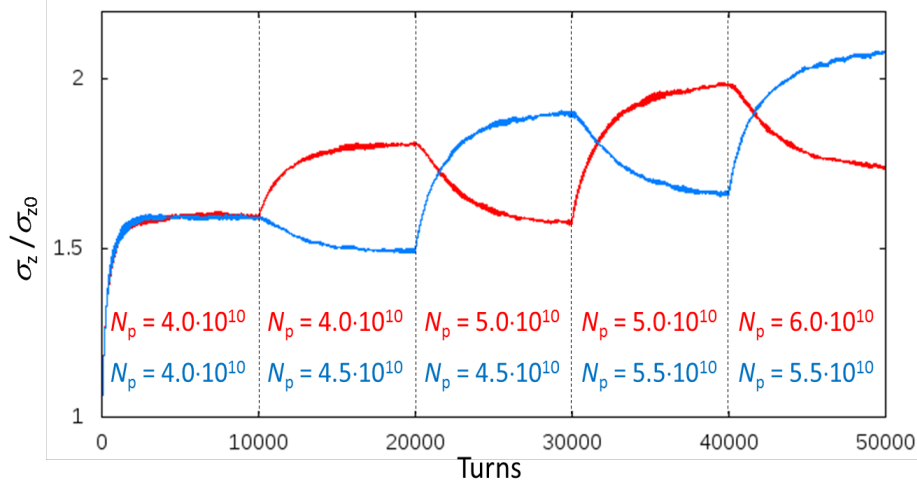


Figure 9: Simulated bootstrapping for Z-pole operation.

2.4.3.4 *Parameters optimization at W and HZ*

As the energy increases, the bunch lengthening and Piwinski angle decrease, while the damping decrements grow. Hereby both instabilities weaken, but still continue to be determining factors. In connection with this, the procedure for optimizing the parameters was similar to that at Z-pole and consisted of the following steps:

- 1) The RF voltage is made small, but so that RF acceptance still exceeds the energy acceptance, and this defines ν_s . Then ν_x is selected in the range of $0.565 \div 0.580$ with a condition $\nu_x \approx 0.5 + \nu_s \cdot (m + 0.5)$, and $\nu_y = \nu_x + 0.03 \div 0.04$.
- 2) At this working point, we look for β_x^* at which the coherent X-Z instability disappears, while N_p is set to some reasonable value – as we said above, the threshold does not depend on this. The final value of β_x^* is selected slightly below the threshold (namely, 20 cm at 80 GeV and 30 cm at 120 GeV). In this case, the 3D flip-flop usually also disappears, and if not, just move ν_x a little.
- 3) The lattice optimization is performed for the selected β_x^* (and $\beta_y^* = 1$ mm) in order to maximize the dynamic aperture and energy acceptance [3]; hereby we obtain η (namely, 1.3% and 1.5%).
- 4) Then quasi-strong-strong simulations are performed with asymmetry $\pm 3\%$ (this is determined by the required beam lifetime and the injection cycle time). The bunch population N_p is scanned, while the restriction is the lifetime of the weak bunch. In this way, we determine the maximum N_p and luminosity.

Note that at 120 GeV single high-energy BS photons also become important, and they impose a limit on N_p , but β^* should be optimized from other considerations.

2.4.4 **Conclusion**

FCC-ee is designed for a wide range of energies, so the parameters optimization looks different at different points. The biggest problem at low energies is represented by two new phenomena found in simulations: 3D flip-flop and coherent X-Z instability. To combat them, the following steps were taken: an increase in the momentum compaction factor (at Z-peak only), a decrease in β_x^* and U_{RF} (and thereby in ν_s), an increase in $\nu_{x,y}$

by about 0.03 compared to the original design, and a neat choice of ν_x between synchrotron resonances. Note that an increase in $\nu_{x,y}$ has one more benefit: the tunes of the entire ring move farther from the integer, that facilitates the tuning of linear optics.

At the top energy, the instabilities are suppressed by very strong damping, but another problem becomes dominant: the lifetime limitation by single high-energy beamstrahlung photons. Therefore, in contrast to low energies, optimization requires an increase in beta-functions. It should also be noted that in the entire energy range, beamstrahlung plays a decisive role and luminosity is limited by the energy acceptance.

2.4.5 Acknowledgements

The author would like to thank K. Oide, K. Ohmi and M. Zobov for many useful discussions. This work has been supported by Russian Science Foundation (project N14-50-00080).

2.4.6 References

1. J. Augustin et al., "Limitations on Performance of e+e- Storage Rings and Linear Colliding Beam Systems at High Energy", eConf C781015, 009 (1978).
2. V. Telnov, "Restriction on the Energy and Luminosity of e+e- Storage Rings due to Beamstrahlung", Phys. Rev. Lett. 110, 114801 (2013).
3. K. Oide, "FCC-ee Optics Design", in this Newsletter (2017).
4. P. Raimondi, D. Shatilov, and M. Zobov, "Beam-Beam Issues for Colliding Schemes with Large Piwinski Angle and Crabbed Waist", LNF-07-003-IR (2007), e-Print: physics/0702033.
5. M. Zobov et al., "Test of Crab Waist Collisions at DAΦNE Phi Factory", Phys. Rev. Lett. 104, 174801 (2010).
6. P. Raimondi and M. Zobov, "Tune shift in beam-beam collisions with a crossing angle", DAFNE Tech. Note G-58 (2003).
7. A. Bogomyagkov, E. Levichev and D. Shatilov, "Beam-beam effects investigation and parameters optimization for a circular e+e- collider at very high energies", Phys. Rev. ST Accel. Beams, 17, 041004 (2014).
8. D. Shatilov, "Flip-flop Instability in FCC-ee at Low Energies", presented at eeFACT2016, Daresbury, UK (2016).
9. K. Ohmi, "Study of Coherent Head-tail Instability Due to Beam-beam Interaction in Circular Colliders Based on Crab Waist Scheme", in Proc. of eeFACT2016, Daresbury, UK (2016).
10. K. Ohmi, N. Kuroo et al., "Coherent Beam-Beam Instability in Collisions with a Large Crossing Angle", Phys. Rev. Lett. 119, 134801 (2017).
11. D. Shatilov, "Simulation of X-Z Coherent Instability in FCC-ee @ 45.5 GeV Using Quasi-Strong-Strong Model", 47th FCC-ee Optics Design Meeting, February 24 (2017), <https://indico.cern.ch/event/615842/>.
12. K. Oide et al., "Progress in the Design of Beam Optics for FCC-ee Collider Ring", in Proc. of IPAC2017, Copenhagen, Denmark (2017).

2.5 Strategy, Site Selection Process and CE Studies for CEPC-SppC

Jie Gao
Institute of High Energy Physics
Yuquan Road 19, 100049, Beijing, China
(gaoj@ihep.ac.cn)

2.5.1 CEPC-SppC Strategy and Status

With the discovery of the Higgs particle at the Large Hadron Collider at CERN in July 2012, after more than 50 years of searching, particle physics has finally entered the era of the Higgs, and the door for human beings to understand the unknown part of the Universe is wide open! Thanks to the low energy of Higgs, it is possible to produce clean Higgs with circular electron positron colliders in addition of linear colliders, such as ILC and CLIC, with reasonable luminosity, technology, cost, and power consumption.

In September 2012, Chinese scientists proposed a Circular Electron Positron Collider (CEPC) in China at 240 GeV centre of mass for Higgs studies with two detectors situated in a very long tunnel more than twice the size of the LHC at CERN. It could later be used to host a Super Proton Proton Collider (SppC) well beyond LHC energy potential to reach a new energy frontier in the same channel as shown in Fig. 1.

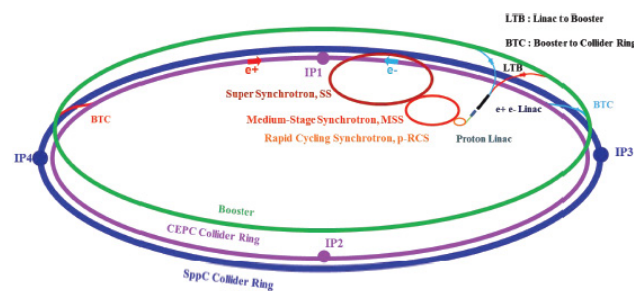


Figure 1: CEPC-SppC schematic layout

After ICFA Higgs Factory Workshop held at Fermi Laboratory in Nov 2012, CERN proposed also a similar one, Future Circular Collider (FCC) with a much longer tunnel than that of LHC.

From 12 to 14 June 2013, the 464th Fragrant Hill Meeting was held in Beijing on the strategy of Chinese high energy physics development after Higgs discovery, and the following consensuses were reached: 1) support ILC and participate to ILC construction with in kind contributions, and request R&D fund from Chinese government; 2) as the next collider after BEPCII in China, a circular electron positron Higgs factory (CEPC) and a Super proton-proton Collider (SppC) afterwards in the same tunnel is an important option as a historical opportunity, and corresponding R&D is needed.

In Feb. and July of 2014, ICFA has given two successive statements, respectively, that ICFA supports studies of energy frontier circular colliders and encourages global coordination; ICFA continues to encourage international studies of circular colliders,

	<i>t</i>	<i>Higgs</i>	<i>Z</i>
Number of IPs		2	
Energy (GeV)	175	120	45.5
Circumference (km)		100	
SR loss/tum (GeV)	7.61	1.68	0.035
Half crossing angle (mrad)		16.5	
Pi winski angle	0.91	2.58	12.1
N_p/bunch (10^{10})	24.15	15	4.8
Bunch number	34	248	9524
Beam current (mA)	3.95	17.9	219.7
SR power /beam (MW)	30	30	7.6
Bending radius (km)		10.9	
Momentum compaction (10^{-5})		1.14	
β_p x/y (m)	1.2/0.0037	0.36/0.001	0.2/0.001
Emittance x/y (nm)	2.24/0.0068	1.21/0.0037	0.17/0.0029
Transverse σ_p (um)	51.8/0.16	20.9/0.061	5.9/0.054
$\epsilon_x/\epsilon_y/\text{IP}$	0.077/0.105	0.031/0.082	0.0094/0.0626
V_{RF} (GV)	8.93	2.14	0.1
f_{RF} (MHz) (harmonic)		650 (217500)	
Nature bunch length σ_z (mm)	2.54	2.72	2.38
Bunch length σ_z (mm)	2.87	3.26	4.33
HOM power/cavity (kw)	0.53 (5cell)	0.56 (2cell)	0.95(2cell)
Energy spread (%)	0.14	0.098	0.037
Energy acceptance requirement (%)	1.57	1.52	
Energy acceptance by RF (%)	2.67	2.06	1.7
Photon number due to beamstrahlung	0.19	0.29	0.33
Lifetime due to beamstrahlung (hour)	1.0	1.0	
Lifetime (hour)		0.33 (20 min)	
F (hour glass)	0.89	0.81	0.97
L_{max}/IP ($10^{24}\text{cm}^{-2}\text{s}^{-1}$)	0.38	3.1	13.2

Table 1: CEPC parameters

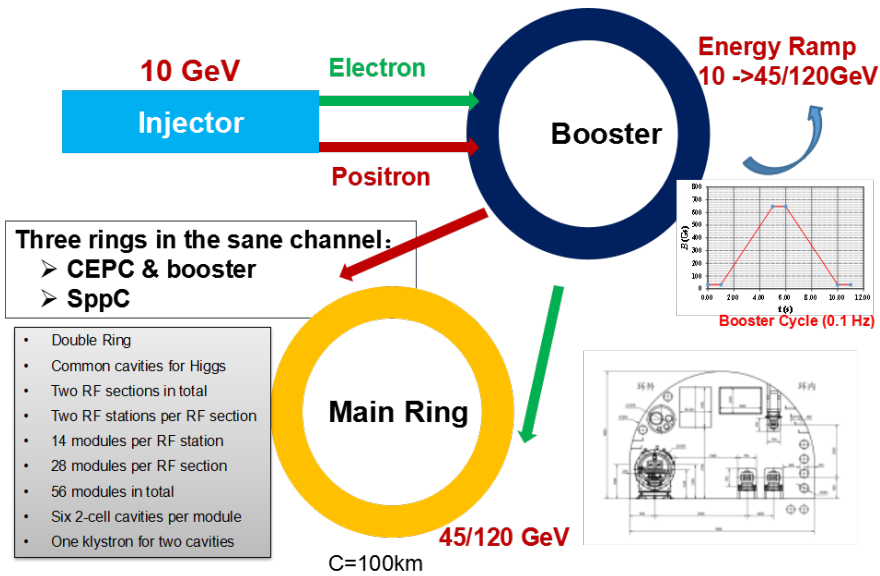


Figure 3: CEPC subsystem schematic layout

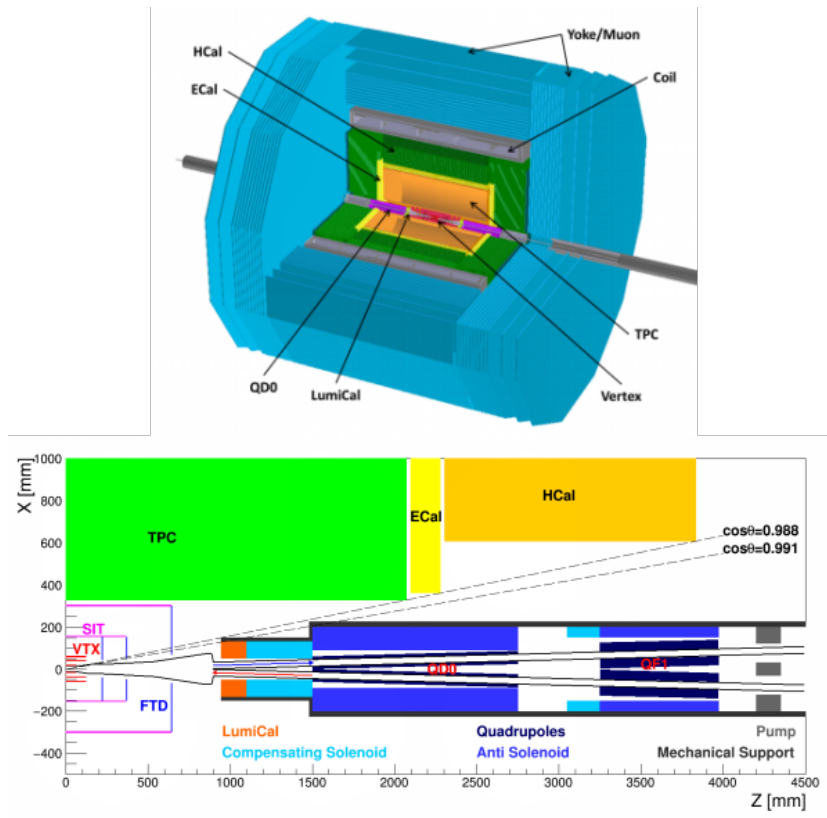


Figure 4: CEPC detector and MDI schematic layout

Concerning SppC baseline as shown in Fig. 6, it is decided to start with 12T dipole of iron based high temperature superconducting magnets, at the center of mass energy of 75TeV and luminosity of $1 \cdot 10^{35}/\text{cm}^2\text{s}$ as shown in Tab. 2 .

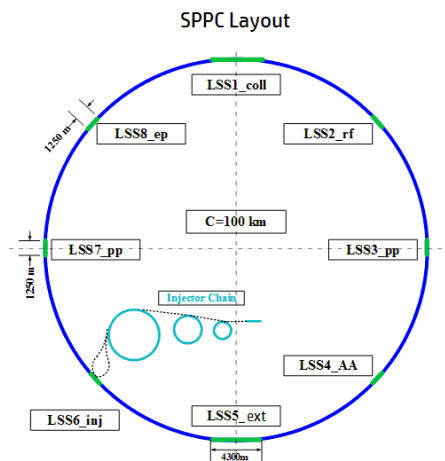


Figure 5: SppC baseline schematic layout

	SPPC (Pre-CDR)	SPPC 61Km	SPPC 100Km	SPPC 100Km	SPPC 82Km	SPPC phase 1	SPPC phase 2
Main parameters and geometrical aspects							
c.m. Energy[E_0]/TeV	71.2	70	100.0	128.0	100.0	75.0	125.0-150.0
Circumference[C_0]/km	54.7	61.0	100.0	100.0	82.0	100.0	100.0
Dipole field[B]/T	20	19.88	16.02	19.98	19.74	12.00	20-24
Dipole curvature radius[ρ]/m	5928	5889.64	10676.1	10676.1	8441.6	10415.4	-
Bunch filling factor[f_2]	0.8	0.8	0.8	0.8	0.8	0.8	-
Arc filling factor[f_1]	0.79	0.78	0.78	0.78	0.78	0.78	-
Total dipole length [L_{Dipole}]/m	37246	37006	67080	67080	53040	65442	-
Arc length[L_{ARC}]/m	47146	47443	86000	86000	68000	83900	-
Straight section length[L_{SS}]/m	7554	13557	14000	14000	14000	16100	-
Physics performance and beam parameters							
Peak luminosity per IP[L]/ $cm^{-2}s^{-1}$	1.1×10^{35}	1.2×10^{35}	1.5×10^{35}	1.0×10^{36}	1.5×10^{35}	1.0×10^{35}	1.0×10^{36}
Beta function at collision[β^*]/m	0.75	0.85	0.99	0.22	1.06	0.71	-
Max beam-beam tune shift per IP[ξ_p]	0.006	0.0065	0.0068	0.0079	0.0073	0.0058	-
Number of IPs contributes to ΔQ	2	2	2	2	2	2	2
Max total beam-beam tune shift	0.012	0.0130	0.0136	0.0158	0.0146	0.0116	-
Circulating beam current[I_b]/A	1.0	1.024	1.024	1.024	1.024	0.768	-
Bunch separation[Δt]/ns	25	25	25	25	25	25	-
Number of bunches[n_b]	5835	6506	10667	10667	8747	10667	-
Bunch population[N_p] (10^{11})	2.0	2.0	2.0	2.0	2.0	1.5	-
Normalized RMS transverse emittance[ϵ]/ μm	4.10	3.72	3.59	3.11	3.35	3.16	-
RMS IP spot size[σ^*]/ μm	9.0	8.85	7.86	3.04	7.86	7.22	-
Beta at the 1st parasitic encounter[β_1]/m	19.5	18.67	16.26	69.35	15.31	22.03	-
RMS spot size at the 1st parasitic encounter[σ_1]/ μm	45.9	43.13	33.10	56.19	31.03	41.76	-
RMS bunch length[σ_z]/mm	75.5	56.69	66.13	14.62	70.89	47.39	-
Full crossing angle[θ_c]/ μrad	146	138.03	105.93	179.82	99.29	133.65	-
Reduction factor due to cross angle[F_{ca}]	0.8514	0.9257	0.9247	0.9283	0.9241	0.9265	-
Reduction factor due to hour glass effect[F_h]	0.9975	0.9989	0.9989	0.9989	0.9989	0.9989	-
Energy loss per turn[U_0]/MeV	2.10	1.98	4.55	12.23	5.76	1.48	-
Critical photon energy[E_c]/keV	2.73	2.61	4.20	8.81	5.32	1.82	-
SR power per ring[P_0]/MW	2.1	2.03	4.66	12.52	5.90	1.13	-
Transverse damping time [τ_x]/h	1.71	1.994	2.032	0.969	1.32	4.70	-
Longitudinal damping time [τ_z]/h	0.85	0.997	1.016	0.4845	0.66	2.35	-

Table 2: SppC baseline parameter (phase-1)

As for CEPC-SppC study fund situation, in 2016, Chinese Ministry of Science and Technology (MOST) has allocated 36 Million RMB for CEPC study, and in 2018, another 40 Million RMB on CEPC R&D will be allocated also. Surely, MOST is only one of funding channels, there are other channels also to fund CEPC-SppC studies, such as NSFC, CAS and local Governments. For example, in 2017, CAS allocated 200 Million RMB to study high temperature materials for magnets, including studies on materials science, industries and projects, such as SppC.

A CEPC-SppC Progress Report has been published in April of 2017 [7], and the Conceptual Design Report (CDR) will be finished by the end of 2017.

On Nov. 2017, CEPC-SppC Industrial Promotion Consortium (CIPC) has been established with the aim of mutual supporting between CEPC-SppC and Industries.

The optimization design, relevant technologies and industrialization preparation could be ready after a five years R&D dedicated Technical Design Report (TDR) period started from 2018 before CEPC starts its construction around 2022 and completed around 2028. CEPC will operate about 10 ten years with two detectors to accumulate one million Higgs as Higgs Factory and 100 million of Z particle. As for SppC, it is planed to start the SppC construction from 2038 and complete the construction in 2045.

The CEPC-SppC TDR phase after CDR is very critical, both for key components' R&D and industrialization. The R&D on high Q high field 1.3GHz and 650MHz SC cavities; 650MHz high power high efficiency klystron; 12kW@4K cryogenic system, 12T iron based high temperature superconducting dipole, etc. have started. Taking CEPC SCRF R&D for example, the civil construction of Platform of Advanced Photon Source (PAPS)- SCRF facility has been started since May 31, 2017 in Beijing, which is a modern 4500m² SCRF Laboratory to be completed in 2020.

In 2017, Chinese Government has established a new decision making process for large scientific projects with international collaboration, such as CEPC-SppC.

CEPC-SppC is a Chinese scientists proposed project to be built in China, but its nature is an International Collaboration Project for the high energy physics community world wide. In 2015, an International Advisory Committee of CEPC-SppC has been established, and many MoUs have been signed with many Institutes and Universities around the world.

In August 2017, ICFA endorsed International Linear Collider (ILC) 250GeV (center of mass energy) with upgrade possibilities in the future. Even CEPC and ILC250 starts with the same Higgs energy, but their ultimate goals are totally different from each other, SppC is for 100TeV proton proton collider and ILC is for 1TeV electron positron collider. Apparently, the relation between CEPC-SppC and ILC is complementary.

The specific feature of CEPC is its small scale SCRF system (2GeV in the main collider ring for Higgs) instead of 125GeV for ILC, and relative large AC power consumption of $\sim 350\text{MW}$ for CEPC instead of $\sim 110\text{MW}$ for ILC250. As for the cost, CEPC in the first phase has included part of the cost of SppC for its long tunnel, however, ILC have to upgrade its energy by increasing tunnel length accordingly later.

2.5.2 CEPC-SppC Site Selection Process and Status

CEPC-SppC site selection technical criteria can be roughly quantified as follows: earthquake intensity less than 7; earthquake gravitation less than 0.1g; ground surface vibration amplitude less than $20\text{nm}@1-100\text{Hz}$; granite bed rock is around 50~100m underground, etc. The site selection has been started since Feb. 2015, till 2017, four sites have been considered, Qinhuangdao in Hebei Province, Shenshan Special District in Guangdong Province, Huangling county in Shanxi Province, and Baoding (Xiongan) in Hebei Province as shown in Fig. 6, where the first three sites have been prospected underground. More sites will be considered in the future before a final selection decision.



Figure 6: CEPC-SppC site selection status

2.5.3 Civil Engineering Studies

CEPC-SppC is designed as a whole facility with both machines co-existing in the same tunnel. CEPC-SppC have totally 4 detector experimental halls of around 2000m², two for CEPC and another two for SppC. The tunnel width is around 7m in width and 4.8m in height, where hosts CEPC main ring (two beam pipes), CEPC booster and SppC. The SppC could be inside (as shown in Fig. 7 left) or outside (as shown in Fig. 7 right) of CEPC, and the final decision is depending on more studies on radiation protection and other collision modes, for example, electron proton collision scheme in the far future.

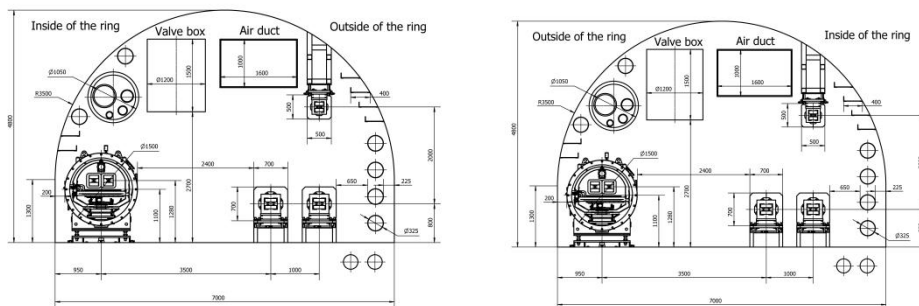


Figure 7: CEPC-SppC tunnel layouts: CEPC is outside of SppC (left); CEPC is inside of SppC (right)

2.5.4 Conclusions

In this article we have given a general strategy (both national and international) and historical progress review of CEPC-SppC project. CEPC-SppC baseline and alternative schemes have been introduced for CDR to be finished by the end of 2017. Key issues, such as, CEPC-SppC R&D, funding situation, international collaboration, CEPC-SppC/ILC relations, government decision making process, costing, siting, and civil engineering, etc. have been discussed.

In short, CEPC-SppC has kept the scheduled pace both in design and R&D together with team development.

2.5.5 Acknowledgments

The author of this article thanks for the great efforts from CEPC-SppC team and international collaborations.

2.5.6 References

1. CEPC-SppC Pre-CDR, *Scaling Behavior of Circular Colliders Dominated by Synchrotron Radiation*, <http://cepc.ihep.ac.cn/preCDR/volume.html>.
2. J. Gao, IHEP-AC-LC 2013-012.
3. M. Koratzinos and F. Zimmermann, IPAC 2015.
4. J. Gao, *The advanced partial double ring scheme for CEPC*, IHEP-AC-LC 2016-002.

5. K. Oide, FCC(ee) Design, 2016.
6. J. Gao, CEPC-SPPC Accelerator Status towards CDR, International Journal of Modern Physics A (TBD), (2017).
7. CEPC-SppC Progress Report, <http://cepc.ihep.ac.cn/Progress%20Report.pdf>.

2.6 CEPC Design Highlights

C. H. Yu, Y. W. Wang, Y. Zhang, D. Wang, N. Wang, S. Bai, T. J. Bian, X. H. Cui,
Y. D. Liu, H. P. Geng, D. H. Ji, Y. Y. Wei
Institute of High Energy Physics- Yuquan Road 19b, Beijing 100049
Mail to: yuch@ihep.ac.cn

2.6.1 Introduction

CEPC is a double ring collider with two interaction points (IP). According to the goal of high energy physics, it is required that the CEPC provides e^+e^- collisions at the center-of-mass energy of 240GeV and delivers a peak luminosity of $2 \times 10^{34} \text{ cm}^{-2}\text{s}^{-1}$ at each interaction point. CEPC should be compatible with W and Z experiments which the energies are 160GeV and 91GeV respectively. The luminosity at the Z-pole should be above $1 \times 10^{34} \text{ cm}^{-2}\text{s}^{-1}$ per IP. The CEPC design highlights will be introduced in detail in this paper.

2.6.2 Main parameters

The circumference of CEPC is decided by the geometry requirement of SPPC. The synchrotron radiation (SR) power per beam is limited around 30 MW due to the project power budget. The luminosity constraint of Z mode is mainly from the consideration of machine cost. The parameters for Z mode are designed without increasing machine budget base on the Higgs factory. The main parameters are listed in Table 1.

Table 1: CEPC parameters

	Higgs	W	Z
Number of IPs	2		
Beam Energy (GeV)	120	80	45.5
Circumference (km)	100		
SR loss/turn (GeV)	1.68	0.33	0.035
Half crossing angle (mrad)	16.5		
Piwinski angle	2.75	4.39	10.8
N_e/bunch (10^{10})	12.9	3.6	1.6
Bunch number	286	5220	10900
Beam current (mA)	17.7	90.3	83.8
SR power /beam (MW)	30	30	2.9
Bending radius (km)	10.9		
Momentum compaction (10^{-5})	1.14		
$\beta_{IP} x/y$ (m)	0.36/0.002		

Emittance x/y (nm)	1.21/0.0036	0.54/0.0018	0.17/0.0029
Transverse σ_{IP} (μm)	20.9/0.086	13.9/0.060	7.91/0.076
$\xi_x/\xi_y/IP$	0.024/0.094	0.009/0.055	0.005/0.0165
RF Phase (degree)	128	134.4	138.6
V_{RF} (GV)	2.14	0.465	0.053
f_{RF} (MHz) (harmonic)	650 (217500)		
Nature bunch length σ_z (mm)	2.72	2.98	3.67
Bunch length σ_z (mm)	3.48	3.7	5.18
HOM power/cavity (kw)	0.46 (2cell)	0.32(2cell)	0.11(2cell)
Energy spread (%)	0.098	0.066	0.037
Energy acceptance requirement (%)	1.21		
Energy acceptance by RF (%)	2.06	1.48	0.75
Photon number due to beamstrahlung	0.25	0.11	0.08
Lifetime due to beamstrahlung (hour)	1.0		
F (hour glass)	0.93	0.96	0.986
L_{max}/IP ($10^{34}\text{cm}^{-2}\text{s}^{-1}$)	2.0	4.1	1.0

The design luminosity of H is $2.0 \times 10^{34} \text{ cm}^{-2}\text{s}^{-1}$ with 286 bunches collision. At Z pole, the luminosity is $1.0 \times 10^{34} \text{ cm}^{-2}\text{s}^{-1}$ and the according bunch number is 10900 which is limited by the e-cloud instability of positron beam. The minimum bunch spacing for Z mode should be larger than 25 ns according to the results of simulation. The luminosities include the bunch lengthening effect according to the impedance budget. The bunch lengthening is about 30% for H, 24% for W and 40% for Z. The beamstrahlung effect is the dominant constraint for beam lifetime in energy frontier e+ e- circular colliders. For CEPC, the beam lifetime due to beamstrahlung effect is about 1.0 hour at Higgs energy by theoretical calculations so that the according energy acceptance of dynamic aperture should be larger than 1.21%. The energy spread due to beamstrahlung is about 20 percent of nature energy spread. The beamstrahlung lifetime for W and Z is large enough. The vertical emittance growth for Z mode is the most serious among the three energies due to the coupling effect caused by the fringe field of detector solenoid (3T) and anti-solenoids. A larger coupling factor of 1.7% has to be chosen at Z pole, while it is 0.3% for Higgs and W.

2.6.3 Geometry of CEPC

The crossing angle at the IP is 33mrad. The length of interaction region is about 3.8km for the compatibility to the SPPC. The design of CEPC is optimized at Higgs energy with shared RF cavities by both beams. Each beam will be only filled in half ring. For the W and Z modes RF cavities of e- and e+ are independent so that the beams can be filled along the whole ring. The layout of CEPC collider ring is shown in the Fig. 1. W and Z modes adopt the same cavities which used in H mode to save budget. Half number of the cavities are distributed in W and Z modes.

Twin-aperture of dipoles and quadrupoles are adopt in the arc region. The distance between two beams is 0.35 m. The design of twin-aperture magnets has been finished. The magnets in the other regions are independent type for the optics flexibility.

2.6.4 The design of interaction region

The detector consists of a cylindrical drift chamber surrounded by an electromagnetic calorimeter, which is immersed in the superconducting solenoid with 3 T magnetic field and length of 15.2m. The accelerator components inside the detector must be within a conical space with an opening angle of 13.6° . The electron and positron beams collide at the IP with a horizontal angle of 33mrad. The final focusing magnet is 2.2m away from the IP. Luminosity calorimeter will be installed in longitudinal 0.95~1.11m, with inner radius 28.5mm and outer radius 100mm. The layout nearby the interaction point is shown in Fig. 2.

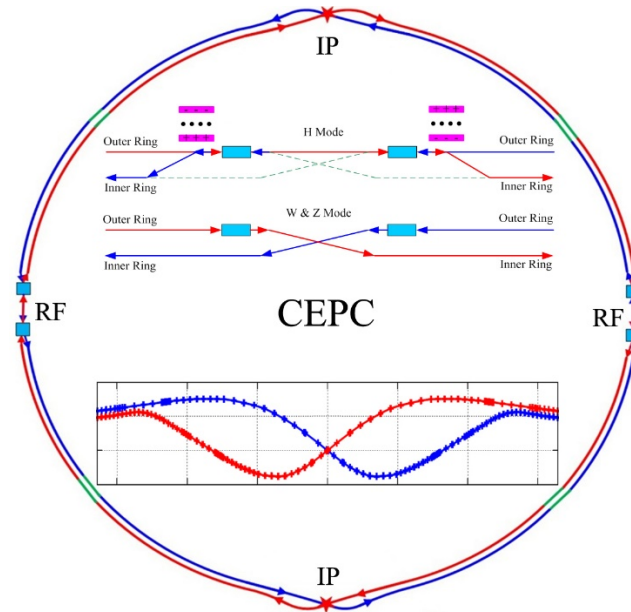


Figure 1: The layout of CEPC collider ring

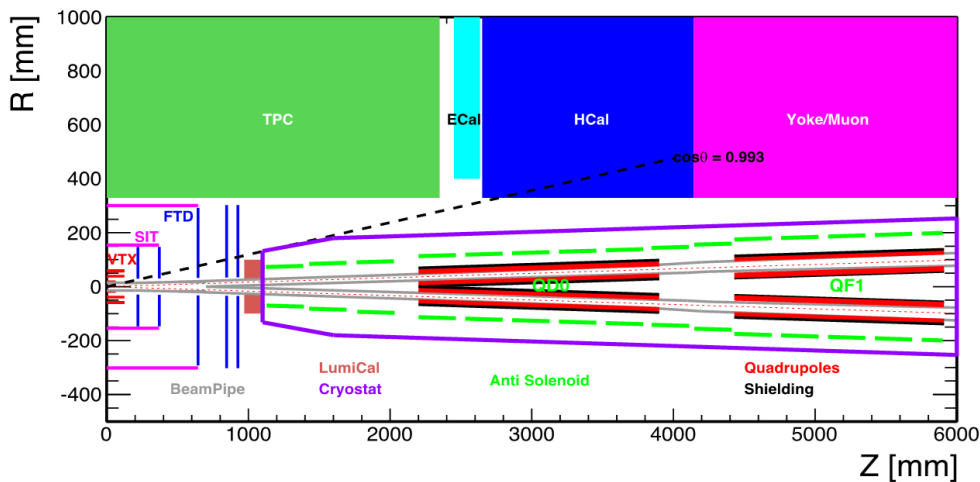


Figure2: The layout nearby the interaction point

On each side of the IP, a final doublet of quadrupoles (QD0 and QF1) is used to provide the focusing to control the beta function at the IP. Both of QD0 and QF1 are double aperture superconducting coils. The definition of beam stay clear of the collider ring in horizontal and vertical are $BSC_x = \pm(20\sigma_x + 3\text{mm})$ and $BSC_y = \pm(30\sigma_y + 3\text{mm})$ according to the considerations of injection and beam tail effect after collision. The design of final doublet quadrupoles is shown in Fig 3.

Anti-solenoids shown in the Figure 2 are designed to compensate the solenoid field from the detector. The integral longitudinal field $\int B_z ds$ within 0~2.12m is 0 and B_z is less than 460Gauss after 2.12m away from the IP which is shown in Fig. 4. The skew quadrupole coils are designed to make fine tuning of B_z over the QF1 and QD0 region instead of the mechanical rotation.

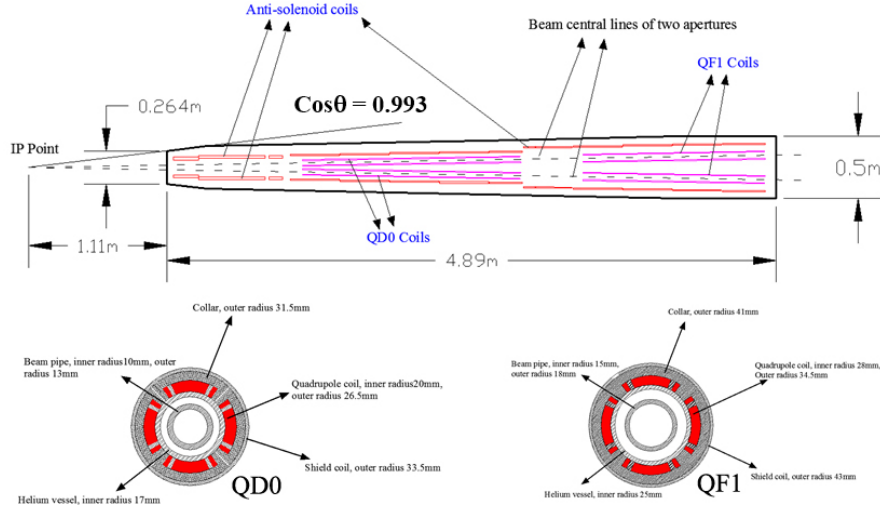


Figure 3: The design of final doublet quadrupoles

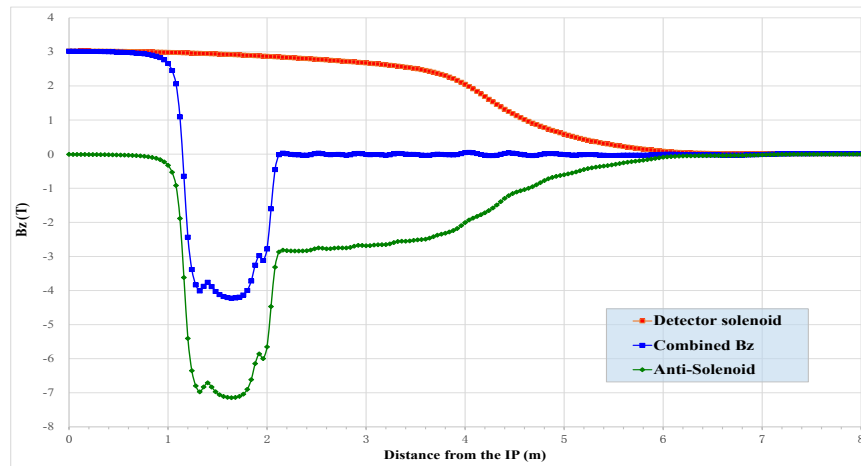


Figure 4: The compensation of detector solenoid

The inner diameter of the beryllium pipe is decided to be 28mm by considering both the mechanical assembly and beam background issues. The length of beryllium pipe is 14cm in longitudinal. Due to beamstrahlung incoherent pairs, The shape of beam pipe between 0.2~0.5m is selected as cone. There is bellows for the requirements of installation in the crotch region where is located about 0.7m away from the IP. The water cooling structure is considered due to heating problem of HOM.

An asymmetric lattice adopted to allow softer bends in the upstream of IP. Reverse bending direction of last bends is applied to avoid synchrotron radiation hitting IP vacuum chamber. For the upstream of IP, the critical energy of synchrotron radiation from the bending magnets is controlled less than 47keV within 66m and 100keV within 400 m. For the downstream of IP, no bends in the last 70 m and the critical energy is less than 95keV within 120 m and 300keV within 250 m.

The total SR power generated by the QD0 magnet is 603W in horizontal and 157W in vertical. The critical energy of photons is about 1.3 MeV and 186W in vertical. The critical energy of photons is about 423 keV. The total SR power generated by the QF1 magnet is 1387W in horizontal and 30W in vertical. The critical energy of photons is about 1.5MeV. The critical energy of photons is about 189keV. There is no SR photons within $6\sigma_x$ directly hitting or once-scattering to the detector beam pipe.

2.6.5 Lattice of the collider ring

The interaction region is designed to provide local correction of chromaticity generated by the final doublet magnets and crab-waist collision. It consists of modular sections including the final transformer (FT), chromaticity correction for vertical plane (CCY), chromaticity correction for horizontal plane (CCX), crab-waist section (CW) and matching transformer (MT). The FT consists of two quadrupole doublets. The phase advance is π on the vertical plane and a bit less than π on the horizontal plane as the not very small. At the end of FT, there's the first image point. The CCY is actually consist of four FODO cells whose phase advances are $\pi/2$ for both planes and begin with a half defocusing quadrupole. Four identical dipoles are used to make dispersion bumps. A pair of sextupoles is placed at the two peaks of beta to compensate the vertical chromaticity generated by the final defocusing quadrupole. The geometric sextupole aberrations are cancelled by the $-I$ transformation between the paired sextupoles. At the end of CCY, there's the second image point which is identical to the first one. The CCX is similar to the CCY while begin with a half focusing quadrupole. The MT also consists of two quadrupole doublets. Twiss parameters are matched to the ARC section of the ring and make the total phase advances of FF to be 6π . The optics is shown in Fig. 5.

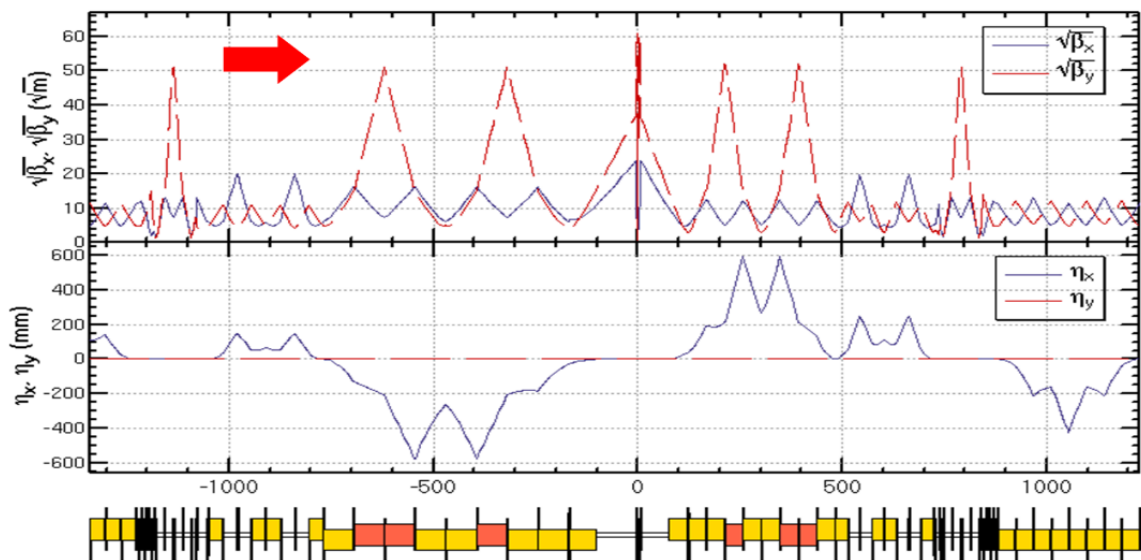


Figure5: Optics of the interaction region

Up to 3rd order chromaticity are corrected with pairs of main sextupoles, phase tuning and additional sextupoles respectively. All the 3rd and 4th resonance driving terms (RDT) due to sextupoles are almost cancelled. The tune shift due to finite length of main sextupoles is corrected with additional weak sextupoles.

For the Arc region, the FODO cell structure is chosen to provide a large filling factor. The 90/90 degrees phase advances and non-interleaved sextupole scheme are selected

due to its property of aberration cancellation: The tune shift is very small even with small emittance; In each 20 cells, all the 3rd and 4th resonance driving terms due to sextupoles cancelled, except small $4Q_x$, $2Q_x+2Q_y$, $4Q_y$, $2Q_x-2Q_y$. The left aberration is mainly chromaticity which could be corrected with many families of arc sextupoles. The dispersion suppressor at the ends of arc region is designed with same FODO structure and re-matched quadrupoles.

2.6.6 Dynamic aperture

32 arc sextupole families, 10 IR sextupole families and 8 phase advance tuning knob between different sections in the ring are used to optimize the dynamic aperture, while the working point is kept constant. The optimized dynamic aperture is shown in Fig. 6 and Fig. 7. The momentum acceptance is larger than 0.017 and transverse dynamic aperture is $20\sigma_x \times 20\sigma_y$ at Higgs energy without errors. The requirement of energy acceptance due to lifetime is 0.012. The basic requirements of horizontal transverse aperture due to injection is $16\sigma_x$ and vertical transverse aperture due to beam tail effect after collision is $7\sigma_y$. The dynamic aperture with errors are being studied. A relaxed lattice with very larger dynamic aperture is needed during first stage of commissioning.

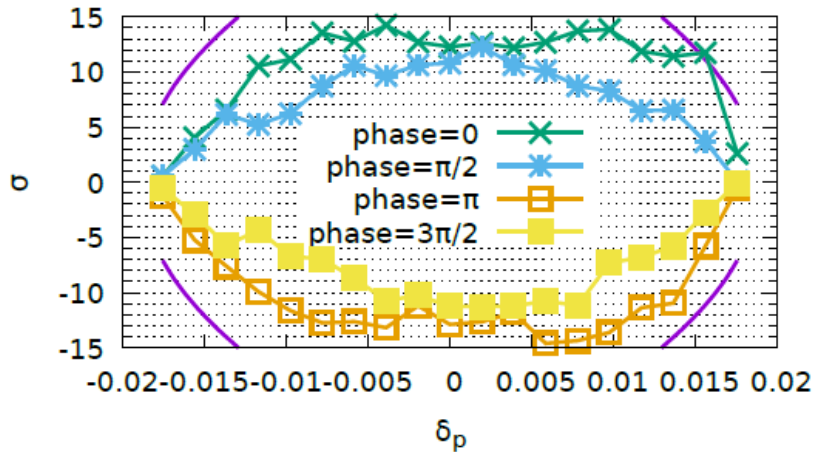


Figure 6: Minimum Dynamic Aperture of 100 samples. Radiation fluctuation is included. 0.3% emittance coupling. 200 turns are tracked.

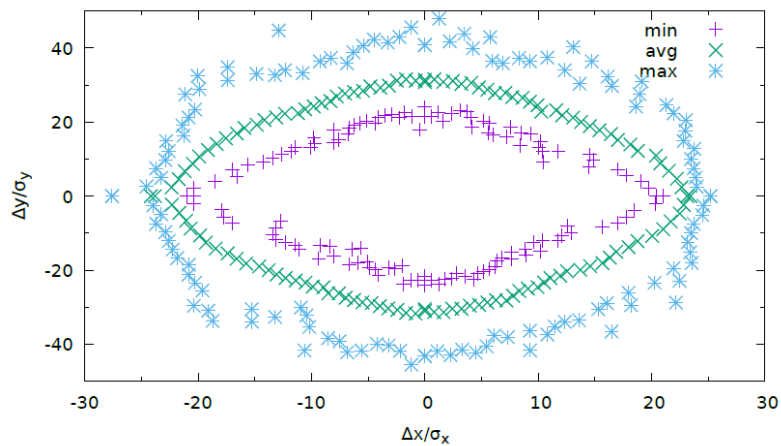


Figure 7: Dynamic Aperture of on-momentum particles; 100 samples tracked over 200 turns.

2.6.7 Summary

The physical design can meet the basic luminosity requirements at Higgs and Z. Dedicated lattices in the RF region are designed for the optimized beam performance of Higgs and Z modes. The finalization of the beam parameters and the specification of special magnets have been finished. The optimization to reduce machine cost and improve the beam performance is always under studying.

2.7 Collective effects in CEPC

Na Wang, Yudong Liu, Hongjuan Zheng, Dianjun Gong, Jun He
 Mail to: wangn@ihep.ac.cn
 Institute of High Energy Physics, Beijing 100049, China

2.7.1 Introduction

The Circular Electron Positron Collider (CEPC) is a high-energy lepton collider covering beam energy from Z to Higgs. In CEPC, high beam current is required to achieve the design luminosity. Interaction of an intense charged particle beam with the vacuum chamber may lead to collective instabilities. These instabilities can induce beam quality degradation or beam losses, and finally restrict the performance of the machine. In order to estimate the influence of the collective effects, the impedance model for the CEPC collider is developed. Based on the impedance studies, critical beam instability issues due to single bunch and multi bunch effects are discussed for different operation scenarios. The instabilities due to interaction of the electron beam with the residual ions and instabilities from positron beam interaction with the electron cloud are also investigated.

2.7.2 Impedance studies

2.7.2.1 Impedance threshold

The impedance thresholds are estimated analytically, which give a rough estimation on the impedance requirements. The limitation on the longitudinal broadband impedance mainly comes from the microwave instability and the bunch lengthening. Since longer bunch will degrade the luminosity, and beam intensity above the instability threshold can induce energy spread increase, so this is an important concern for a collider. The threshold of microwave instability is estimated according to the Boussard or Keil-Schnell criteria [1, 2].

The limitation on the transverse broadband impedance mainly comes from the transverse mode coupling instability, which occurs when the frequencies of two neighboring head tail modes approach each other. For Gaussian bunches, the threshold current can be expressed with the transverse kick factor [3, 4],

$$I_0^{\text{th}} = \frac{2v_s \omega_0 E / e}{\sum_j \beta_{y,j} \kappa_{y,j}} \Theta \quad (1)$$

where ν_s is the synchrotron tune, ω_0 is the angular revolution frequency, E is the beam energy, $\beta_{y,j}$ is the betatron function at the j th impedance element, κ is the transverse kick factor, and $\Theta \approx 0.7$.

The narrowband impedances are mainly contributed by cavity like structures. These impedances may induce coupled bunch instabilities in both longitudinal and transverse planes. The limitation on the shunt impedance of a HOM is evaluated in a resonant condition when the HOM frequency overlaps the beam spectrum line, and the growth rate of the coupled bunch instability is less than the synchrotron radiation damping.

The main parameters and impedance thresholds for different operation scenarios are listed in Table 1. The result shows that the design of Z gives the most critical restriction for both broadband and narrowband impedances. Therefore, the instability issues of Z are mainly discussed in the following.

Table 1: Main beam parameters and analytical impedance threshold.

Parameter	Symbol, Unit	H	W	Z
Beam energy	E_k , GeV	120	80	45.5
Circumference	C , km	100		
Beam current	I_0 , mA	17.7	90.3	83.8
Bunch number	n_b	286	5220	10900
Momentum compaction	α_p , 10^{-5}	1.14		
Natural bunch length	σ_z , mm	2.7	3.0	3.7
Transverse tune (x/y)	ν_x/ν_y	355.08/355.22		
Synchrotron tune	ν_s	0.064	0.04	0.018
Energy spread	σ_e , 10^{-4}	9.8	6.6	3.7
Radiation damping (x/y/z)	$\tau_x/\tau_y/\tau_z$, ms	48/48/24	162/162/81	871/871/436
Long. broadband impedance	$ Z_{ }/n _{th}$, $m\Omega$	9.4	10.8	5.3
Trans. broadband impedance	$k_{y,th}$, kV/pC/m	73.0	108.9	62.7
Long. narrowband impedance	$f\text{Re}Z_{ }$, GHz-G Ω	3.2	0.08	3.9×10^{-3}
Trans. narrowband impedance	$\text{Re}Z_y$, G Ω /m	2.1	0.08	9.3×10^{-3}

2.7.2.2 Impedance model

The impedance and wake are calculated with analytical formulae along with numerical simulations with ABCI [5] and CST [6]. The impedance contributions of different impedance objects are listed in Table 2, where $Z_{||}/n$ is the longitudinal effective impedance, and k_y is the transverse kick factor. The calculation gives total longitudinal effective impedance of 20.6 $m\Omega$, and total transverse kick factor of 32.1 kV/pC/m. Both longitudinal and transverse impedances are dominated by the resistive wall impedance and elements with large quantity.

Table 2: Summary of the impedance budget.

Components	$Z_{ }/n$, $m\Omega$	k_y, kV/pC/m
Resistive wall	16.3	23.0
RF cavities	-1.4	0.4
Flanges	2.8	2.8
BPMs	0.1	0.3

Bellows	2.2	2.9
Pumping ports	0.02	0.6
IP chambers	0.02	1.3
Electrostatic separators	-0.19	0.2
Transitions	0.8	0.5
Total	20.6	32.1

2.7.3 Impedance-driven instabilities

2.7.3.1 Microwave instability and bunch lengthening

The microwave instability will rarely induce beam losses, but may reduce the luminosity due to the deformed beam distribution and increased beam energy spread. With the impedance model developed, the microwave instability and bunch lengthening are simulated with Elegant [7]. Figure 1 shows the dependences of bunch lengthening and beam energy spread on the beam intensity. At the design bunch intensity of 2.6 nC, the bunch length is increased by 40%, and the beam energy spread is increased by about 2%.

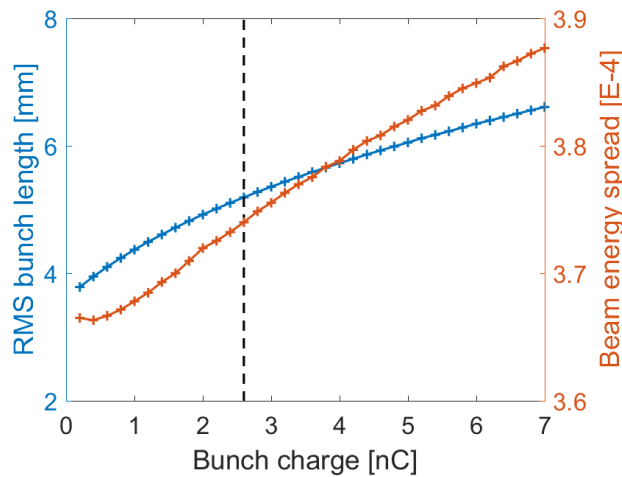


Figure 1: Dependence of bunch length and beam energy spread on bunch intensity

2.7.3.2 Transverse mode coupling instability

The threshold for the transverse mode coupling instability is estimated using Eigen mode analysis. Figure 2 shows the dependence of the head-tail mode frequencies on the bunch intensity. The analysis gives threshold bunch intensity of 8 nC, which is about 3 times of the design bunch intensity. So that we still have some safety margin to avoid the instability.

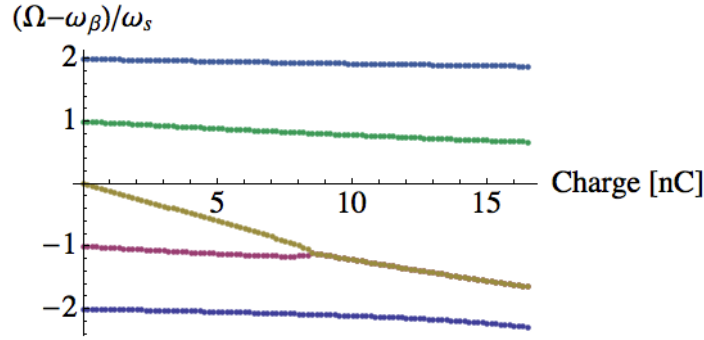


Figure 2: Head-tail mode frequency vs. bunch intensity

2.7.3.3 *Transverse resistive wall instability*

In large-scale circular colliders, the revolution frequency is low, and this results in the generation of dense beam spectrum lines. Therefore, the beam is more easily to be coupled to the narrowband impedances. One dominant contribution to the coupled bunch instability is the transverse resistive wall impedance, which has a high resonance around zero frequency. The instability growth time for different transverse oscillation modes are calculated and shown in Figure 3. The growth time for the most dangerous mode is 23 ms, which is much faster than the radiation damping of 871 ms. Therefore, an effective transverse feedback system is needed to damp the instability.

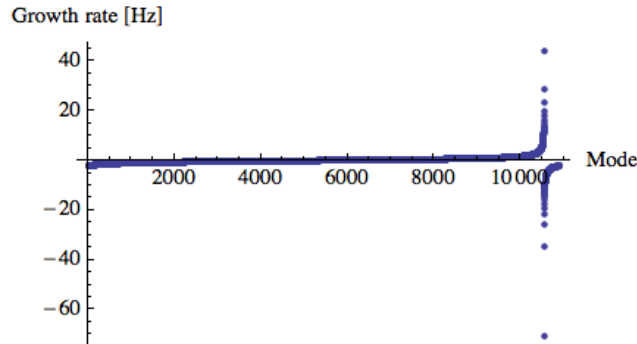


Figure 3: Growth rate of the transverse resistive wall instability with transverse mode number.

2.7.3.4 *Coupled bunch instability induced by the RF HOMs*

Another important contribution to the coupled bunch instability is the HOMs of the accelerating cavities. More than one hundred 2-cell superconducting RF cavities will be used in the scenario of Z. In order to keep the beam stable, the rise time of any oscillation mode should be larger than the radiation damping time or possible feedback. The HOM impedance below cutoff is compared with the thresholds, as shown in Figure 4. With a sophisticated HOM coupler design and a feedback system of 10 turns, all modes below cutoff frequency except TM011 modes, can be well damped.

Here, we assume all the cavities have the exact same impedance. However, considering the whole RF system, the threshold value greatly depends on the frequency spread from cavity to cavity due to the actual tolerances of the cavity construction. Large HOM frequency spread can further relax the instability requirement. As shown in Figure 4, with a frequency spread of 0.1MHz and 1MHz, the effective shunt impedance of the

HOMs can be reduced by an order of one or two. Accordingly, the instability growth time of the TM011 is increased from 1ms to 20 ms and 80 ms, respectively.

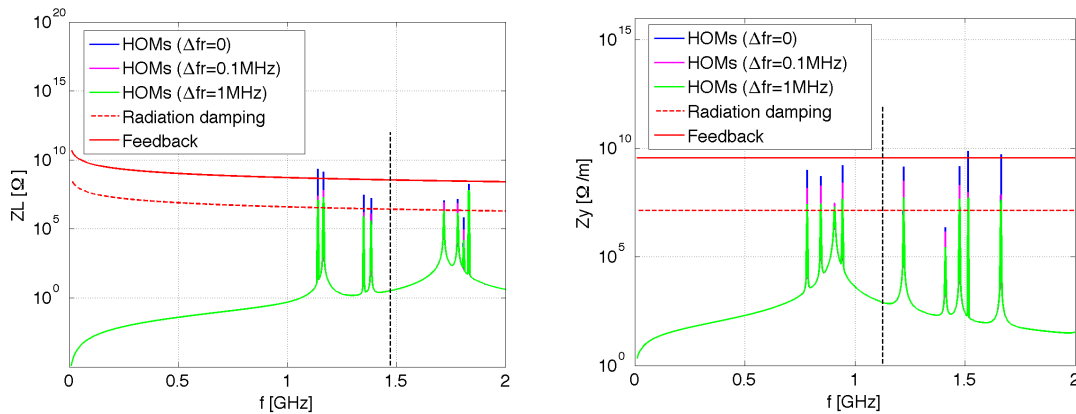


Figure 4: Impedance of the RF cavity monopole (left) and dipole (right) HOMs compared with the threshold determined by radiation damping and feedback damping of 10 turns.

2.7.4 Electron cloud

The buildup of accumulated photon electrons and secondary electrons is one of the most serious restrictions on collider luminosity [9, 10]. The electron cloud can induce emittance blow-up and beam instabilities, and finally lead to luminosity degradation. For CEPC, photon electrons and secondary electron emission will be the main contribution to the electron cloud. The electron cloud density is simulated for different secondary electron emission yield (SEY) and varies bunch spacing. The results are shown in Figure 5. The red dashed lines represent the threshold density for the head-tail instability. According to the analysis, a SEY lower than 1.6 and bunch spacing longer than 25 ns will be needed to eliminate the electron cloud instability.

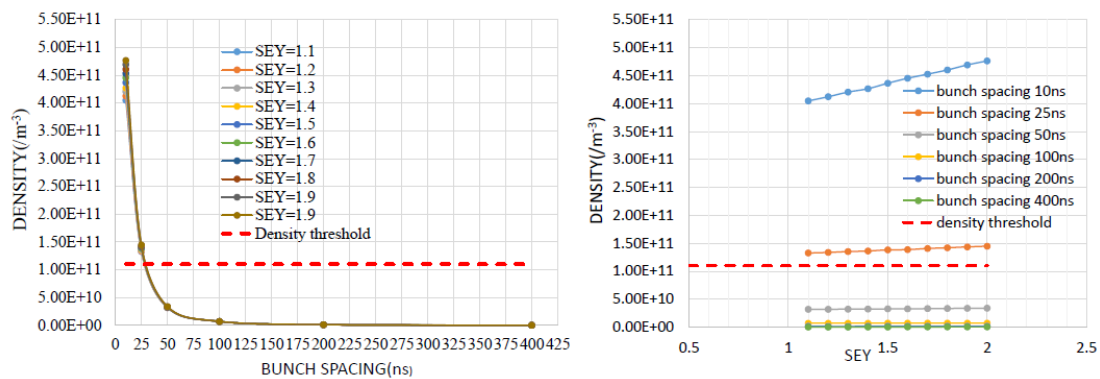


Figure 5: Electron cloud density for different SEY and bunch spacing.

2.7.5 Beam ion instabilities

In the electron ring, instabilities can be excited by residual gas ions accumulated in the potential well of the electron beam. With uniform filling, the threshold relative molecular mass is calculated with [11]

$$A = \frac{N_b r_p S_b}{2(\sigma_x + \sigma_y) \min(\sigma_x, \sigma_y)} \quad (2)$$

where σ_x and σ_y are transverse rms beam size, N_b is the number of protons per bunch, r_p is the classical proton radius, and S_b is the bunch spacing in meters. The trapped ion masses are calculated along one quarter of the ring, and the critical mass values are shown in Figure 6. The minimal critical mass of trapped ions is equal to 5, which locates at the IP straight section. So that ionized species with mass greater than 5 can be trapped. Thus a cleaning gap is required to avoid the ion trapping.

Besides ion trapping, fast beam ion instability can be excited by ions accumulated in a single passage of the bunch train. The equilibrium average ion density is $1.8 \times 10^{11} \text{ m}^{-3}$, where a characteristic damping time equal to the ion oscillation frequency has been used. The growth time for the fast beam ion instability is calculated as [12]

$$\frac{1}{\tau} = \frac{r_e c_0 \beta_y \rho_{ion} Q}{\gamma} \quad (2)$$

where r_e is the classical proton radius, c_0 is the speed of light, β_y is the betatron function, ρ_{ion} is the average ion density over the bunch train, Q is the quality factor characterizes the frequency spread of the ions, and γ is the relativistic beam energy. The analysis gives a growth time of about 10 ms, which is much faster than the radiation damping time. Therefore, a transverse feedback is also required to damping the instability.

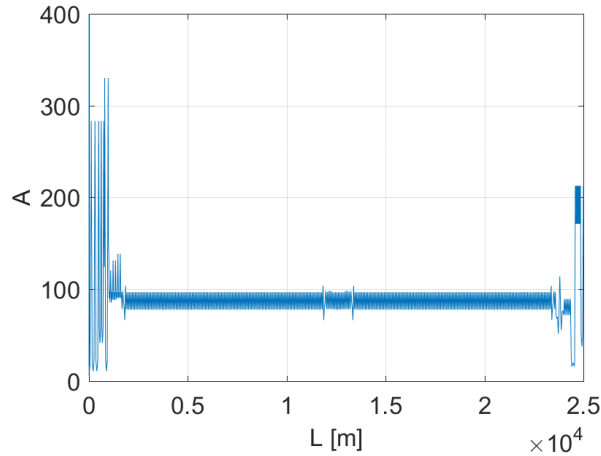


Figure 6: Threshold relative molecular mass along one quarter of the ring

2.7.6 Summary

An impedance model has been developed for the CEPC collider. Based on the impedance model, the potential instability issues for the operation scenario of Z are investigated. The results show that due to the longitudinal broadband impedance, the bunch will be lengthened by 40% and the beam energy spread will be increased by 2% at the design bunch current. The transverse broadband impedance is well below the transverse impedance threshold determined by TMCI. The coupled bunch instability can be excited by transverse resistive wall or monopole and dipole HOMs of the RF cavities. The analysis of the beam ion instability also shows a growth time of tens of millisecond.

Therefore, both transverse and longitudinal feedback systems are required to damp the multi-bunch instabilities. The electron cloud density is calculated with different SEY and bunch spacing. A SEY lower than 1.6 and bunch spacing longer than 25 ns are suggested to eliminate the electron cloud instability.

2.7.7 References

1. E. Keil and W. Schnell, CERN Report, TH-RF/69-48 (1969).
2. D. Boussard, CERN LAB II/RF/Int./75-2 (1975).
3. A. Chao, "Physics of collective beam instabilities in high energy accelerators", John Wiley & Sons, Inc. (1993).
4. S. Krinsky, et al., "Collective effects in the NSLS-II storage ring", Proceedings of PAC07, TUPMS074 (2007).
5. ABCI Home Page, <http://abci.kek.jp/abci.htm>
6. www.cst.com
7. M. Borland, "elegant: A Flexible SDDS-Compliant Code for Accelerator Simulation", Advanced Photon Source LS-287 (2000).
8. Y. Wang and M. Borland, "Pelegant: A Parallel Accelerator Simulation Code for Electron Generation and Tracking", Proceedings of the 12th Advanced Accelerator Concepts Workshop, AIP Conf. Proc. 877, 241 (2006).
9. F. Zimmermann, G. Rumolo, "Two-stream Problems in Accelerators", CERN SL-2001-057(AP) (2001).
10. E. Benedetto, D. Schulte and F. Zimmermann, "Simulation study of electron cloud induced instabilities and emittance growth for the CERN Large Hadron Collider proton beam", Phys. Rev. ST Accel. Beams 8, 124402 (2005).
11. Y. Baconnier and G. Brianti, "The stability of ions in bunched beam machines", CERN/SPS/80-2 (1980).
12. L. Wang, Y. Cai and T.O. Raubenheimer, "Suppression of beam-ion instability in electron rings with multibunch train beam fillings", Phys. Rev. ST Accel. Beams 14, 084401 (2011).

2.8 Some critical collective effects for the FCC-ee collider

Eleonora Belli^{1,2}, Giovanni Castorina², Mauro Migliorati², Serena Persichelli⁴,
G. Rumolo¹, Bruno Spataro³, Mikhail Zobov³

¹CERN, Geneva, Switzerland

²University of Rome 'La Sapienza' and INFN Sez. Roma1, Rome, Italy

³INFN/LNF, Frascati, Rome

⁴LBNL, Berkeley, California

Mail to: eleonora.belli@cern.ch

2.8.1 Introduction

In the framework of the Future Circular Collider (FCC) design studies at CERN [1], the high luminosity electron-positron collider FCC-ee is considered as a possible first step towards FCC-hh, a 100 TeV hadron collider in the same tunnel of about 100 km. Table 1 summarizes the main beam parameters at four different center-of-mass energies from

45.6 GeV (Z pole) to 175 GeV (top pair threshold). One of the major issues for such a kind of machine is represented by collective effects due to electromagnetic fields generated by the interaction of the beam with the vacuum chamber, which could produce instabilities, thus limiting the machine operation and performance. An impedance model is needed to study these instabilities, to predict their effects on the beam dynamics and to find a possible solution for their mitigation. Another critical aspect for the future lepton collider is represented by the electron cloud which will be discussed in the last section of this contribution, together with possible strategies to suppress its effects.

Table 1: FCC-ee baseline beam parameters [2].

Energy E_0 [GeV]	45.6	80	120	175
Circumference C [km]	97.75			
Bunch population N_p [10^{11}]	1.7	1.5	1.5	2.7
Number of bunches/beam	16640	2000	393	48
Beam current [mA]	1390	147	29	6.4
Momentum compaction α_c [10^{-5}]	1.48	0.73	0.73	0.73
Bunch length $\sigma_{z,SR}/\sigma_{z,BS}$ [mm]	3.5/12.1	3.3/7.65	3.15/4.9	2.45/3.25
Energy spread $\sigma_{dp,SR}/\sigma_{dp,BS}$ [%]	0.038/0.132	0.066/0.153	0.099/0.151	0.147/0.192
Horizontal tune Q_x	269.138	389.154	389.129	389.104
Vertical tune Q_y	269.22	391.22	391.199	391.176
Synchrotron tune Q_s	0.0248	0.0229	0.0357	0.0672
Horizontal emittance ε_x [nm]	0.27	0.28	0.63	1.34
Vertical emittance ε_y [pm]	1.0	1.0	2.3	2.7
SR energy loss per turn [GeV]	0.036	0.34	1.72	7.8
RF voltage [GV]	0.1	0.44	2.0	9.5

2.8.2 Wake fields and impedances

Collective beam instabilities induced by wake fields represent an active subject in the design of a particle accelerator and the theory behind this topic has been elaborated and refined over many years by several authors [3,4,5,6]. This section will describe the contributions of specific machine components to the total impedance budget and discuss their effects on the beam stability. Single bunch instability thresholds due to the resistive wall (RW) impedance will be estimated in both transverse and longitudinal planes and a longitudinal impedance budget including the contributions of several vacuum chamber components will be provided for the lowest energy case (Z pole at 45.6 GeV).

2.8.2.1 Resistive wall impedance and effects on beam dynamics

When the beam passes through a vacuum chamber which is not perfectly conducting but characterized by a finite resistivity, it generates wake fields that can act on the following particles and perturb their motion, giving rise to instabilities that can occur in both the longitudinal and transverse planes. For a circular beam pipe with radius b and a single layer of infinite thickness, the longitudinal and transverse impedances per unit length are given, respectively, by [7,8,9]

$$\frac{Z_{\parallel}(\omega)}{C} = \frac{Z_0 c}{\pi} \frac{1}{[1 + i \operatorname{sgn}(\omega)] 2bc \sqrt{\frac{Z_0 c \sigma_c}{2|\omega|}} - ib^2 \omega} \quad (1)$$

and

$$\frac{Z_{\perp}(\omega)}{C} = \frac{Z_0 c^2}{\pi} \frac{1}{[\operatorname{sgn}(\omega) + i] b^3 c \sqrt{2\sigma_c Z_0 c |\omega|} - ib^4 \omega^2} \quad (2)$$

where C is the machine circumference, Z_0 the vacuum impedance, c the speed of light and σ_c the material conductivity. In the case of FCC-ee, the value of the RW impedance produced by the finite conductivity of the copper chamber is increased by thin films of non-evaporable getter (NEG) materials. This coating is required to mitigate the electron cloud build up in the machine and to improve the pumping system [10,11], being characterized by a low Secondary Electron Yield (SEY), a low desorption yield and a very high pumping speed. The effect of the NEG coatings renders the contribution of the RW to the impedance budget critical for the machine design. It has been observed [12] that the thickness of the coating plays a fundamental role: The RW impedance decreases for a thinner coating and this results in higher single bunch instability thresholds, thus improving the beam stability during machine operation.

When computing the RW impedances with the ImpedanceWake2D code [13] (see Figure 1), the vacuum chamber is assumed to be circular with 35 mm radius and three layers (a first layer of copper with 2 mm thickness, then 6 mm of dielectric and finally iron with resistivity $\rho = 10^{-7} \Omega\text{m}$), coated with NEG films of three different thicknesses (1 μm , 250 nm and 100 nm).

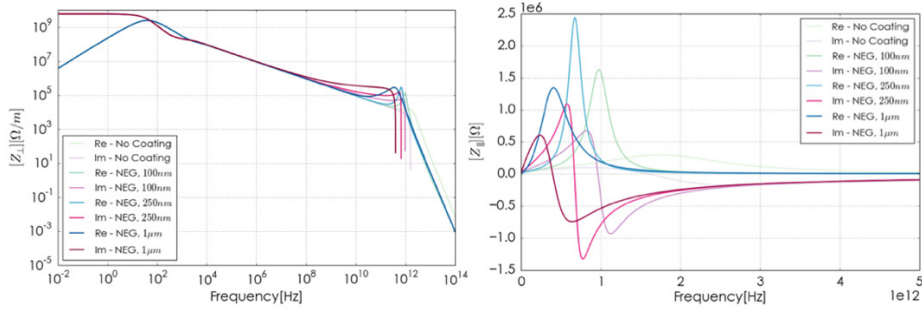


Figure 1: Real and imaginary part of the transverse (left) and longitudinal (right) RW impedances as a function of the frequency in the case of no coating and NEG coating with different thicknesses.

The following sections are focused on the most important effects of the RW on the single bunch dynamics: the Microwave Instability (MI) and the Transverse Mode Coupling Instability (TMCI) in the longitudinal and transverse planes, respectively. The main parameters used for the simulations are listed in Table 1.

2.8.2.1.1 Microwave instability

One consequence of the longitudinal microwave instability is the bunch lengthening, together with changes in the energy spread, which starts to increase above the instability

threshold. The bunch length and the energy spread as a function of the bunch intensity obtained from the macroparticle tracking code PyHEADTAIL [14] are shown in Figure 2, for all the cases under study. It is clearly visible that NEG film coatings must be thin(ner) to ensure the beam stability. In fact, in the case of 100 nm thickness the MI threshold is about two times larger than the nominal bunch intensity, while for a thicker coating of 1 μm the bunch is unstable. It is important to note that these studies do not take into account the beamstrahlung with colliding beams, which gives a much longer bunch and a higher energy spread, thus helping to increase the MI threshold.

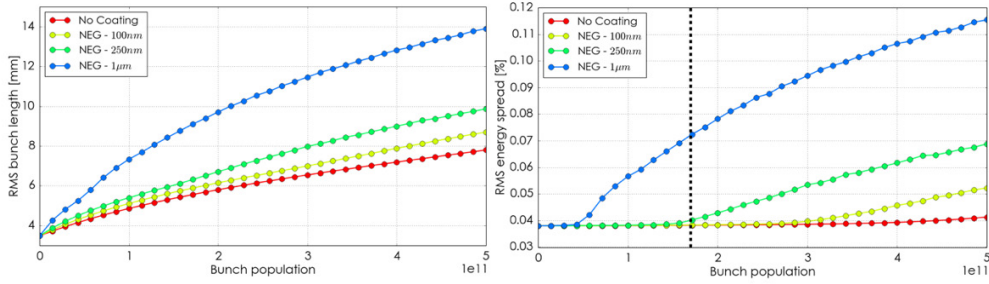


Figure 2: Bunch length and energy spread as a function of the bunch intensity by considering only the RW contribution for different thicknesses of the NEG films. The dashed black line represents the nominal bunch intensity.

2.8.2.1.2 Transverse mode coupling instability

It is well known from theory [4] that the betatron frequencies of the intra-bunch modes shift when the bunch intensity increases and the instability occurs when the mode frequency lines merge. Unlike the longitudinal case, above the instability threshold the bunch is lost in the transverse case and this makes the TMCI very dangerous for the beam.

Figure 3 shows the real part of the tune shift of the first two radial modes (with azimuthal number from -2 to 2) as a function of the bunch population for the case of 100 nm coating. The eigenfrequencies of the coherent modes (azimuthal and radial) in the transverse plane are computed with the analytical Vlasov solver DELPHI [15] by taking into account the bunch lengthening due to the longitudinal wake (yellow curve in Figure 2).

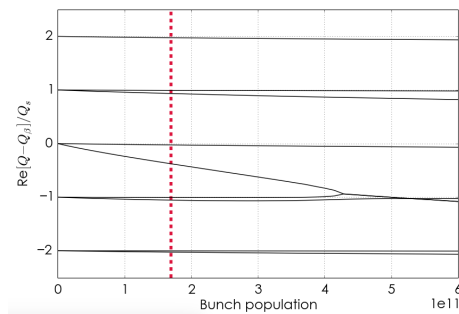


Figure 3: TMC1 threshold, evaluated by considering only the RW contribution in the case of 100 nm thick NEG coating, and taking into account the bunch lengthening due to the longitudinal wake. The dashed red line represents the nominal bunch intensity.

2.8.2.2 *Other impedance sources*

Besides the RW, there are other important impedance sources in the machine to be analysed with particular care (see Figure 4). First of all, for Z running, the RF system consists of about fifty-six single-cell 400 MHz cavities, which will be arranged in groups of 4 cavities, connected by tapers. In addition, 10000 absorbers will be needed to cope with the synchrotron radiation (SR), which is an important source of heat and photoelectrons for high-energy lepton machines. In order to reduce the impedance contribution of the photon absorbers, it was decided to use a circular vacuum chamber with 35 mm radius and two rectangular antechambers on both sides, inside which the SR absorbers can be installed, as is the case for the SuperKEKB beam pipe [16]. Diagnostic elements like four-button beam position monitors (BPMs) [17] are also planned to be installed for a total number of about 4000, with a rotation angle of 45° in order to place them directly on the winglet chamber and to avoid special winglet-to-circular tapers whose contribution has been observed to be not negligible compared to the RW one [18]. Finally, a total number of 20 collimators [19] (10 for each plane) are considered in this model.

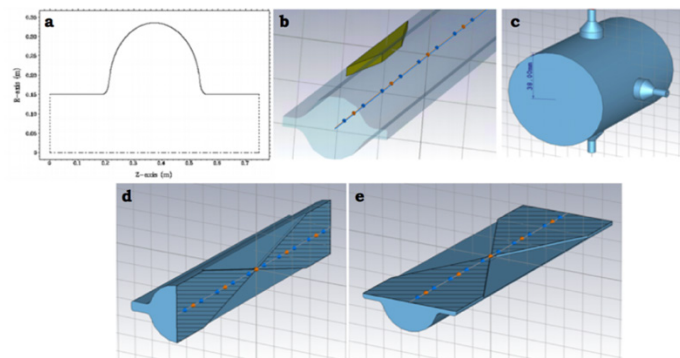


Figure 4: ABCI and CST models for a) RF cavities, b) SR absorbers, c) BPMs, d) vertical collimators and e) horizontal collimators.

In order to evaluate the contribution of all these components to the longitudinal impedance budget, CST [20] simulations in time domain were performed by considering a Gaussian bunch at the nominal bunch length of $\sigma_z = 3.5 \text{ mm}$. Figure 5 shows the comparison of the longitudinal wake potentials of each component with the RW one, obtained analytically as the convolution between the wake function computed by ImpedanceWake2D in the case of no coating and a 3.5 mm Gaussian bunch.

Figure 5 also contains an estimate of the loss factors for each component, corresponding to a total dissipated power of about 24.6 MW at the nominal intensity, about a factor 4 smaller than the total SR power dissipated by the two beams of about 100 MW. However, this value of power loss has to be considered as a conservative one and it is expected to be lower due to the bunch lengthening effect.

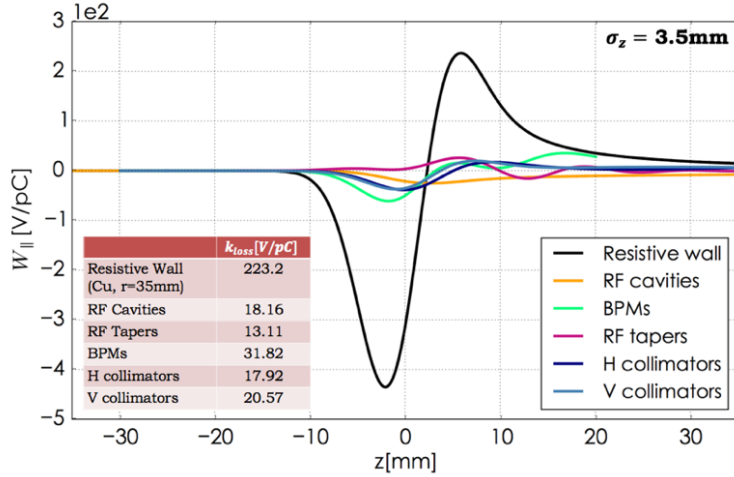


Figure 5: Total wake potentials for the nominal bunch length $\sigma_z = 3.5mm$ due to the several vacuum chamber components compared with the RW contribution (black line).

2.8.3 Electron cloud

Electron cloud (EC) effects represent one of the main performance limitations for both hadron and lepton machines [21, 22]. In the case of the lepton collider FCC-ee, primary electrons are attracted and accelerated by the positron beam and the electron accumulation in the vacuum chamber can cause the heating of the pipe walls and instabilities, beam losses, emittance growth and vacuum and diagnostics degradation. This section presents recent EC studies for FCC-ee. The EC build up will be analyzed in the arc dipoles of the machine and the use of EC maps will allow finding optimal filling schemes to reduce the heat load. An analytical estimation of the fast head-tail instability threshold will be given for all beam energies.

2.8.3.1 Electron cloud maps for FCC-ee dipoles

The numerical simulations have been performed with the PyECLoud code [23]. Primary electrons in the vacuum chamber are assumed to be generated by photoemission due to SR. In the case of FCC-ee at 45.6 GeV, the number of photoelectrons per particle per meter is given by $N_{ph} = N_\gamma Y$ where $N_\gamma = \frac{5\alpha}{2\sqrt{3}} \frac{\gamma}{\rho} = 0.085$ is the number of photons per particle per meter and $Y = 0.04$ is the photoelectron yield, i.e. the probability of electron emission per impinging photon. A reflectivity of $R = 80\%$ is assumed in our simulations (in the presence of antechambers and photon stops, this assumption may be quite pessimistic), meaning that 80% of photoelectrons are generated by photons which are reflected from the chamber. Simulations were performed for FCC-ee dipoles with magnetic field $B = 0.014 T$, at the nominal bunch population of 1.7×10^{11} and a bunch spacing of 2.5 ns, by scanning the SEY from 1.0 to 2.0.

Figure 6 shows the total number of electrons in the FCC-ee dipole chamber, assumed to be circular with radius $r = 35mm$, during the passage of a train of 1000 successive positron bunches followed by 400 empty bunches and for $\delta_{max} = 1.2$.

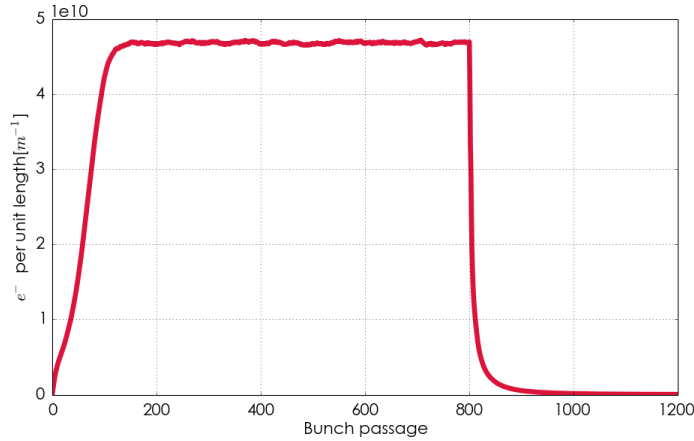


Figure 6: Time evolution of the total number of electrons in the chamber of the FCC-ee arc dipoles, for $Y = 0.04$, $R = 80\%$ and $\delta_{max} = 1.2$.

The electron density grows exponentially until a saturation level due to the space charge in the cloud of electrons and then it decays after the passage of the train. The rise time of the build up process and the decay time corresponding to the passage of the empty bunches can be expressed by means of a cubic map [24]

$$\rho_{m+1} = a\rho_m + b\rho_m^2 + c\rho_m^3 \quad (3)$$

whose coefficients depend only on the chamber (SEY, dimensions, etc.) and the beam parameters. Once these coefficients are extrapolated from a detailed build up simulation with a long train of bunches, they can be used to evaluate the electron density and the heat load evolution for different filling patterns. One possible application of the map formalism is the study of optimal filling schemes to reduce the build up process in the machine, with the advantage of a significant reduction of the simulation time.

Figure 7 shows the time evolution of the electron density and the heat load as a function of the SEY in the FCC-ee dipoles for three different filling schemes:

1. a long uniform train of 16640 bunches
2. 140 trains of 120 successive bunches followed by 200 empty bunches
3. 550 trains of 30 successive bunches followed by 100 empty bunches

The insertion of additional gaps in the bunch train allow to reduce the EC induced heat load by a factor of about 10. For comparison, the local heat load from synchrotron radiation is about 800 W/m.

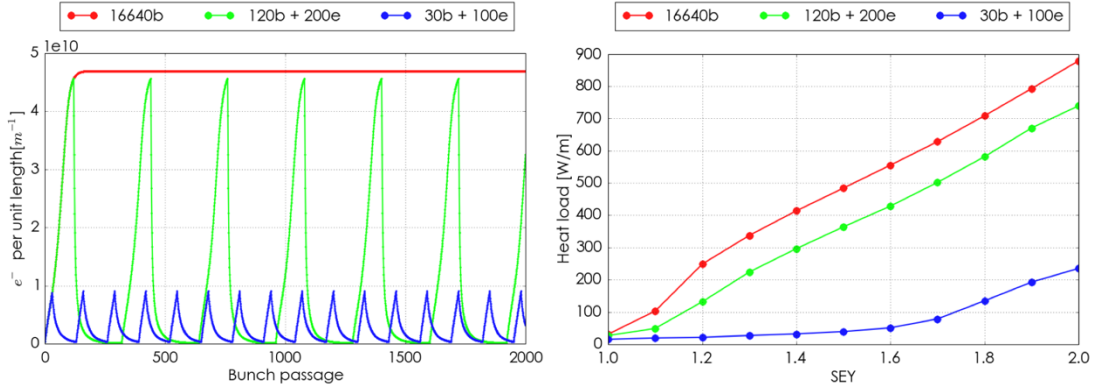


Figure 7: Electron density evolution (on the left) and heat load as a function of the SEY (on the right) in the FCC-ee arc dipoles for three different filling patterns, at nominal intensity $N = 1.7 \cdot 10^{11}$ and for $\delta_{max} = 1.2$.

2.8.3.2 Electron density threshold for the single bunch head-tail instability

EC single bunch head tail instability has been analysed and observed in several machines [25, 26]. This instability depends on the electron density near the beam whose threshold is given by

$$\rho_{th} = \frac{2\gamma Q_s}{\sqrt{3}Qr_e\beta C} \quad (3)$$

where r_e is the classical electron radius, $\beta_{x,y} = \frac{c}{2\pi Q_{x,y}}$ is the average beta of the machine and $Q = \min\left(\frac{\omega_e \sigma_z}{c}, 7\right)$ with ω_e the frequency of the electron oscillation near the beam centre [27]. Table 2 summarizes the electron density thresholds for FCC-ee at four energies, considering the baseline beam parameters shown in Table 1. Such low thresholds can create potential problems for the collider operation and this issue certainly deserves further investigations.

Table 2: Density thresholds of the fast head-tail instability for FCC-ee.

Energy E_0 [GeV]	45.6	80	120	175
Electron frequency $\frac{\omega_e}{2\pi}$ [GHz]	393.25	454.136	308.08	375.58
Electron oscillation $\frac{\omega_e \sigma_z}{c}$	28.847	31.41	20.34	19.28
Electron density threshold $\rho_{th}[10^{10}/m^3]$	2.29	5.39	12.6	34.6

2.8.4 References

1. <https://fcc.web.cern.ch>
2. D. Shatilov, “Luminosity optimization for FCC-ee: recent results”, 59th FCC-ee Optics Design meeting, 25 Aug 2017, CERN, Geneva, Switzerland.
3. L. Palumbo, V.G. Vaccaro, M. Zobov, “Wake fields and impedances”, Report No. LNF-94-041-P, 1994 and arXiv preprint physics/0309023 (2003).
4. A.W. Chao, “Physics of collective beam instabilities in high energy accelerators”,

- Wiley, 1993.
5. B. Zotter, S. Kheifets, "Impedances and Wakes in High Energy Particle Accelerators", World Scientific, 1998.
 6. K.Y. Ng, "Physics of intensity dependent beam instabilities", World Scientific, 2006.
 7. K.Y. Ng and K. Bane, "Explicit Expressions of Impedances and Wake Functions", SLAC-PUB-15078, 2010.
 8. E. Belli, M. Migliorati, S. Persichelli and M. Zobov, "Single beam collective effects in FCC-ee due to beam coupling impedance", arXiv preprint arXiv:1609.03495, 2016.
 9. M. Migliorati et al., "Collective effects issues for FCC-ee", eeFACT-2016-TUT3AH1.
 10. <https://kt.cern/technologies/non-evaporable-getter-neg-thin-film-coatings>
 11. A. Rossi, "SEY and electron cloud build-up with NEG materials", 2005, CERN, Geneva, Switzerland.
 12. E. Belli, "Impedance model and collective effects for FCC-ee", FCC Week 2017, 29 May- 2 Jun 2017, Berlin, Germany.
 13. <https://twiki.cern.ch/twiki/bin/view/ABPCComputing/ImpedanceWake2D>
 14. <https://github.com/PyCOMPLETE/PyHEADTAIL>
 15. <https://twiki.cern.ch/twiki/bin/view/ABPCComputing/DELPHI>
 16. Y. Suetsugu, K. Kanazawa, K. Shibata, T. Ishibashi, H. Hisamatsu et al., "Design and construction of the SuperKEKB vacuum system", Journal of Vacuum Science & Technology A: Vacuum, Surfaces, and Films 30.3 (2012): 031602.
 17. A. R. D. Rodrigues et al. "Sirius status report." 7th International Particle Accelerator Conference (IPAC'16), Busan, Korea, May 8-13, 2016.
 18. E. Belli et al., "Coupling impedances and collective effects for FCC-ee", IPAC-2017-THPAB020.
 19. T. Ishibashi et al., "Low impedance movable collimators for SuperKEKB", Proceedings of IPAC'17, Copenhagen, Denmark, May 14-19, 2017.
 20. <https://www.cst.com>
 21. H. Fukuma, "Electron cloud instability in KEKB and SuperKEKB", ICFA BDNL 48, p.112, Apr.2009.
 22. G. Iadarola, "Electron cloud studies for CERN particle accelerators and simulation code development", 2014.
 23. <https://github.com/PyCOMPLETE/PyECLOUD>
 24. U. Iriso, S. Peggs, "Maps for electron clouds", Physical Review Special Topics-Accelerators and Beams 8.2 (2005): 024403.
 25. G. Rumolo and F. Zimmermann, "Theory and Simulation of the Electron cloud instability." Proceedings of the LHC Workshop Chamonix XI. 2001.
 26. K. Ohmi, F. Zimmermann, "Head-Tail Instability Caused by Electron Clouds in Positron Storage Rings", PRL 85(18), pg.3821-3824 (2000).
 27. K. Ohmi, F. Zimmermann and E. Perevedentsev, "Study of the fast head-tail instability caused by the electron cloud", CERN-SL-2001-011 AP.

2.9 Interaction Region for the FCC-ee Design

M. Boscolo
 INFN-LNF, Via E. Fermi, 40 I-00044 Frascati (Rome), Italy;
 M.K. Sullivan
 SLAC, Menlo Park, California 94025, USA
 Mail to: manuela.boscolo@lnf.infn.it, sullivan@slac.stanford.edu

2.9.1 Introduction

We present here a current snapshot of the Interaction Region (IR) design for the Future Circular Collider electron-positron accelerator (FCC-ee) [1]. We introduce the IR design based on accelerator requirements and describe the additional details important in the study of backgrounds in the detector as well as to the needs of the detector. The requirements of the detector and of the accelerator at the collision point together make the IR one of the more challenging parts of the overall design. The challenge is to maximize performance in terms of integrated luminosity and minimize beam related backgrounds for the experiments. This includes minimizing synchrotron radiation in the IR.

2.9.2 Present IR design

2.9.2.1 *Accelerator Parameters used in the IR*

We list in Table 1 below the most important accelerator parameters used in designing the IR. We note in particular the high beam current and high luminosity of the Z operating point. The B-factories (PEP-II and KEKB) had such high beam currents but only about 1% of the luminosity. Even so, the B-factories had significant backgrounds from luminosity processes, in particular, radiative Bhabhas. On the other hand, the $t\bar{t}$ operating point while having low beam currents has the highest beam energy of 182.5 GeV and therefore the highest photon energy spectra from Synchrotron Radiation (SR).

The crab-waist collision scheme [2,3] associated with a large Piwinski angle and a very low vertical beta function has been chosen for the FCC-ee design. This scheme reduces the hourglass effect, allowing the vertical beta function β_y at the interaction point (IP) to be smaller than the bunch length. There is a net luminosity gain due to the small beam size at the interaction point and this gain is obtained with lower beam currents than those required for a conventional collision scheme. This scheme requires a large Piwinski angle, obtained with a small horizontal beam size and a large crossing angle (30 mrad). The large crossing angle at the interaction point allows for the beams to enter/exit separate beam pipes at about ± 1.2 m after the IP. So, the initial final focus defocusing quadrupole (QC1) can be a separate magnet for each beam. There is about 6 cm of space between the beams at the face of QC1 (± 2.2 m).

One of the most significant consequences of this large crossing angle scheme at the IP is the large bending of the incoming and outgoing beam trajectories in order to achieve this large angle. To minimize the effect on the IR of SR fans from these bend magnets we use an asymmetric optics such that the inner ring goes into the IP with soft upstream bend magnets. The beam is then bent more strongly after the IP in order to merge back close to the incoming beam ring.

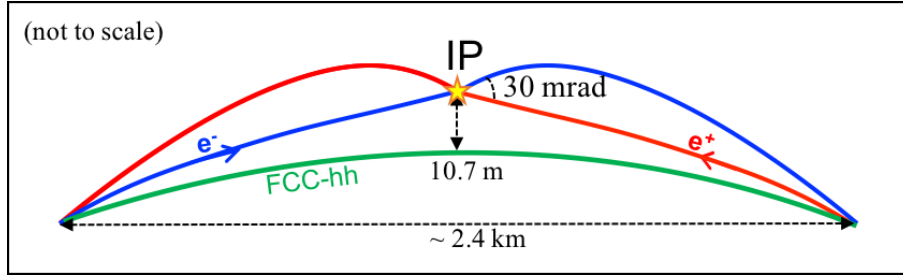


Figure 1: Sketch of the FCC-ee beam trajectories at IR.

Figure 1 shows a not-to-scale sketch of the FCC-ee IR together with the FCC hadron (FCC-hh) collider trajectory. The tunnel is defined by the FCC-hh design, and FCC-ee design has to adapt its layout to this footprint. The green line in the plot is the FCC-hh trajectory and in red and blue are the e^+ and e^- trajectories, asymmetric with respect to the IP. The distance between the FCC-ee IP with FCC-hh beamline is 10.7 m. Outside the IR, the FCC-ee and FCC-hh trajectories are on the same orbit. However, inside the FCC-ee IR, an additional tunnel is necessary for ± 1.2 km around the IP in order to allow for the crab-waist collision scheme with a large crossing angle. The interaction region is nevertheless locally symmetric, as is shown in Figure 3 and will be discussed in the next section.

Table 1: FCC-ee accelerator parameters that influence the IR design [4].

	<i>Unit</i>	<i>Z</i>	<i>WW</i>	<i>Higgs</i>	<i>t\bar{t}</i>
Circumference	km			97.756	
Crossing angle	mrad			30	
L^*	m			2.2	
Beam Energy	GeV	45.6	80	120	182.5
Beam current	mA	1390	147	29	5.4
Number of Bunches	#	16640	2000	393	39
Particles/bunch	$\times 10^{10}$	17	15	15	28
Hor. emittance	nm-rad	0.27	0.28	0.63	1.45
Ver. emittance	pm-rad	1.0	1.0	1.26	2.68
β_x at IP	m	0.15	0.2	0.3	1.0
β_y at IP	mm	0.8	1.0	1.0	2.0
σ_x at IP	μm	6.4	7.5	13.8	38.1
σ_y at IP	nm	28	32	36	73
Bunch length (SR/BS)	mm	3.5 / 12.1	3.3 / 7.65	3.15/4.9	2.5/3.3
Energy spread (SR/BS)	%	0.038 / 0.132	0.066 / 0.153	0.099 / 0.151	0.15 / 0.20
Energy acceptance	%	1.3	1.3	1.5	2.5
Luminosity	$\times 10^{34}$	230	32	7.8	1.5

Crab sextupoles are the other ingredient of this scheme. They rotate the β_y function so that its waist is on the central trajectory of the opposite colliding beam and, in addition, they suppress betatron and synchro-betatron resonances introduced by the large Piwinski

angle. These crab sextupoles have to be at the proper phase advance with respect to the IP (0.5π and π for the vertical and horizontal plane, respectively) and with the proper strength $k = \frac{1}{\theta} \frac{1}{\beta_y^* \beta_y} \sqrt{\frac{\beta_x^*}{\beta_x}}$. The FCC-ee IR implements this collision scheme at very high energy, so the design has to cope with high synchrotron radiation induced by incoming bending trajectories at the IR. The optics that minimizes SR fans into the experiments is asymmetric for the bending magnets as well as for the sextupoles needed for the vertical chromaticity correction.

The design of the beam optics is described in Refs. [5,6] and we refer here to lattice version 208_nosol [7]. The current IR design (below) attempts to accommodate all operating points for the accelerator, so the IR optics is rescaled in energy and the β functions at IP are optimized for each running energy. In fact, to mitigate the coherent beam-beam instabilities at the Z [8] the β_x^* is reduced to 15 cm with respect to 1 m at the $t\bar{t}$ energy. β_y^* goes from 0.8 mm at the Z to 2 mm at the $t\bar{t}$. On the other hand, at highest energies the beamstrahlung effect is stronger, limiting the beam lifetime. Thus, at the highest energy run, the required energy acceptance is larger (2.5%) due to the increase of the energy spread. Top-up injection is also planned in order to increase efficiency and manage with a beamstrahlung lifetime of less than one hour.

Figure 2 shows the $\sqrt{\beta_x}$, $\sqrt{\beta_y}$ and dispersion functions before 900 m and after 500 m from the IP for the top energy ($t\bar{t}$). It can be seen that the IR optics is asymmetric. The last bending magnet before the IP ends at about 114 m from the IP while the first bending magnet after the IP is as close as 25 m.

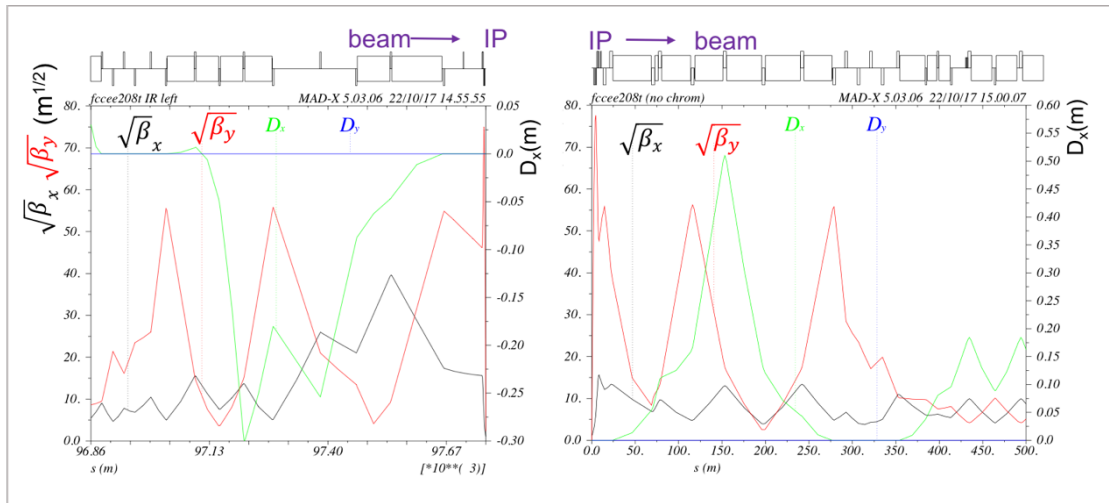


Figure 2: $\sqrt{\beta_x}$ and $\sqrt{\beta_y}$ functions and dispersion from 900 m to the IP (left) and from the IP to 500 m (right).

2.9.2.2 The Interaction Region Layout

Figure 3 displays the current interaction region layout in an expanded horizontal scale in order to show more detail in the X dimension. The face of the final focus magnets is 2.2 m from the Interaction Point (IP) which is the definition of L^* in Table 1. The final focus magnets are super-conducting and there is a compensating solenoid for the detector magnetic field located from 1.25 to 2.2 m from the IP on either side. Just in front of the

last dipole at about 150 m before the IP, in this location $20 \sigma_x$ correspond to 30 mm, but the pipe is 60 mm.

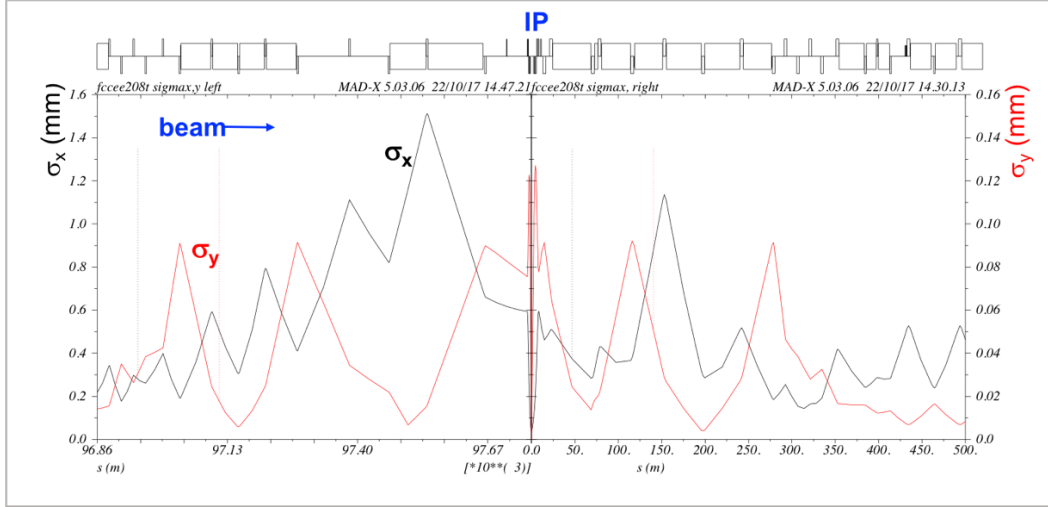


Figure 4: Beam sizes upstream -900 m and downstream $+500$ m from the IP for the top energy for a $\Delta p/p=0.2\%$. Left and right axis refer to σ_x and σ_y in mm.

The complicated geometry of the region where the two beam pipes are merged together keeping a constant aperture of 3 cm has been designed with CAD and checked with CTS and HFSS codes to analyse electro-magnetic fields in the IR (see Figure 5). These studies show that the cut-off frequency of electro-magnetic fields generated or trapped in the IR is at a safe value. High order mode absorbers have also been designed following the PEP-II experience [11]. The beam pipe will be at room temperature and water cooling is foreseen to mainly cool the area where HOM are placed due to the absorption of deposited power and where the SR masks are located.

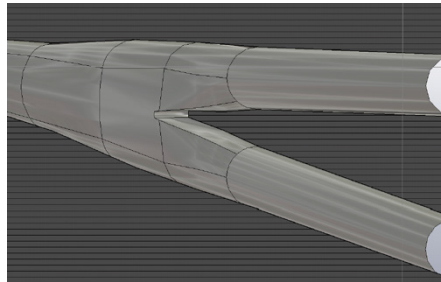


Figure 5: Smooth geometrical transitions from double to single vacuum pipe [13].

The beam pipe will be made of copper with an optimized coating to control the electron cloud build up and the transverse and longitudinal impedances [12]. However, the beam pipe of the central region (± 0.9 m from the IP), which includes the luminosity monitor window, needs to be made from a low-Z material like Beryllium (Be) (see Fig. 3). In addition, the central Be chamber will need to be cooled especially during the high-current Z running.

2.9.3 SR backgrounds from the last bend magnet before the IR

The possible sources of background from SR come from the last bending magnet before the collision point and from the quadrupoles between the bending magnet and the

IP. In order to minimize SR backgrounds from the last bend magnet we have requested the magnetic field to be as low as possible and near 100 keV for the critical energy of the bend radiation coming from this bend field out to 500 m from the IP. This requirement comes after the LEP2 experience, where the highest experimental limit was a critical energy of 72 keV from 260 m to the IP [13], which resulted in manageable detector backgrounds. The last bend magnet before the IP will always send a beam of SR photons down into the IR. In order to minimize this radiation fan the last bend magnet is approximately positioned between 100 and 200 m upstream of the collision point. Nevertheless, at the $t\bar{t}$ beam energy this radiation fan is the dominant source of SR background for the detector. We have placed SR mask tips at 2.1 m upstream of the IP, just in front of the first final focus defocusing quadrupole, in order to intercept this radiation fan and prevent the photons from directly striking the central Be beam pipe. The next level of SR background then comes from photons that strike near the tip of these masks, forward scatter through the mask and then strike the central beam pipe. At the $t\bar{t}$ energy, most of these scattered photons will penetrate the Be beam pipe and then cause backgrounds in the detector. To reduce the effect of this SR source on the experiment we propose to add a thin layer of high-Z material, for example gold, to the inside of the Be beam pipe. This is under study and we have found that at the top energy any reasonable thickness of gold (up to 10 μm) is not very effective due to the high energy of the scattered photons from the mask tip while at the Z energy the tip-scattered photons are so few and so soft that a gold layer is probably not needed. However, a layer of high conductivity metal will be needed (especially at the Z) in order to minimize beam pipe heating from image charge currents. Table 2 is a partial summary of the SR study up to now with details about the photon rate from the mask tip and the hit rate on the inside of the central Be beam pipe for the four different beam energies of the FCC-ee. This Table gives only the number of SR photons incident on the very central part of the IR Be beam pipe (± 12.5 cm). Full GEANT4 studies (which include a model of the entire beam pipe and of the nearby sub-detectors) of the scattered photons from these mask tips are needed and are underway with very encouraging preliminary results [9]

Synchrotron radiation adds an additional requirement on the overall optics design by requiring the critical energy throughout the ring to be no higher than 1 MeV in order to minimize the effects of neutron production via the giant dipole resonance. A complete description of the approach used to study and control the SR in the FCC-ee IR is in Ref. [15].

Table 2: Synchrotron Radiation background calculations for the fan from the last upstream bend magnet. The central beam pipe is a cylinder ± 12.5 cm in Z with a radius of 15 mm.

<i>Number of photons</i>	<i>Z</i>	<i>WW</i>	<i>Higgs</i>	<i>$t\bar{t}$</i>
Per bunch from the last bend magnet	6.69×10^{10}	1.03×10^{11}	1.55×10^{11}	1.37×10^{13}
Total incident on mask at 2.1 m	4.93×10^8	7.61×10^8	1.15×10^9	3.27×10^9
Incident on mask > 1 keV	7.38×10^7	3.33×10^8	7.00×10^8	2.41×10^9
Scattered from the mask tip > 1 keV	8	9390	2.58×10^5	7.87×10^6
Inc. on the central beam pipe > 1 keV	< 0.0037	< 0.033	3	787
Critical energy of bend radiation (keV)	1.63	8.45	28.5	100

2.9.4 SR backgrounds from the final focus quadrupoles

The final focus quadrupoles are very powerful in order to focus the beam to the required small spot at the collision point. This means the beta functions inside these quadrupoles are very large and therefore some fraction of beam particles experience very high magnetic fields in these magnets. The result of this is that the 4 quadrupoles (2 upstream and 2 downstream of the IP) for each beam generate quite intense (2.09 kW at $t\bar{t}$), very high energy photon beams that exit the IR. These photon beams will eventually strike the vacuum chamber as it bends with the outgoing beam as the beam goes through the downstream bending magnet. Although the photons in these SR beams have a rapidly falling energy spectrum there are still a significant number of photons greater than 1 MeV at the $t\bar{t}$ beam energy and some fraction of these photons could excite the giant dipole resonance. This will require a detailed study in order to understand and perhaps protect the detector from a possible nearby source of neutron background.

2.9.5 Other beam related backgrounds

The IR has been modelled starting from the CLIC detector design using Geant4 for full simulation of all the subdetectors. The effects of IP backgrounds such as radiative Bhabha, beamstrahlung, e^+e^- pair production and $\gamma\gamma$ to hadrons are being studied in terms of hit density, occupancy and deposited energy.

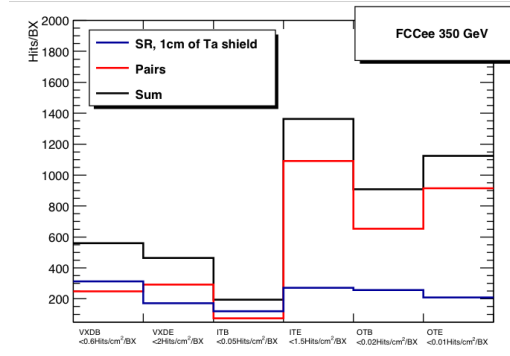


Figure 6: Hits per subdetector per bunch crossing. The plot shows the importance of a high-z shielding (in this case Tantalum [Ta]) around the beam pipe where possible (blue line).

An additional relevant source of beam related backgrounds in the detector can be beam-gas scattered particles (beam-gas bremsstrahlung and Coulomb scattering). Simulation studies are in progress, and preliminary results indicate that these sources are under control. Touschek scattering can in principle induce detector background from the small intense beam size in the IR. However, due to the high beam energy, this effect is not dominant as it is for low energy colliders. We see from Table 2 that SR backgrounds are clearly most important for the $t\bar{t}$ energy machine and that these backgrounds rapidly diminish as the beam energies go down. We actually see essentially no background from SR at either the Z or the WW machines. However, as the beam current increases with decreasing beam energy the lost beam particle backgrounds will become more significant and a careful study of the vacuum pressure along with collimator placement around the

rings will become very important. In addition, with the decrease in beam energy there is also an increase in luminosity and for the lower energy machines the luminosity backgrounds (radiative Bhabha, e^+e^- pair production, $\gamma\gamma$ to hadrons...) will dominate. At the $t\bar{t}$ energy one major concern is beamstrahlung which also determines the beam lifetime.

2.9.6 Conclusion

We have described the IR layout of the FCC-ee collider, a challenging and innovative machine that aims at precision studies and rare decay observations in the range of 90 to 365 GeV centre-of-mass energy. We have shown the key challenges but also the feasibility of the design.

We have discussed the constraints of the design imposed by the beam optics, the parameter choices and the collision scheme, together with the physics requirements, the luminosity measurement precision, and backgrounds, in particular synchrotron radiation. Synchrotron radiation is in fact a major contributor to this layout and we have shown the countermeasures that reduce this effect to manageable levels.

2.9.7 Acknowledgements

The authors wish to thank M. Benedikt, H. Burkhardt, A. Kolano, R. Kersevan, M. Koratzinos, K. Oide, G. Voutsinas, F. Zimmermann for useful discussions and suggestions.

2.9.8 References

1. The FCC-ee study, <http://cern.ch/fcc> .
2. P. Raimondi, D. Shatilov, M. Zobov, arXiv:physics/0702033 (2007).
3. M. Zobov *et al.*, PRL **104**, 174801 (2010).
4. A. Blondel, P. Janot, K. Oide, D. Shatilov, F. Zimmermann, FCC-ee parameter update, 6 October (2017).
5. K. Oide *et al.*, Phys. Rev. Accel. Beams **19** (2016) no.11, 111005.
6. K. Oide *et al.*, in Proc. IPAC17, TUOCB1, Copenhagen, May 2017.
7. K. Oide, private communication, October 2017.
8. K. Ohmi, N. Kuroo, K. Oide, D. Zhou and F. Zimmermann, Phys. Rev. Lett. **119** (2017) no.13, 134801.
9. G. Voutsinas, N. Bacchetta, P. Janot, A. Kolano, E. F. Perez, N.A. Tehrani, M. Boscolo, M.K. Sullivan, in Proc. IPAC17, WEPIKP004, Copenhagen, May 2017. See also presentation at the FCC WEEK 2017.
10. S. Sinyatkin, M. Koratzinos, presented at the FCC-ee MDI workshop, January (2017), <https://indico.cern.ch/event/596695>
11. A. Novokhatski, this ICFA edition.
12. E. Belli *et al.*, in Proc. IPAC17, THPAB020, Copenhagen, May 2017.
13. Courtesy of Miguel Gil Costa, May (2017).
14. G. von Holtey *et al.*, Nucl. Instrum. Meth. A 403 (1998) 205.
15. M. Boscolo, H. Burkhardt and M. Sullivan, Phys. Rev. Accel. Beams **20** (2017) no.1, 011008.

2.10 HOM mitigation for FCC-ee

Alexander Novokhatski

Mail to: novo@slac.stanford.edu

SLAC National Accelerator Laboratory, Menlo Park, CA, USA

2.10.1 Introduction

High electron and positron currents (1.5 A) are planned to be used in the Future Circular electron-positron Collider (FCC-ee) with a goal to archive high luminosity of order of $2.3 \cdot 10^{36} \text{ cm}^{-2}\text{s}^{-2}$ at the Z-production collision at the beam energy of 45.6 GeV [1, 2]. Coherent effects at the high-current machine impose certain limitations on the magnitude of the impedance of the machine. The potential well distortion due to inductive part of the impedance may give a large bunch lengthening. The microwave longitudinal and transverse instability set the total limit on the effective impedance. The multi bunch longitudinal and transverse mode-coupling can be more dangerous for the beam dynamics, but fortunately the feedback system can be used to damp these instabilities. An additional effect of the resonance part of the impedance is the HOM (Higher Order Modes) heating. It can happen not only in the RF cavities, but anywhere in the machine beam pipe where trapped mode or traveling waves absorb their power. Temperature raise due to HOM heating can be very high in the closed volumes without cooling. Very important the HOM heating is in the Interaction Region (IR), because it brings an additional background. The local heating in the IR can reach tens of kW of power. Some part of the electromagnetic waves, excited by the beam, with a frequency above the cutoff frequency will travel away from the IR and go down the beam pipe. The absorption of these waves can bring heating problems to other parts of the accelerator. A large energy loss of the beams in the interaction region can be a severe problem. The temperature of the IR chamber will go up and the vacuum will be spoiled. If the IR chamber has small gaps or hidden cavities (like in shielded bellows or valves), then electric sparks or arcing may cause additional vacuum spikes. Heating of nonevaporable getters (if they are will be used in the IR) may bring vacuum instability (the temperature can go above the recovery level). All of these things can make the backgrounds much higher. One can find a description of these effects in publications [3, 4]. Impedance study for FCC-ee can be found in reference [5].

2.10.2 HOM excitation.

The dominant contribution to the impedance comes from the resistive-wall wake fields excited in the beam pipe; wake field generated in the very complicated beam pipe geometry like the IR and RF cavities (even HOM damped). There are several other beam pipe elements, which can bring more impedance. They are: beam collimators; feedback cavities and BPMs; injector and abort kickers; bellows and vacuum valves; pumping holes and screens; wall coating. Some of these elements can also adsorb the power of propagating waves, generated in other places and consequently become the HOM heating elements.

2.10.2.1 Propagating waves

In general the reason of excitation of the propagating waves is an obstacle in the beam pipe, like for example a collimator. An energy loss of a point charge due to diffraction of its own field on an obstacle is proportional to the particle energy γmc^2

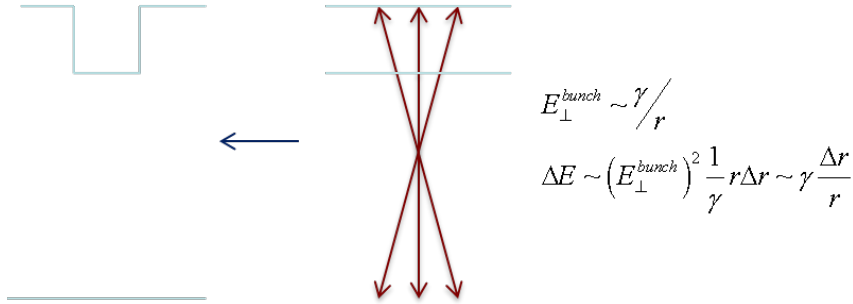


Figure 1: A point charge field energy, diffracted at the obstacle.

We may consider radiation of a point charge as a high frequency part of the radiation of a bunch of particles. However we know that the low frequency part does not depend on the energy in the ultra-relativistic case. That means that radiation of many particles is coherent in the low frequency part and the radiation power will increase in quadrature with a number of particles. To fulfill the coherence condition in this case we need a smaller bunch length in comparison with a wavelength of an excited wave. In the FCC-ee the bunch length will vary in the region of 3-12 mm, which is smaller than the beam pipe transverse dimensions and therefore the radiation will not be shielded by the wall chamber.

A simple estimate of the energy loss factor for an obstacle Δr in a pipe with a radius $r=a$

$$k \sim \frac{Z_0 c}{2\pi^{3/2} \sigma} \frac{\Delta r}{a} \quad (1)$$

For the case when a bunch length σ is 1 mm; pipe radius a is 10 mm; and the size of an obstacle Δr is 1mm the loss factor is 0.1 V/pC.

Usually these waves propagate away before the next bunch comes to this place. However these waves can be dangerous too as they can propagate long distances and be absorbed in low resistance elements like NEG's or vacuum pumps. Wake fields due to roughness surface or dielectric layer can be also include in this category, as a representative of the Cherenkov radiation.

2.10.2.2 Trapped modes

Trapped modes could exist in a cavity-like element in the beam pipe. A trapped mode has a smaller frequency than a cut-off frequency of the beam pipe for a corresponding electromagnetic field distribution (monopole, dipole, etc.). Sometimes a frequency of a trapped mode is exactly equal to some of the beam spectrum line or a rotation frequency harmonic. The amplitude of the field in this cavity increases linear with a number of bunches passing nearby until the self-saturation due to resistivity of the metal walls. The

power of radiation in the resonance case is determined by the beam current squared I^2 , a trapped mode loss factor k and a damping time τ_n of this mode. If a bunch spacing τ_b is much shorter than the damping time then

$$\tau_n \gg \tau_b \quad P_{coh} = 2I^2 \sum_n k_n \tau_n \quad (2)$$

In other case when the damping is smaller than a bunch spacing the power will be determined by a bunch spacing

$$\tau_n \ll \tau_b \quad P_{in} = I^2 \sum_n k_n \tau_b \quad (3)$$

If a bunch spacing is equal to a damping time than the resonance power is only two time larger than in the case when a trapped mode frequency is not coincident with a bunch spacing harmonics.

To make an estimate of the radiation power (which will be somewhere be absorbed) we may assume relative to the FCC-ee parameter that the bunch spacing is 2.5 nsec, loss factor as in the previous example is 0.1 V/pC and the beam current is 2 A (this number correspond to the case when only three quarter of a ring is filled with a beam, then effective current becomes larger than the nominal). If we use the last formula for the power will found that the power is 1 kW. This means that loss factor of order of 0.1 V/pC will be responsible for a power of a microwave store. Every small irregularity in the beam pipe becomes very important.

2.10.2.3 *HOM heating*

If electromagnetic power dissipates in the place without any outside cooling (water or air), the temperature can rise to very high level up to the melting point. Some “cavities” can be hidden outside the beam pipe but have a coupling to the beam through small holes in the metal wall or ceramic windows. Usually they are shielded bellows; shielded vacuum valves and BPM or vacuum pumps feed-through.

I will argue with some “researchers”, who allow small gaps in the beam pipe. A small gap in a vacuum chamber can be a source of high intensity wake fields, which may cause electric breakdowns. And usually a small gap in a beam pipe couples the bunch field with an outside “cavity”.

HOM absorbers can be used to take away the generated from some unavoidable places like IR and collimator. Longitude wake field can be suppressed by longitudinal shielded metal fingers; however transverse wake fields may escape through the slots between the fingers. They must be absorbed by the HOM absorber. It is planned to use HOM absorbers in the FCC-ee interaction region [6]. The plot of IR with HOM absorbers is shown in Fig. 2.

Due to a smooth geometry of the vacuum chamber IR has a relatively small impedance and only one trapped mode. In the case of the bunch length of 2.5 mm and the beam current of 1.45 A the electromagnetic power is approximately 5 KW in each set of pipe connection, which includes power of the trapped mode and the power of all propagating modes. This power will be mainly absorbed in the HOM absorbers.

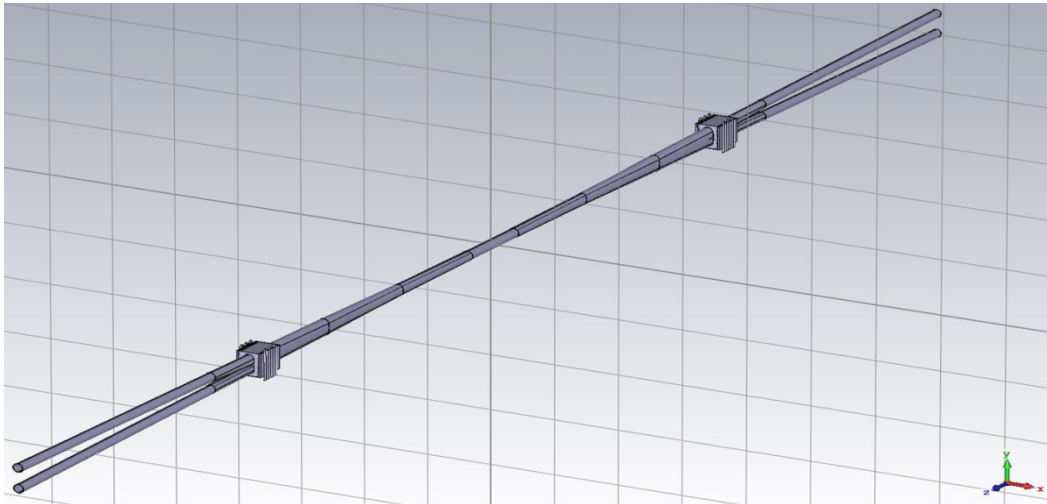


Figure 2: FCC-ee IR beam pipe with HOM absorbers.

2.10.2.4 *Concept of HOM absorber in IR*

A sketch of the HOM absorber in IR is shown in Fig. 3. The absorber vacuum box is situated near (around) beam pipe connection. Inside the box we have ceramic absorbing tiles and copper plates (walls). The beam pipe has longitudinal slots in this place. These slots connect the beam pipe and the absorber box. Outside the box we have stainless steel water-cooling tubes, braised to the copper plates. HOM fields, which are generating by the beam in the IR have a transverse electrical component and can pass through the longitudinal slots in the beam pipe. Inside the absorber box these fields are absorbed by ceramic tiles, which have high value of the loss tangent. Ceramic tiles are braised to copper plates with columns. The heat from ceramic tiles is transported through the copper plates to water cooling tubes.

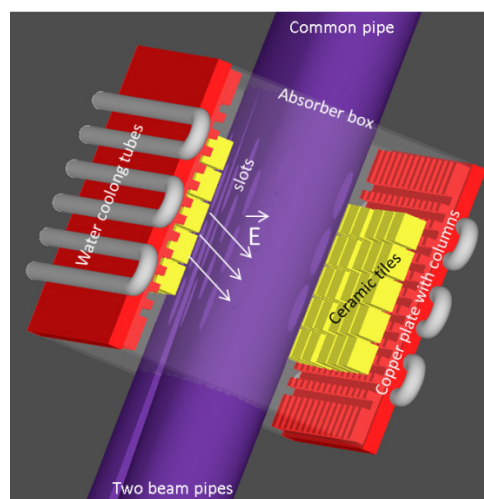


Figure 3: A HOM absorber for FCC-ee IR.

2.10.3 **Summary with recommendations on the beam pipe geometry.**

Electron and positron bunches generate electromagnetic fields at any discontinuity of the vacuum chamber. These fields can travel long distance and penetrate inside bellows,

pumps and vacuum valves. Vacuum chamber must be very smooth. HOM absorbers must be installed in every region that has unavoidable discontinuity of the vacuum chamber. Maximum attention to the RF seals designs. Design of a BPM button would contain a cooling possibility. No open (to the beam) ceramic or ferrite tiles. Increase the bunch length as possible. We don't have to forget that beam pipe heating due to resistive-wall wake fields make the beam pipe to be water cooled.

2.10.4 References

16. M. Benedikt and F. Zimmermann, "Towards future circular colliders", J. Korean Phys. Soc. 69, 893 (2016).
17. FCC week 2017, Berlin, Germany,
<https://indico.cern.ch/event/556692/timetable/#20170531.detailed>
18. A. Novokhatski, J. Seeman, and M. Sullivan, Analysis of the wake field effects in the PEP-II storage rings with extremely high currents, Nucl. Instrum. Methods Phys. Res., Sect. A 735, 349 (2014).
19. A. Novokhatski, J. Seeman, M. Sullivan, and U. Wienands, Electromagnetic waves excitation, propagation and absorption in the high current storage rings, IEEE Trans. Nucl. Sci. 63, 812 (2016).
20. E. Belli, M. Migliorati, G. Castorina, B. Spataro, M. Zobov, A. Novokhatski, S. Persichelli, "Coupling Impedances and Collective Effects for FCC-ee", Proceedings of IPAC2017, Copenhagen, Denmark, THPAB020, p. 3734.
21. A. Novokhatski, M. Sullivan, E. Belli, M. Gil Costa and R. Kersevan, "Unavoidable trapped mode in the interaction region of colliding beams", Phys. Rev. Accelerators and Beams 20, 111005 (2017)

2.11 Final twin quadrupole design for the FCC-ee based on the canted cosine theta concept

M. Koratzinos

Mail to: m.koratzinos@cern.ch

University of Geneva, Switzerland.

2.11.1 Introduction

The FCC-ee is part of the FCC study [1], an ambitious post-LHC accelerator complex study in the Geneva area. FCC-ee is a powerful e^+e^- circular collider with ultimate luminosity performance. This is achieved partly through extremely small vertical emittances of around 1pm. The FCC-ee interaction region [2] is very challenging, in part because the final focus quadrupoles, 2.2 m from the interaction point (IP) sit very close to each other. The field quality of these magnets needs to be excellent and in any case better than one unit of 10^{-4} . The angle between the 30 mm diameter beam pipes of the electrons and positrons is 30 mrad in the horizontal plane, translating to a distance between the centres of the two quadrupoles at the tip of 6.6 cm. This calls for a very compact design, which also needs to have very high field quality. The use of iron to shield the magnetic field of the neighbouring quadrupole can only work at low fields. For the fields needed here (100 T/m field gradient) the iron will saturate and important cross talk

would be present. For this reason we have concentrated on an iron-free design and have developed a technique of designing-out field imperfections due to cross talk and edge effects using the canted-cosine-theta (CCT) concept.

CCT magnets have been known since the seventies [1], however only recently have they become popular with magnet designers [3], due to the advent of modern manufacturing techniques (CNC machines and 3D printing). The CCT design concept is based around a pair of conductors wound and powered such that their transverse field components sum up and their axial (solenoidal) fields cancel. In practice the conductor is wound on a pre-cut groove in a supporting hollow cylinder or *mandrel*. The area between grooves is referred to as the *rib* and the supporting solid substrate the *spar*. The difference with a conventional design is that stresses cannot accumulate between conductors but instead forces are intercepted by ribs that transfer the stress to the spar.

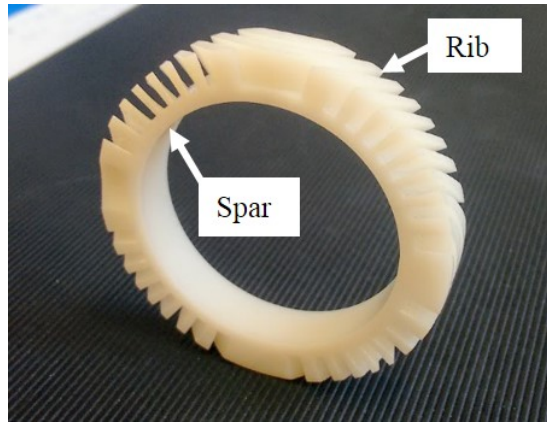


Figure 2: A slice of one of the two layers of a CCT magnet (a quadrupole). The spar is 2 mm wide, followed by a 4 mm rib where the grooves for the cable are located.

In the general case of a coil that produces an arbitrary selection of multipole fields, the centre-line defining the shape of the groove (and the position of the centre of the powered cable) for one of the two coils of the CCT is described by the equation

$$\begin{aligned}
 x &= R \cos \theta ; \\
 y &= R \sin \theta ; \\
 z &= \sum_{n_B} \left[\frac{R \sin(n_B \theta)}{n_B \tan \alpha_{n_B}} + \frac{\omega \theta}{2\pi} \right] + \sum_{n_A} \left[\frac{R \cos(n_A \theta)}{n_A \tan \alpha_{n_A}} + \frac{\omega \theta}{2\pi} \right] \quad (1)
 \end{aligned}$$

Where R is the radius of the coil, A and B are the skew and normal components of the field, n_A and n_B are the skew and normal multipoles ($n_B = 1$ is the dipole component, $n_B = 2$ the quadrupole component, etc., same with $n_A = 1$: skew dipole component, etc.). The angles α_{n_A} , which could be a function of z , are the angles of the groove (or wire) with respect to the horizontal on the mid plane per desired multipole (called the skew angles). An angle of zero would ensure no relevant multipole component. θ runs from 0 to $2\pi n_t$ where n_t is the number of turns. For the second layer, R is slightly increased (depending on the thickness of the spar and the cable) and the skew angle has the opposite sign. The start and end of both layers are located on top of one another. We

can see from equation (1) that the groove and cable describe a circle in the x-y plane whereas in the longitudinal (z) direction there is a longitudinal shift parameter ω per revolution, plus the multipole component.

The CCT design offers significant advantages over traditional magnet design for certain applications. Their field quality is excellent due to the purity of the design and due to the fact that the cable grooves can be very precisely machined; they are easy to manufacture using CNC machines or even 3D printing techniques, leading to very fast prototyping; there is no need for coil pre-stress during assembly, leading to simple and fast winding; reduced coil stresses improve magnet training; the design gives total freedom to implement any multipole arrangement, therefore capable of producing compact double aperture magnets with the required field quality, as demonstrated in this paper; and finally this concept uses fewer components and is considerably lighter than traditional designs, leading to reduced overall costs.

The disadvantage of the CCT design is that the two magnet coils work against each other to cancel the longitudinal field, leading to more conductor material per Tesla produced. Since our application is not a high field application, we are not affected by this potential limitation in this design.

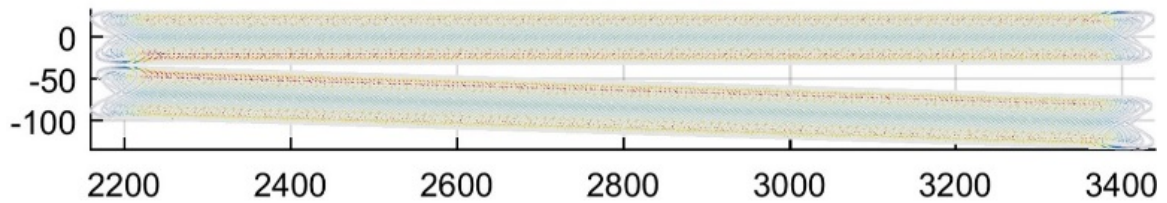


Figure 3: The position of the two QC1L1 magnets, at an angle of 30 mrad and at a distance of 2.2 m from the IP. The axes go through the positron beamline. Horizontal plane. Distances in mm.

2.11.2 Edges Correction

2.11.2.1 *The coil*

The FCC-ee final focus quadrupole comprises six coils [5], three per beam, out of which the most challenging is the QC1L1 pair that sits closer to the IP at a distance of 2200 mm (see Figure 3). Its length is 1200 mm and has an inner bore of 40 mm diameter. The cable of the inner coil has an inner and outer radius of 22 and 26 mm, and the outer coil 28 and 32 mm. The inner spar occupies the area of radius 20 to 22 mm and the middle spar a radius of 26 to 28 mm. The grooves are 2 mm wide and 4 mm high, leaving a possible cross section for the cable of 8 mm². The pitch between grooves is 5 mm, leaving a minimum rib width of 1mm. The beam pipe is expected to have a diameter of 30 mm, so all multipoles are calculated at a radius of 10 mm, at an aperture of 2/3. This quadrupole produces a gradient of 100 T/m for a total current of around 5800 A. The transverse components of the magnet can be seen in Figure 4.

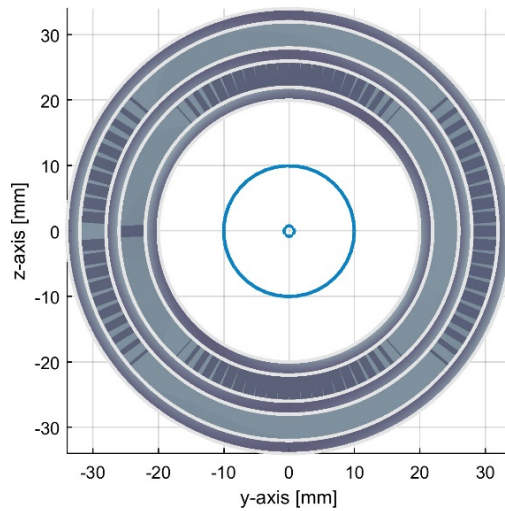


Figure 4: A view in the transverse plane of the quadrupole CCT magnet QC1L1. The blue circle (radius 10mm) is where multipoles are calculated.

The software used throughout this analysis is the Field 2017 suite of programs [6].

The multipole components around both edges of such a magnet can be seen in Figure 5. Only one magnet edge is shown (the one at negative z). The other edge has components which are antisymmetric. All A and B components integrate to zero when integrating over the length of the magnet. However, only the B components integrate to zero locally (per edge). As this magnet will be placed in an area of rapidly varying optics functions, it is beneficial if an edge correction could be applied so that the multipoles would integrate to zero locally.

The integral of the multipole components (normalized to the B2 field, in units of 10^{-4}) can be seen in Figure 6.

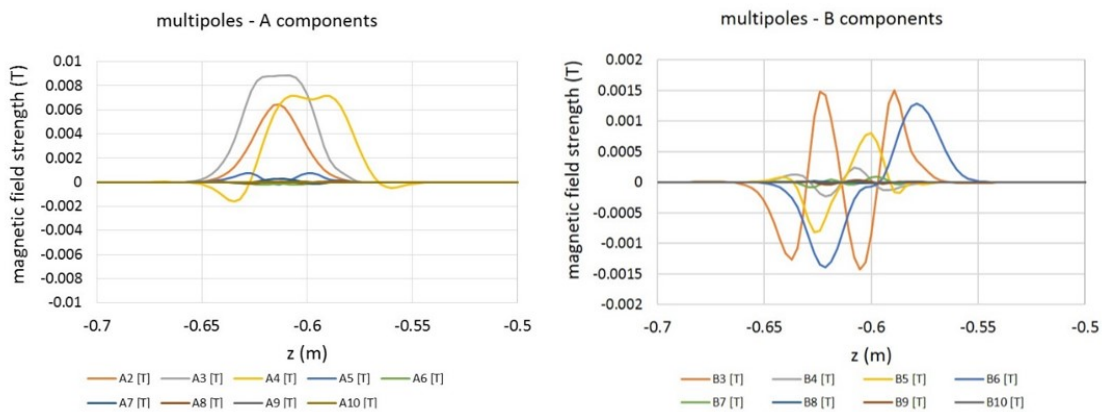


Figure 5: A and B multipole components up to order 10 on the left edge of the coil. The A, B1 and B2 components have been omitted. The right edge has components with a flipped sign.

2.11.2.2 *The correction*

The correction needs to be applied locally to the A components. This is done by applying non-zero multipole components for the first two turns of the coil. To make sure that the cable does not turn back on itself (i.e. that the gap between the adjacent windings of the cable is always larger than zero) the pitch for these first two windings has been increased to 15mm from 5 mm for the rest of the coil. Corrections up to order 6 are

performed (for higher orders the residual effect is too small). Following the A corrections, some B component corrections need to be also applied, again for the first two turns of the coil. This analysis is performed in the absence of any alignment or positioning errors. The integrated multipole plot after the correction can be seen in Figure 7. This demonstrates that a correction to an arbitrary degree of accuracy can be achieved (here we have stopped the process when an accuracy of 0.05 units or better had been achieved). The magnitude of the edge corrections can be seen in Table 1.

Table 1: Size of edge correction (in degrees) for the first and last windings of the magnet for all corrected multipoles. B2, the main component, is also given for reference.

	A2	A3	A4	A5	A6	B2	B3	B4	B5	B6
α left	-3.1	19	-38	6	6	60	-5	-3.5	6.5	1.5
α right	3.1	-19	38	-6	-6	60	-5	-3.5	6.5	1.5

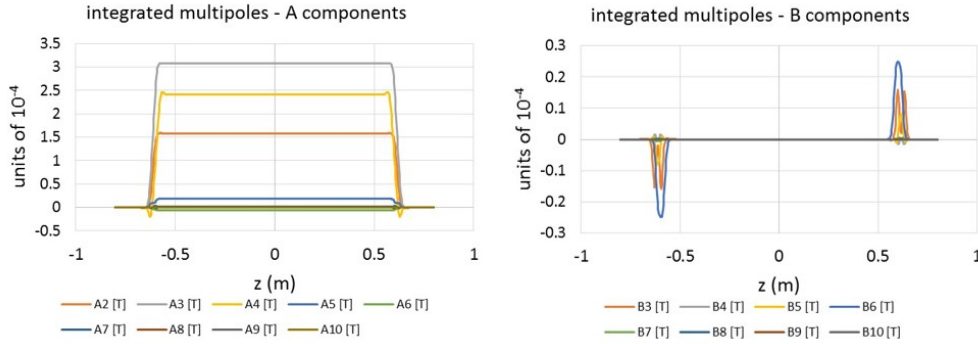


Figure 6: Integrated multipoles, before correction, in units of 10^{-4} . The A1, B1 and B2 components have been left out for clarity. The A1 and B1 components do not need to be corrected, whereas the B2 component has a final integrated value (by definition) of 10,000.

2.11.3 Crosstalk compensation

2.11.3.1 The coils

The edges correction is applied to a single coil in standalone mode. However, in the case of the FCC-ee the QC1L1 magnets sit in close proximity and at a variable distance from each other, as seen in Figure 3. Their distance from their magnetic centres is 66 mm at the tip and 102 mm at the end away from the IP (the magnets are 1.2 m long). The FCC-ee final focus system has many more magnetic elements, but we will concentrate on the crosstalk compensation of the two QC1L1 magnets, which is the most challenging problem. No iron is present in the vicinity of the magnets. The two QC1L1 magnets are

a mirror image of each other (the hypothetical mirror standing vertically between the two beamlines) and are powdered together by the same power supply.

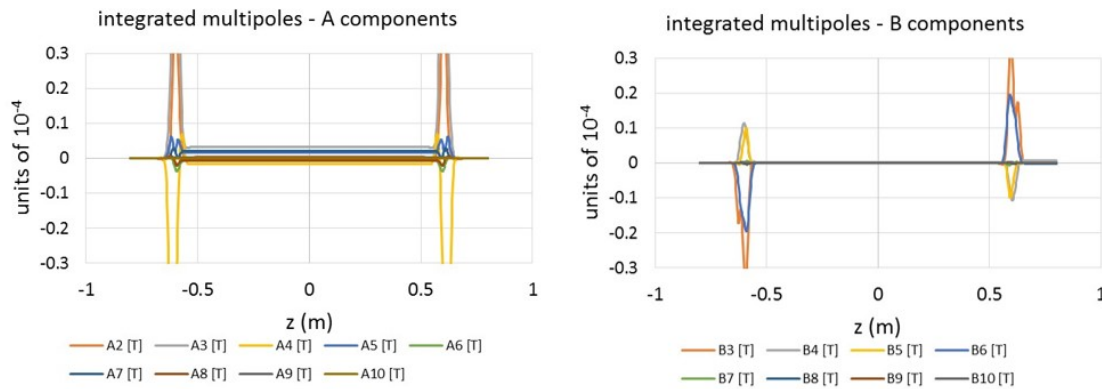


Figure 7: Integrated multipoles in units of 10^{-4} after correction. Note the different scale compared to Figure 6.

The uncorrected multipoles from this arrangement can be seen in Figure 8. There are significant components due to the close proximity of the other coil.

2.11.3.2 *The method*

Every effort is made to perform any needed correction locally. Currently the correction is performed empirically, with plans to develop an automated minimization procedure in the near future. Multipole corrections are nearly orthogonal to each other, so the minimization process converges rapidly. Only exception is the edges A2 correction which is affected by other multipoles, therefore the correction for A2 should be performed last.

It is not clear where the limits of the method are with respect to the level of compensation possible. We simply stopped at a level (around 0.05 units) where we felt that other distortions (for instance, due to misalignment or winding errors) would be more important.

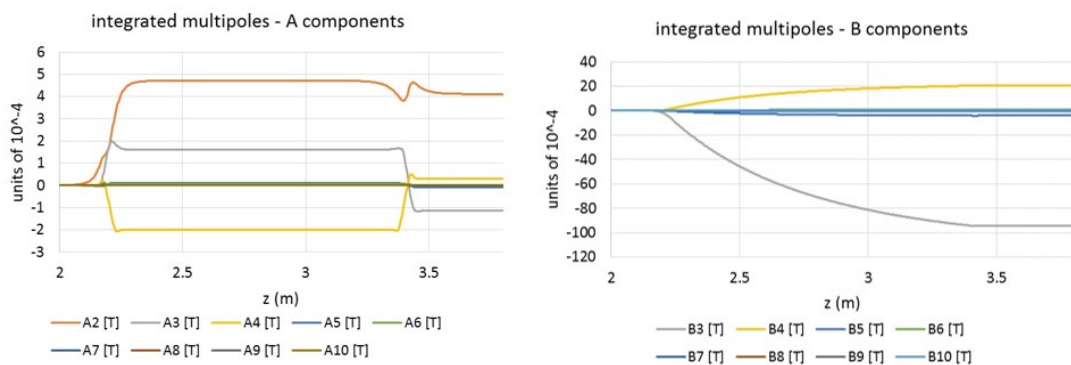


Figure 8: Integrated multipoles in units of 10^{-4} before correction in the case of two side-by-side QC1L1 magnets. As expected from the proximity of the two quadrupoles, the effect of cross talk is large.

2.11.3.3 *The correction*

In contrast to the earlier case, here we need to introduce multipole components along the whole length of the magnet. The results are very encouraging and can be seen in

Figure 9. All multipoles are corrected to within 0.05 units. The maximum and minimum correction along the length of the magnet (excluding the edges where a special correction is performed) can be seen in Table 2.

Table 2: Size of crosstalk correction (in degrees) along the length of the quadrupole. The edges have been excluded from this table. B2, the main component, is also given for reference

	A2	A3	A4	A5	A6	B2	B3	B4	B5	B6
α max	0	0	0	0	0	60	5.1	-4.0	2.0	-1.4
α min	0	0	0	0	0	60	0.8	-0.3	0.1	-0.0

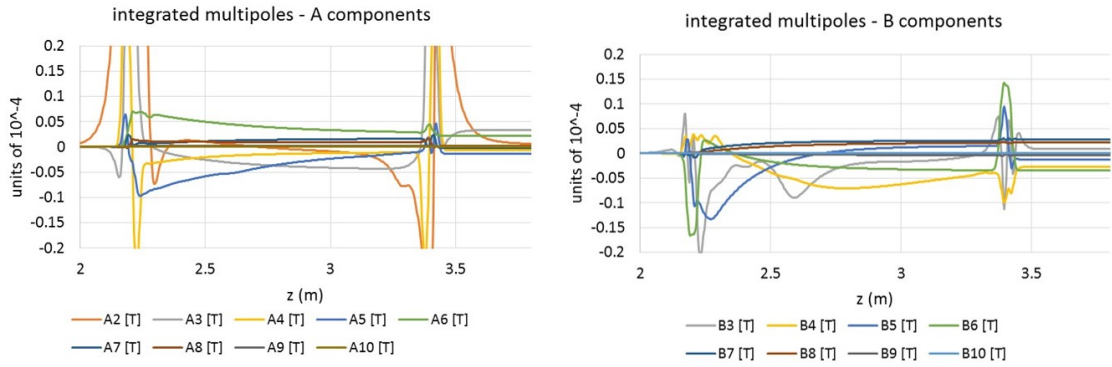


Figure 9: Integrated multipoles in units of 10^{-4} after correction for the effect of crosstalk from the adjacent quadrupole. All multipoles can be corrected to better than 0.05 units

2.11.4 Conclusions

The CCT magnet concept offers a versatility seldom associated with magnet design. Any multipole arrangement can be designed and implemented. We have first demonstrated that the inevitable edge effects of our test CCT quadrupole magnet (and therefore any CCT magnet) can be eliminated to below 0.05 units. We have further demonstrated that in an iron-free environment we can create two nearly-perfect parallel powered quadrupoles that have a gap of only 2 mm at one tip and 4 cm at the other. Again, the correction is such that residual multipole components can be kept well below 0.05 units. This design eliminates the need for a large number of corrector magnets and might be important in an application where space is very limited and optics performance very important, like the interaction region of FCC-ee.

2.11.5 Acknowledgements

The financial support of ETH Zurich to this work is gratefully acknowledged.

2.11.6 References

1. D. I. Meyer and R. Flasck. (n.d.). A new configuration for a dipole magnet for use in high energy physics applications. *NIM A 80.2 (1970)*, pp 339-341.
2. F. Bosi et al. (n.d.). Compact Superconducting High Gradient Quadrupole Magnets for the Interaction Regions of High Luminosity Colliders. *IEEE Transactions on Applied Superconductivity*, VOL. 23, NO. 3, JUNE 2013.

3. J. van Nugteren. (2011). *Internship Report: CERN, Software development for the Science and Design behind Superconducting Magnet Systems*. tech. rep., Twente University: Energy Materials and Systems and CERN: ATLAS magnet team.
4. M. Koratzinos et al. (THOPOR023). The FCC-ee Interaction Region Magnet Design. *IPAC 2016*. Busan, Korea.
5. S. Caspi. (n.d.). Design, Fabrication and Test of a Superconducting Dipole Magnet Based on Tilted Solenoids. *IEEE Trans. Appl. Supercond.* 17.2 (2007), pp. 2266-2269.
6. The FCC-ee study. (n.d.). <http://cern.ch/fcc> . Retrieved from <http://cern.ch/fcc>

2.12 Proposed RF Staging Scenario for FCC-ee

O. Brunner, A. Butterworth, I. Karpov, S. Aull, N. Schwerg
CERN, Geneva, Switzerland
 (Dated: November 15, 2017)

2.12.1 Introduction

FCC-ee is a proposed high-energy electron positron circular collider that could initially occupy the 100-km tunnel of the future 100 TeV FCC-hh hadron collider. The parameter range for the e^+e^- collider is large, operating at center-of-mass energies from 90 GeV to 365 GeV with beam currents ranging between 1.39 A and 5.4 mA, at fixed synchrotron radiation power of 50 MW per beam. These are challenging parameters for the radiofrequency (RF) system because of the extreme voltage requirements and beam loading conditions. This document details a scenario for gradual evolution of the FCC-ee complex by step-wise expansion and reconfiguration of the superconducting RF system.

2.12.2 Operation model

The main center-of-mass operating points with large physics interest are around 91 GeV (Z-pole), 160 GeV (W pair production threshold), 240 GeV (Higgs resonance) and 365 GeV (above top-antitop ($t\bar{t}$) threshold). The construction of FCC-ee will therefore proceed in five steps, combining eight months of operation periods with four months of interleaved winter shutdowns during which the hardware upgrades for energy increase can take place.

In order to collect the required luminosity and allow for interesting physics at each energy step, it is planned to run the machine four years at the Z-pole, one year at the W pair production threshold, three years at the Higgs resonance and finally four years at the highest energy, one year at the $t\bar{t}$ threshold, followed by three years at 182.5 GeV per beam. The main machine parameters are summarized in Table 1 [1].

Table 1: FCC_ee machine parameters

<i>Parameter</i>	<i>Z</i>	<i>W</i>	<i>H</i>	<i>ttbar₁</i>	<i>ttbar₂</i>
Beam energy in GeV	45.6	80	120	175	182.5
Beam current in mA	1390	147	29	6.4	5.4
Nb of bunches	16640	2000	393	48	39
Beam RF voltage in MV	100	440	2000	9500	11000
Runtime [year]	4	1	3	1	3

2.12.3 RF configurations

As shown in table 1, the RF voltage requirement is very broad, spanning from 0.1 to 11GV. Running at the Z-pole the FCC-ee is an ampere class, heavy beam loaded machine, while at the ttbar threshold it becomes an extremely high energy machine.

For the Z-pole machine, the cavity shape must be carefully optimized with regard to higher order modes (HOM). This favours low frequency, low shunt resistance and low number of cells per cavity. For this energy step, a 400 MHz continuous wave (CW) RF system made up of fifty-two single-cell Nb/Cu cavities per beam is considered. This frequency is indeed the natural choice for the FCC-hh, which will profit from the LHC as injector. The LHC also employs a 400 MHz RF system. The 400 MHz choice offers good perspectives for the FCC-ee low energy machines, and thus the opportunity to re-use a large part of the hardware and infrastructure for later use in FCC-hh.

High acceleration efficiency is necessary to optimize the total size and cost of the highest energy point, for which about 2600 cells are required to produce the total RF voltage of 11 GV. At this energy, the small number of bunches and the low beam loading suggest looking into the possibility of a common RF system for both beams. This can be accomplished by re-aligning the cavities used for the Higgs production on a common beam axis, and installing additional cavities to produce the extra 7 GV. For this, the relatively modest CW RF power per cavity offers the possibility to use 800 MHz bulk Nb five-cell cavities. Although these cavities must be operated at 2 K, this choice provides a better acceleration efficiency and a significantly reduced overall footprint, hence potentially significant cost savings, considering the overall size of the ttbar RF system.

Higher frequencies have been eliminated due to transverse impedance considerations and power coupler limitation for CW operation.

2.12.4 Cavity material options

A detailed analysis of SRF performance data for different RF frequencies, temperatures and materials and the perspective for future R&D is presented in [2]. Although the cavity material decision vs frequency is clear, it is demonstrated that a sustained and concerted R&D program on Nb/Cu films could potentially decrease the surface resistance by a factor two to three, and as a result making the Nb/Cu technology operated at 4.5 K competitive with bulk Nb, operated at 2 K.

This is very attractive, in particular, for the H machine, which requires a high RF acceleration efficiency with several hundreds of kW power input per cavity, and for which a lower transverse impedance is certainly beneficial. This choice also facilitates the re-use of the existing RF power system.

The A15 compounds potentially show great promise for the future. They could offer even more cryogenic cost savings, but require a much longer R&D effort [3].

2.12.5 Beam-cavity interaction and beam dynamic issues

In order to maximize the luminosity of the FCC-ee at the different energy steps, sufficient current must be stored in both beams. Higher-order mode (HOM) losses, single- and coupled-bunch instabilities that might seriously affect the final performance of the machines, have been studied in detail. Most of these issues appear to be more prominent in the high-current “low-energy” operation at the Z pole.

The microwave instability thresholds have been calculated with the BLoND code, a macro-particle tracking code developed at CERN for longitudinal beam dynamics simulations [4]. Its latest release supports new functions to accurately compute synchrotron radiation effects in leptons and very high energy hadron synchrotrons [5]. At nominal beam current, the machine impedance leads to increased energy spread and bunch length, despite the strong synchrotron radiation damping, but does not result in unstable growth [6]. This is consistent with previous analysis [7, 8].

The coupled-bunch instability thresholds were calculated using an analytical approach [9]. Although the single-cell cavity for the Z-pole machine must be further optimized, its longitudinal impedance spectrum above the cut-off frequency of the pipe sits well inside the coupled-bunch stability zone. For the impedance spectrum below the cut-off frequency, HOMs should be damped according to the calculated limit. The further analysis needs to focus on the cavity fundamental-driven coupled-bunch instabilities and on the potential impact of the large detuning angle.

A detailed analysis of the HOM power and damping requirements has been performed for all FCC-ee machines [10]. Power losses were evaluated for different cavity designs, cryomodule arrangements, including beam pipes and tapers, and various filling schemes. Proper bunch spacing selection and carefully designed cavities help to keep the HOM power per cavity below a few kilowatts, and LHC-like superconducting hook couplers are appropriate for this.

2.12.6 A flavor of other R&D challenges

The challenges ahead are numerous, and the important R&D areas have been carefully identified. In addition to those already addressed in the previous paragraphs, we may note the impressive 2×50 MW of continuous RF power; this sets the overall scale of the RF power system. Improving energy efficiency and reducing energy demand is absolutely crucial for future big accelerators such as FCC, and the development of high-efficiency RF power sources must be at the core of the R&D program [11].

For the proposed configuration of the Z-pole and W-threshold machines to be realized, the RF coupler technology must also be pushed forward to increase their CW power transfer capability: the higher order mode couplers will have to deal with high beam loading and must effectively extract kW's of RF power, while progress on the fundamental power couplers (FPC) will be decisive for limiting the cost and size of the RF system. The target value is 1 MW CW per power coupler at 400 MHz [12]. FPC design must ensure easy adaptation of their coupling coefficient to the different machines.

2.12.7 Installation and staging plan

The RF system will be expanded in steps, with rising maximum voltage, as shown in Figure 1. First of all, twenty-six four single-cavity cryomodules will be installed for the Z-pole machine. Each cavity will be fed by about 1 MW CW RF power for supplying the 2x50MW beam power. A number of possible solutions exist to produce the required RF power, but in any case, as the space in the tunnel is restricted, the large, bulky power equipment will be installed on the surface. The underground areas will only accommodate the RF power amplification, the D.C power distribution, the fast servos & control and protection systems. In the perspective of the different energy upgrades, using a combination of two or four medium-size RF power sources seems very attractive.

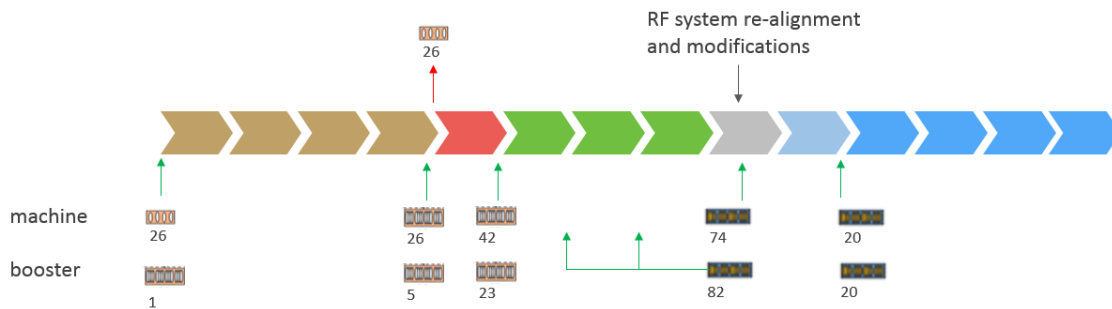


Figure 1: Proposed FCC-ee staging schedule. The figures underneath indicate the numbers of cryomodules to be newly installed during the various winter shutdowns.

During the winter shutdown at the end of the Z-pole campaign, these cryomodules will be replaced by twenty-six four-cell cavity cryomodules to allow for the W-threshold machine operation. The RF power sources, the control systems and the RF power distribution will remain unchanged.

The step between the W and H machines requires the installation of forty-two additional four-cell four-cavity cryomodules to produce the necessary RF voltage of 2 GV/beam. The fast RF feedback requirements and the still large number of bunches favor a single cavity per power source. The RF power system initially installed for the Z machine will be reconfigured to adapt to the new power requirement per cavity, and additional new RF power stations will complete the installation. The detailed powering scheme and the associated workload must be carefully studied to be in line with the available timeframe, and the pre-installation effort must be spread over several annual winter shutdowns (e.g. cabling and installation campaigns).

When transiting towards the highest beam energy of 182.5 GeV, it is attractive to rearrange the existing RF system and to share it between the two beams, so as to double the RF voltage available for either beam. The sharing of cavities by the two beams is possible thanks to the small number of bunches in this mode of operation. The sixty-eight RF cryomodules will be moved transversally and separators will be installed at the entrance and exit of each RF straight section. The system will be completed by ninety-four additional 800 MHz five-cell four-cavity cryomodules installed in series to produce the extra 7 GV. These 2 K cryomodules will be connected to form long cold segments in order to minimize the warm beamline sections, and the relatively modest power requirement per cavity will allow for the gradual introduction of less powerful and less expensive RF power sources. A one-year shutdown will be necessary to cope with this

major intervention. It will be followed by one-year intermediate operation stage at 175 GeV, as requested by the particle physicists.

The main changes to the RF unit's configuration in tandem with the required beam-energy changes are depicted in Figure 2. The RF parameters for each stage are detailed in Table 2.

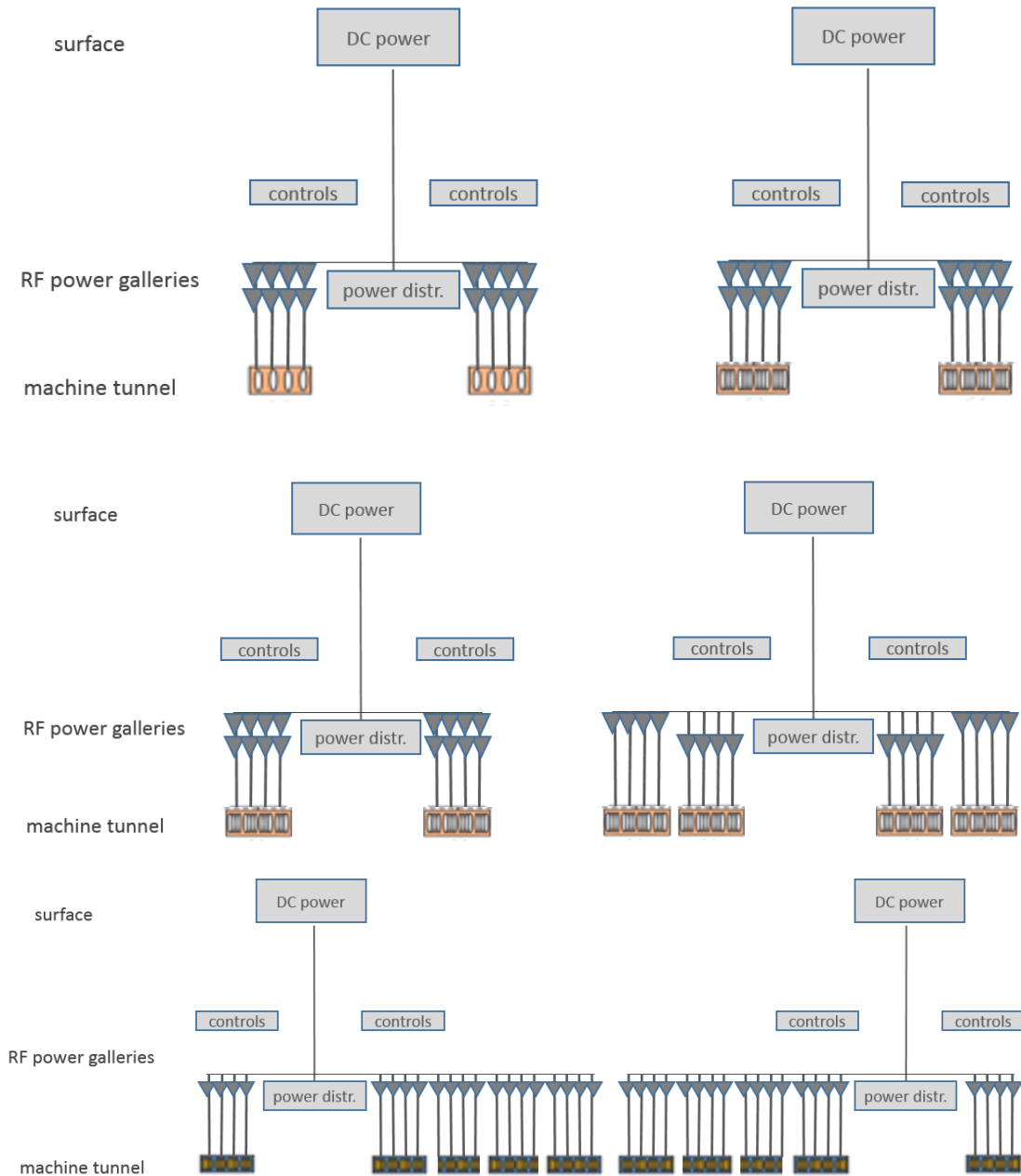


Figure 2: Schematic view of the RF unit evolution.

Top: Z => W: Single-cell cavity CM are replaced by 4-cell cavity CM

Centre: W => H: existing RF power units (triangles) are split and moved to power new cryomodules. New RF units are installed.

Bottom: New 800 MHz RF units are installed. The modest RF power per cavity allows each power distribution unit to power several cryomodules, which will be connected to form long cold segments.

Table 2: Detailed RF configuration of each machine and booster ring

	Z		W		H		ttbar₁		ttbar₂	
	per beam	booster	per beam	booster	per beam	booster	2 beams	booster	2 beams	booster
RF voltage [MV]	100	36	440	340	2000	1720	9500	7800	10930	9210
frequency [MHz]	400									
RF voltage [MV]	100	36	440	340	2000	1720	4000	1720	4000	1720
# cell / cav	1	4	4		4		4		4	
V _{cavity} [MV]	1.92	9	8.4	14.2	14.7	14.8	15		15	
# cavities	52	4	52	24	136	116	272	116	272	116
# CM	13	1	13	6	34	29	34	29	68	29
T operation [K]	4.5		4.5		4.5		4.5		4.5	
dyn losses/cav [W]	14	11	66	26	202	29	210	30	210	30
P _{cav} [kW]	962	125	961	21	368	4.5	21		21	
frequency [MHz]	800									
RF voltage [MV]							5500	6080	7000	7580
# cell / cav							5		5	
V _{cavity} [MV]							18.6	18.6	18.6	18.6
# cavities							296	328	376	408
# CM							74	82	94	102
T operation [K]							2		2	
Q dyn/cav [W]							66	10	66	10
P _{cav} [kW]							88	1.6	88	1.6

2.12.8 The booster ring

Beside the collider rings, a fast repetition rate booster [13] of the same size must provide beams for top-up injection at collision energy to sustain the extremely high luminosity. The booster's rated voltage corresponds to the energy loss per turn via synchrotron radiation emission. The RF configuration of the booster ring for each running step is shown in Table 2. In order to optimize the cryogenic system and distribution, it is proposed to use the same technology as for the collider-ring itself. The relatively modest duty cycle of the booster (~10%) offers the possibility to use compact RF power systems.

The low beam loading allows for multi-cell cavities at all energies and for a staged installation distributed between all winter shutdowns.

2.12.9 Summary

We have presented a baseline scenario for gradual evolution of the FCC-ee complex by step-wise expansion and reconfiguration of the superconducting RF system. This scenario matches the latest FCC-ee parameter and timeline. While a 400 MHz RF system for the Z, W, H and FCC-hh maximizes the re-use of the existing hardware, a hybrid 400/800 MHz system offers the best perspectives for the highest energy ttbar machine, in terms of cost, diversity of technology and integration constraints. Each of the energy stages requires extensive preparatory and pre-installation work to be carried out within

the available short time frame. Although it is deemed to be feasible, the management and organization of the shutdown workload remains a major challenge.

2.12.10 Acknowledgments

The authors thank the subjects whose participation made this study possible: E. Chapochnikova, E. Jensen, I. Syratchev, E. Montesinos, W. Venturini-Delsolaro, S. Gorgi Zadeh, L. Taviani, F. Zimmermann and R. Calaga.

2.12.11 References

22. A. Blondel, P. Janot, K. Oide, D. Shatilov, F. Zimmermann, "FCC-ee parameter update", private communication, October 2017
23. S. Aull, O. Brunner, A. Butterworth, N. Schwerg, "Material Options for the Superconducting RF System of the Future Circular Collider", FCC-DRAFT-TECH-2017-002, <https://cds.cern.ch/record/2289506>, 2017.
24. S Posen, D. L. Hall, "Nb3Sn superconducting radiofrequency cavities: fabrication, results, properties, and prospects", Superconductor Science and Technology, 2017.
25. <http://blond.web.cern.ch>
26. J. F. Esteban Müller, "Modification of the simulation code BLonD for lepton rings", FCC-DRAFT-TECH-2017-001, <https://cds.cern.ch/record/2284587>, 2017.
27. J. F. Esteban Müller, "FCC-ee broadband impedance and longitudinal single bunch stability", FCC-DRAFT-ACC-2017-035, <http://cds.cern.ch/record/2289514>, 2017.
28. R. Calaga, "Beam dynamics issues for FCC-ee", first FCC-ee RF mini review, CERN, 2016.
29. A. Butterworth, "Cavity design and beam-cavity interaction", in the third Annual Meeting of the Future Circular Collider study, Berlin, Germany, 2017.
30. M. Migliorati, "FCC-ee Single-beam collective effects," second Annual Meeting of the Future Circular Collider study, Rome, Italy, 2016.
31. I. Karpov, "HOM power in FCC-ee cavities", 2017, to be published.
32. I. Syratchev, "High efficiency klystron technology", third Annual Meeting of the Future Circular Collider study, Berlin, Germany, 2017.
33. E. Montesinos, "FPC challenges and perspectives for FCC", third Annual Meeting of the Future Circular Collider study, Berlin, Germany, 2017.
34. O Etisken, Y Papaphilippou, A K Ciftci, "Conceptual design of a pre-booster ring for FCC e+e- injector", Journal of Physics: Conference Series, Volume 874, 2017.

2.13 Lessons from the LHC and Technology Advances for HL-LHC

Oliver Brüning and Frank Zimmermann

CERN, Route de Meyrin, 1211 Geneva 23, Switzerland

Mail to: oliver.bruning@cern.ch or frank.zimmermann@cern.ch

2.13.1 Introduction

The Large Hadron Collider was designed for proton-proton collisions at 14 TeV centre-of-mass with a luminosity of $10^{34} \text{ cm}^{-2}\text{s}^{-1}$. Its actual performance in terms of both peak and integrated luminosity is remarkable; see Fig. 1.

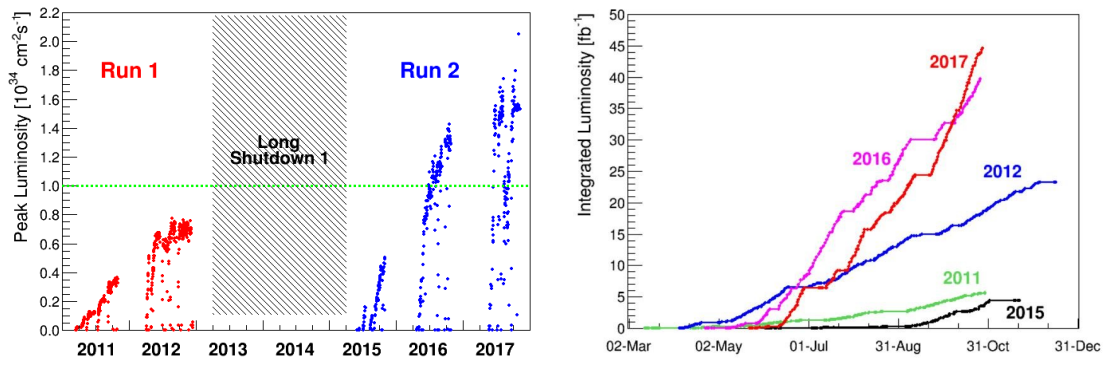


Figure 1: LHC peak (left) and integrated luminosity (courtesy J. Wenninger and CERN).

The LHC was developed starting in 1983, the first beam was injected in 2008, and the first real physics collisions were delivered in 2010. The beam energy was slowly increased, from 3.5 TeV in 2011 via 4 TeV in 2012 to 6.5 TeV since 2015. After the Long Shutdown 2, or “LS2” (2019-20), the collision energy is expected to reach the design value of 7 TeV, which still requires an additional magnet training campaign.

During LS2 (2019-20) the injector complex will be upgraded [35]. The following Long Shutdown “LS3” (2024-25) will witness a major upgrade in the LHC itself [36,37]. Together the two upgrades will enable a ten-fold increase in the integrated luminosity.

2.13.2 Lessons from the LHC

These lessons had been assembled and reviewed for the FCC Week in Washington [38]. Three types of lessons are distinguished: (1) LHC specifics and compromises coming from building the LHC machine in the old LEP tunnel, (2) experience for specific concerns raised in the design phase, (3) important lessons learned from the LHC installation, and (4) important lessons learned from the LHC operation.

Among LHC constraints from the pre-existing tunnel figure the dispersion suppressor, whose geometry was defined by the LEP FODO cell, and which for the LHC, with its longer cell length, required quadrupole tuning for dispersion matching; the combined experimental interaction and injection regions, implying risk of beam loss and detector damage and imposing additional constraints and elements for optics matching and machine protection; the radiation to electronics components in the tunnel resulting in limited underground space for installation of sensitive components (e.g. power

converters), impacting machine availability and efficiency, and ultimately requiring a “superconducting link” to power converters installed far away and a new cavern for the HL-LHC.

One LHC specific design choice was the powering in 8 separate sectors (stored electro-magnetic energy per sector $\approx 1\text{GJ}$) which required power-converter tracking at the ppm level; the LHC power converters perform exceedingly well, and indeed track the main-magnet currents at the ppm level. A second design choice is the common triplet for both beams and for the debris leaving the IR, with a warm separation dipole D1 and efficient triplet cooling. Some machine protection issues were uncovered for the warm magnets. A third specific design choice is the anti-symmetric optics design, driven by the goal to facilitate a simultaneous optics matching for Beam1 & Beam2. The dispersion is not anti-symmetric with respect to the IP, which is addressed by dedicated trim quadrupole circuits in the dispersion suppressor section that break the strict antisymmetry of the insertion region. This design choice should be reassessed for future machines like the FCC (which could operate e.g. with flat beams etc.). In addition, the series powering of Beam1 and Beam2 quadrupoles limits the flexibility of choosing different phase advances for the two beams. Also this choice could be reassessed for the FCC. Power converter noise at locations with $\beta > 4\text{ km}$ has been a specific concern, and was addressed by the triplet powering layout (in series for intrinsic compensation).

A major concern in the LHC design phase has been the noise from klystron-driven superconducting RF, where the actual LHC experience has been excellent. As another positive news, the LHC mechanic and dynamic apertures are excellent thanks to sorting and to the exquisite magnet field quality. Differently from past superconducting hadron storage rings, for the LHC there is an excellent agreement between predicted and observed dynamic aperture, which is attributed to the almost noise-free power converters and radiofrequency system as well as to the excellent optics control. Electron-cloud effects appeared late on the LHC design table. Mitigation measures could not be fully incorporated by a redesign of the beam screen. Surface conditioning by “beam scrubbing” and the flexibility of the LHC injector complex for preparing different beam types and bunch separation patterns have been the primary means for raising the beam current and achieving the design luminosity. Emittance blow-up had been a big worry for the beam instrumentation and lead to careful estimates for the LHC. Again, the performance of the machine is superb also in this regard. A novel tune measurement principle (“BBQ” for base band tune measurement) helped keeping the emittance growth low. A positive surprise has been the hadron beam-beam limit: experience at the SppS, Tevatron and HERA suggested strong limits for the maximum acceptable beam-beam parameter. The LHC achieved higher than expected beam-beam parameters, which again is attributed to the low level of noise.

Sorting during installation was initially judged difficult due to small sample number with the original delivery and installation schedule (≈ 10). A problem with the LHC cryogenic supply line in the tunnel (QRL) during the installation delayed the installation process of the magnets and provided a unique opportunity for the magnet sorting: almost all of the 1200 LHC dipole magnets were stored on the CERN site before their installation. This allowed sorting by geometry and field quality. The LHC operation clearly benefits from the sorting. This scheme requires significant space on site, and also sufficient capacity for cryostating and testing. The LHC demonstrated the capability for tackling major problems, such as the QRL problem, collapsed plug-in modules (RF shielded vacuum interconnections between the magnets), collapsed He cooling lines in the triplet

magnets, He leaks and electric shorts in the DFB powering lines and a major accident in 2008 based on faulty inter-magnet connections. The Superconducting Magnets and Circuits Consolidation (SMACC) effort after the aforementioned incident was a monumental effort involving over 350 persons, including ~1,000,000 working hours of preparation and requiring the opening, validation and consolidation of all magnet interconnections.

Concerning lessons from commissioning and Run2, the beam lifetime had initially been expected to be rather poor and featured sharp spikes, leading to overly pessimistic estimates of intensity limitations (at e.g. $\approx 20\%$ of the nominal value). An unexplained noise sources exciting the beam, like the so-called ‘hump’, raised concerns initially. Luckily, this effect disappeared after the first year of operation. Its origin has still not been fully understood, albeit it disappeared after all undistruptible power supplies (USP) have been changed in the machine. The LHC operation also revealed the importance of a powerful, flexible and mature injector complex, allowing the production of various kinds of beams, such as 8b4e (8 bunches followed by 4 empty bunches) for e-cloud mitigation, a “bunchlet” scheme for enhanced scrubbing, a batch compression, merging and splitting scheme (BCMS) as low emittance option, and an 80 bunch injection scheme to SPS. Time needed for cryogenic maintenance has led to a new running paradigm, alternating 3 years of operation with a long shutdown. The definition of ‘good’ magnets during production (fast training to ‘ultimate’ current) turned out not to be correlated to the magnets ability to keep its training after installation in the tunnel. Several magnets feature a ‘de-training’ of their ability to reach the nominal operating field in the tunnel, requiring a time consuming re-training campaign in the tunnel. This led to the choice of a reduced ‘efficient’ beam energy, where the design beam energy of 7 TeV had to be lowered to 6.5 TeV in order to reduce the required time for magnet training in the tunnel and to arrive at an efficient running schedule. The machine efficiency has been limited by “UFO’s”, sharp losses that have been attributed to beam collisions with Unidentified Falling Objects in the vacuum chamber, radiation to electronics, and loss spikes. Beam aborts were triggered by very small beam losses, indicating that margins do exist. Only 30% of all fills in the LHC Run1 have been terminated by operators. Electron-cloud scrubbing, changes to the bema-loss-monitor thresholds and a position optimization of sensitive electronics in the tunnel after the Long Shutdown 1, have drastically improved the availability.

The co-called “snap back” at the start of the ramp and other dynamic effects are under control thanks to detailed magnet measurements and an elaborated magnet modelling procedure that takes into account the magnet powering history and is integrated into the LHC controls system (no need for reference magnets). The LHC has achieved a very high level of machine reproducibility and stability. The machine reproducibility is key for high efficiency of the cleaning insertions and for machine protection. Troublesome losses in the Dispersion Suppressor suggest that future projects should, already in the design stage, integrate collimators in the dispersion suppressor.

2.13.3 Novel Technologies for the HL-LHC

The LHC Injector Upgrade in LS2 consists in the development of a new H^- source, connecting the new H^- LINAC4 accelerator to the PS booster, implementation of charge exchange injection into the PS booster, increasing the booster extraction energy, and instability mitigations and RF upgrades in the SPS. The LIU upgrades will approximately

double the beam brightness and also the total intensity of the beam available for injection into the LHC.

The High-Luminosity LHC upgrades during LS2 and LS3 include: new final-triplet quadrupoles with larger aperture, based on Nb₃Sn superconductor with a peak field at the coil of about 12 T; additional collimators in the dispersion suppressors of the betatron cleaning insertion, enabled by more compact Nb₃Sn dipoles with a field of 11 T – the first time this type of superconducting magnet is installed in a collider; new low-impedance robust collimator jaws; novel crab-cavity RF systems; a novel cold powering scheme based on superconducting links; etc.

2.13.4 Outlook

The lessons learned from the LHC and the novel technologies developed for HL-LHC prepare the ground for future higher-energy hadron colliders like HE-LHC or FCC-hh, which will require 100's or 1000's of Nb₃Sn dipole and quadrupole magnets with a peak field in excess of 15 Tesla, bright proton beams, robust absorber and collimator materials, low impedance components (collimators and vacuum system) and RF crab cavity systems.

2.13.5 References

35. H. Damerou et al. (eds.), “LHC Injectors Upgrade, Technical Design Report, Vol. I: Protons,” CERN-ACC-2014-0337 (2014).
36. G. Apollinari et al. (eds.), “High-Luminosity Large Hadron Collider (HL-LHC): Preliminary Design Report,” CERN-2015-005 (2015).
37. O. Brüning and L. Rossi (eds.), “The High Luminosity Large Hadron Collider: the new machine for illuminating the mysteries of Universe,” World Scientific, Hackensack, NJ, World Scientific (2015).
38. O. Brüning, “Lessons learnt from LHC,” FCC Week 2015, Washington DC (2015).

2.14 FCC-hh Design Highlights

D. Schulte

Mail to: daniel.schulte@cern.ch

CERN, route de Meyrin, 1121, Geneva, Switzerland

2.14.1 Introduction

The FCC-hh will provide proton-proton collisions with 100 TeV centre-of-mass energy, about seven times more than LHC, with a luminosity much higher than in HL-LHC. For the ultimate parameters the luminosity can reach up to $3 \times 10^{35} \text{cm}^{-2}\text{s}^{-1}$ and allows to reach an integrated value of 17.5ab^{-1} , corresponding to the physics goals [1].

In the following, the layout and main parameters of FCC-hh are presented first followed by the luminosity considerations. Limited space then allows for only a few key design highlights and prevents to cover the full range of important topics.

2.14.2 Layout and Key Parameters

The layout of FCC-hh is shown in Fig.1 and the key parameters are shown in table 1, both taken from [2]. The layout fulfils a number of criteria:

- The accelerator fits into the Geneva area [3]. In particular, the layout limits the tunnel in limestone as much as possible to reduce the risk and cost of the civil engineering. Similarly, it avoid going under the deep part of lake Geneva. In addition, the injection insertions are positioned such that one can conveniently inject beam either from the LHC or the SPS tunnel. To achieve this design, a range of layout options has been evaluated and the best picked.
- The two high luminosity experiments are located on opposite insertions (A and G). This ensures highest luminosity and best compensation of beam-beam effects independent of the beam-filling pattern.
- Two additional, lower luminosity experiments are located together with the injection in insertions B and L.
- The transverse beam cleaning is located in insertion J and the beam extraction in insertion D. Both systems are challenging due to the high energy in the beams. Hence the insertions are twice as long than the others to give more flexibility to the optics design and leave more room for protection devices.
- The longitudinal beam cleaning is placed in insertion F.
- The RF systems and the fast feedback are placed in insertion H.

2.14.3 Energy considerations

The beam energy E that one can reach in the collider is given by the ability of the dipole magnets in the arc to keep the beam on a circular orbit:

$$E = 0.0476 \text{ TeV} \frac{B \eta (C - L)}{T \text{ km}}$$

Here, C is the circumference of the collider, L is the length reserved for straight insertions, η the fraction of the arcs filled with magnets and B the magnetic field strength of the dipoles. A total of 14 km has been allocated for the insertions and a filling factor for the arcs of about 80% has been achieved [4]. Consequently, a circumference of 97.75 km and a magnetic field of 16 T have been chosen. This size is consistent with the site boundaries close to CERN and with the expected maximum field reach that the superconducting TiNb3 technology can provide. An important R&D programme is ongoing to achieve this field level and to reduce the cost of the technology to an acceptable level.

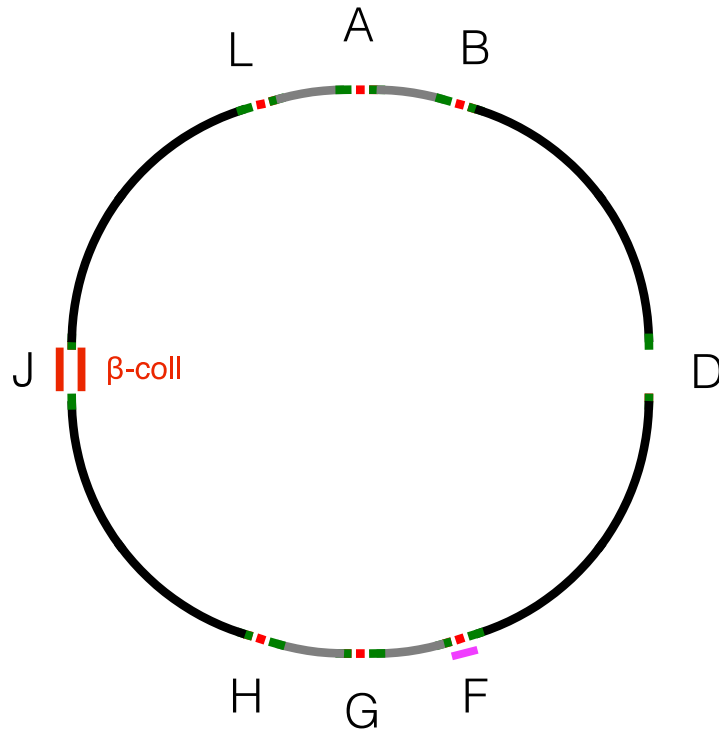


Figure 1: The FCC-hh conceptual layout.

2.14.4 Injector considerations

Different injector options are being considered [5], the baseline is to use the LHC to inject the beam at an energy of 3.3 TeV into the FCC. This option requires some changes of the LHC. In particular the powering of the magnets needs to be modified in order to allow to ramp the LHC much faster than today [6]. This choice of injection energy leads to a range from minimum to full field in the magnets of a factor 15, similar to the LHC. The collider has been designed to ensure that the injected beam is stable at this energy and that enough beam stay clear is provided in the machine and collimation system.

Table 1: The main FCC-hh parameters.

	LHC (Design)	HL-LHC	FCC-hh baseline	FCC-hh ultimate
c.m. Energy [TeV]		14		100
Circumference C [km]		26.7		97.75
Dipole field [T]		8.33		<16
Arc filling factor		0.79		0.79
Straight sections		8 x 528 m		6 x 1400 m + 2 x 2800 m
Number of Ips		2 + 2		2 + 2
Injection energy [TeV]		0.45		3.3
Peak luminosity [10^{34} cm ⁻² s ⁻¹]	1.0	5.0	5.0	< 30.0
Peak no. of inelastic events / crossing	27	135 (lev)	171	1006

Alternatively, a new machine in the SPS tunnel could provide beam at 1.3 TeV using fast ramping and cost effective superconducting magnets with a field of 6 T. As an other alternative, a new superferric accelerator in the LHC tunnel could be envisaged or an injector in the FCC tunnel could be considered. However, using a lower injection energy than 3.3 TeV will reduce the beam stay clear and stability at injection. Studies are ongoing to precisely identify the safe limit.

2.14.5 Luminosity Considerations

The luminosity of the collider can be expressed as a function of the beam current I , the beam-beam tune shift ξ , the beam gamma factor γ , and the beta-function at the collision point β^* as

$$L = \xi \frac{I}{e} \frac{\gamma}{\beta^*} \frac{1}{r_p} F$$

Here, r_p is the classical proton radius and e its charge. The form factor F includes geometric luminosity reduction effects, for example the hour glass effect; it is neglected for the further discussion. Hence, to reach high luminosity, one has to use a very brilliant beam, achieve small betafunctions and use a large beam current.

The useable brilliance of the beam is limited by beam-beam effects. We have assumed that one can tolerate a beam-beam tuneshift of up to 0.03 for the two main experiments together. Simulation studies [7-10] for the current working point confirm that this value is acceptable. The fraction of beam that is lost into the transverse tails due to beam-beam effects remains below 10^{-3} per hour and also the emittance growth induced by beam-beam jitter would remain limited. In contrast, a slightly larger tuneshift would increase the loss rate rapidly and the beam emittance would increase significantly faster for the same jitter amplitudes. Studies indicate that other working points might allow a larger tuneshift; further investigations are planned. For the ultimate parameters, a crossing angle of about $200\mu\text{rad}$ is required to limit the impact of parasitic beam-beam crossings. The associate luminosity reduction is mitigated by the use of crab cavities.

A small betafunction at the collision point makes the design of the experimental insertion optics demanding. It also leads to a large beam in the focusing triplets around the experiments. This poses challenges for the magnet design and protection and the collimation system that has to scrape off tails that can hit the triplets.

The beam current is limited by the synchrotron radiation that even the proton beam emits at these high energies. In FCC-hh both beams emit about 5 MW of radiation that has to be removed by the cryogenics system. The magnets are protected from the radiation by a beamscreen as in LHC. These screens are operated at around 50 K. In this case the power required to drive the cryogenic system is about 100 MW, due to the Carnot inefficiency and the technical inefficiency of the system [11].

In order to reduce the magnet cost the beam aperture must be minimised. This leads to important collective effects in combination with the high beam current. The best compromise thus has to be found using possible mitigation methods to stabilise the beam. Finally the high amount of kinetic energy stored in the beam leads to important challenges for the machine protection system. This is in particular the case for the collimation section, which cleans the beams and protects the machine from high losses, and the beam extraction section.

Table 2: Other key FCC-hh parameters.

	LHC (Design)	HL-LHC	FCC-hh baseline	FCC-hh ultimate
Number of bunches n	2808		10400	
Bunch population $N[10^{11}]$	1.15	2.2	1.0	
Nominal transv. normal. emittance [μm]	3.75	2.5	2.2	2.2
Number of IPs contributing to ΔQ	3	2	2	2
Maximum total b-b tune shift ΔQ	0.01	0.015	0.01	0.03
RMS bunch length [cm]	7.55		8	
IP beta function [m]	0.55	0.15 (min)	1.1	0.3
RMS IP spot size [μm]	16.7	7.1 (min)	6.8	3.5
Full crossing angle [μrad]	285	590	91	200
Stored energy per beam [GJ]	0.392	0.694	8.4	
SR power per ring [MW]	0.0036	0.0073	2.4	
Arc SR heat load [W/m/aperture]	0.17	0.33	28.4	
Longitudinal emittance damping time [h]	12.9		0.5	
Horizontal emittance damping time [h]	25.8		1.0	
Dipole coil aperture [mm]	56		50	
Minimum arc beam half aperture [mm]	~18		13	
Installed RF voltage (400.79 MHz) [MV]	16		48	
Harmonic number	35640		130680	

During the luminosity operation the beam parameters will change strongly [12]. The beam current is rapidly reduced due to beam burn-off in the experiments. At the same time the transverse emittances will shrink due to the emission of synchrotron radiation. As a result the luminosity will first increase and then decrease during a run, see Fig. 2. The synchrotron radiation also damps the longitudinal emittance. The RF system will be used to heat the beam to keep the emittance and bunch length constant.

The total time of luminosity operation is limited for each fill. This is another reason to maximise the beam current. However, the turn-around time from the end of one luminosity run to the beginning of the next is important for the integrated luminosity. A goal of 4 h has been set. Studies of the LHC performance indicate that a minimum turn-around time of about 2 h can be reached in FCC [13,14]. The studies also indicate that the main reason for longer turn-around times is given by the need to repair the machine after a failure before the new beam can be injected. The injection process itself is not much slower than predicted.

It is assumed that the operational cycle of the machine will take 5 years [15]. During this cycle a shut-down of 1.5 years is foreseen. Machine commission, development and technical stops are estimate to take a total of 12 months, leaving a scheduled operation time for luminosity production of 2.5 years. We assume that the effective luminosity operation time is 70% of the scheduled time [16,17]. Based on these targets, the machine will operate an effective 625 days over the full five-year cycle. With the baseline parameters 2 fb^{-1} per day can be achieved. This allows to provide 1250 fb^{-1} for each five-year operation cycle. The ultimate parameters yield $8 \text{ fb}^{-1}/\text{day}$ resulting in 5000 fb^{-1} per

five-year period. A scenario with 10 years of operation using the baseline parameters followed by 15 years of ultimate, would reach 17.5 ab^{-1} .

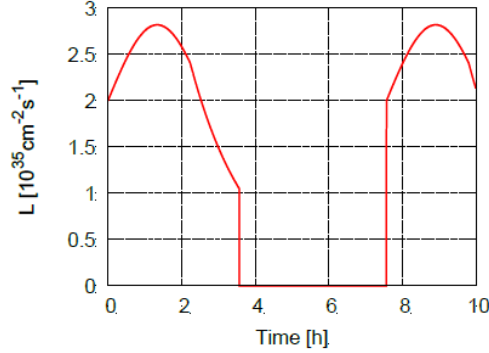


Figure 2: Luminosity evolution during a run with ultimate parameter set.

2.14.6 Key Design Components

2.14.6.1 Lattice Design

A complete lattice has been developed for the collider ring that is consistent with the layout and the energy reach [4]. The arc lattice consists of FODO cells of more than 200 m length and with a phase advance of 90° . Integrated studies of the lattice performance are ongoing and already gave important feedback on the magnet design, in particular for the field quality. With the previous design good dynamic apertures have been reached [18]. With the current change in beam separation in the arcs, the field quality of the magnets has degraded significantly and a new round of studies tries to address this. The alignment tolerances are similar to LHC with some tighter values for the quadrupole alignment [19].

2.14.6.2 Experimental Insertions

The key challenge of the high luminosity experimental insertions is to obtain very small betafuncions in the collision point and to protect machine and experiments from the large power of the collision debris.

The ambitious luminosity goal requires beta functions of only 0.3 m in the collision points for the ultimate parameters. This is more challenging than the goal of 0.15 m envisaged for HL-LHC due to the higher beam energy. Different designs have been developed that can reach even smaller betafuncions [20]. They use long final triplets with large aperture and leave a distance of 40 m from the end of the magnet to the collision point. Also a flat optics is being investigated as an alternative.

The high luminosity leads to a large rate of proton-proton collisions in the collision points, i.e. a high power of the collision debris, which can reach about 500 kW in the high luminosity detectors. This threatens the magnets of the beam lines surrounding the experiments. In particular, the final triplets next to the experiments are exposed. To protect them a masking system has been designed that absorbs most of the power [21]. The shielding has also to protect the inner bore of the magnets. This requires a large magnet aperture in order to leave enough space for the beam inside of the shielding. Hence the magnetic field gradient is limited which is the main reason to use a very long triplet.

A similar approach has been chosen in the design of the additional experimental insertions [22]. One can expect luminosities of the order of $2 \times 10^{34} \text{ cm}^{-2} \text{ s}^{-1}$.

2.14.6.3 *Arc Vacuum System*

Due to their high energy each proton beam emits about 30 W/m of synchrotron radiation in the arcs. The cold bore of the magnets is protected from this radiation by a beamscreen [23] that is cooled at 50 K. The beamscreen removes the heat from the synchrotron radiation, ensures very good vacuum, provides an acceptable impedance and suppresses the electron cloud effect.

The vacuum quality has to reach at least 100 h of beam lifetime, preferably 500 h. At 100 h, the protons lost by beam-gas scattering will induce a total power in the arc dipole magnets that requires about 30 MW of power for cooling. The beamscreen has pumping holes, as in the LHC, to achieve the required vacuum. Unlike in LHC, these holes are shielded from the beam since they would produce a very high impedance otherwise that would render the beam unstable. The minimum aperture of the beamscreen is 26 mm and it is coated with 0.3 mm of copper in order to limit the impedance effect at injection energy. Adding the required space for the cooling fluids and beamscreen led to the choice of 50 mm for the magnet aperture.

In order to prevent the build-up of electron clouds to render the beams unstable a secondary emission yield of below 1.0-1.1 has to be reached [24,25]. Two technical solutions are being considered. One is to coat the beamscreen with amorphous carbon and the other to roughen the inner surface with a laser treatment. Both solutions can achieve the required secondary emission yield. The increase of the impedance by the carbon coating is acceptable. For the laser treatment further investigations are ongoing since the impedance depends on the details of the treatment.

Also, the direct production has to be suppressed of electrons that are generated in the main part of the beamscreen by backscattered synchrotron radiation. The goal to have less than 0.01 electrons per photon is addressed by using a sawtooth pattern on the side of the beamscreen to suppress the backscattering of photons into the main part of the chamber.

2.14.6.4 *RF, Impedance and Collective Instabilities*

The baseline RF system design [26] is similar to the one of LHC, and has an RF frequency of 400.8 MHz. The installed voltage will be 48 MV, three times more than in the LHC. In the longitudinal plane, already a lower value of 16 MV corresponds to the minimum necessary to ensure beam stability, assuming an inductive longitudinal impedance budget of $\text{Im}Z/n = 0.2 \Omega$ similar to the one of LHC (0.1Ω). Due to synchrotron radiation damping, controlled longitudinal emittance blow-up (by band-limited RF phase noise) will be required not only during the acceleration ramp but also in the coast at 50 TeV beam energy.

In FCC-hh, transverse impedance effects are important design drivers [27-31]. We require that the impedances remain a factor three below the estimated limit of beam stability. This margin is consistent with the observation that in the LHC a factor two difference can be found between calculated and measured impedance effects.

At injection, the arcs will be the largest source of impedance. The larger beam stiffness, compared to LHC, is roughly compensated by the larger circumference and arc beta-functions. Hence, the smaller aperture, needed for cost reduction, increases the impedance

effects beyond those of LHC by a significant factor. The beamscreen aperture has been chosen to be still consistent with a stable beam. Currently, estimates of the different impedances are being made and show that one can expect to achieve the goal to stay away from instabilities. This requires that the several collimators are coated with molybdaenum. Fast transverse dampers will be used to suppress rigid multi-bunch instabilities at injection and collision, even without chromaticity [32]. They can cure instabilities with rise times of up to 20 turns at injection and 100 turns at top energy. Only non-rigid bunch modes, which have slower rise times, need to be cured by the use of octupoles. Alternatives using electron lenses or RF quadrupoles are also being explored [33-35].

2.14.6.5 *Beam Power, Collimation System*

Each FCC-hh beam has a total energy of 8.4 GJ; this exceeds the energy in the LHC beams by more than a factor 20. Consequently, losses pose an even larger threat than in LHC and machine protection and beam cleaning are more demanding.

Fast failures are mitigated by passive and active protection. The operational limit is set to a minimum beam lifetime of 12 minutes, i.e. a beam loss of about 12 MW. Such a short lifetime is rare in the LHC and it might be possible to relax this requirement.

First designs of the collimation insertions exist and are being refined [36-39]. A free aperture of 15.5 times the RMS beam size is required in the machine and the primary, secondary and tertiary collimators will have gaps of 7.2, 9.7 and 13.7 RMS beam sizes, respectively, and the extraction protection 11.4 sigmas.

For 12 minutes lifetime high power loads are seen in some collimators [38] and the collimators are being redesigned to reduce these loads. Proton losses that can lead to quench of magnets in the arcs are captured with a dedicated protection system. The system also limits the leakage into the arcs of showers induced by the captured protons [40].

2.14.6.6 *Injection and Extraction*

Also the injection and extraction insertions as well as the dump lines have been designed[41,42]. The injection and extraction strategies are similar to LHC. The largest risk exists in the extraction insertion. Here, the beam can be extracted by firing a series of kickers during a gap in the bunch train to move the beam into a septum, which increases the deflection, into a transferline toward the beam dump. To avoid that the high energy beam drills a hole into the beam dump fast kickers have will be used that move the point of impact on the beam dump rapidly. While a similar scheme is used in LHC it has to be greatly refined for the FCC-hh.

Another risk arises from the extraction kickers. Their power supplies have to be permanently charged in order to be able to guarantee that the beam can be extracted at any time. However, an extraction kicker can thus fire unvoluntarily. In the LHC the beam is in this case extracted rapidly (asynchronous dump) without waiting for the extraction gap. Hence, a few bunches can escape into the arcs with larger amplitude or be lost on the extraction devices. The protection from these loses is more demanding in the FCC-hh due to the high beam energy. An alternative solution is therefore studied, where the failure of a single kicker allows to leave the beam in the machine until the next abort gap arrives.

2.14.7 Ion Operation

A first parameter set for the ion operation has been developed [43-45]. A preliminary estimate has been made of the integrated luminosity that can be achieved per experiment in 30 days, assuming that two experiments are operating. The expectation is 6 pb^{-1} and 18 pb^{-1} for proton-lead ion operation with baseline and ultimate parameters, respectively. For lead-ion lead-ion operation 23 nb^{-1} and 65 nb^{-1} could be expected. More detailed studies will be carried out to address the key issues in the ion production and collimation and to review the luminosity predictions.

Table 2: Tentative FCC-hh baseline parameters for ion operation.

	LHC achieved	HL-LHC baseline	FCC-hh baseline	FCC-hh ultimate
Bunch population $N[10^8]$	2.2	1.8	2.0	
Nominal transv. normal. emittance [μm]	1.5	1.65	1.5	1.5
Number of bunches n	518	1256	2760	5400
IP beta function [m]	0.6	0.5	1.1	0.3
Beam energy E [Z TeV]	6.5	7	50	50

2.14.8 Conclusion

The FCC-hh design addresses the key issues of a high-energy hadron-hadron collider. It is progressing very well toward the CDR.

2.14.9 Acknowledgements

The European Circular Energy-Frontier Collider Study (EuroCirCol) project has received funding from the European Union’s Horizon 2020 research and innovation programme under grant No 654305. The information herein only reflects the views of its authors and the European Commission is not responsible for any use that may be made of the information.

2.14.10 General References

Information is mainly available in presentations given in the FCC week 2017 in Berlin (they can be found at <https://indico.cern.ch/event/556692/>) and in the EuroCirCol meeting 2017 at CERN (<https://indico.cern.ch/event/669849/>). Detailed information will become available with the FCC-hh conceptual design report that is to be published next year.

2.14.11 Specific References

1. I. Hinchcliffe et al., “Luminosity goals for a 100 TeV pp collider”, Preprint CERN-PH-TH-2015-089.
2. D. Schulte et al. “Collider complex layout and parameters”, <https://fcc.web.cern.ch/eurocircol/Documents/WP1/Milestone%20and%20Deliverables/D1.3/EuroCirCol-1707281830-P2-WP1-D1->

[3_ColliderComplexLayoutAndParameters_V0100.pdf](#)

3. V. Mertens et al., “Civil Engineering, Infrastructure and Operation”, talk at FCC week 2017, Berlin.
4. A. Chance et al., ”Updates on the Optics of the Future Hadron-Hadron Collider FCC-hh”, Proc. IPAC 2017, Copenhagen, Denmark.
5. L.S. Stoel et al., “High Energy Booster Options for A Future Circular Collider at CERN”, Proc. IPAC 2016, Busan, Korea.
6. A. Milanese, B. Goddard, M. Solfaroli Camillocci, “Faster Magnet Ramps for Using the LHC as FCC injector”, CERN-ACC-2015-0133.
7. R. Tomás, X. Buffat, S. White, J. Barranco, P. Gonçalves Jorge, and T. Pieloni, "Beam-beam amplitude detuning with forced oscillations", Phys. Rev. Accel. Beams 20, 101002
8. J. Barranco et al., "Beam-Beam Studies for FCC-hh", Proc. IPAC 2017, Copenhagen, Denmark.
9. T. Pieloni et al., "Study of Beam-Beam Long Range Compensation with Octupoles", Proc. IPAC 2017, Copenhagen, Denmark.
10. P. Goncalves, "Observations and measurements of dynamic effects due to beam-beam interactions in the LHC and extrapolation to the FCC-hh", EPFL Master Thesis , 2017.
11. Ph. Lebrun. L. Tavian, private communication.
12. X. Buffat, D. Schulte, “Evolution of the Beam Parameters During Luminosity Production in the Future Circular Collider”, Proc. IPAC 2016, Busan, Korea.
13. R. Alemany Fernandez et al. “FCC-hh Turn-around Cycle” CERN-ACC-2016-0341.
14. D. Niebet, K. Fuchsberger, “Update on Turn-around Based on LHC 2016 Experience” talk at <https://indico.cern.ch/event/625274/>.
15. A. Niemi et al. “FCC-hh Operation Schedule”, talk at <https://indico.cern.ch/event/625274/>
16. A. Niemi et al. Phys. Rev. Accel. Beams **19**, 121003
17. A. Apollonio et al. “FCC Availability Studies”, talk at FCC week 2017, Berlin.
18. B. Dalena et al., “Advance of Dynamic Aperture at Injection for FCC-hh”, Proc. IPAC 2017, Copenhagen, Denmark.
19. D. Boutin et al., “Progress on the Optics Corrections of FCC-hh”, Proc. IPAC 2017, Copenhagen, Denmark.
20. A. Seryi at al, “Overview of Design Development of FCC-hh Experimental Interaction Regions”, Proc. IPAC 2017, Copenhagen, Denmark.
21. R. Martin, M. I. Besana, F. Cerutti, A. Langner, R. Tomás, E. Cruz-Alaniz, and B. Dalena, “Interaction region design driven by energy deposition”, Phys. Rev. Accel. Beams 20, 081005
22. M. Hofer at al., “3.3 TeV beam injection into combined experimental and injection FCC machine insertions”, talk at the FCC week 2017, Berlin.
23. J. Fernandez Topham, C. Garion, “FCC-hh BEamscreen Design”, talk at the the EuroCirCol meeting 2017, CERN (at <https://indico.cern.ch/event/670504/>).
24. L. Methner et al., “FCC-hh Electron Cloud”, talk at the FCC week 2017, Berlin
25. L. Methner et al., “Electron Cloud Studies”, EuroCirCol Meeting 2017, CERN.
26. E. Shaposhnikova, “Longitudinal Beam Dynamics and RF requirements”, talk at the FCC week 2017, Berlin.
27. O. Boine-Frankenheim et al., “FCC-hh Impedances and Instabilities”, talk at the

- EuroCirCol meeting 2017, CERN.
28. O. Boine-Frankenheim et al., “Landau Damping Requirements for FCC-hh”, to be published.
 29. O. Boine-Frankenheim et al., “High-Temperature Superconductor Coating for Coupling Impedance Reduction in the FCC-hh Beam Screen”, submitted to NIM A.
 30. S. Arsenyev, “Update of the FCC-hh Impedance Database”, EuroCirCol meeting 2017, CERN.
 31. B. Riemann, “Resistive Wall Impedance of Interaction Regions”, EuroCirCol meeting 2017, CERN.
 32. W. Hofle, “Update on FCC-hh Transverse Feedback Systems”, EuroCirCol meeting 2017, CERN.
 33. V. Kornilov, “Update on Landau Damping”, EuroCirCol meeting 2017, CERN.
 34. A. Grudiev, M. Schenk, “RF-Quadrupole for Landau Damping”, talk at <https://indico.cern.ch/event/604588/>.
 35. A. Burov, “Stabilizing E-lens for FCC-hh”, talk at <https://indico.cern.ch/event/674155/>.
 36. M. Fiascaris, et al., “First Design of a Proton Collimation System for 50 TeV FCC-hh”, Proceedings of IPAC16, Busan, Korea.
 37. J. Molson, et al., “Status of the FCC-hh collimation system”, Proceedings of IPAC17, Copenhagen, Denmark.
 38. M. I. Besana, et al., “Energy deposition in the betatron collimation insertion of the 100 TeV future circular collider”, Proceedings of IPAC17, Copenhagen, Denmark.
 39. J. Molson, et al., “A comparison of interaction physics for proton collimation systems in current simulation tools”, Proceedings of IPAC17, Copenhagen, Denmark.
 40. A. Krainer, “Dispersion Suppressor Protection”, talk at EuroCirCol meeting 2017, CERN.
 41. F. Burkart et al., “Injection and Extraction Insertions”, talk at FCC week 2017, Berlin.
 42. W. Bartmann et al. Phys. Rev. “Dump System Concepts for the Future Circular Collider”, *Accel. Beams* **20** 031001.
 43. M. Schaumann, “Ion Considerations”, talk at FCC week 2017, Berlin.
 44. M. Schaumann, “Potential performance for Pb-Pb, p-Pb and p-p collisions in a future circular collider”, *Phys. Rev. ST Accel. Beams* **18**, 091002 (2015).
 45. A. Dainese et al., “Heavy ions at the Future Circular Collider,” CERN-TH-2016-107, arXiv:1605.01389 [hep-ph]

2.15 R&D towards 16 T Nb₃Sn dipole magnets

Stephen A. Gourlay¹ and Davide Tommasini²

¹ LBNL, Berkeley, CA 94720, USA

² CERN, 1211 Geneva, Switzerland

Mail to: sagourlay@lbl.gov ; davide.tommasini@cern.ch

2.15.1 Introduction

A new proton collider representing a step forward with respect to the LHC shall provide collisions at a center of mass energy of the order of 100 TeV. This can be achieved, as proposed for example by the Future Circular Collider (FCC) study [1], with bending magnets operating at 16 T in a 100 km long circular machine. Magnets operating in the same field range could also be considered in case an interest will arise to double the energy of the LHC (HE-LHC) [2]. This is about twice the magnetic field amplitude produced by the Nb-Ti LHC magnets, and about 5 T higher than the one produced by the Nb₃Sn magnets being developed for the High Luminosity LHC (HL-LHC) [3]-[4], which will be the first high field Nb₃Sn magnets ever operating in a particle accelerator. Unless a major new development/discovery will affect cost and performance of high temperature superconductors in the next years, the same Nb₃Sn technology will remain the only practical one for use on a large accelerator operating at 16 T [5].

The paper describes the required R&D efforts towards the development of these 16 T Nb₃Sn dipole magnets and summarizes the relevant programs being deployed in Europe and in the U.S.

2.15.2 R&D directions

The main objectives of a R&D on 16 T Nb₃Sn dipole magnets for a large particle accelerator are to prove that these types of magnets are feasible in accelerator quality and to ensure an adequate performance at an affordable cost. In particular, the link between performance and cost may be strongly influenced, in the range of one order of magnitude in cost, by a successful R&D program.

Directions to pursue are: the increase of the conductor performance beyond the one considered for the HL-LHC, the reduction of the required “margin on the load line” with consequent reduction of conductor use and magnet size, the elaboration of an optimized magnet design maximizing performance with respect to cost.

2.15.3 Overview of development programs towards 16 T Nb₃Sn magnets

The development programs presently in place towards 16 T Nb₃Sn magnets can be schematically organized within three initiatives. First, the WP5 EuroCirCol Program, exploring different magnet design options on the same basis, charged of the write-up of the FCC Conceptual Design Report. Second, a supporting 16 T Magnet Technology Program, which includes a conductor development program, the electromechanical characterization of magnet components as well as the manufacture of R&D magnets. Third, the U.S. Magnet Development Program (US MDP), initially focused to the design

and manufacture of a 15 T cosinetheta model and to the exploration of canted-cosinetheta configurations.

2.15.3.1 *WP5 of EuroCirCol*

The WP5 of EuroCirCol [6] is gathering CEA, CERN, CIEMAT, INFN, KEK, the University of Geneva, the Technical University of Tampere (TUT) and the University of Twente (UT) to explore different design options for 16 T dipole magnets to give a baseline for future development. The results will be the core of the FCC Conceptual Design Report (FCC-CDR) to be delivered by end 2018. The design options under study are block-coil type performed by CEA, common-coil type performed by CIEMAT and cosinetheta type performed by INFN. Furthermore a fourth option, of canted-cosinetheta type, is also being explored thanks to a contribution of PSI. All options are elaborated with the same assumptions (in particular on the conductor performance and all magnet specifications) and analyzed with the same tools (for example the quench protection analysis is coordinated by TUT for all design options).

2.15.3.2 *16 T Magnets Technology Program*

The 16 T Magnets Technology Program, managed by CERN, centralizes the technological support to the design and development of the 16 T dipole magnets for the FCC or the HE-LHC.

The main targets of the program are to improve the state of the art performance conductor, to demonstrate the 16 T field reach, to develop the basic magnet technology (grading and splicing, instrumentation), to explore and optimize the performance (including training and field quality) with tailored R&D magnets, and finally to design, manufacture and test short model magnets.

Most of these activities are carried out in collaboration between CERN and partner institutes. In particular, for the conductor development agreements have been established between CERN and KEK (Japan), the Botchvar Institute (Russia) and KAT (Korea), and for the short model magnets agreements are being finalized between CERN, CEA (France), CIEMAT (Spain) and INFN (Italy).

2.15.3.3 *U.S. Magnet Development Program*

Along with other international activities, in the US, the recent Particle Physics Project Priority Panel (P5) [7] has strongly supported a future high-energy proton-proton collider as part of an overall strategy. Subsequently, the DOE Office of High Energy Physics commissioned a HEPAP (High Energy Physics Advisory Panel) subpanel [8] to advise on medium and long term national goals for US Accelerator R&D in accelerator based particle physics. consistent with the P5 report. In response to the P5 and HEPAP subpanel recommendations the DOE Office of High Energy Physics created the US Magnet Development Program (MDP). The initial program is formed around three US superconducting materials and magnet programs: Lawrence Berkeley National Laboratory, Fermi National Accelerator Laboratory and the National High Magnetic Field Laboratory/Florida State University. The MDP has 4 main goals: 1) Explore the performance limits of Nb₃Sn accelerator magnets, 2) Develop and demonstrate an HTS magnet with a self-field up to 5T, 3) Pursue Nb₃Sn and HTS conductor R&D with clear targets to increase performance and reduce the cost of accelerator magnets, and 4)

Address fundamental aspects of magnet design, technology and performance that could lead to substantial reduction of magnet cost.

The high field Nb₃Sn dipole development is broken down into two components. One is establishment of a baseline design to demonstrate feasibility based on the well-known cosine-theta geometry using 4-layers to achieve a design field of approximately 15T [9]. The second is aimed at higher risk innovative concepts to reduce cost and is based on the Canted-Cosine-Theta (CCT) concept to reduce cost and simplify fabrication [10].

2.15.4 Conclusion

R&D programs in the EU and US are actively pursuing the challenge of developing the technology that will produce viable accelerator magnets operating up to 16 T. High energy physics is explicitly an international endeavour. Developing close working relationships with international partners is a critical step towards building a world-wide collaboration that will be necessary for high energy physics to advance to the next stage. The magnitude of the challenge we face in constructing a next generation proton-proton collider such as the FCC exceeds the capacity and capabilities of any one region. Collaboration with international partners ensures a highly leveraged and complementary means of achieving the ambitious goals.

2.15.5 References

1. CERN, “The European Strategy for Particle Physics”, CERN-Council-S/106, CERN, Brussels, 2013.
2. Proceedings of the EuCARD-AccNet-EuroLumi Workshop, Oct. 2010, Republic of Malta, <http://cds.cern.ch/record/1344820>.
3. F.Savary et al, “Progress on the Development of the Nb₃Sn 11T Dipole Magnet for the High Luminosity Upgrade of the LHC”, IEEE Trans. Appl. Supercond., vol. 27, no. 4, June 2017
4. P.Ferracin et al, “Development of MQXF: The Nb₃Sn Low- β Quadrupole for the HiLumi LHC”, IEEE Trans. Appl. Supercond., vol.26, no.4, June 2016
5. D.Larbalestier, “Superconductors for HEP use: in the next few (10?) years”, <https://conferences.lbl.gov/event/73/session/3/contribution/31/material/slides/0.pdf>
6. Horizon 2020 EuroCirCol Consortium Agreement, number 654305.
7. Building for Discovery: Strategic Plan for U.S. Particle Physics in the Global Context, P5 Report, http://science.energy.gov/~media/hep/hepap/pdf/May%202014/FINAL_P5_Report_053014.pdf
8. Accelerating Discovery A Strategic Plan for Accelerator R&D in the U.S, (HEPAP Accelerator R&D Subpanel Report, April 2015); see at <http://science.energy.gov/hep/hepap/reports/>
9. I. Novitski, et al., “Development of a 15T Nb₃Sn Accelerator Dipole Demonstrator at Fermilab,” <http://dx.doi.org/10.1109/TASC.2016.2517024>
10. S. Caspi, et al., “Canted-Cosine-Theta Magnet (CCT) – A Concept for High Field Accelerator Magnets,” IEEE Transactions on Applied Superconductivity 24(3):1-4 · June 2014

2.16 Faster Magnet Ramps for Using the LHC as FCC Injector

A. Milanese, B. Goddard, M. Solfaroli Camillocci
 Mail to: amilanes@cern.ch
 CERN - The European Organization for Nuclear Research
 CH-1211 Geneva, Switzerland

2.16.1 Introduction and motivation

A faster ramp of the LHC magnets is a key ingredient towards an effective reconfiguration of the machine from a collider to a “High Energy hadron Booster” (HEB). Such a HEB could fill, over several cycles, a Future Circular Collider (FCC-hh) of 80-100 km length and a proton-proton centre-of-mass energy of 100 TeV [1].

In this paper, we recall the present LHC ramp settings and we analyze the constraints related to the current rate dI/dt of the magnets. We then describe possible scenarios – with different hardware modifications – to shorten the ramps.

These target durations can be used to define a proper filling of the downstream FCC-hh collider, whose injection energy is fixed here at the baseline value of 3.3 TeV.

The material of this paper builds upon a previous work [2], where we proposed also dedicated Machine Developments (MD) in the LHC. Parts of these MDs have now been successfully carried out, and first results are presented in [3].

2.16.2 The present situation

A ramp in the LHC involves around 1700 magnet circuits – the great majority of which are superconducting. Circuits and power converters are grouped in families [4]; this grouping is reflected in the clusters of Fig. 1, where we plot the minimum ramp time (from 0 to rated current, using the available voltage of the power converter) vs. the rated current, using data from [5]. The 13 kA circuits – main dipoles (MB) and main quadrupoles (MQ) – with their large inductances dictate the overall ramp rate of the machine. The MB are powered by thyristor line-commutated converters, which can provide negative voltage during normal de-excitation of the circuit. On the other hand, the MQ – as well as the insertion quadrupoles, the separator dipoles and other 6 kA circuits – are powered by one-quadrant converters, with inherent limitations during the ramp down. The inner triplet quadrupoles have a similar maximum ramp rate as the 13 kA circuits; however, these insertions will undergo heavy modifications for HL-LHC [6], and they are anyway not needed in a HEB reconfiguration [7]. Then, the 600 A and lower current circuits of the LHC can already be ramped up / down in a matter of a few minutes. For these reasons, we focus here on the MB and MQ cases.

The minimum ramp rates reported in Fig. 1 assume a purely linear slope, from 0 to rated current. In reality, a ramp up starts from an injection current I_{inj} to reach a flattop current I_{fl} , with smooth transitions in between. In the LHC, a PELP (Parabolic-Exponential-Linear-Parabolic) function is used for the ramp up [3-8]. During the first parabolic branch, the snap-back region is gently crossed, while adjusting in a feed forward way the strength of the sextupole spool pieces. Then, an intermediate exponential segment – with a constant ratio between B and dB/dt , hence with similar normalized field distortions from eddy currents – brings over to the linear part, where the maximum available ramp rate is exploited. Today, this maximum slope for the MB circuit is 10 A/s.

Finally, a second parabolic part rounds off the end of the ramp. This PELP function is fully characterized by 7 parameters, for example

$$I_{inj} = 760 \text{ A}, \quad I_{ft} = 5573 \text{ A}, \quad dI/dt_{max} = 10 \text{ A/s},$$

$$\Delta I_{snb} = 12 \text{ A}, \quad dI/dt_{snb} = 0.9 \text{ A/s}, \quad B_{exp,max} = 1.6 \text{ T}, \quad \Delta I_{p2} = 0.02 I_{ft}$$

correspond to the settings used in operation up to now (excluding the previously mentioned MD), with the only exception of the flattop current, which is adjusted here for 3.3 TeV. The PELP ramp obtained with these values is plotted in Fig. 2. The overall duration is 643 s, with an average ramp rate of 7.5 A/s compared to a maximum slope in the linear part of 10 A/s. The relative duration of the initial parabolic and exponential parts is rather significant, at 46%.

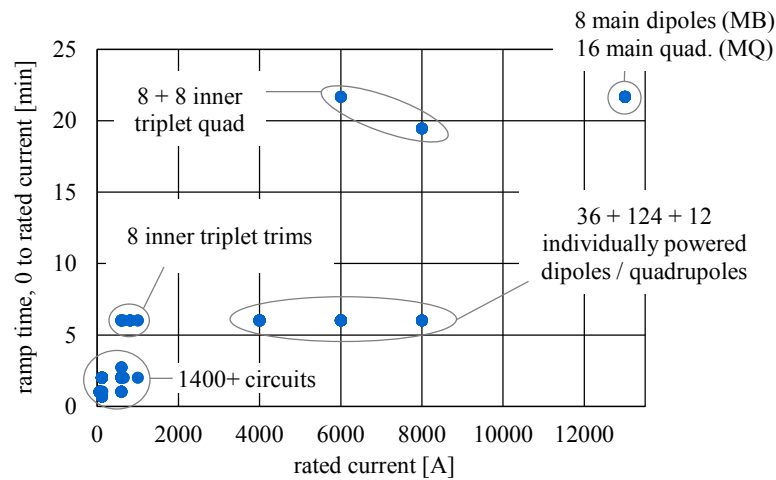


Figure 1: Minimum ramp up times of the present LHC circuits [5].

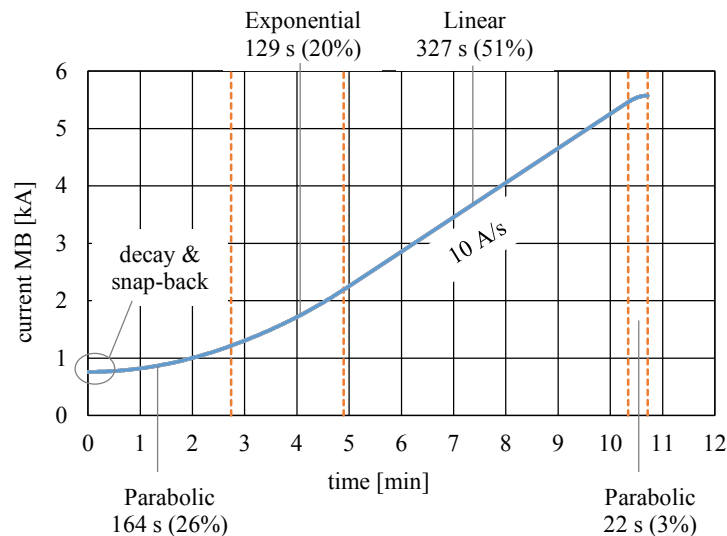


Figure 2: Ramp up to 3.3 TeV, with the present settings.

The ramp down – since there is no beam in – could be fast and linear. This is not the case now, see for example in Fig. 3 typical curves for the main dipoles and quadrupoles (focusing and defocusing). The data correspond to a ramp down from 6.5 TeV taken during 2016 beam commissioning. As the MB are driven down at -10 A/s, in a linear way

and with negative voltage, the MQ are left floating down with an exponential. With no modifications to these circuits and related one-quadrant power converters, ramping down from 3.3 TeV in a similar way corresponds to about 12.5 minutes for the MQ, which are then slower than the MB.

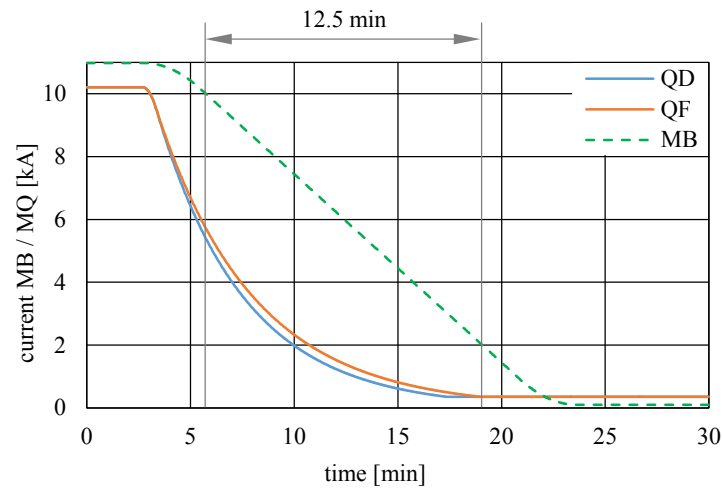


Figure 3: Present ramp down of the 13 kA circuits. The part indicated with an arrow relates to the ramp down of the MQ from 3.3 TeV.

2.16.3 Constraints for faster ramps

In this section we comment on the main constraints – in somehow decreasing order of importance – limiting the ramp rate of the LHC magnet circuits. Similar conclusions on the ramp rates apply also to the superconducting magnets of HL-LHC, including Nb₃Sn insertion quadrupoles and 11 T dipoles [6].

2.16.3.1 Power converters

When introducing the work, we already touched on the limitations coming from the voltage in the power converters, to sustain the inductive component during ramp up / down. In fact, the 13 kA converters were optimized for a ramp up to 7 TeV lasting about 20 min ($dI/dt_{max} = 10$ A/s). This is well compatible for exploitation of the LHC as a collider and it involves a power of the order of a few MVA at the end of the ramp. Any increase in ramp rate will therefore need a hardware upgrade of the main 13 kA power converters and their own powering.

Besides a maximum available voltage, the controllers of the power converters are also configured for a maximum slew rate – that is, the rate of change of the voltage with respect to time is finite. This value is currently 25 V/s for the 13 kA circuits [9], which yields a minimum duration for the parabolic round off at the end of the MB ramp of $190/25 \approx 8$ s. This is well below the length of the second parabolic part of the current PELP ramp (for ex., 22 s in Fig. 2).

2.16.3.2 Voltages

Increased inductive voltages can become a limitation not only for the power converters, but also for the superconducting magnets circuits.

The more challenging case is the MB, where each of the 8 strings in the machine have an inductance of 15 H [4]. This brings an inductive voltage of 150 V at 10 A/s, and (for example) of 750 V at 50 A/s. The magnets themselves are tested at 1.9 kV at cold and they experience ± 475 V at the beginning of a fast extraction. Setting a comfortable maximum voltage to be used routinely for operating the LHC magnets on the FCC time horizon is not straightforward, though we see unlikely the possibility of going much above 50 A/s without introducing a further powering sectorization of the arcs.

2.16.3.3 Protection diodes

The protection diode mounted in parallel on every main dipole has a cold turn-on voltage of about 6 V [4], which – given the 0.1 H inductance of a single MB – results in a dI/dt limited to 60 A/s.

A hardware modification could be studied to sustain a ramp rate above 60 A/s. In any case, a reconfiguration of the diodes is needed to match the change of magnet polarity, to enable a different beam crossing scheme [7]. This rewiring of the diode leads also applies to the main quadrupoles, were their polarity reversed.

2.16.3.4 Cryogenic loads (AC losses) / premature quenches

Faster ramps bring increased AC losses. This additional cryogenic load is estimated in Table 1 for the MB, considering 10 A/s at 7 TeV and 50 A/s (as to fix as a working hypothesis an increased dI/dt) to 3.3 TeV. The data is compiled from [10], using though an inter-strand contact resistance R_c of 40 $\mu\Omega$ [11] instead of the (pessimistic) 2 $\mu\Omega$ considered back in 1995. The energy per ramp is quite similar in the two cases: the increase of the various eddy current contributions when going from 10 A/s to 50 A/s is balanced off by the shorter duration. The increased transient load can be dealt with by the heat capacity of the liquid helium in the cold masses. In fact, the system was designed to keep the temperature below the λ line assuming a release of 3000 J/m during a fast ramp down in 80 s. There is thus good margin to absorb ramp rates of 100 A/s and more, even up to full field.

Table 1: Estimated losses per meter for a twin aperture LHC dipole.

<i>loss per ramp [J/m]</i>	<i>10 A/s to 7 TeV</i>	<i>50 A/s to 3.3 TeV</i>
hysteresis in superconductor	200	200
resistive in splices	26	3
hysteresis in iron yoke	20	20
inter-strand coupling currents	10	22
inter-filament coupling currents	6	13
eddy currents in wedges / collars	2	4
total	264	262
power during ramp [W/m]	0.24	1.28

This is consistent with the experience gathered during cold tests at CERN and this is also confirmed by LHC operation: when a fast power abort is triggered in a MB circuit (at 6.5 TeV) the magnets sustain about -120 A/s at the beginning of the exponential without quenching. Therefore, we consider that the AC losses coming from a few repeated ramps up / down to 3.3 TeV at 50 A/s do not introduce particular constraints.

2.16.3.5 *Quench detection*

As recalled just above, at the beginning of a fast power abort – when the extraction switches close the circuit to the dump resistances – the main dipoles see -120 A/s. This does not trigger the QPS, which is still active. This is encouraging for operation at higher ramp rates, though it does not imply directly that the present quench detection scheme is already compatible with, for example, 100 A/s. In particular, attention should be given to the voltage waves travelling in the string following a fast power abort occurring during a ramp. In fact, when the waves reach a dipole with a different AC behavior in the two apertures, a voltage difference arises, which can be misinterpreted as a quench signal. Presently, this voltage unbalance – when the fast power abort is triggered at 10 A/s – is in the worst cases of the order of 200 mV [12]. Possible solutions could be either at the circuit level (to attenuate the waves) or at the quench detection board themselves (setting appropriate thresholds and verification times, to filter out the peaks of the waves, lasting a few ms).

Although the actual settings might need to be revisited – which applies also to the lower current circuits, with electronic compensation of the inductive voltage – we do not consider here the quench detection as being a main constraint to increase the ramp rate of a factor 5 (or more), considering also the increased margins coming from operation at lower fields (3.3 TeV) and the most probable upgrade of the QPS electronic cards in the FCC time horizon.

2.16.3.6 *Field quality*

A different ramp rate affects the field quality through two main effects: a faster crossing of the snap-back in the very initial part (for MB) and the different eddy currents (in all circuits).

Actually, the snap-back following the decay at the injection plateau does not depend on the ramp rate at which it is crossed; it does depend, though, on the ramp rate of the previous cycle(s) [13], which is relevant if the cycles are put back-to-back. At 50 A/s, the amplitude of the decay is about twice with respect to the present 10 A/s. Analyses of the actual corrections implemented through snap-back with the sextupole spool pieces show that there is enough voltage margin to handle twice larger (or more) decays in the same time. As anyway this region is very limited in current – of the order of 10 to 20 A – the very initial part of the ramp can be made as gentle as needed to keep good control over the chromaticity.

As for the eddy currents, the dominant term there comes from inter-strand coupling currents. As an example, the measured change of sextupole component at the reference radius (Δb_3) in the pre-series dipoles at the start of the 10 A/s ramp was $0.05 \cdot 10^{-4}$ [14]. Extrapolating this value to 50 A/s – which is conservative as the R_c in the series magnets was higher – brings Δb_3 to $0.25 \cdot 10^{-4}$: this is one order of magnitude smaller than the change typically occurring during decay at the injection plateau. Besides affecting the

field quality, eddy currents also change slightly the main field component. This effect applies to all circuits, including for example the main quadrupoles, though it is rather limited and it can be compensated with proper corrections to the ramp.

Our conclusion regarding field quality is that FiDeL (the Field Model of the LHC) [15] would need to be checked and updated for increased ramp rates, though up to at least 50 A/s field quality itself would not be a limiting factor.

2.16.4 Options for faster ramps up

Considering the various constraints detailed in the previous section, we consider here options for faster ramps up of the MB spanning the range 10 to 50 A/s. This implies mainly three scenarios in terms of hardware modifications:

- at 10 A/s (for the MB), no hardware change is needed;
- above 10 A/s and up to about 35 A/s (for the MB), the main 13 kA power converters need an upgrade;
- above 35 A/s (for the MB), also the 6 kA power converters would need to be upgraded.

We do not consider ramps faster than 50 A/s (for the MB) to avoid hitting more hardware limits – such as the cold turn-on voltage of the diodes – with a marginal gain in shortening the overall cycle length.

2.16.4.1 A faster PELP

As recalled above, a PELP ramp function is defined by 7 parameters. Considering that injection (I_{inj}) and flattop (I_{ft}) currents are fixed, there remain 5 free variables:

- ΔI_{snb} and dI/dt_{snb} , to control the snap-back crossing;
- $B_{exp,max}$, the field at the end of the exponential segment;
- dI/dt_{max} , the slope in the linear part;
- ΔI_{p2} , defining the final parabolic round off.

Since the various segments are tied up with continuity conditions, there are some mathematical constraints among them. In particular, the variables describing the snap-back crossing (ΔI_{snb} and dI/dt_{snb}) force a minimum possible $B_{exp,max}$. As a result, the initial parabolic branch extends much longer than the actual snap-back; for ex., in Fig. 2 the first parabola lasts for 456 A, although ΔI_{snb} is set to a mere 12 A, and $B_{exp,max}$ is close to the minimum allowable setting. Keeping this PELP formulation forces – as dI/dt_{max} is increased – also to set more aggressive ΔI_{snb} and dI/dt_{snb} parameters.

Table 2 (adapted from calculations reported in [2]) lists possible PELP options, built at 10, 30 and 50 A/s and with various dI/dt_{snb} . Both $B_{exp,max}$ and ΔI_{p2} are kept as small as possible, to speed the ramp, though for some combinations of parameters it is not possible to find a solution for $B_{exp,max}$. The last row in Table 2 reports the maximum ratio $(dI/dt)/I$, which is proportional to the maximum contribution of eddy currents to field quality. With a dI/dt_{max} of 10 A/s, the ramps up last between 10'31" and 8'21"; the shorter duration is obtained with a steep (factor of 3) increase of the initial snap-back crossing. Going to 30 and 50 A/s, the present setting for ΔI_{snb} and dI/dt_{snb} simply cannot be kept – for the way the function is mathematically defined. The shortest ramp – at 50 A/s – in Table 2 lasts for 3'31" and it is rather inefficient, as the average ramp rate is only 26 A/s.

Table 2: PELP ramps of MB from 450 GeV to 3.3 TeV.

dI/dt_{max}	[A/s]	10			30			50		
ΔI_{snb}	[A]	12			12			12		
dI/dt_{snb}	[A/s]	0.9	1.8	2.7	0.9	1.8	2.7	0.9	1.8	2.7
$B_{exp,max}$	[T]	1.55	0.83	0.68	none	2.32	1.55	none	none	2.58
ΔI_{p2}	[A]	31			283			785		
total duration	[s]	631	522	501	not feasible	274	219	not feasible	not feasible	187
P duration	[%]	33	14	7		38	32			37
E duration	[%]	11	0	0		30	11			33
L duration	[%]	54	85	92		26	48			13
P duration	[%]	1	1	1		7	9			17
time up to ΔI_{snb}	[s]	27	13	9		13	9			9
average dI/dt	[A/s]	7.6	9.2	9.6		17.6	22.0			25.7
max $(dI/dt)/I$	[1/s]	0.0047	0.0088	0.0108		0.0094	0.0141			0.0141

2.16.4.2 From PELP to PPLP

To overcome the drawbacks of the PELP formulation when handling faster linear ramp rates, we proposed in [2] a PPLP function, substituting the exponential branch with another parabolic part, for a swift transition from an initial, gentle crossing of the snap-back region, to the linear part at dI/dt_{max} . The curvature of this second parabola is mostly dictated by the slew rate of the power converter. The advantage of this solution is that the parameters defining the snap-back crossing are in a way uncoupled from the rest of the ramp. The disadvantage is that the eddy currents contributions are higher in this low field part; this is not particularly worrisome, considering the value of R_c for the series dipoles, and the limited amount of field distortion coming from eddy currents in absolute. All details about the mathematical formulation of the PPLP can be found in [2].

Table 3 (adapted from [2]) lists possible PPLP ramps. We assume 25 V/s as maximum slew rate in all cases but the last, where we take 100 V/s, to show the impact of dV/dt_{max} on the overall ramp. Already at 10 A/s, this scheme is faster than the PELP, with for example a net gain of 1'58" for the same snap-back crossing. This tendency becomes more predominant at higher ramp rates, for which the average current slope gets closer to the dI/dt_{max} of the linear part. With the present ΔI_{snb} and dI/dt_{snb} and 25 V/s for the slew rate, the ramp lasts 3'25" at 30 A/s and 2'34" at 50 A/s. With a slew rate up at 100 V/s and keeping 50 A/s in the linear part, the overall duration goes below 2 min, at 1'52".

A subset of the options listed in Tables 2 and 3 – including the present snap-back settings – is plotted in Fig. 4.

2.16.5 Options for faster ramps down

The overall ramp down is presently limited by a number of one-quadrant power converters, in particular the MQ, as shown in Fig. 3. Hardware modifications on these circuits are needed for any decrease of the ramp down duration.

If negative voltage were available – following an upgrade of the power converters – then the ramp down function could be simply linear, with short parabolic round offs at the beginning and the end to match the available slew rates. In this scenario, the durations are very close to those obtained during ramp up with the PPLP and a fast crossing of the

snap-back (Table 3), and they are therefore not separately reported here.

Another option is to discharge the energy stored in these slow circuits on parallel warm resistances, similarly as it is done during a fast power abort.

Table 3: PPLP ramps of MB from 450 GeV to 3.3 TeV.

dI/dt_{max}	[A/s]	10		30		50		50
ΔI_{snb}	[A]	12		12		12		12
dI/dt_{snb}	[A/s]	0.9	2.7	0.9	2.7	0.9	2.7	2.7
dV/dt_{max}	[V/s]	25		25		25		100
total duration	[s]	513	494	205	186	154	135	112
P duration	[%]	5	2	13	5	17	7	8
P duration	[%]	1	1	9	9	20	22	7
L duration	[%]	92	96	69	76	42	48	78
P duration	[%]	1	1	9	10	20	23	7
time up to ΔI_{snb}	[s]	27	9	27	9	27	9	9
average dI/dt	[A/s]	9.4	9.7	23.5	25.9	31.3	35.7	42.8
max $(dI/dt)/I$	[1/s]	0.0125	0.0125	0.0284	0.0285	0.0321	0.0322	0.0517

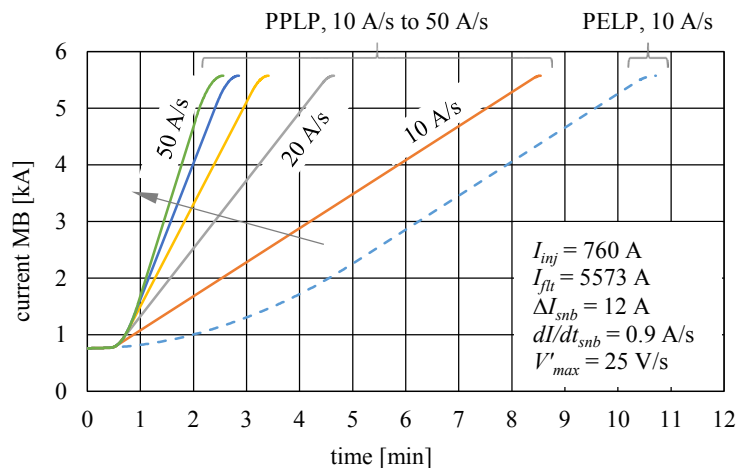


Figure 4: Several options for ramps up from 450 GeV to 3.3 TeV.

2.16.6 Conclusions

With no hardware modifications – that is, at 10 A/s on the main dipole magnets (MB) – the LHC ramp up to 3.3 TeV can last 9 min, while the ramp down takes about 12.5 min.

Considering upgrades of the power converters, a change in the ramp up function, for example a PPLP instead of the present PELP, becomes rather essential to benefit from the increased linear ramp rate. In this case, the ramp up (or down) can last 5 min for an MB maximum ramp rate of 20 A/s, which is further reduced to 2.5-3 min when pushing the MB at 50 A/s. Such a factor of 5 increase in linear ramp rate can be sustained by the magnets. Going faster is more challenging and it is not that rewarding, as then the overall duration of the cycle is given more by the injection and extraction plateaus.

The five times faster ramp rates make the LHC an attractive option for an injector for FCC-hh.

2.16.7 Acknowledgements

We acknowledge L. Bottura, M. Lamont, M. Modena, E. Todesco, D. Tommasini, A. Verweij and L. Walckiers for fruitful discussions on the topic.

2.16.8 References

1. Ball *et al.*, “Future Circular Collider study hadron collider parameters”, FCC-ACC-SPC-0001, CERN EDMS 1342402, Feb. 2014.
2. Milanese, B. Goddard, M. Solfaroli Camillocci, “Faster ramp of LHC for use as an FCC High Energy hadron booster”, CERN-ACC-2015-133, Nov. 2015.
3. O. Brüning *et al.*, “LHC Design Report”, CERN-2004-003, Jun. 2004.
4. M. Solfaroli Camillocci, “MD2429, PPLP ramp MD, first results”, Aug. 2017, indico.cern.ch/event/657430.
5. CERN Electrical Layout Database, layout.web.cern.ch.
6. O. Brüning and L. Rossi, “The High Luminosity Large Hadron Collider”, v. 24 in *Advanced Series on Directions in High Energy Physics*, World Scientific, 2015.
7. B. Goddard *et al.*, “Main changes to LHC layout for reuse as FCC-hh High Energy Booster”, CERN-ACC-2015-030, Mar. 2015.
8. L. Bottura *et al.*, “LHC main dipoles proposed baseline current ramping”, LHC Project Report 172, Mar. 1998.
9. CERN Function Generator / Controller database, cern.ch/fgc.
10. A. Verweij, “Electrodynamics of superconducting cables in accelerator magnets”, Ph.D. thesis, Univ. Twente, The Netherlands, 1995.
11. L. Rossi and L. Bottura, “Superconducting Magnets for Particle Accelerators”, *Reviews of Accelerator Science and Technology*, v. 5 (2012), pp. 51-89.
12. E. Ravaioli *et al.*, “Modeling of the voltage waves in the LHC main dipole circuits”, *IEEE Trans. Appl. Superc.*, v. 22, n. 3, Jun. 2012.
13. N. Sammut *et al.*, “Mathematical formulation to predict the harmonics of the superconducting Large Hadron Collider magnets. III. Precycle ramp rate effects and magnet characterization”, *Phys. Rev. ST Accel. Beams* 12, 102401, 2009.
14. L. Bottura *et al.*, “Field quality of the LHC dipole magnets in operating conditions”, EPAC 2002 proceedings.
15. N. Aquilina *et al.*, “The FiDeL model at 7 TeV”, IPAC 2014 proceedings; also, cern.ch/fidel.

2.17 Update on the SPPC design

Jingyu Tang for the SPPC study group

Mail to: tangjy@ihep.ac.cn,

Institute of High Energy Physics, CAS, Beijing 100049

2.17.1 1 Introduction

With a recent change on the tunnel circumference from 50-60 km to 100 km, we have an updated design on the CEPC-SPPC project [1-2]. As the second phase of the project,

with CEPC being electron-positron collider to exploit Higgs physics, SPPC (Super Proton-Proton Collider) is envisioned to be an extremely powerful proton-proton collider, and both colliders share a 100-km circumference tunnel. The primary design goal of SPPC is to have a center of mass energy 75 TeV, a nominal luminosity of $1.0 \times 10^{35} \text{ cm}^{-2} \text{ s}^{-1}$ per IP, and an integrated luminosity of 30 ab^{-1} assuming 2 interaction points and ten years of running. A later upgrade to even higher luminosities is also possible. It is true that luminosity has a more modest effect on energy reach, in comparison with higher beam energy [3], but raising the luminosity will likely be much cheaper than increasing the energy. The ultimate upgrading phase for SPPC is to explore physics at the center of mass energy of 125-150 TeV by using higher-field magnets. Some key parameters are shown in Table 1.

Table 1: Key parameters of the SPPC baseline design

<i>Parameter</i>	<i>Value</i>		<i>Unit</i>
	Phase-I	Ultimate	
Center of mass energy	75	125-150	TeV
Nominal luminosity	1.0×10^{35}	-	$\text{cm}^{-2} \text{s}^{-1}$
Number of IPs	2	2	
Circumference	100	100	Km
Injection energy	2.1	4.2	TeV
Overall cycle time	9-14	-	Hours
Dipole field	12	20-24	T

SPPC is a complex accelerator facility and will be able to support research in different fields of physics, similar to the multi-use accelerator complex at CERN. Besides the energy frontier physics program in the collider, the beams from each of the four accelerators in the injector chain can also support their own physics programs. The four stages, shown in Figure 1 and with more details in Table 3, are a proton linac (p-Linac), a rapid cycling synchrotron (p-RCS), a medium-stage synchrotron (MSS) and the final stage super synchrotron (SS). This research can occur during periods when beam is not required by the next-stage accelerator.

The option of heavy ion collisions also expands the SPPC program into a deeper level of nuclear matter studies. There would also be the possibility of electron-proton and electron ion interactions.

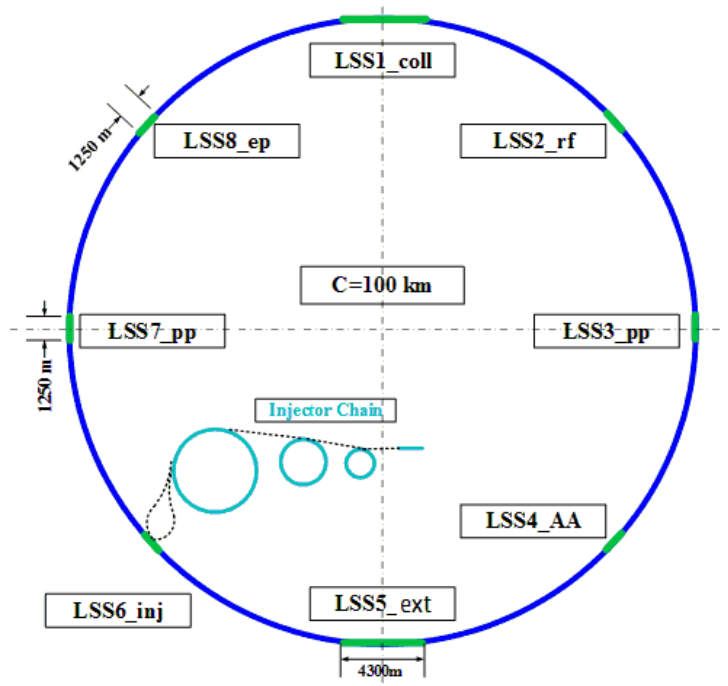


Figure 1: Schematic for the SPPC accelerator complex

2.17.2 Lattice

Different lattice schemes have been studied. The solution with eight arcs and eight long straight sections has been accepted by both CEPC and SPPC. To comply with the two colliders in the same tunnel, a LHC-like lattice was chosen for the arcs for its good flexibility to match the different cell lengths of the two colliders. The arc sections should be designed to be as compact as possible to provide necessary long straight sections. Traditional FODO focusing is everywhere, except at the IPs where triplets are used to produce the very small β^* . The arcs represent most of the circumference, and the arc filling factor is taken as 0.78, similar to LHC [4]. Long straight sections are crucial to host interaction sections with large detectors, beam injection and extraction systems, collimation systems and RF stations. Figure 2 shows the lattice functions at one of the IP regions. The some main parameters are listed in Table 2.

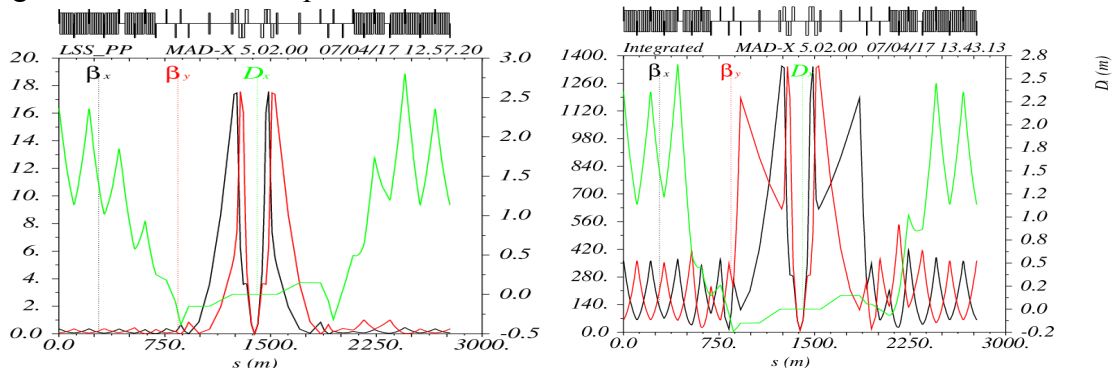


Figure 2: Lattice at one of the two main IRs. Left: at collision energy; Right: at injection energy.

Table 2: Some main SPPC parameters

<i>Parameter</i>	<i>Value</i>	<i>Unit</i>
Circumference	100	km
Beam energy	37.5	TeV
Dipole field	12	T
Arc filling factor	0.78	
Total dipole magnet length	65.442	km
Number of long straight sections	8	
Total straight section length	16.1	km
Injection energy	2.1	TeV
Number of IPs	2	
Revolution frequency	3.00	kHz
Nominal luminosity per IP	1.0×10^{35}	$\text{cm}^{-2}\text{s}^{-1}$
Beta function at collision	0.75	m
Circulating beam current	0.70	A
Nominal beam-beam tune shift limit per IP	0.0075	
Bunch separation	25	ns
Number of bunches	10080	
Bunch population	1.5×10^{11}	
Normalized rms transverse emittance	2.4	μm
Beam life time due to burn-off	14.2	hours
Full crossing angle	110	μrad
rms bunch length	75.5	mm
Stored energy per beam	9.1	GJ
SR power per beam	1.1	MW
SR heat load at arc per aperture	12.8	W/m
Energy loss per turn	1.48	MeV

2.17.3 Luminosity and leveling

Although the initial luminosity (or nominal luminosity) of $1.0 \times 10^{35} \text{ cm}^{-2}\text{s}^{-1}$ is modest for a next-generation proton-proton collider. It is comparable to FCC-hh [5-6] and lower than in the HL-LHC [7]. This design also allows future luminosity upgrading.

Besides the synchrotron radiation power limits the circulation current and luminosity, the number of interactions per bunch crossing is also a limit to the luminosity. It is believed that ongoing R&D efforts on detectors and general technical evolution will be able to solve the data pile-up problem. On the other hand, it is important to increase the average, and thus integrated luminosity while maintaining the maximum instantaneous luminosity [8]. Thus one kind of luminosity leveling scheme should be applied. By taking into account the loss of stored protons from collisions, cycle turnaround time, shrinking of the transverse emittance due to synchrotron radiation, and beam-beam shift, one can design different leveling schemes, as shown in Figure 3. An emittance blow-up system is needed to control the emittance shrinkage. Another method to increase the luminosity is to adjust β^* during the collisions by taking advantage of emittance shrinking while keeping the beam-beam tune shift constant.

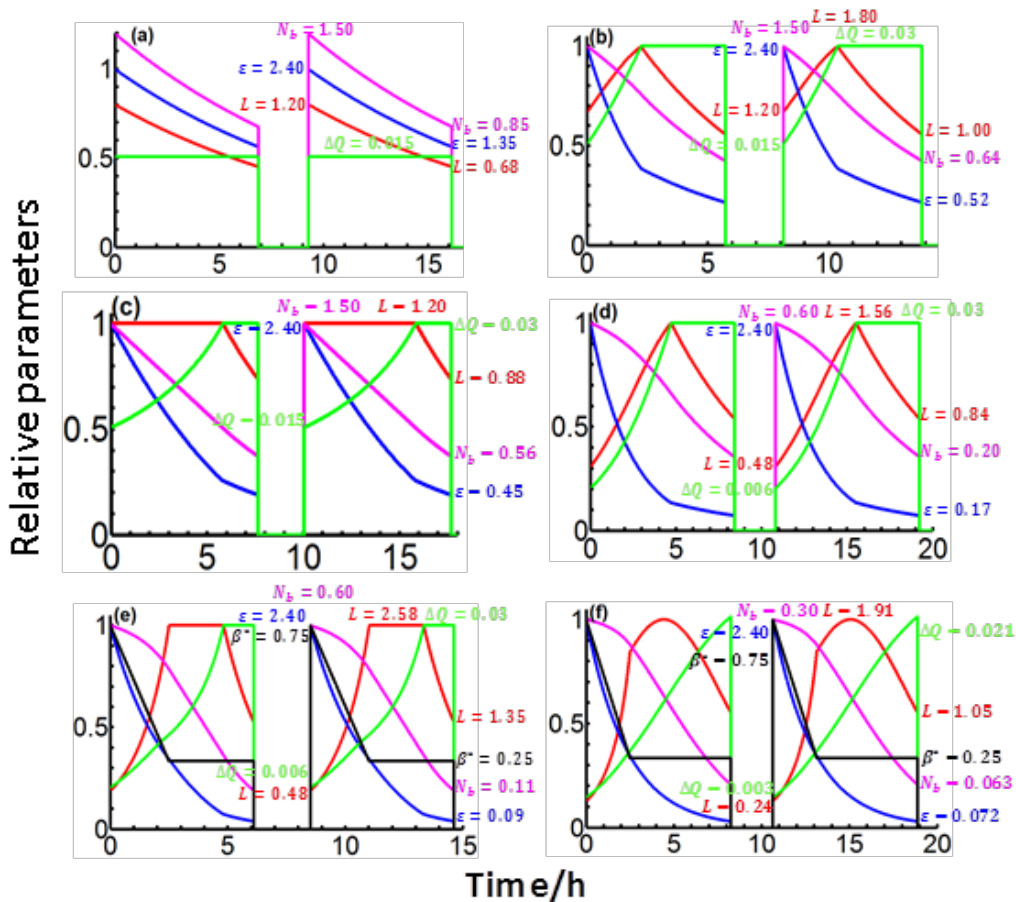


Figure 3: Evolution of parameters vs time with a turnaround time of 2.4 hours and bunch spacing of 25 ns. Red: luminosity, magenta: number of protons per bunch, blue: transverse emittance, green: beam-beam tune shift, black: beta* at the IP. (a) with fixed tune shift; (b) allowing the tune shift to rise to 0.03; (c) as in (b) but with the luminosity “leveled” at its initial value; (d) as in (c) but bunch spacing of 10 ns; (e) as for (d) but reducing beta* in proportion to emittance down to 25 cm; (f) as for (e) but with bunch spacing of 5 ns. In plots a), b), c) and d), beta* is kept constant at the nominal 0.75 m.

2.17.4 Collimation

Beam losses will be extremely important for safe operation in a machine like SPPC where the stored beam energy will be 9.1 GJ per beam. The radiation from the lost particles will trigger quenching of the superconducting magnets, generate unacceptable background in detectors, damage radiation-sensitive devices, and cause residual radioactivity that prevents hands-on maintenance. These problems can be addressed by sophisticated multi-stage collimation systems. At SPPC, extremely high collimation efficiency is required to deal with the huge stored energy. In addition, it is very difficult to collimate very high energy protons efficiently and the material for the collimators becomes a problem due to impedance and radiation resistance issues.

A five-stage collimation system has been studied for the betatron collimation to reach the required cleaning inefficiency of only 3.0×10^{-6} [9]. To avoid the critical SD (Single Diffractive) scattering [10-12] which becomes very important at tens TeV energy, we developed a novel concept by combining the betatron collimation and momentum

collimation in a same long straight section, see Figure 4. In this way, the particles from the SD effect at the betatron primary collimators can be cleaned by the momentum collimation system, and we can avoid warm collimators in the downstream arc sections. One of the two very long straight sections of about 4.3 km is used to host the collimation system. Low-field superconducting magnets with protection in the betatron collimation section are found very much helpful in reducing the collimation inefficiency, as shown in Figure 5.

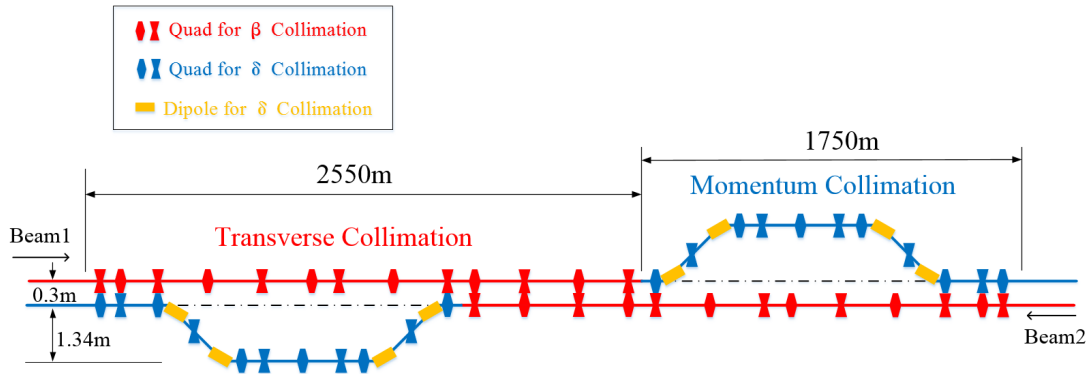


Figure 4: Combined transverse and momentum collimation scheme for SPPC

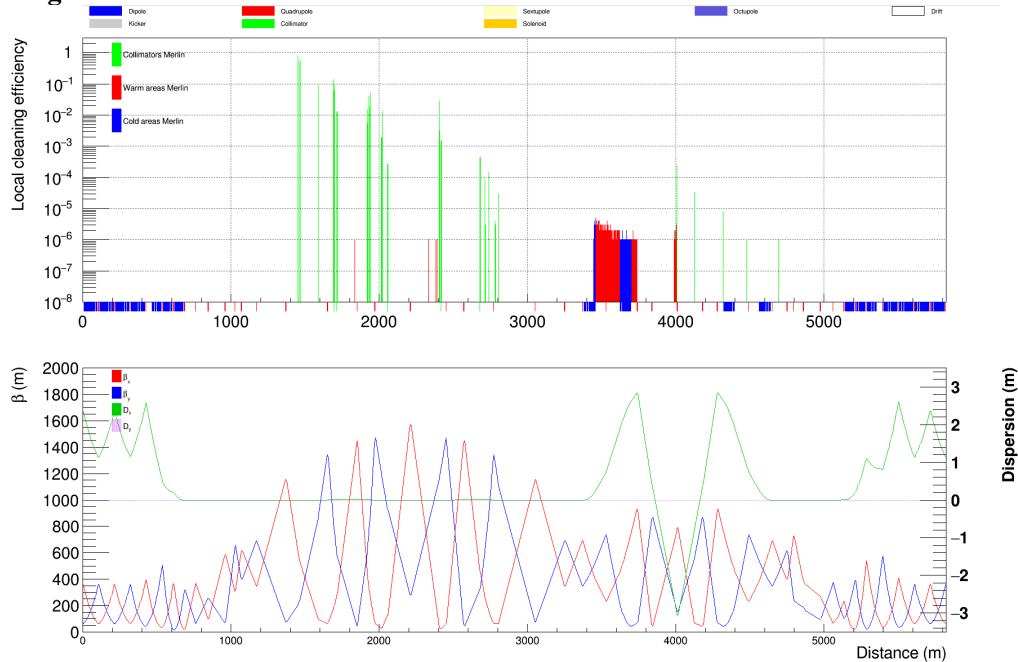


Figure 5: Loss distribution in the collimation section and lattice functions, protected superconductor magnets are used in the section

2.17.5 High-field superconducting magnets

With a circumference of 100 km, a modest dipole field of 12 T is required to reach the design goal for the 75-TeV center of mass energy, which is not far from the state-of-art magnet technology using Nb_3Sn superconductors [13]. However, Iron-based HTS technology has a bright expectation to be available and much cheaper in 10-15 years, and to generate a field higher than 20 T in far future. Thus Fe-HTS magnet technology is chosen for SPPC [14]. The nominal aperture for the arc magnets is 50 mm. A field

uniformity of 10^{-4} should be attained up to $2/3$ of the aperture radius. The magnets are designed to have two beam apertures of opposite magnetic polarity within the same yoke (2-in-1) to save space and cost. The currently assumed distance between the two apertures in the main dipoles is about 300 mm, but this could be changed based on detailed design optimization to control cross-talk effect between the two apertures, and with consideration of overall magnet size. The current magnet design is focused on a common-coil type which is still under developing. Figure 6 shows such a design.

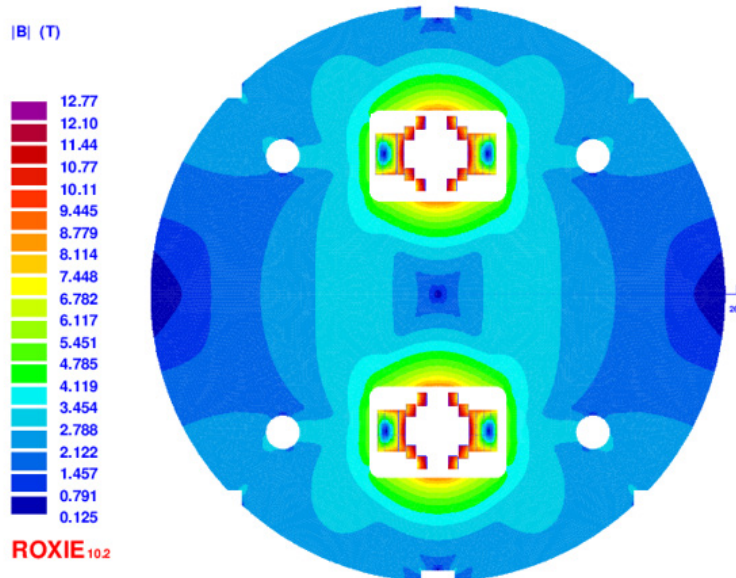


Figure 6: Dipole magnet in common coil type is under design

2.17.6 Vacuum and beam screen

SPPC has three vacuum systems: Insulation vacuum for the cryogenic system; beam vacuum for the low-temperature sections; and beam vacuum for the chambers in the room-temperature sections. The critical part is the cryogenic vacuum. The main problem comes from synchrotron radiation. It produces huge heat load to the cryogenic system, and critical electron cloud which risks important beam instabilities. Following the successful application at LHC, a beam screen between the beam and cold bore working at a higher temperature is being studied. However, due to much higher synchrotron radiation power, the beam screen at SPPC becomes much more challenging. A beam screen scheme is shown at Figure 7, which is somewhat similar to the one proposed by FCC [15]. A special layer with a slit which allows entering of synchrotron rays but avoid exiting of secondary electrons is considered to solve the electron cloud problem. The operating temperature of the screen must be high enough to avoid excessive wall power needed to remove the heat, but not too high to avoid excessive resistivity, e.g. 50-70K. High-temperature superconducting material (e.g. YBCO) coating on its inside surfaces to reduce the impedance is also under investigation.

The temperature for the cold bore is also under investigation, 1.9 K or about 4 K, which is mainly related to the hydrogen pumping issue.

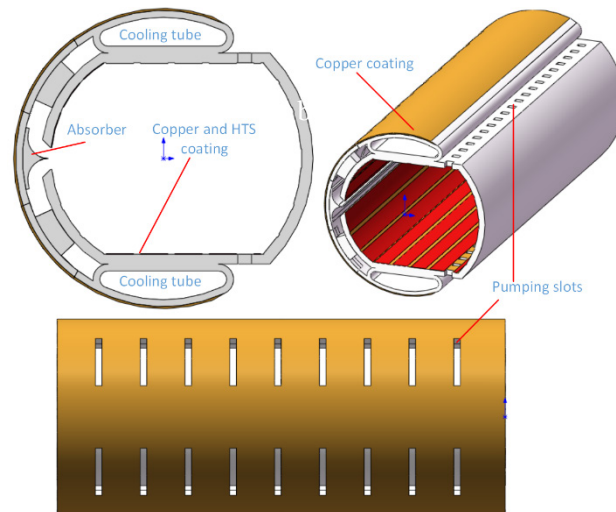


Figure 7: Schematic for the beam screens with inner HTS coating

2.17.7 Injector chain

The injector chain by itself is an extremely large accelerator complex. To reach the beam energy of 2.1 TeV required for the injection into the SPPC, we require a four-stage acceleration system, with energy gains per stage between 8 and 18. It not only accelerates the beam to the energy for injection into the SPPC, but also prepares the beam with the required properties such as the bunch current, bunch structure, and emittance, as well as the beam fill period. Some key parameters are given in Table 3. The preliminary physics design work for all the four stages is also under going.

Table 3: Main parameters for the injector chain at SPPC

	<i>Energy</i>	<i>Average current</i>	<i>Length/Circum.</i>	<i>Repetition Rate</i>	<i>Max. beam power or energy</i>	<i>Dipole field</i>	<i>Duty factor for next stage</i>
	GeV	mA	km	Hz	MW/MJ	T	%
p-Linac	1.2	1.4	~0.3	50	1.6/	-	50
p-RCS	10	0.34	0.97	25	3.4/	1.0	6
MSS	180	0.02	3.5	0.5	3.7/	1.7	13.3
SS	2100	-	7.2	1/30	/34	8.3	1.3

2.17.8 Summary

The report presents the recent design update of the SPPC accelerators. In particular, the tunnel circumference is increased from the previous 50-60 km in the Pre-CDR to 100 km, and Iron-based HTS magnets of 12 T are used to reach a center-of-mass energy of 75 TeV. Future energy upgrade with higher-field magnets is reserved.

2.17.9 Acknowledgements

The work is partially supported by National Natural Science Foundation of China (Projects 11575214, 11675193), and the CAS hundred talents program (Qingjin Xu).

2.17.10 References:

1. Jingyu Tang et al., Concept for a Future Super Proton-Proton Collider, arXiv: 1507.03224
2. The CEPC-SPPC Study Group, CEPC-SPPC Preliminary Conceptual Design Report, Volume II – Accelerator, IHEP-CEPC-DR-2015-01, IHEP-AC-2015-01, 2015
3. I. Hinchliffe, A. Kotwal, M.L. Mangano, C. Quigg and L.T. Wang, “Luminosity goals for a 100-TeV pp collider,” arXiv:1504.06108v1, (2015).
4. LHC Design Report, The LHC Main Ring, Vol.1, CERN-2004-003.
5. Future Circular Collider Study Hadron Collider Parameters, FCC-ACC-SPC-0001, 2014.
6. M. Benedikt and F. Zimmermann, Future Circular Collider Study Status and Plans, FCC Week 2017, Berlin, Germany, May 29-June 2, 2017
7. F. Zimmermann, HL-LHC: PARAMETER SPACE, CONSTRAINTS & POSSIBLE OPTIONS, EuCARD-CON-2011-002; F. Zimmermann, O. Brüning, Parameter Space for the LHC Luminosity Upgrade, Proc. of IPAC 2012, New Orleans, (2012) p.127.
8. M. Benedikt, D. Schulte and F. Zimmermann, Optimizing integrated luminosity of future colliders, PRST-AB 18, 101002 (2015)
9. Ye Zou, Jianquan Yang, Jingyu Tang, A novel collimation method for large hadron colliders, arXiv: 1611.05492
10. G. Apollinari, et al., High-Luminosity Large Hadron Collider (HL-LHC) preliminary design report: Chapter 5. CERN-2015-005, 2015.
11. K. Goulianos, Diffractive interactions of hadrons at high energies, Physics Reports, 101(3):169-219, 1983.
12. R. Bruce et al., Cleaning performance with 11T dipoles and local dispersion suppressor collimation at the LHC, Proceedings of IPAC14, Dresden, Germany (2014), p. 170
13. D.R. Dietderich, A. Godeke, Cryogenics 48, (2008) p. 331–340.
14. Q.J. Xu, Status of high field magnet R&D for CEPC-SPPC, FCC Week 2017, Berlin, Germany, May 29-June 2, 2017
15. C. Garion, “Arc vacuum considerations and beam screen design,” presentation at FCC Week 2015, Washington DC, (2015).

2.18 Development of Fe-based HTS Wire and Conceptual Design Study of the Magnet for Future High Energy Accelerators

Chao Yao and Yanwei Ma

Mail to: ywma@mail.iee.ac.cn

Key Laboratory of Applied Superconductivity, Institute of Electrical Engineering,
Chinese Academy of Sciences, Beijing 100190, China

Ershuai Kong, Chengtao Wang and Qingjin Xu

Mail to: xuqj@ihep.ac.cn

Accelerator Division, Institute of High Energy Physics, Chinese Academy of
Sciences, Beijing 100049, China

2.18.1 Introduction

Iron-based superconductors (IBSs) discovered in 2008 formed the second high- T_c superconductor family after cuprate superconductors, and have aroused extensive research for their physical nature and application potential [1,2]. According to different chemical compositions and crystal structures, IBSs can be categorized into several types, such as ‘1111’ type (e.g. $\text{LaFeAsO}_{1-x}\text{F}_x$ and $\text{SmFeAsO}_{1-x}\text{F}_x$), ‘122’ type (e.g. $\text{Ba}_{1-x}\text{K}_x\text{Fe}_2\text{As}_2$ and $\text{Sr}_{1-x}\text{K}_x\text{Fe}_2\text{As}_2$), ‘111’ type (e.g. LiFeAs) and ‘11’ type (e.g. FeSe , $\text{FeSe}_{1-x}\text{Te}_x$). IBSs have very high upper critical fields (H_{c2}) above 100 T, small electromagnetic anisotropy (1.5-2 for ‘122’ IBS), relatively high superconducting transition temperatures (T_c) (up to 38 K for ‘122’ IBS and 56 K for ‘1111’ IBS), and large critical current density (J_c) over 10^6 A/cm² in thin films. Nowadays, high-field magnets are one of the most important aspects for the applications of high- T_c superconductors, so H_{c2} is a key property we must concern about. As shown in Figure 1, the conventional low- T_c superconductors (NbTi and Nb₃Sn) restrict the magnets with field below 25 T at liquid helium temperature. For ‘122’ and ‘1111’ IBS, the H_{c2} is much higher than that of low- T_c superconductors, and is still above 40 T at 20 K. In addition to its low anisotropy, IBS is quite attractive for the construction of high-field magnets, which are desired for the next generation of NMR, accelerator, and fusion magnets, and can work at liquid helium temperature and also in moderate temperature range around 20 K, which can be obtained by cryocoolers.

Studies on the grain boundary nature in ‘122’ IBS epitaxial film suggested that intergrain currents across mismatched grains in iron-based superconductors are deteriorated to a lesser extent than in YBCO superconductors [4]. Therefore, the low-cost powder-in-tube (PIT) method, which has been utilized in commercial Nb₃Sn, Bi-2223 and MgB₂ wires, is promising for IBS wires manufacture. On the other hand, in contrast to BiSrCaCuO wires, whose sheath material was limited to silver or some silver rich alloys due to the oxygen permeability for sheath material, the IBS wires have more choices for sheath materials. Though silver is the most widely used sheath material for 1111- and 122-type IBS wires at present, since it is chemically stable and not easy to react with IBS phase during heat treatment of IBS wires, using other cheap and stiff metal material as the outer sheath for IBS/Ag composite conductors can be a practical proposal to reduce the ratio of silver cost, provide sheath chemical stability, and enhance mechanical properties at the same time. Therefore, the low-cost, high-strength and high J_c performance IBS wire and tape conductors are very promising based on PIT method.

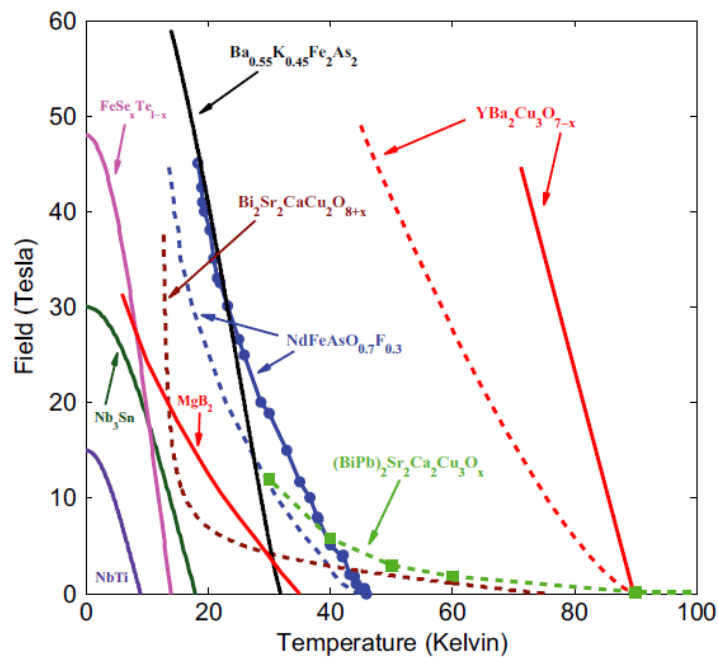


Figure 1: Comparative T-H phase diagram for different superconducting materials. Here the solid and dashed lines show the upper critical field $H_{c2}(T)$ and the irreversibility fields $H^*(T)$ for $H//c$, respectively [3].

A conceptual design study of 12-T 2-in-1 dipole magnets is ongoing with the Iron-based superconducting (IBS) technology, to fulfill the requirements and need of a proposed large-scale superconducting accelerator: Super Proton Proton Collider (SPPC), which aims to discover the new physics beyond the standard model with a 100-km circumference tunnel and 70 TeV center-of-mass energy. The design study is carried out with an expected J_e level of IBS in 10 years, i.e., about 10 times higher than the present level. Besides the significant improvement of J_e , we are also expecting that the IBS superconductor would have much better mechanical performance comparing with present high field conductors like Nb_3Sn , ReBCO and Bi-2212, and the much lower cost than them.

The aperture diameter of the magnets is 45 mm. The main field is 12 T in the two apertures per magnet with 10^{-4} field uniformity. The common-coil configuration is adopted for the coil layout because of its simple structure and easy to fabricate. Two types of coil ends are considered and compared for the field quality and structure optimization: soft-way bending and hard-way bending. For the hard-way bending the coil is wound with flared ends and in such way the needed superconductors is minimized. The main parameters, coil layouts and the field quality optimization of this design study will be presented.

2.18.2 Development of Advanced IBS HTS Wire

IBS wire and tape conductors with high transport current density are essential for practical applications. In 2008, the first iron-based superconducting wires are developed in Institute of Electrical Engineering, Chinese Academy of Sciences (IEECAS) by *in-situ* powder-in-tube (PIT) method, which starts by packing the powders of unreacted precursor materials into a metallic tube in a high purity Ar atmosphere. However, the

defects in the material such as micro cracks, low density, phase inhomogeneity, and impurity phase still restricted the transport current in wires. By using *ex-situ* PIT method, in which reacted and well ground superconducting materials are packed into metallic tubes, the mass density and phase homogeneity of the wire after the final heat treatment are significantly improved in ‘1111’ and ‘122’ IBS wires [5].

In the recent years, mechanical deformation processes such as flat rolling, hot isostatic pressing and uniaxial pressing have significantly improved the mass density of superconducting phase, resulting in a dramatic increase for the transport J_c of 122-type IBS wires and tapes. In 2012, the Florida State University achieved a transport J_c of 8.5×10^3 A/cm² at 4.2 K and 10 T in Cu/Ag clad Ba_{1-x}K_xFe₂As₂ (Ba-122) wires, which were processed using a hot isostatic press technique (HIP) and low-temperature sintering to obtain high mass density and fine grains [6]. With a further optimized HIP process, the transport J_c for Ba-122 round wires were recently increased to 2×10^4 A/cm² at 4.2 K and 10 T by the University of Tokyo [7]. Using combination process of cold flat rolling and uniaxial pressing, which can increase the density of superconducting cores and change in the microcrack structure, high transport J_c of 8.6×10^4 A/cm² at 4.2 K and 10 T were obtained in silver sheathed Ba-122 tapes in National Institute for Materials Science (NIMS) [8]. In 2014, researchers in IEECAS processed the as-rolled Sr_{1-x}K_xFe₂As₂ (Sr-122) tapes by a hot press technique, which significantly increased the mass density of the superconducting core, and eliminated the residual micro-cracks induced during the deformation process, thus improving the transport J_c to practical level of 10^5 A/cm² (4.2 K, 10 T) for the first time [9].

In addition to the material defects mentioned above, the high-angle grain boundary in iron pnictides also deteriorated the transport currents, so the misoriented grains should be improved to further enhance the J_c performance for IBS wires and tapes. In 2011, IEECAS first reported c-axis textured Sr-122 tapes with Fe sheath by flat rolling. Recently, by using optimized hot press process to achieved a higher degree of grain texture, the transport J_c was further increase to 1.5×10^5 A/cm² ($I_c = 437$ A) at 4.2 K and 10 T in Ba-122 tapes, as shown in Figure 2. The transport J_c measured at 4.2 K under high magnetic fields of 27 T is still on the level of 5.5×10^4 A/cm². Moreover, at 20 K and 5 T the transport J_c is also as high as 5.4×10^4 A/cm², showing a great application potential in moderate temperature range which can be reached by liquid hydrogen or cryogenic cooling [10].

The mechanical properties of wires and tapes is another important issue, since conductor strength and its tolerance to the mechanical load are quite crucial for practical application, especially for operations under high magnetic field. By using a U-shaped bending spring (U-spring) method, the compressive strain dependence of transport J_c for silver sheathed ‘122’ IBS tapes was investigated. Reversible J_c performance under lager compressive strain of -0.6% in high magnetic field of 10 T was observed. This result demonstrates the great potential of ‘122’ IBS for high-field application, in which conductors are designed to work under compression strain for safety [11].

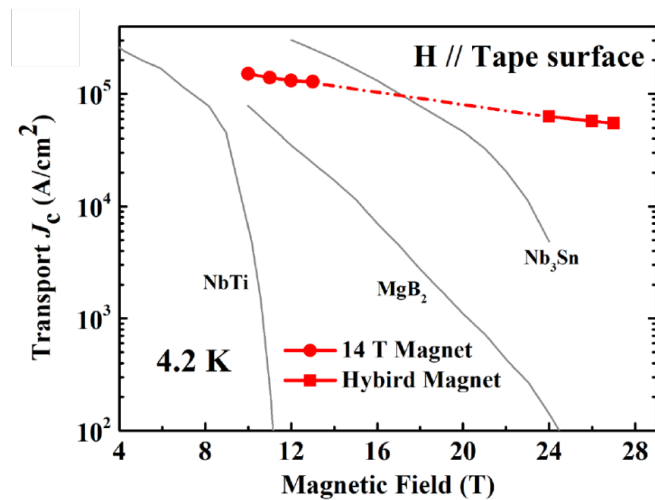


Figure 2: The field dependence of transport J_c values at 4.2 K for hot pressed Sr-122 tapes, compared with commercial NbTi, Nb₃Sn and MgB₂ wires.

For practical applications of iron-based superconductors, fabricating wires and tapes with multifilaments in metal matrix to protect against flux jumps and thermal quenching is an important step. Based on the techniques used in the single-core IBS wires, Ag/Fe clad 7-filament Sr-122 wires and tapes were successfully fabricated in IEECAS in 2013 [12]. After that, Ag/Fe sheathed 114-filament Sr-122/Fe wires and tapes were also produced, as shown in Figure 3. Processed with hot press, a high transport J_c of 3.6×10^4 A/cm² at 4.2 K and 10 T can be achieved in 7-filament Sr-122/Monel tapes, which exhibits an improved mechanical strength and very weak field dependence for transport J_c . In addition, using copper instead of expensive silver as sheath material was attempted for Sr-122 tapes. By shortening the time of heat treatment to control the reaction between sheath material and IBS core, a high transport J_c of 3.5×10^4 A/cm² and 1.6×10^4 A/cm² was achieved at 4.2 K, 10 T and 26 T in Cu-sheathed Sr-122 tapes, respectively [13]. This result is very significant for fabricating high-performance and low-cost IBS wires, since copper is cost effective, has good mechanical properties, and can provides reliable thermal stabilization in practical applications.

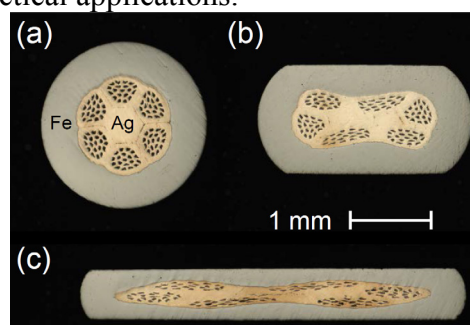


Figure 3: Optical images of the transverse cross section for 114-filament Sr-122/Ag/Fe (a) wires of 2.0mm in diameter and tapes of (b) 1.0mm and (c) 0.6mm in thickness.

Though high J_c properties can be obtained in short ‘122’ IBS samples, practical applications need wire and tape conductors with sufficient length. In 2014, the IEECAS group fabricated the first 11 m long Sr-122/Ag tape by a scalable rolling process. The J_c

of this tape exhibits a uniform distribution, fluctuating between 2.12 and 1.68×10^4 A/cm² (4.2 K, 10 T), with an average J_c value of 1.84×10^4 A/cm² [14]. After carefully optimizing the long-length wire fabricating process to achieve a higher-level uniformity of deformation, the world's first 100 meter-class IBS tapes was produced by the same group [15]. As presented in Figure 4, this 115 m long 7-filament Sr-122/Ag tape shows a uniform J_c distribution throughout the tape with a minimum J_c of 1.2×10^4 A/cm² (4.2 K, 10 T), demonstrating great potential in large-scale manufacture and a promising future of iron-based superconductors for practical applications. In the future, by further optimizing the wire architecture, cold work process and heat treatment parameters, it can be expected that the high J_c performance in short IBS samples to be realized in high-strength long-length multifilamentary IBS wires, which are desirable for high-field applications.

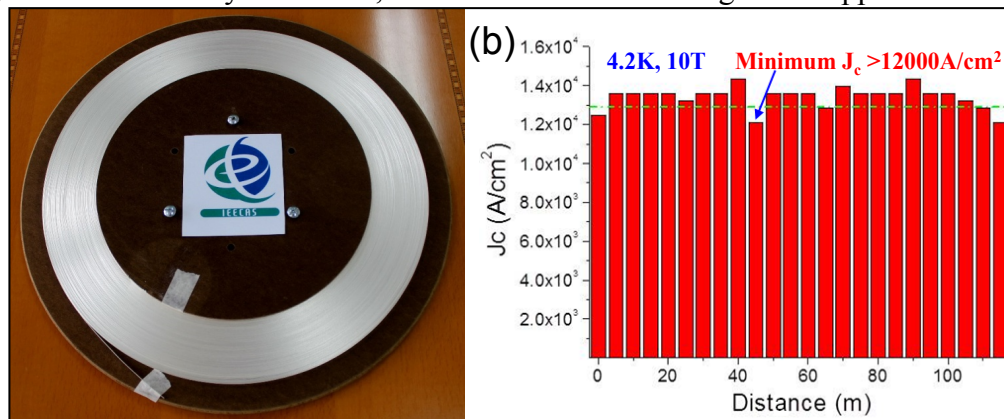


Figure 4: (a) World's first 100 meter-class iron-based superconducting wire developed in Institute of Electrical Engineering, Chinese Academy of Sciences (IEECAS), and (b) the distribution of critical current density J_c throughout the wire.

2.18.3 Conceptual Design Study of the Dipole Magnet for Future High Energy Accelerators

SPPC needs thousands of 12~24 T (upgrading phase) dipole and quadrupole magnets to bend and focus proton beams [16, 17]. The nominal aperture in these magnets is 40~50 mm. A field uniformity of 10^{-4} should be attained in up to 2/3 of the aperture radius. The magnets will have two beam apertures of opposite magnetic polarity within the same yoke to save space and cost. The currently assumed distance between the two apertures in the main dipoles is 200~300 mm, but this could be changed based on the detailed design optimization to control cross-talk between the two apertures, and with considerations on the overall magnet size. The outer diameter of the main dipole and quadrupole magnets should not be larger than 900 mm, so that they can be placed inside cryostats having an outer diameter of 1500 mm. The total magnetic length of the main dipole magnets is about 65.4 km out of the total circumference of 100 km. If the length of each dipole magnet is about 15 m, then about 4360 dipole magnets are required.

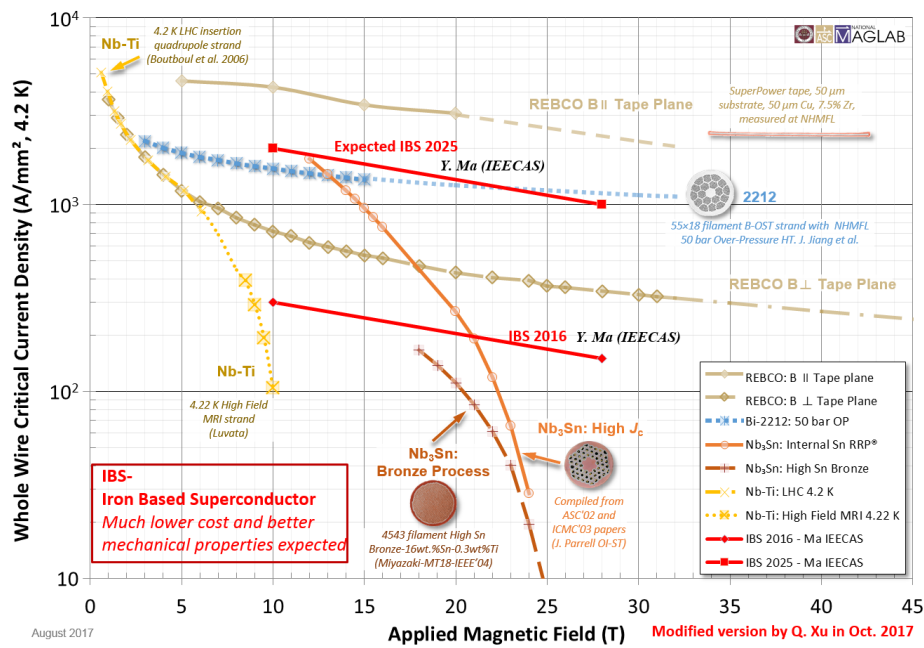


Figure 5: J_c of IBS in 10 years comparing with other practical materials

All the superconducting magnets used in present accelerators are based on NbTi technology. These magnets work at significantly lower field than the required 12~24 T, e.g., 3.5 T at 4.2 K at RHIC and 8.3 T at 1.9 K at LHC [18, 19]. There are a total of 4 coil configurations which can provide dipole magnetic field for accelerators: cos-theta type [20], common coil type [21], block type [22] and canted cos-theta type [23]. Among these the common coil type is the simplest structure. The coils have much larger bending radius and there is much less strain level in the coils. Since both Nb₃Sn and HTS superconducting materials are strain-sensitive, which means the critical current density J_c of superconductors will be largely reduced by the high strain level, the common coil configuration has been chosen as the first option for the design study of the SPPC dipole magnets. A conceptual design study of the 12-T 2-in-1 dipole magnets is ongoing with the Iron-based superconducting (IBS) technology. The study is carried out with an expected J_c level of IBS in 10 years, i.e., about 10 times higher than the present level, as shown in Figure 5 [24]. Besides the significant improvement of J_c , we are also expecting that the IBS superconductor would have much better mechanical performance comparing with present high field conductors like Nb₃Sn and Bi-2212, and the much lower cost than them.

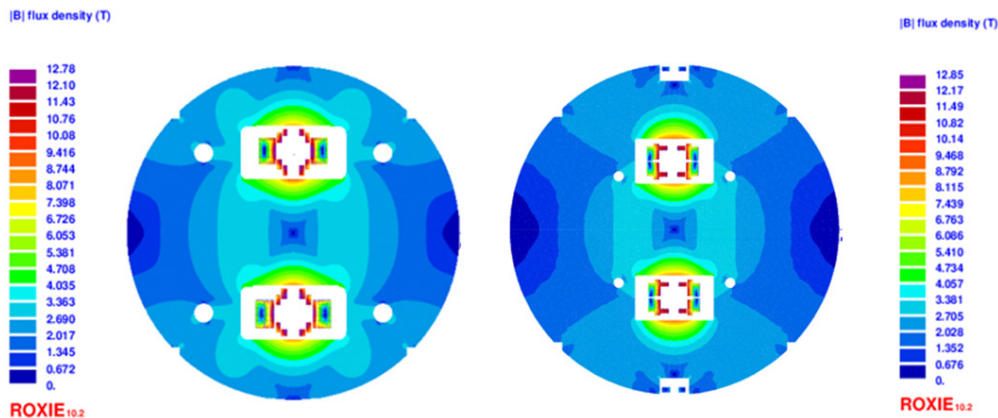


Figure 6: Field distribution of the design 1 (left) and design 2 (right).

The aperture diameter of the magnets is 45 mm. The main field is 12 T in the two apertures per magnet with 10^{-4} field uniformity. Two types of coil ends are considered and compared for the field quality and structure optimization: soft-way bending and hard-way bending. For the hard-way bending the coil is wound with flared ends and in such way the needed amount of superconductors is minimized. Study of two coil layouts have been completed, as shown in Figure 6. The main parameters of the magnets are listed in Table 1. The minimum bending radius of the cables is around 80 mm. The outer diameter of the magnet is temporarily set to 620 mm and the inter-aperture spacing is 236-258 mm. For design 1, we put 4 coil blocks with 8 turns per block in the inner two layers, 4 coil blocks with 21 turns per block in the middle and outside. With a current of 9400 A, we can get 12 T main field in the aperture and 12.78 T peak field in coils. For design 2, there are 4 coil blocks with 4 turns per block in the inner two layers, 2 coil blocks with 33(16+17 for gap) turns per block in the middle and 2 coil blocks with 28(14+14) turns per block in the outside. We can get a 12 T main field and 12.85 peak field with a current of 8100 A. Field distributions of the two designs are shown in Fig. 6. The operating margin is 21% at 4.2 K for the two designs.

As shown in Fig 7, for design 1, we choose to bend the upper two blocks in hard-way to save conductors and make space for beam pipes. Hard-way bending parts are on an ellipsoid with 5 degree of inclination angle to decrease the influence to field quality. For design 2, we bend all the coil blocks in soft-way. By optimizing lengths of coil straight sections one can achieve a 10^{-4} integrated field quality along axis. Fig. 8 shows field harmonics variation along axis for the design 2.

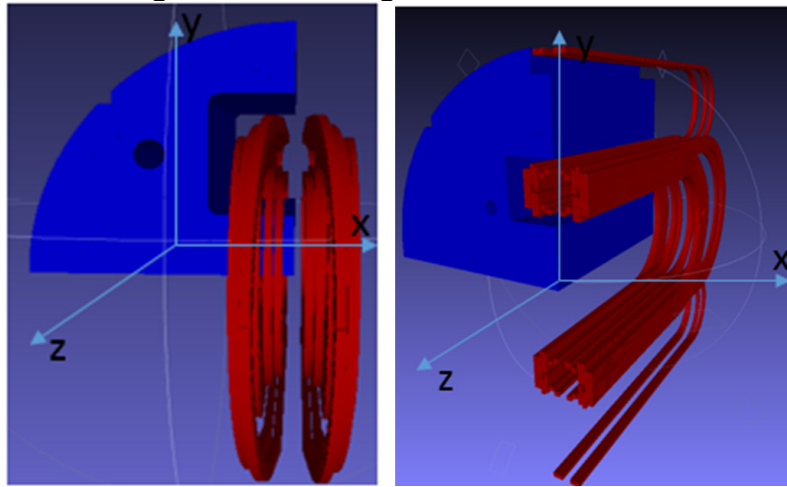


Figure 7. Left: the layout of hard-way coil ends. Right: the layout of soft-way coil ends

Table 1. Main parameters of the 12-T iron-based dipole magnet

Parameter	Unit	Value
Number of apertures	-	2
Aperture diameter	mm	45
Inter-aperture spacing	mm	236/258
Operating current	A	9400/8100
Operating temperature	K	4.2
Load line ratio	/	79%
Main field in the aperture	T	12
Coil peak field	T	12.78/12.85
Number of iron-based coils	-	6
Outer diameter of the magnet	mm	620
Minimum bending radius	mm	85/77

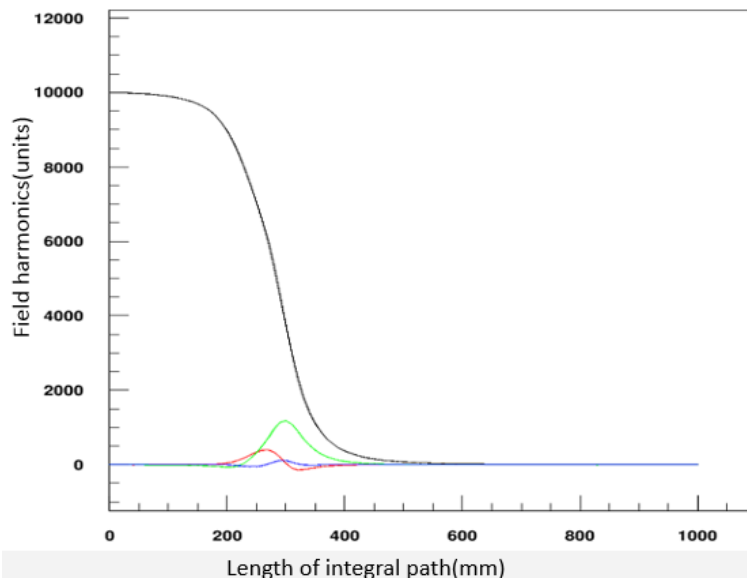


Figure 8. Field harmonics variation along axis for the design 2# (Black line stands for b_1 , green line for b_3 , red line for b_5 , and blue line for a_2).

2.18.4 References

1. Y. Kamihara, T. Watanabe, M. Hirano, and H. Hosono, *J. Am. Chem. Soc.* **130**, 3296 (2008).
2. H. Hosono, K. Tanabe, E. Takayama-Muromachi, H. Kageyama, S. Yamanaka, H. Kumakura, M. Nohara, H. Hiramatsu, and S. Fujitsu, *Sci. Technol. Adv. Mater.* **16**, 033503 (2015).
3. A. Gurevich, *Rep. Prog. Phys.* **74**, 124501 (2011).
4. T. Katase, Y. Ishimaru, A. Tsukamoto, H. Hiramatsu, T. Kamiya, K. Tanabe, and H. Hosono, *Nat. Commun.* **2**, 409 (2011).
5. Y. W. Ma, *Supercond. Sci. Technol.* **25**, 113001 (2012).
6. J. D. Weiss, C. Tarantini, J. Jiang, F. Kametani, A. A. Polyanskii, D. C. Larbalestier, and E.E. Hellstrom, *Nat. Mater.* **11** 682 (2012).
7. S. Pyon, T. Suwa, A. Park et al. *Supercond. Sci. Technol.* **29**, 115002 (2016).
8. Z. Gao, K. Togano, A. Matsumoto, and H. Kumakura, *Sci. Rep.* **4** 4065 (2014).
9. X. P. Zhang, C. Yao, H. Lin, Y. Cai, Z. Chen, J. Q. Li, C. H. Dong, Q. J. Zhang, D. L. Wang, Y. W. Ma, H. Oguro, S. Awaji, and K. Watanabe, *Appl. Phys. Lett.* **104**, 202601 (2014).
10. H. Huang, C. Yao, C. H. Dong, X. P. Zhang, D. L. Wang, Z. Cheng, J. Q. Li, S. Awaji, and Y.W. Ma, arXiv:1705.09788 (2017)
11. F. Liu, C. Yao, H. Liu et al. *Supercond. Sci. Technol.* **30**, 07LT01 (2017).
12. C. Yao, Y. W. Ma, X. P. Zhang, D. L. Wang, C. L. Wang, H. Lin, and Q. J. Zhang, *Appl. Phys. Lett.* **102**, 082602 (2013).
13. K. L. Lin, C. Yao, X. P. Zhang, et al. *Supercond. Sci. Technol.* **29**, 095006 (2016).
14. Y. W. Ma, *Physica C* **516**, 17 (2015).
15. X. P. Zhang, H.Oguro, C. Yao, C. H. Dong, Z. T. Xu, D. L. Wang, S. Awaji, K. Watanabe, and Y. W. Ma, *IEEE Trans. Appl. Supercond.* **27**, 7300705 (2017).
16. E. Kong et. al., Conceptual Design Study of Iron-based Superconducting Dipole Magnets for SPPC, to be published.

17. Q. Xu et. al., 20-T Dipole Magnet with Common Coil Configuration: Main Characteristics and Challenges, IEEE Trans. Appl. Supercond., VOL. 26, NO. 4, 2016, 4000404.
18. A. Greene et al., “The Magnet System of the Relativistic Heavy Ion Collider (RHIC)”, IEEE Trans. Mag., VOL. 32, NO. 4, JULY 1996, pp 2041-2046.
19. LHC design report: The LHC Main Ring, Chapter 7: Main Magnets in the Arcs, [Online]. Available: <http://ab-div.web.cern.ch/ab-div/Publications/LHC-DesignReport.html>.
20. Alvin Tollestrup, Ezio Todesco, “The Development of Superconducting Magnets for Use in Particle Accelerators: From the Tevatron to the LHC,” Reviews of Accelerator Science and Technology 04/2012; 01(01). DOI: 10.1142/S1793626808000101.
21. R. Gupta, “A Common Coil Design for High Field 2-in-1 Accelerator Magnets,” Proceedings of the 1997 Particle Accelerator Conference, Vol. 3, May 1997, pp. 3344-3346.
22. Sabbi G et al., “Design of HD2: a 15 Tesla Nb₃Sn dipole with a 35 mm bore,” IEEE Trans. on Appl. Supercond. 15, 2005, pp 1128-1131.
23. S. Caspi et al., “Canted–Cosine–Theta Magnet (CCT)—A Concept for High Field Accelerator Magnets”, IEEE Trans. on Appl. Supercond., VOL. 24, NO. 3, JUNE 2014 4001804
24. Peter Lee, Engineering Critical Current Density vs. Applied Field, <https://nationalmaglab.org/magnet-development/applied-superconductivity-center/plots>

2.19 HE-LHC Overview, Parameters and Challenges

Frank Zimmermann
CERN, Route de Meyrin, 1211 Geneva 23, Switzerland

Mail to: frank.zimmermann@cern.ch

2.19.1 Introduction

In the frame of the Future Circular Collider (FCC) study [1], the FCC collaboration is designing a 27 TeV hadron collider installed in the existing LHC tunnel, called the High Energy LHC (HE-LHC). The HE-LHC shall be realized by replacing the LHC’s 8.33 Tesla Nb-Ti dipole magnets with 16 Tesla Nb₃Sn magnets being developed for the 100 TeV hadron collider FCC-hh [1,1].

We note that this new version of the HE-LHC differs from the HE-LHC studied in the year 2010 [3,4], which featured a higher centre-of-mass energy of 33 TeV (based on 20 Tesla hybrid magnets also containing high-temperature superconductor), along with a reduced beam current, and lower luminosity.

2.19.2 Design Targets and Constraints

The HE-LHC physics goals call for a doubling the LHC collision energy, which can be achieved with the help of FCC-hh magnet technology, i.e. by replacing the existing

LHC dipole magnets with a nominal field of 8.33 T by FCC-type 16 Tesla dipole magnets. The target value for the integrated luminosity is four times the HL-LHC goal, since the cross sections for most process decrease roughly in proportion to the inverse energy square, $\sigma \propto 1/E^2$). Achieving the target energy of 27 TeV with 16 Tesla magnets requires an arc optics with a high dipole-filling factor [5].

In addition to the FCC-hh magnets, also the cryogenic beam vacuum system of the HE-LHC is adopted from the FCC-hh design. The FCC-hh beamscreen [6] can more economically intercept and remove the heat from the much increased synchrotron radiation power. The FCC-hh and HE-LHC beam screens operate at an elevated temperature of 50 K instead of the LHC's 5-20 K, which improves the Carnot efficiency. The new beamscreen also features greatly enlarged cooling capillaries for increased helium mass flow, shielded pumping slots for reduced impedance, and a kind of “folded antechamber” for minimizing the number of photoelectrons generated in the beam pipe proper.

The HL-LHC R&D effort [7] provides other novel elements, e.g. items such as crab cavities, electron lenses, less resistive collimators, long-range beam-beam compensation, and new optics solutions, from which also the HE-LHC may profit.

Last not least, after the realization of the LHC Injector Upgrade (LIU) [35], by 2020, an extremely bright proton beam will be available for injection into the HE-LHC, with a bunch population of 2.2×10^{11} , and a normalized transverse emittance of $2.5 \mu\text{m}$. A bunch spacing of 25 ns, as in the LHC, is the present HE-LHC design baseline. For this spacing the peak pile up in the experiments is close to 1000 events per bunch crossing, i.e. much higher than the HL-LHC design value of 140 events per crossing. Halving the bunch spacing from 25 ns to 12.5 ns would also halve the pile up. It may be difficult to produce beams with even smaller bunch spacing, in the present LHC injector complex, and the experiments may not necessarily benefit from so short a spacing.

2.19.3 Baseline Parameters

The HE-LHC baseline design parameters are summarized in Table 1, which also presents a comparison with the corresponding values for LHC, HL-LHC and FCC-hh.

Table 1: **Key parameters of HE-LHC compared with FCC-hh, HL-LHC and LHC.**

parameter	FCC-hh		HE-LHC	(HL) LHC
collision energy cms [TeV]	100		27	14
dipole field [T]	16		16	8.3
circumference [km]	100		27	27
beam current [A]	0.5		1.12	(1.12) 0.58
bunch population [10^{11}]	1 (0.5)		2.2	(2.2) 1.15
bunch spacing [ns]	25 (12.5)		25 (12.5)	25
norm. emittance $\gamma\epsilon_{x,y}$ [μm]	2.2 (2.2)		2.5 (1.25)	(2.5) 3.75
IP $\beta^*_{x,y}$ [m]	1.1	0.3	0.25	(0.15) 0.55

luminosity/IP [$10^{34}\text{cm}^{-2}\text{s}^{-1}$]	5	30	25	(5) 1
peak #events / bunch Xing	170	1000 (500)	800 (400)	(135) 27
stored energy / beam [GJ]		8.4	1.4	(0.7) 0.36
SR power / beam [kW]		2400	100	(7.3) 3.6
transv. emit. damping time [h]		1.1	3.6	25.8
initial proton burn off time [h]	17.0	3.4	3.0	(15) 40

2.19.4 Challenges

Tunnel integration in the existing LEP/LHC tunnel with an inner diameter of 3.8 m only limits the maximum outer size of the magnet cryostat, calling for a compact design of the 16 Tesla magnets [9], with implications for field quality at injection and residual stray field outside the cryostat.

The 16 Tesla magnets of the FCC-hh have an inner cold bore of 50 cm, about 10% smaller than the LHC's (56 mm). This smaller magnet bore along with the more complex beamscreen structure significantly reduces the physical aperture available for the beam, e.g. in the horizontal plane from about ± 22 mm to ± 13.8 mm. This has consequences for the physical aperture in the arc, collimation efficiency, the impedance [10], and, thereby, indirectly for the HE-LHC injection energy. Figure 1 compares the beamscreen dimensions and the 6- σ beam size inside a focusing arc quadrupole for the HL-LHC at 450 GeV, the FCC-hh at 3.3 TeV, and the HE-LHC at three different injection energies. The present design baseline assumes injection at 1.3 TeV beam energy, which requires a new (superconducting) SPS, the scSPS, and new transfer lines from the SPS tunnel to the HE-LHC. Choosing an injection energy higher than the LHC's (450 GeV) also reduces the nonlinear field errors at injection for the 16 Tesla magnets.

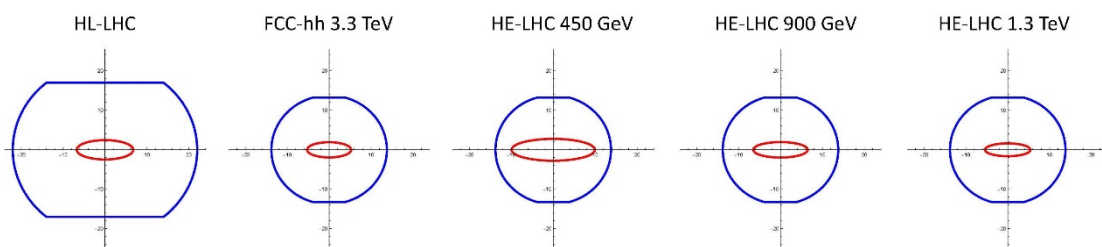


Figure 1: 6σ beam envelope inside the beamscreen of HL-LHC, FCC-hh and HE-LHC at different choices of injection energy.

All insertions must fit into the existing straight sections and no length scaling with energy can be applied. This poses challenges, in particular, for the low-beta insertions, for the cleaning insertions, and for the extraction insertion.

The low-beta optics for the experimental insertions must accommodate a shielded quadrupole triplet even longer than the HL-LHC's, which can support a β^* of 25 cm, and survive an integrated luminosity above $10/\text{ab}$. The feasibility of such a system has been demonstrated [11,12].

When collimating at a similar number of rms beam stay sizes the physical gaps of the collimators decrease, leading to higher impedance, to a reduced cleaning efficiency, and to a greater sensitivity to optics errors or misalignments [13].

Extracting a beam of twice the energy, requires, in principle, doubling the lengths of extraction kickers, septa and dilution kickers. However, an increased injection energy reduces the physical size of the injected beam and permits reducing the gaps of the extraction elements [14].

2.19.5 References

1. M. Benedikt and F. Zimmermann, “Towards future circular colliders,” *Journal of the Korean Physical Society* 69, 893–902 (2016).
2. D. Schulte, “FCC-hh Design Highlights,” this Newsletter (2017).
3. R. Assmann et al., “First Thoughts on a Higher-Energy LHC,” CERN-ATS-2010-177 (2010).
4. E. Todesco and F. Zimmermann (eds.), *Proceedings of EuCARD-AccNet-EuroLumi Workshop: The High-Energy Large Hadron Collider (HE-LHC10)*, Villa Bigli, Malta, Republic of Malta, 14-16 October 2010, arXiv:1111.7188; EUCARD-CON-2011-001; CERN-2011-003 (2011).
5. Y. Cai, Y. Nosochkov et al., “HE-LHC Optics Development,” this Newsletter (2017).
6. R. Kersevan, “Research program on the cryogenic beam vacuum of the FCC-hh,” at *Int. Conf. on High Energy Physics, Chicago*, 3-10 August 2016 (2016).
7. G. Apollinari et al. (eds.), “High-Luminosity Large Hadron Collider (HL-LHC): Preliminary Design Report,” CERN-2015-005 (2015).
8. H. Damerou et al. (eds.), “LHC Injectors Upgrade, Technical Design Report, Vol. I: Protons,” CERN-ACC-2014-0337 (2014).
9. S.A. Gourlay and D. Tommasini, “R&D towards 16 T Nb₃Sn dipole magnets,” this Newsletter
10. D. Amorim et al., “Single-beam transverse collective effects for HE-LHC,” this Newsletter (2017).
11. L. van Riesen-Haupt, “Triplet Update and Stay Clear for SLHC Optics,” LHC Design Meeting no. 16, 6 July 2017.
12. J. Abelleira, “Triplet Energy Deposition with Shielding,” LHC Design Meeting no. 16, 6 July 2017.
13. M. Crouch, “Options for collimation in the HE-LHC,” LHC Design Meeting no. 21, 31 October 2017.
14. B. Goddard, “HE-LHC Beam Dump,” LHC Design Meeting no. 11, 3 April 2017.

2.20 HE-LHC Optics Development

Yunhai Cai and Yuri Nosochkov
SLAC National Accelerator Laboratory, Menlo Park, CA, USA

Mail to: yuri@slac.stanford.edu

Massimo Giovannozzi, Thys Risselada, Ezio Todesco, Demin Zhou*
and Frank Zimmermann

CERN, Route de Meyrin, 1211 Geneva 23, Switzerland

* KEK, Tsukuba, Japan

Mail to: dmzhou@post.kek.jp, frank.zimmermann@cern.ch

2.20.1 Introduction

The High Energy LHC (HE-LHC) proton-proton collider is a proposed replacement of the LHC [1] in the existing 27-km tunnel, with the goal of increasing a centre-of-mass (CM) beam energy from 14 to 27 TeV. Some of the challenges of this machine are:

- A factor of almost two higher dipole field
- Higher field in quadrupoles and sextupoles
- Attaining sufficient dynamic aperture (DA) in presence of potentially larger field errors
- Fitting the ring close to the present LHC layout

The nominal LHC arc magnets have the aperture of 56 mm, and provide the field up to 8.33 T in dipoles, 223 T/m in quadrupoles, and 4430 T/m² in sextupoles [1]. The high field required at the HE-LHC beam energy can be realized by taking advantage of the magnet technology being developed for the 100-km FCC-hh design [2]. The latter aims at reaching 16 T field in dipoles, 400 T/m gradient in quadrupoles, and 7800 T/m² in sextupoles, where the magnet aperture is 50 mm [3,4]. Scaling of the present LHC to 27 TeV CM energy yields the magnet field exceeding the FCC specifications. Therefore, a new lattice design is required.

Design of the FCC 16-T dipole is based on Nb₃Sn superconductor; this however may potentially degrade the field quality (FQ), compared to the LHC dipole based on Nb-Ti superconductor. Further FQ degradation may be caused by a large swing between the HE-LHC injection and collision energies, and due to the slightly smaller magnet aperture. The resulting larger non-linear field errors may limit the ring dynamic aperture, especially at injection energy, where the field errors are typically larger than at collision energy as well as the beam size. The quadrupole and sextupole strengths increase with the energy, but also depend on beam optics. It is desirable to minimize the strengths of these magnets for the HE-LHC, so the cost-effective Nb-Ti technology could be used, wherever possible.

2.20.2 Lattice Design

As a first step of designing the HE-LHC lattice, we consider a simplified model of injection lattice with realistic arcs, but simple Interaction Regions (IR) without dipoles. Later, we apply the realistic IR layout with dipoles, specific to each location.

The two rings of the present LHC consist of eight octants, where each octant contains an arc made of twenty three 90° FODO cells, a dispersion suppressor at each arc end, and an IR. The rings cross each other four times as shown in Fig. 1, hence there are four long and four short arcs in each ring. Beam focusing is anti-symmetric with respect to each Interaction Point (IP), so the two beams see the same optics pattern. Layout of the simplified HE-LHC model represents approximately the average layout of the two LHC

rings, as shown in blue in Fig. 1. The model arcs are of the same (average) length, the IRs are straight without dipoles, and the ring has four-fold optics symmetry.

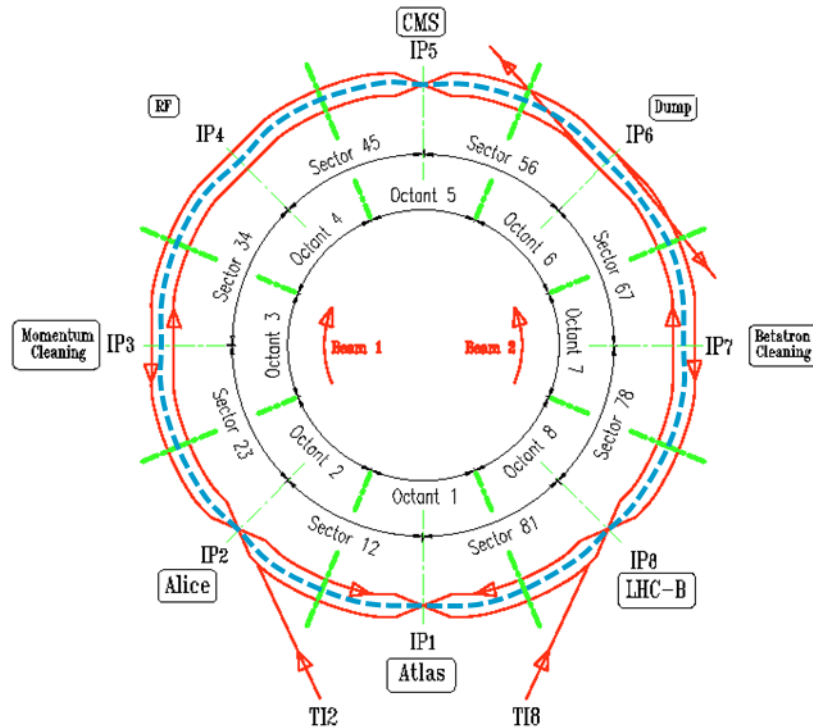


Figure 1: Layout of two LHC rings with long and short arcs (red); and schematic of simplified HE-LHC model with average length arcs and straight IRs (blue dash).

2.20.2.1 Design strategy

The goal of the HE-LHC lattice design is to minimize the magnet strengths and reduce the impact of non-linear field errors on dynamic aperture. Two methods are considered for the reduction of the magnet strengths in the arcs:

- A lower phase advance μ_c per arc FODO cell, and
- A longer arc cell L_c (the number of arc cells is reduced as $N_c \sim 1/L_c$)

Both of these methods, however, increase dispersion in the arcs; moreover a longer cell yields larger beta functions ($\sim L_c$). The resulting larger beam size may be more challenging for the collimation system, and a larger momentum compaction factor may require higher RF voltage.

The proposed strategy to reduce the effects of non-linear field errors is to choose the number of arc cells and the cell phase advance such that $N_c \mu_c = 2\pi \times \text{integer}$ [5-7]. This provides cancellation of second-order effects from periodic sextupoles and suppression of many non-linear resonances driven by systematic non-linear field errors in the periodic arcs. As a result, looser tolerances on the field quality may be acceptable.

2.20.2.2 Lattice models

Several injection lattice models have been designed having the following common features:

- Circumference $C = 26658.8832$ m, identical to the LHC
- Ring closely fits the LHC ring geometry

- FODO cell arc optics
- Same quadrupole and sextupole lengths and magnet-to-magnet distances as in the LHC
- One type dipole in arcs and dispersion suppressors
- Dipole length is within the acceptable limit of 14.3 m
- Simplified IR layout without dipoles
- Anti-symmetric optics relative to each IP, as in the LHC
- Fractional tune of 0.28/0.31 as in the LHC injection lattice
- Arc phase advance of $N_c \mu_c = 2\pi \times \text{integer}$ in most models

Parameters of the designed lattices are shown in Table 1, where the LHC injection lattice V6.503 is included for comparison. The strengths of arc magnets are scaled to 13.5 TeV to determine the required maximum field. The dipole and quadrupole strengths of the nominal LHC exceed the FCC limits of 16 T and 400 T/m, respectively; therefore, this lattice is not considered for the HE-LHC. The dipole length and the fill factor in the modeled arc cells are maximized for the lowest dipole field, assuming the same quadrupole and sextupole lengths and magnet-to-magnet distances as in the LHC. With the latter conditions, longer cells yield a lower dipole field. For a strict limit of 16 T field in dipoles, including a small operational margin, only the models with 18 cells per arc in Table 1 qualify for further consideration.

All the models satisfy the FCC field limit in arc quadrupoles and sextupoles. Their strengths are lower in longer cells with a lower phase advance. The sextupole strength, however, may increase in collision optics due to large chromaticity created in the low-beta IR1 and IR5.

Matching the circumference and fitting the ring layout is done by optimizing the lengths of the arc cell and the dispersion suppressor. The resulting trajectory offsets relative to the LHC are typically within 10 cm. The three ring models with 18 cells per arc, shown in Table 1, have identical geometry.

Peak beta functions are proportional to the cell length, and only minor affected by the cell phase advance within the 60° to 90° range. Peak dispersion quadratically increases with the cell length, and strongly increases as the phase advance is reduced. Cell optics functions in the $18 \times 60^\circ$ and $18 \times 90^\circ$ arcs are shown in Fig. 2 for comparison.

Dispersion suppressor connects the arc and the IR, and consists of two FODO cells with 8 dipoles. The design is based on the LHC layout, where adjustments are made to the cell and dipole lengths. As in the LHC, the optics match between the arc and the IR is done using the dispersion suppressor quadrupoles and the two quadrupoles in the adjacent arc cell. The IR dispersion is fully cancelled in the designed models.

For the injection lattice, we use a simplified IR layout without dipoles, and injection-type IR optics with small beta functions. This design should be adequate for the study of dynamic aperture, since the effects of IR errors are not significant in injection lattice. Example of the IR and dispersion suppressor optics for $18 \times 90^\circ$ model is shown in Fig. 3, where the IP beta function is 15 m. The complete ring optics is shown in Fig. 4. Geometrically, the model ring is eight-fold symmetric having identical octant layouts. The optics, however, is four-fold symmetric since the focusing is anti-symmetric with respect to each IP, and hence the quadrupole polarities change sign from octant to octant.

Table 1: Parameters of HE-LHC injection lattice models and the LHC V6.503 injection lattice, where magnet field is at 13.5 TeV beam energy.

	<i>LHC V6.503</i> $23 \times 90^\circ$	<i>Model</i> $24 \times 60^\circ$	<i>Model</i> $20 \times 90^\circ$	<i>Model</i> $18 \times 60^\circ$	<i>Model</i> $18 \times 80^\circ$	<i>Model</i> $18 \times 90^\circ$
Cells per arc	23	24	20	18	18	18
Cell phase advance, deg	90	60	90	60	80	90
Cell length, m	106.90	102.45	122.94	137.23	137.23	137.23
Dipole length, m	14.3	13.56	12.625	14.18	14.18	14.18
Dipoles per arc cell	6	6	8	8	8	8
Total number of dipoles	1232	1280	1424	1280	1280	1280
Arc dipoles fill factor	0.803	0.794	0.809	0.827	0.827	0.827
Dipole B, T	16.06	16.30	15.92	15.59	15.59	15.59
Arc quad B', T/m	404.8	289.5	334.8	214.9	276.3	304.0
Sextupole B'', T/m ²	4883	2057	2940	866	1824	2475
Max/Min arc β function, m	184 / 29	177 / 60	208 / 38	237 / 80	228 / 50	233 / 40
Max/Min arc dispersion, m	2.03 / 0.96	3.75 / 2.26	3.0 / 1.5	6.73 / 4.06	4.30 / 2.22	3.64 / 1.75
Tune, x/y	64.28 / 59.31	49.28 / 47.31	55.28 / 54.31	38.28 / 37.31	47.28 / 48.31	54.28 / 53.31
Momentum compaction	$3.22 \cdot 10^{-4}$	$6.41 \cdot 10^{-4}$	$4.70 \cdot 10^{-4}$	$1.12 \cdot 10^{-3}$	$6.83 \cdot 10^{-4}$	$5.58 \cdot 10^{-4}$
Natural chromaticity	-86 / -82	-63 / -63	-73 / -72	-47 / -47	-62 / -63	-73 / -73

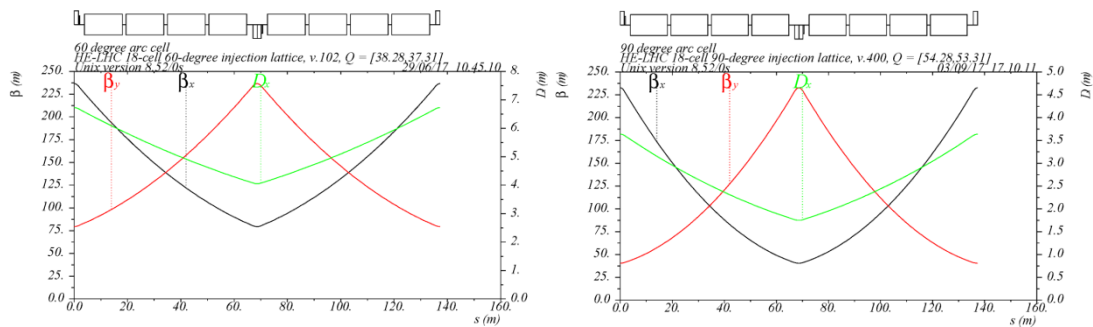


Figure 2: Cell optics functions in the $18 \times 60^\circ$ (left) and $18 \times 90^\circ$ arcs (right).

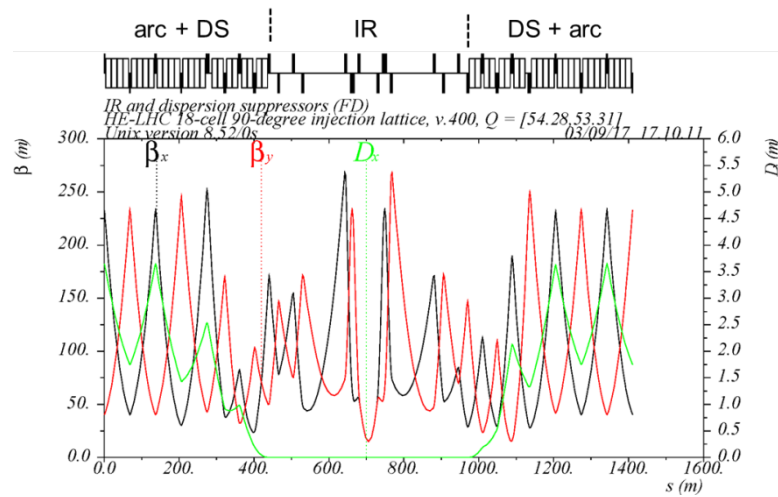


Figure 3: Optics functions in the IR, dispersion suppressors (DS) and the last two arc cells at each arc end in $18 \times 90^\circ$ model.

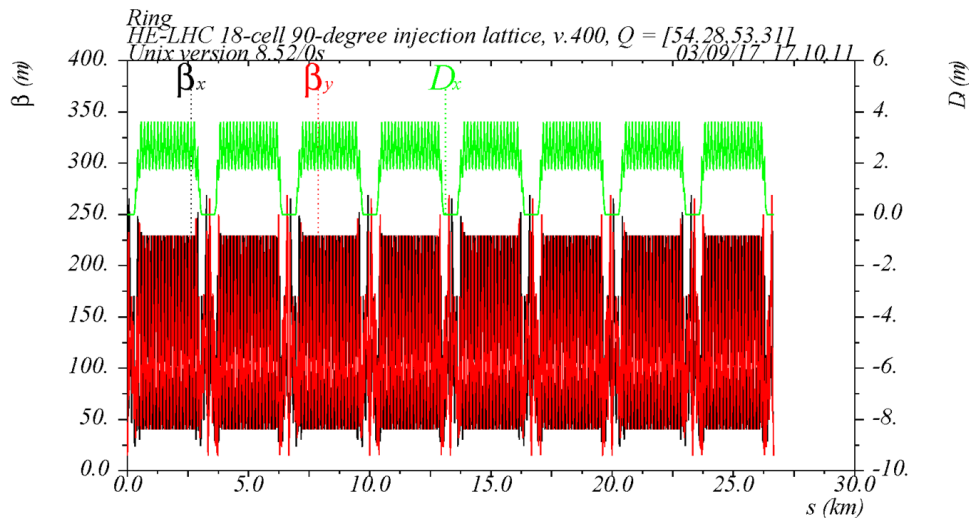


Figure 4: Optics functions in the complete $18 \times 90^\circ$ injection lattice model with simple IRs.

2.20.3 Dynamic Aperture

In view of a possible degradation of the dipole field quality at injection energy, the HE-LHC model lattice includes non-linear field compensation properties. This is implemented by setting the total arc phase advance to $N_c \mu_c = 2\pi \times \text{integer}$ in both planes (except in the $18 \times 90^\circ$ model). For a completely periodic arc, this condition results in suppression of many resonances driven by arc sextupoles and systematic non-linear field errors in the arc magnets [5-7]. Figure 5 shows a perfect cancellation of many 3rd order resonance driving terms generated by the periodic arc sextupoles in $18 \times 60^\circ$ lattice option, where all arc cells are identical.

In the actual lattice design, presented in Table 1, strengths of quadrupoles in the first and the last arc cells are somewhat adjusted to improve the dispersion suppressor match; hence, the optics functions in these cells are not exactly periodic. The result is a deviation from perfect sextupole compensation over the full arc, although the exact cancellation

still holds for a shorter part of the arc corresponding to the number of identical cells where total phase advance is multiple of 2π .

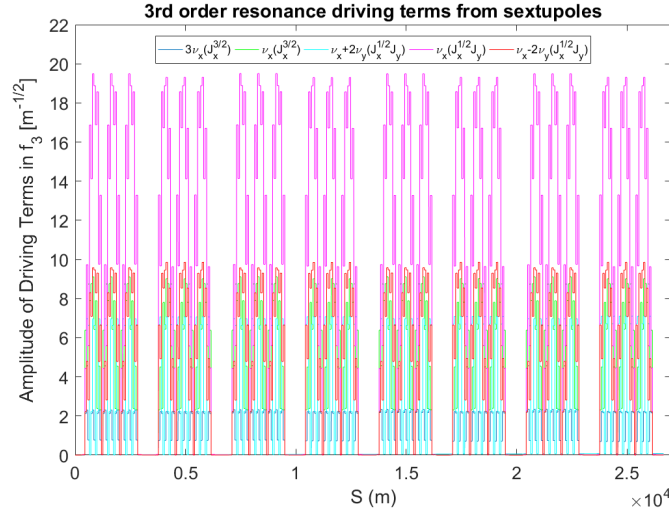


Figure 5: Accumulation and compensation of the 3rd order resonance driving terms from arc sextupoles in $18 \times 60^\circ$ lattice where all arc cells are identical.

Similarly, compensation of the non-linear effects caused by systematic field errors in dipoles is limited to the periodic cells with total $2\pi \times \text{integer}$ phase advance, while residual effects are expected from dipole errors in the arc matching cells and dispersion suppressors. The lattice model with $18 \times 90^\circ$ arcs differs from the other models because by design the arc phase advance is not multiple of 2π . In this case, the non-linear field cancellation is limited to the inner 16 cells. This lattice model has more optimal dispersion suppressor optics, since the latter is originally designed for the 90° LHC arcs. The 90° cells are also more readily compatible with the Achromatic Telescopic Squeezing (ATS) scheme for chromatic aberrations compensation [8].

2.20.3.1 Tracking simulations

The short-term DA of the designed lattice models is evaluated using LEGO [9] and SAD [10] codes. The DA is performed at 450 GeV injection energy and expressed in units of rms beam size for normalized beam emittance of $2.5 \mu\text{m-rad}$. Typical tracking simulation is performed for 1024 turns, with initial momentum offset up to 7.5×10^{-4} , and linear chromaticity of +3.

Figure 6 shows DA of the three 18-cell models without errors for the initial momentum offset of $\Delta p/p = 0$ and 7.5×10^{-4} . The DA of all models is significantly larger than the DA of the present LHC injection lattice. This is due to the four-fold symmetry of the simple models resulting in cancellation of many resonances, and built-in non-linear compensation in the arcs which reduce the effects of sextupoles. Without the errors, the DA increases as the cell phase advance is reduced, while the effect of non-zero $\Delta p/p$ is small.

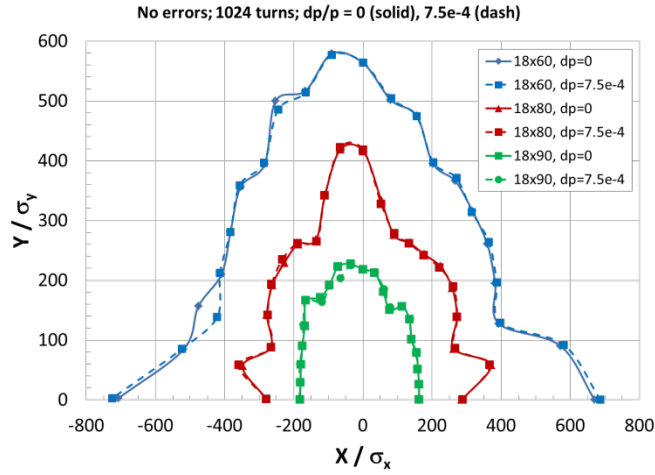


Figure 6: Dynamic aperture of $18 \times 60^\circ$, $18 \times 80^\circ$, and $18 \times 90^\circ$ injection lattices without errors for initial momentum offset of $\Delta p/p = 0$ and 7.5×10^{-4} .

2.20.3.2 Non-linear field errors in dipoles

A possible degradation of dipole field quality at injection energy is a concern for the HE-LHC dynamic aperture. Estimates of the dipole FQ for FCC-hh at injection energy [11] predict that the lowest order allowed field components are in the range of

- $b_{3S} = 7, b_{3R} = b_{3U} = 1.6$
- $b_{5S} = 1, b_{5R} = b_{5U} = 0.1$
- $b_{7S} = -1.5, b_{7R} = b_{7U} = 0.03,$

where S, R and U stand for the systematic, random and uncertainty components, and the reference radius is 17 mm. The full value of b_n is obtained using the formula [12]

$$b_n = b_{nS} + \frac{\xi_U}{1.5} b_{nU} + \xi_R b_{nR},$$

where ξ_U, ξ_R are random Gaussian values with $\sigma = 1$, cut at 1.5σ and 3σ , respectively. Here, the ξ_U is the same for all magnets of a given class, but changes from seed to seed and for the different field components; while ξ_R changes from magnet to magnet.

Similar to the LHC correction system, we consider that b_3 and b_5 correctors are included at each dipole to compensate the dipole systematic b_{3S} and b_{5S} errors. However, in this tracking study these correctors are not included. In order to simulate such a correction, we make an assumption that the b_{3S} and b_{5S} errors after correction are effectively reduced to 5% and 30%, respectively, of the values shown above, i.e. the residual $b_{3S} = 0.35$ and $b_{5S} = 0.3$.

Additionally, the LEGO tracking code allows only the systematic and random error components to be included. To take into account the uncertainty component, we make another assumption, where the ξ_U is made random in all magnets, and that the ξ_U and ξ_R are independent. We then combine them into one random component ξ_R corresponding to $b_{3R} = 1.92, b_{5R} = 0.12,$ and $b_{7R} = 0.036$. These new values along with the systematic components shown above are used in the tracking.

2.20.3.3 Dynamic aperture with dipole field errors

Impact of the systematic dipole field errors $b_{3S}, b_{5S},$ and b_{7S} on the DA of 18-cell lattice models is dominated by the b_{5S} and b_{7S} components. The impact of b_{3S} is relatively

small due to the lattice non-linear compensation properties, and the chromaticity correction provided by the sextupoles.

Dynamic aperture with the systematic and random b_3, b_5, b_7 field errors in dipoles for five random seeds is shown in Fig. 7 for the initial $\Delta p/p = 0$ and 7.5×10^{-4} . One can see that the $18 \times 80^\circ$ and $18 \times 90^\circ$ models have a larger aperture as compared to the $18 \times 60^\circ$ model. The aperture is reduced in the case of non-zero momentum offset, but remains sufficient for the $18 \times 80^\circ$ and $18 \times 90^\circ$ models. The optimal value of the momentum offset at injection energy needs to be further specified.

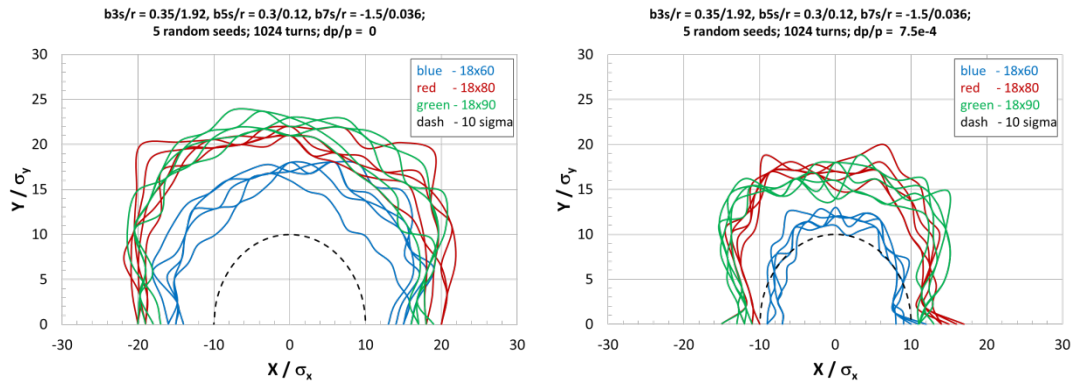


Figure 7: Dynamic aperture of $18 \times 60^\circ$, $18 \times 80^\circ$, and $18 \times 90^\circ$ injection lattices with systematic and random b_3, b_5, b_7 field errors in dipoles for the initial $\Delta p/p = 0$ (left) and 7.5×10^{-4} (right) and 5 random seeds.

2.20.4 Realistic Injection Lattice Model

Design of the HE-LHC injection lattice with realistic IR layout is in progress. One lattice based on a combination of $18 \times 90^\circ$ arcs and IR geometry from the SLHCV3.1a lattice layout is designed. The ring is matched to the LHC layout to within about 1 cm accuracy. The complete lattice functions are shown in Fig. 8, where one can see the different optics in different IRs.

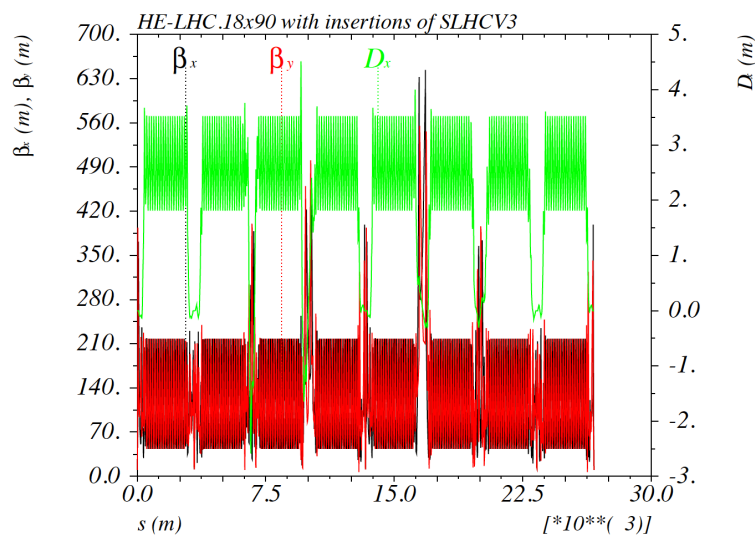


Figure 8: Lattice functions in the HE-LHC injection model with realistic IRs and $18 \times 90^\circ$ arcs.

The realistic IRs require strong dipoles due to the high 13.5 TeV collision energy and the assumed larger beam separation (204 mm) between the rings in the arcs. These magnets include 12-T D1, D2 and 8-T D3, D4 superconducting dipoles in the IR4, and 1.8 T normal conducting dipoles D3, D4 in the IR3 and IR7. Further optimization of this preliminary IR design is underway.

Dynamic aperture of the realistic lattice without errors is very large, as can be seen in Fig. 9. The tracking is performed using SAD [10] based on standard frequency map analysis algorithm. Since the lattice is based on the 18-cell arcs, the dipole field at top energy is comfortably below the 16 T limit. This realistic design is compatible with the HE-LHC requirements.

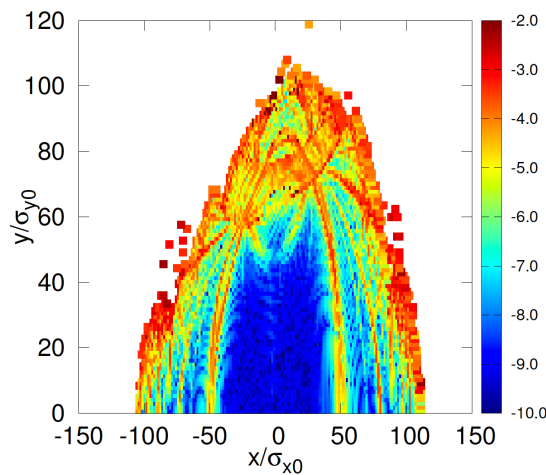


Figure 9: Dynamic aperture of the HE-LHC injection lattice with realistic IRs and $18 \times 90^\circ$ arcs without errors.

2.20.5 Conclusion

Several models of the HE-LHC injection lattice with simple IRs are designed and compared. They feature low magnet strengths and include built-in non-linear field compensation properties in the arcs. The optimal models are based on the 18-cell arcs and cell phase advance of 80° and 90° , yielding sufficient dynamic aperture with the expected dipole field errors. The initial realistic design based on the $18 \times 90^\circ$ arcs and the IR layout of the SLHCV3.1a lattice is complete. This design satisfies the HE-LHC magnet field requirements, and provides a close match to the LHC ring layout and a large dynamic aperture without errors.

2.20.6 References

1. LHC Design Report, Vol. I, 2004.
2. M. Benedikt, F. Zimmermann, "Future Circular Colliders", in Proceedings of Science, LeptonPhoton2015, 052, and CERN-ACC-2015-0165 (2016).
3. D. Tommasini et al, "The 16 T dipole development program for FCC", IEEE Transactions on Applied Superconductivity, Vol. 27, 4 (2017).
4. D. Schoerling, "Magnet status towards the CDR", FCC Week 2017, Berlin, Germany (2017).

5. K. L. Brown, “A second order magnetic optical achromat”, SLAC-PUB-2257 (1979).
6. A. Verdier, “Resonance free lattices for AG machines”, CERN-SL-99-018-AP, CERN-SL-99-18-AP (1999).
7. Y. Cai, K. Bane, R. Hettel, Y. Nosochkov, M.-H. Wang, M. Borland, “Ultimate storage ring based on fourth-order geometric achromats”, Phys.Rev.ST Accel. Beams 15 054002 (2012).
8. S. Fartoukh, “Achromatic telescopic squeezing scheme and its application to the LHC and its luminosity upgrade”, Phys. Rev. ST Accel. Beams 16, 111002 (2013).
9. Y. Cai, M. Donald, J. Irwin and Y. Yan, “LEGO: a modular accelerator design code”, SLAC-PUB-7642 (1997).
10. <http://acc-physics.kek.jp/SAD/index.html>.
11. B. Dalena, “Status of dynamic aperture and alignment for FCC-hh”, FCC Week 2017, Berlin, Germany (2017).
12. M. Giovannozzi, S. Fartoukh, R. De Maria, “Specification of a system of correctors for the triplets and separation dipoles of the LHC upgrade”, in Proc. IPAC 2013 Shanghai, China, WEPEA048 (2013).
13. S. Fartoukh, private communication.

2.21 Single-beam transverse collective effects for HE-LHC

David Amorim[#], Sergey Antipov[#], Sergey Arsenyev[#], Nicolo Biancacci[#], Xavier Buffat[#], Adrian Oeftiger[#], Lotta Methner^{*}, Elias Métral[#], Tatiana Pieloni^{*}, Benoit Salvant[#], Claudia Tambasco^{*}, Frank Zimmermann[#].

^{*}Particle Accelerator Physics Laboratory, Institute of Physics, EPFL, Lausanne, Switzerland,

[#]CERN, CH-1211 Geneva 23, Switzerland

Mail to: Claudia.Tambasco@epfl.ch

2.21.1 Introduction

The High-Energy LHC (HE-LHC) aims at doubling the collision energy of beams circulating in the LHC tunnel thanks to the replacement of the current LHC magnets with magnets that can reach higher magnetic field [1].

This contribution describes the current status of studies on single beam collective effects in the transverse plane: space charge effects, transverse impedance and related beam stability and electron cloud effects. It is important to stress that this contribution is based on current assumptions and parameters, which may change significantly in the near future.

The list of parameters at the time of writing this contribution is in Table 1.

Table 1: List of HE-LHC parameters.

Parameter	Machine state	
	Injection	Flat top
Beam Energy [TeV]	1.3	13.5
Transverse Norm. Emittance [mm.mrad norm.]	2.5	
Bunch intensity [1E11]	2.2	
Bunch spacing [ns]	25	
RMS bunch length [m]	0.081	0.075
Betatron Tunes (Qx/Qy)	62.31/60.32	
RF Voltage V [MV]	16	30
Synchrotron tune Qs	1.19E-03	2.02E-03
RF harmonic number h_{RF}	35640	
Momentum Compaction Factor	3.23E-04	
Slippage factor	3.22E-04	

2.21.2 Space Charge effects

This subsection briefly discusses the relevance of typical detrimental and beneficial space charge effects for the LHC in the context of the higher-energy upgrade. Potentially detrimental effects include emittance growth inflicted by betatron resonances, dynamic aperture reduction due to tune modulation, and emittance growth due to transverse injection mismatch. On the beneficial side, the direct space charge tune *spread* significantly contributes to Landau damping of higher order single bunch head-tail modes at LHC injection (for the current and the High Luminosity upgrade impedance models). The following paragraphs will elaborate on these space charge effects.

Transverse space charge acts as a defocusing force. In comparison to the injectors, the self-fields of the beam inflict a relatively small negative tune shift on the particles traversing the beam distribution at the high energies of (HE-) LHC. For bunched beams in most synchrotrons, the longitudinal particle motion is much slower compared to the transverse plane. Therefore the transverse space charge detuning depends on the local line charge density in the bunch. For a 6D Gaussian distributed bunch, the maximum incoherent tune shift corresponds to the strong fields in the bunch centre. It amounts to [2]

$$\Delta Q_{x,y}(s) = -\frac{qN}{8\pi^2\epsilon_0 m_p c^2 \gamma^3 \sqrt{2\pi}\sigma_s} \int \frac{\beta_{x,y}(s)}{\sigma_{x,y}(s)(\sigma_x(s)+\sigma_y(s))} ds \quad (1)$$

where the transverse rms beam size reads (e.g. in x):

$$\sigma_x(s) = \sqrt{\frac{\beta_x(s)\epsilon_x}{\gamma} + D_x(s)^2 \delta_{rms}^2} \quad (2)$$

with q the charge per particle, m_p is the proton mass, ε_0 is the vacuum permittivity, N the bunch population, m_p the mass per particle, γ the Lorentz factor, σ_z the rms bunch length, $\varepsilon_{x,y}$ the normalised transverse emittances, δ_{rms} the rms dimensionless momentum deviation, $\beta_{x,y}(s)$ the betatron functions at position s along the ring and $D_x(s)$ the dispersion function. The relativistic speed factor β has been approximated with 1.

The space charge tune shift is largest at injection as it scales with the inverse energy squared, $\Delta Q_{x,y}^{SC} \propto 1/\gamma^2$. Typical tune shift values are on the order of $\Delta Q_{x,y}^{SC} \propto 10^{-3}$. Table 2 summarises some relevant values evaluating the machine integral in Eq. (1) for the HL-LHC v1.3 optics with fixed transverse emittances $\varepsilon_{x,y} = 2.5$ mm.mrad. LHC refers to a bunch population of $N=1.3 \cdot 10^{11}$ and HL-LHC to $N=2.3 \cdot 10^{11}$.

Table 2: Gaussian maximum space charge tune shift for different energies and bunch populations.

Machine	Maximum Direct Space Charge Tune Shift	
	Horizontal ΔQ_x^{SC} [10^{-3}]	Vertical ΔQ_y^{SC} [10^{-3}]
LHC at 0.45TeV	0.79	1.5
HL-LHC at 0.45TeV	1.7	3.2
HL-LHC at 0.9TeV	0.21	0.40
HL-LHC at 1.3TeV	0.070	0.13
LHC at 6.5TeV	3.8×10^{-4}	7.2×10^{-4}
HL-LHC at 13.5TeV	7.2×10^{-5}	1.4×10^{-4}

Since particles undergo synchrotron oscillations, they may sample different transverse self-field strength along the local bunch line charge density. In principle, incoherent tune modulation can increase the chaotic region in phase space and limit the dynamic aperture. Studies on the incoherent tune modulation due to the direct space charge forces with synchrotron motion found no significant impact for the LHC though [3]. For similar synchrotron tunes and equal or smaller space charge detunings in the higher-energy upgrade we do not expect this to change. The same study concludes that emittance growth due to transverse injection mismatch is not an issue for LHC. From current LHC operation and the extrapolation to smaller tune shifts for the HE upgrade, we conclude that betatron resonances are not expected to be a showstopper either.

For Gaussian distributed beams the self-fields are non-linear, thus the incoherent transverse tunes depend on the betatron amplitude. In absence of other detuning effects, the corresponding space charge tune spread reaches from the maximum tune shift to the bare machine tune. In the case of detuning with amplitude e.g. in the case of Landau octupoles, the incoherent tune shifts mix. Presently, the LHC is operated at a Landau octupole current of around 40A at injection, which leads to a tune shift on the order of $\Delta Q^{oct} \propto 10^{-3}$ for particles at a betatron amplitude of about 1 rms beam size. Hence Landau octupoles and direct space charge provide detuning with amplitude of roughly the same

magnitude at LHC injection. Both tune spreads scale with $1/\gamma^2$.

The rigid head-tail mode 0 is unaffected by space charge as the beam self-fields move with the beam. In contrast, octupole magnetic fields as well as an active damper feedback system can suppress mode 0 instabilities, which is discussed later in this document. On the other hand, direct space charge affects the (higher-order) non-rigid head-tail modes: (i.) by depressing the mode frequencies due to the tune shift as well as (ii.) by potentially Landau damping instabilities due to the tune spread. Taking into account only the impedance model at HL-LHC injection (i.e. 450 GeV), the transverse mode coupling instability (TMCI) between mode 0 and mode -1 occurs above a threshold intensity of $N \propto 6 \times 10^{11}$ p/b. Studies including space charge have shown that the mode coupling is cancelled as a direct consequence of (i.) since mode -1 shifts away from mode 0 [4]. Furthermore, simulations for finite chromaticity show that, for HL-LHC beam parameters, space charge can effectively suppress a mode 1 head-tail instability. The instability is recovered when the emittance is increased twentyfold and hence space charge becomes too weak. The same mechanism might explain beam stability at LHC injection, where the mere impedance model including a resistive damper predict higher-order head-tail instabilities for positive chromaticities. These beneficial Landau damping effects of space charge could be lost at higher energies (specifically for increased injection energies) as space charge becomes less relevant: the real part of the coherent tune shift from the impedance decreases with $1/\gamma$ as opposed to $\Delta Q_{x,y}^{SC} \propto 1/\gamma^2$. We recommend to investigate the contribution of space charge to Landau damping for the future injection energies for HE-LHC, as well as to study if lower Landau octupole current are needed at injection to allow for a larger dynamic aperture, since large octupole current is currently needed to fight electron cloud in the LHC.

2.21.3 Beam impedance and stability scalings from FCC-hh and HL-LHC

In this simple analysis we compare the transverse instability effects in the HE-LHC to the ones in the FCC-hh (hadron Future Circular Collider [5]) and the HL-LHC (High Luminosity LHC [6]). For the head-tail mode 0 (the ‘‘rigid bunch’’ mode) we consider two figures of merit: the coupled-bunch (CB) instability rise time in turns, and the ratio of the single-bunch (SB) TMCI threshold to the nominal bunch intensity:

$$n^{turns} \propto \frac{E \Delta s}{N_b \beta_{avg} \text{Re}\{Z_T\}_{eff}^{CB}}$$

$$\frac{N_{th}^{TMCI}}{N_b} \propto \frac{\sqrt{EV_{RF} h_{RF} l_b}}{N_b C \text{Im}\{Z_T\}_{eff}^{SB}}$$

Here E is the energy, Δs is the bunch spacing, β_{avg} is the average betatron function (smooth approximation), l_b is the full (4σ) bunch length, C is the circumference, $\{Z_T\}_{eff}^{CB}$ and $\{Z_T\}_{eff}^{SB}$ are the coupled-bunch and the single-bunch transverse effective impedances weighted with the local betatron functions (defined in agreement with the LHC Design Report [7]).

The absolute numbers for the figures of merit depend on yet undefined instability mitigation techniques. Therefore, in this chapter we only give a relative comparison

between the three colliders and assume no instability mitigation (zero chromaticity, no transverse feedback, and no Landau damping).

We assume that the coupled-bunch impedance is dominated by the low-frequency contribution of the beam screen at both injection and top energy (the contribution of the collimators is small due to the inductive by-pass effect). The most unstable coupled bunch mode samples the impedance at the lowest frequency line $f = (\text{frac}[Q] - 1)f_{rev}$ giving an additional dependence on the circumference. Ignoring the inductive by-pass effect and the multi-layer composition of the beam screen wall, we arrive to a simple scaling law

$$\{Z_T\}_{\text{eff}}^{\text{CB}} \propto \frac{C^{3/2} \rho_{bs}^{1/2} \beta_{arc}}{b_{arc}^3 \beta_{avg}}$$

where ρ_{bs} is the resistivity of the beam screen wall, β_{arc} is the average betatron function in the arc, and b_{arc} is the aperture of the beamscreen in the most critical (vertical) plane. For the single-bunch impedance, the assumed scalings for the beam screen and for the collimators (resistive wall) are

$$\text{bs: } \{Z_T\}_{\text{eff}}^{\text{SB}} \propto \frac{C \rho_{bs}^{1/2} l_b^{1/2} \beta_{arc}}{b_{arc}^3 \beta_{avg}}$$

$$\text{coll: } \{Z_T\}_{\text{eff}}^{\text{SB}} \propto \begin{cases} \frac{L_{coll} l_b^{1/2} \rho_{coll}^{1/2} E^{3/2}}{\beta_{coll}^{1/2} \beta_{avg} \epsilon_N^{3/2}}, & \text{if the number of sigmas is the same} \\ \frac{\max(\beta_{arc})^{3/2} L_{coll} l_b^{1/2} \rho_{coll}^{1/2}}{\beta_{coll}^{1/2} \beta_{avg} b_{arc}^3}, & \text{if gaps are chosen to protect the arc} \end{cases}$$

where L_{coll} and β_{coll} are the total length and the betatron function of the collimators and ϵ_N is the normalized beam transverse emittance.

We assume that at top energy the single-bunch impedance is dominated by the collimators, and that the collimator gaps are chosen to keep the number of sigmas the same. At injection the single-bunch impedance is assumed to be a sum of contributions of the beam screen and the collimators with the gaps given by a scaling law (providing the range of uncertainty). The relative importance of the beam screen and the collimators is chosen based on the absolute numbers for the FCC-hh: $\text{Im}\{Z_T\}_{\text{eff bs}}^{\text{SB}} = 2.7 \text{ M}\Omega/m$, $\text{Im}\{Z_T\}_{\text{eff coll}}^{\text{SB}} = 0.8 \text{ M}\Omega/m$ (molybdenum-graphite collimator jaws with pure molybdenum coating are assumed). The unknown contributions to the impedance (pumping holes, BPMs, etc.) are assumed to scale together with the known contributions.

In the tables below we separate the somewhat uncertain impedances from the relatively well-defined abilities to damp the impedance effects (the columns “ n^{turns} for same Z_T ” and “ N_{th}^{TMCI}/N_b for same Z_T ”). The two numbers are combined in the columns n^{turns} and N_{th}^{TMCI}/N_b . For the estimates the injection energy of the FCC-hh is assumed to be 3.3 TeV. The HE-LHC beamscreen is assumed to be of the FCC type in this paragraph. The lengths and the resistivities of the collimator jaws are the same in all three colliders, and the betatron functions in the collimators are the same in the HL-LHC and the HE-LHC and 5.6 times higher in the FCC-hh. The HE-LHC normalized emittance is $2.5 \mu\text{m}$, the nominal bunch intensity is 2.2×10^{11} , the 4σ bunch length is 1.24 ns in case of 0.45 TeV injection and 1.5 ns in all other cases, the RF voltage is 14 MV at injection and 32 MV at top energy.

Table 3: Comparison at injection: $E_{HL-LHC} = 0.45$ TeV

	Coupled-bunch			Single-bunch		
	n^{turns} for same Z_T	$\{Z_T\}_{eff}^{CB}$	n^{turns}	N_{th}^{TMCI}/N_b for same Z_T	$\{Z_T\}_{eff}^{SB}$	N_{th}^{TMCI}/N_b
HE-LHC compared to FCC-hh	10 times worse	6.8 times better	1.5 times worse	2.5 times worse	1.4 - 3.7 times better	1.8 times worse – 1.5 times better
HE-LHC compared to HL- LHC	1.3 times worse	4.6 times worse	5.8 times worse	1.8 times better	1.8-3.7 times worse	1.0 - 2.1 times worse

Table 4: Comparison at injection: $E_{HL-LHC} = 0.9$ TeV

	Coupled-bunch			Single-bunch		
	n^{turns} for same Z_T	$\{Z_T\}_{eff}^{CB}$	n^{turns}	N_{th}^{TMCI}/N_b for same Z_T	$\{Z_T\}_{eff}^{SB}$	N_{th}^{TMCI}/N_b
HE-LHC compared to FCC-hh	5.0 times worse	6.8 times better	1.3 times better	1.4 times worse	1.3 - 2.6 times better	1.2 times worse – 1.8 times better
HE-LHC compared to HL-LHC	1.6 times better	4.6 times worse	2.9 times worse	3.0 times better	3.3 - 4.0 times worse	1.1 - 1.3 times worse

Table 5: Comparison at injection: $E_{HL-LHC} = 1.3$ TeV

	Coupled-bunch			Single-bunch		
	n^{turns} for same Z_T	$\{Z_T\}_{eff}^{CB}$	n^{turns}	N_{th}^{TMCI}/N_b for same Z_T	$\{Z_T\}_{eff}^{SB}$	N_{th}^{TMCI}/N_b
HE-LHC compared to FCC-hh	3.5 times worse	6.8 times better	1.9 times better	1.2 times worse	1.3 - 2.1 times better	1.0 - 1.8 times better
HE-LHC compared to HL-LHC	2.3 times better	4.6 times worse	2.0 times worse	3.6 times better	4.0 - 4.7 times worse	1.1 - 1.3 times worse

Table 6: Comparison at top energy

	Coupled-bunch			Single-bunch		
	n^{turns} for same Z_T	$\{Z_T\}_{eff}^{CB}$	n^{turns}	N_{th}^{TMCI}/N_b for same Z_T	$\{Z_T\}_{eff}^{SB}$	N_{th}^{TMCI}/N_b
HE-LHC compared to FCC-hh	4.9 times worse	6.6 times better	1.3 times better	1.6 times worse	1.9 times better	1.2 times better
HE-LHC compared to HL-LHC	1.5 times better	3.7 times worse	2.5 times worse	2.7 times better	2.5 times worse	1.1 times better

Based on the relative comparison for n^{turns} and N_{th}^{TMCI}/N_b we can conclude that for all of the studied cases except the injection at 0.45TeV, both figures of merit in the HE-LHC are better than in at least one of the compared colliders (FCC-hh or HL-LHC). Achieving stability in the 0.45TeV case might require more aggressive mitigation techniques than the ones anticipated for either of the compared colliders. In the end, the decision should rely on the absolute numbers rather than the relative comparison (see the detailed study below).

2.21.4 Impedance model

A first version of the HE-LHC impedance was derived from the LHC and HL-LHC impedance models [8, 9]. In these two cases the main sources of impedance are the collimation system and the beam screen.

The impedance simulations were performed for four different cases. These cases include three different injection energies (450 GeV, 900 GeV and 1.3 TeV per beam) and the top energy case (13.5 TeV per beam). The HL-LHC optics for injection and top energy with 48cm squeeze were used to provide the different elements beta functions.

As the collimators are required to sit close to the beam to ensure a sufficient cleaning efficiency, they are one of the main impedance contributors. Their physical gaps in mm were scaled according to the beam energy considered, the reference emittance and the gap in number of collimation sigmas σ_{coll} as reported in Table 7 for the two main collimators families. The physical gaps h are computed as follow:

$$h = n \sigma_{coll} = n \sqrt{\frac{\varepsilon_n}{\gamma_{rel}} (\beta_x \cos^2 \varphi + \beta_y \sin^2 \varphi)}$$

where n is the number of collimation sigmas as reported in Table 2, ε_n is the reference normalized emittance, γ_{rel} is the Lorentz factor, $\beta_{x/y}$ are the Twiss beta function at the position of the collimator and φ is the angle of the collimator with respect to the horizontal plane. For the top energy case, a preliminary collimators parameters file was provided by the collimation study team [10]. In this case, the Twiss beta functions at the collimators are the ones from a preliminary version of the HE-LHC optics. Among all, the primary and secondary collimators are the main contributors to the impedance as their gaps are in the order of a few mm. For the simulations, they are assumed to be made of molybdenum-graphite coated with a 5 μm deposit of molybdenum [11].

Table 7: Reference emittance and collimators gaps in number of beam sigmas for the HE-LHC scenarios considered and the HL-LHC injection and top energy scenarios.

Machine	HE-LHC	HE-LHC	HE-LHC	HE-LHC	HL-LHC	HL-LHC
Machine state	Injection	Injection	Injection	Flat-top	Injection	Flat-top
Beam energy	450 GeV	900 GeV	1.3 TeV	13.5 TeV	450 GeV	7 TeV
Reference emittance	2.5 μm					
Primary collimators	5.0 σ	5.7 σ	5.7 σ	5.0 σ	6.7 σ	6.7 σ
Secondary collimators	6.0 σ	6.7 σ	6.7 σ	6.0 σ	7.9 σ	9.1 σ
Injection protection	7.3 σ	8.0 σ	8.0 σ	N/A	9.5 σ	N/A
Machine aperture	$\sim 8 \sigma$	$> 10.6 \sigma$	$> 10.6 \sigma$	To be defined	12.6 σ	$\sim 10 \sigma$

The impedance model was first computed with the LHC beam screen geometry. To account for the possible usage of the FCC-hh beam screen in HE-LHC, a factor four was applied on the resistive wall contribution of this element [12]. This factor four is an estimation taking into account the tighter mechanical aperture and the increased material resistivity. In the FCC-hh beam screen case, the increased resistivity would come from using a beam screen cooled to 50 K instead of a beam screen cooled to 20 K in the LHC/HL-LHC case.

The horizontal and vertical dipolar impedances are shown in Figure 1 for the 450 GeV injection case, in Figure 2 for the 1.3 TeV injection case and in Figure 3 for the 13.5 TeV top energy case. In these plots the orange curves correspond to the LHC beam screen case and the blue curves to the FCC-hh beam screen case. For frequencies below 100 MHz the beam screen contribution dominates and the effect of the beam screen type is stronger. Above this frequency the collimators contribution dominates and the beam screen type has a small impact at injection energy and no impact at top energy.

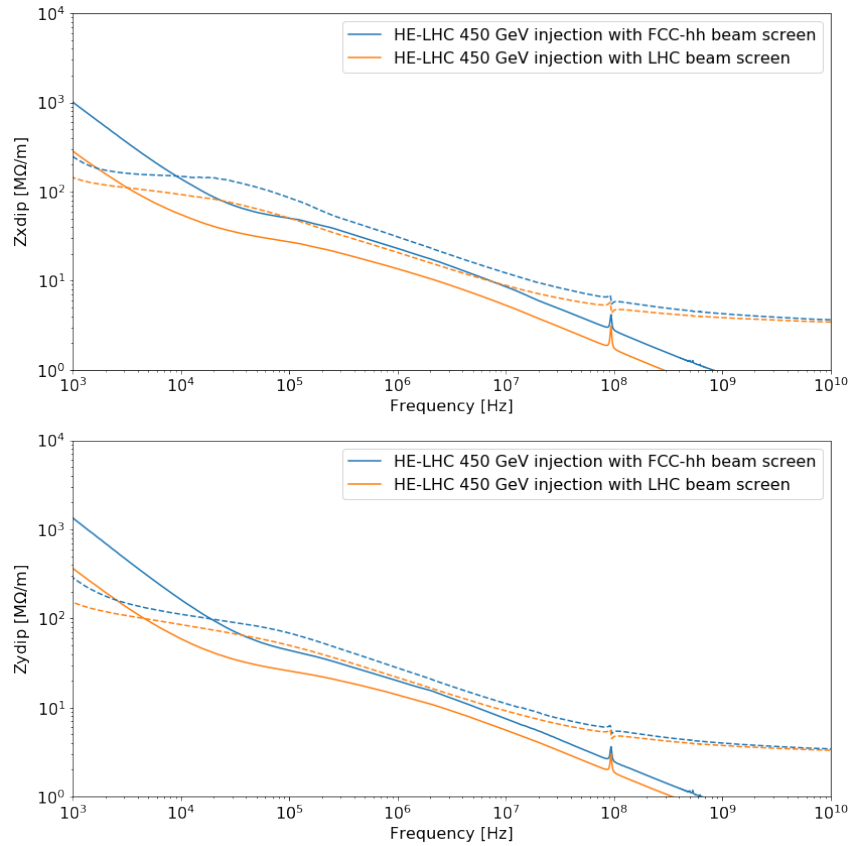


Figure 1: Transverse dipolar impedance at 450GeV injection energy. Solid line: real part. Dashed line: imaginary part.

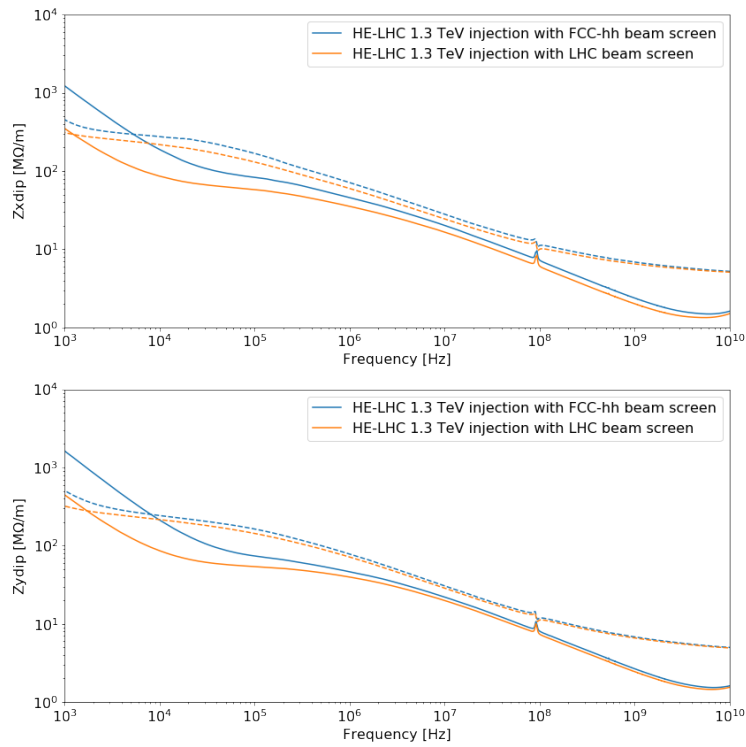


Figure 2: Transverse dipolar impedance at 1.3 TeV injection energy.
Solid line: real part. Dashed line: imaginary part.

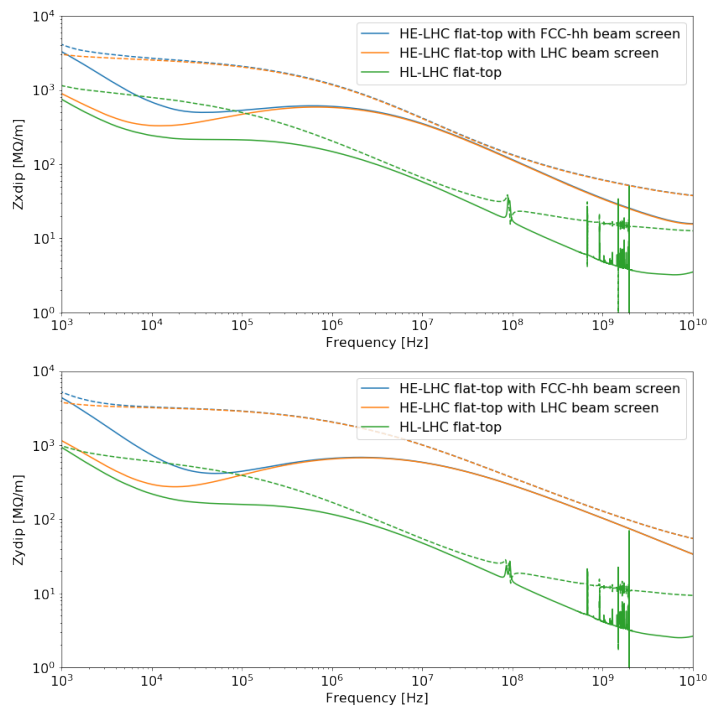


Figure 3: Transverse dipolar impedance at 13.5 TeV top energy.
Solid line: real part. Dashed line: imaginary part.

For the top energy case shown in Figure 3, the green curve shows the HL-LHC impedance model for comparison. For frequencies above 100 MHz, a factor of 10 is present between the HL-LHC and the HE-LHC impedances due to tighter physical

collimator gaps. The HL-LHC impedance model also includes the crab cavities contribution as showed by a series of resonances in the GHz region. The crab cavities contributions were not taken into account for the HE-LHC impedance simulations.

2.21.5 Elements contributions to impedance

As seen previously the contributions of the beam screen and the collimators to the total impedance varies with frequency. Figure 4 and Figure 5 show the respective contributions of these elements for frequencies from 1 kHz to 10 GHz, for the 1.3 TeV injection case and the 13. TeV top energy case. The collimator contribution is split between the geometric impedance (in blue) and the resistive wall impedance (in red). The beam screen contribution is split between the 50 K cooled sections of the beam screen covering 80% of the machine length (in pink) and the warm beam screen (in cyan).

For the 1.3 TeV injection energy case depicted in Figure 4, the real part of the beam screen impedance dominates for frequencies below 100 kHz. However, the imaginary part is dominated by the collimator impedance for all frequencies. The geometric contribution of the collimators dominates the imaginary part for high frequencies (above 1 GHz).

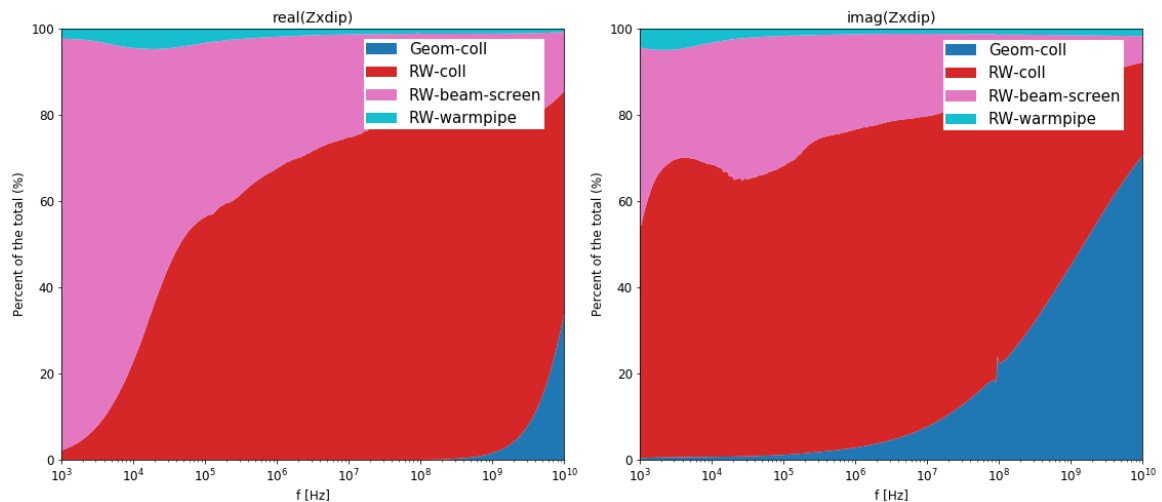


Figure 4: Transverse horizontal impedance contributions (in %) as a function of frequency for the 1.3 TeV injection case.

For the 13.5 TeV top energy case depicted in Figure 5, the distribution of the impedance follows the same behavior as in the injection energy case. However it can be noted that the resistive wall contribution of the collimators is even more important in this case.

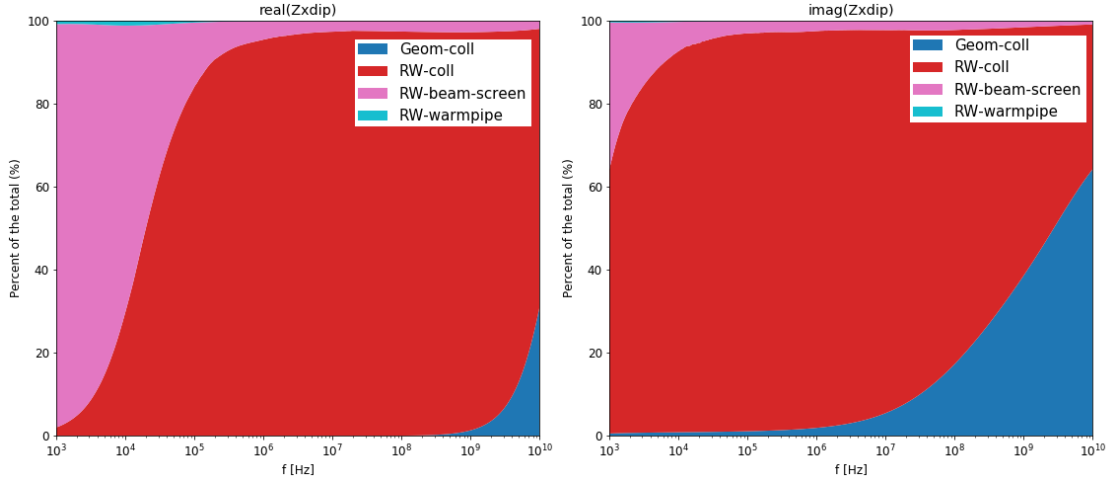


Figure 5: Transverse horizontal impedance contributions (in %) as a function of frequency for the 13.5 TeV top energy case.

We studied three scenarios of the injection energy: 450, 900, and 1300 GeV. The parameters of each scenario are summarized in Table 2. The advantage of the first scenario is that the injection energy can be provided by the current SPS, while the other two would require an upgrade of the injector. Its downside is the very tight aperture constraint at injection. It might be challenging if at all possible to ensure and maintain the hierarchy of the collimation and injection protection systems within the tight aperture constraints. The last option, 1300 GeV, seems preferable from the injection protection point of view and offers sufficient room to build the collimator hierarchy, but would require an expensive superconducting SPS and transfer lines.

From the impedance point of view, the injection energy of 1.3 TeV option is the most challenging one (Fig. 2). The increase of impedance with injection energy is caused by tightening of the collimator gaps, which follow the physical beam size and thus shrink as $E^{-1/2}$, with the E the energy. Compared to HL-LHC injection impedance of all studied options is higher due to smaller reference emittance.

However and similarly to the LHC and HL-LHC cases, the impedance budget of HE-LHC is higher at top energy because of the tighter collimators gaps required to ensure the beam cleaning efficiency. The collimators are the dominant contributor for a large range of frequencies. As the impedance budget is driving the coherent beam stability, alternative collimation systems could complement the present collimators. For example the use of an electron lens for halo collimation is proposed for HL-LHC [13] and could be used in HE-LHC as well.

2.21.6 Beam stability and Landau damping

The impedance driven modes may lead to coherent beam instabilities in hadron colliders, the Landau damping is a passive mechanism to stabilize the beam through the diversification of oscillations frequencies of the particles in the beams (tune spread). In order to be effective, the tune spread must overlap with the frequency of the unstable collective mode that has to be stabilized. At the LHC instability thresholds are evaluated by computation of the dispersion integral for a given detuning $\omega_{x,y}(J_x, J_y)$ and particle distribution $\psi(J_x, J_y)$ as a function of the transverse actions J_x and J_y in each plane [14]:

$$3 \quad SD^{-1} = \frac{-1}{\Delta Q_{x,y}} = \int_0^{\infty} \frac{J_{x,y}}{\Omega - \omega_{x,y}(J_x, J_y)} \frac{d\psi}{dJ_{x,y}} dJ_x dJ_y \quad (3)$$

The solution of Eq. 3 provides the complex tune shifts at the stability limits for each frequency Ω defining the so-called stability diagram. Any non-linearities acting on the beams, such as beam-beam interactions, space charge and electron cloud, introduce a tune spread in the beams. At the LHC, Landau octupole magnets are used to provide enough tune spread to stabilize the beams by Landau damping mechanisms [15]. In particular, a linear detuning from octupoles magnets has been considered in the following analysis in order to evaluate the single beam stability by using the PySSD code [16] for HE-LHC.

The linear detuning from the octupoles magnets has been computed as [18]:

$$4 \quad \begin{aligned} \Delta Q_x &= a \times I_x \varepsilon + b \times I_y \varepsilon \\ \Delta Q_y &= b \times I_x \varepsilon + a \times I_y \varepsilon \end{aligned} \quad (4)$$

where I_x and I_y are the transverse actions normalized to the physical beam emittance and the coefficients a and b are defined as:

$$5 \quad \begin{aligned} a &= 3.28 I_{oct} [\text{A}] \times \varepsilon_n [\text{m}] / E_{beam}^2 [\text{TeV}^2] \\ b &= -2.32 I_{oct} [\text{A}] \times \varepsilon_n [\text{m}] / E_{beam}^2 [\text{TeV}^2] \end{aligned} \quad (5)$$

where the LHC octupoles type has been considered for the evaluation of the coefficients a and b . The stability threshold is quantified in terms of the octupole current in the present LHC Landau octupole system, consisting in 168 octupoles, arranged in two families [15].

2.21.6.1 *Injection energy*

We studied three scenarios of the injection energy: 450, 900, and 1300 GeV. The last option, 1300 GeV, seems preferable from the injection protection point of view and offers sufficient room to build the collimator hierarchy, but would require an expensive superconducting SPS and transfer lines.

From the impedance point of view, the 1.3 TeV option is the most challenging one (Fig. 6). The increase of impedance with injection energy is caused by tightening of the collimator gaps, which follow the physical beam size and thus shrink as $E^{-1/2}$. Compared to HL-LHC injection impedance of all studied options is higher due to tight collimation settings.

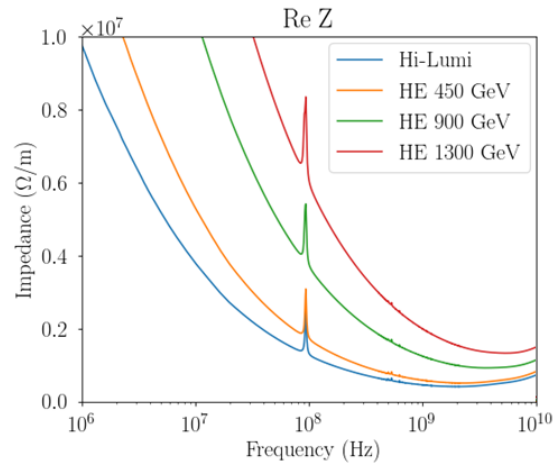


Figure 6: Impedance of HE-LHC at injection exceeds that of HL-LHC for all scenarios. The 1.3 TeV option is the most critical from the impedance point of view.

The tune footprints at injection energy $E = 1.3$ TeV for 6σ particles are shown in Fig. 7 for positive (red line) and negative (blue line) octupole polarity powered with the maximum achievable current of ± 550 A. The footprints were computed by using the COMBI code [16]. In this configuration a maximum tune spread of $\Delta Q_{x,y} \approx 0.085$ both in horizontal and vertical plane is achieved.

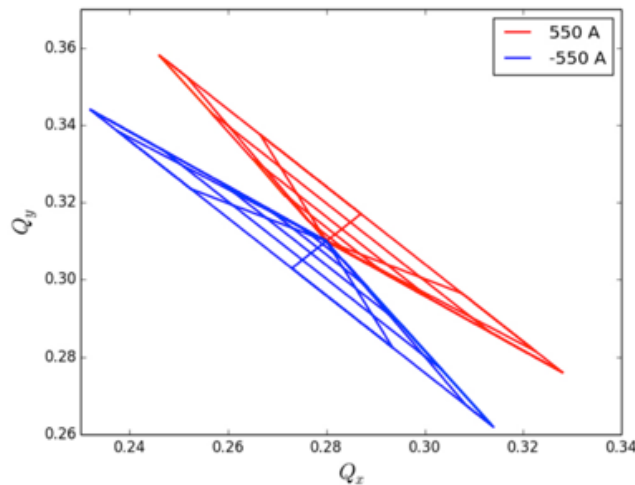


Figure 7: Tune footprint at 1.3 TeV injection energy for positive (red line) and negative (blue line) octupole polarity.

We have studied the coupled-bunch beam stability in the presence of the transverse feedback, chromaticity, and Landau octupoles using the NHT [19], DELPHI [20], and BIM-BIM [18] numerical solvers. The wakefields for NHT and BIM-BIM were extrapolated from the impedance model under the assumptions described before (see Sec. 1.1.4). The codes agree in their estimates, and in this Section we will present the results interchangeably. Since the lattice of HE-LHC is still under discussion, for the purpose of this study we assumed HL-LHC tunes and optics functions [21]; the key parameters for these studies are summarized in Table 8. The stability is quantified in

terms of growth rate of the most critical unstable mode and the amount of stabilizing octupole current required to suppress that mode. For the octupole threshold we assume the same stability diagram as in HL-LHC with negative polarity of the octupoles, quasi-parabolic transverse and normal longitudinal beam distribution, and zero coupling between the two transverse planes.

Table 8: Main beam and optics parameters

<i>Machine state</i>	<i>Injection</i>	<i>Flat-top</i>
Beam energy	450, 900, 1300 GeV	13.5 TeV
Tunes: x, y, s	0.31, 0.32, 0.005	0.31, 0.32, 0.002
Norm. emittance, rms	2 μm	2 μm
Bunch length, rms	9 cm	9 cm

NHT uses a unit convention, where mode frequency shifts $\text{Im} \Delta\omega$ and damper gain g are normalized by the synchrotron frequency ω_s :

$$\begin{aligned}\Gamma[\text{turns}^{-1}] &= 2\pi Q_s \text{Im} \Delta\omega / \omega_s, \\ d[\text{turns}^{-1}] &= 2\pi Q_s g.\end{aligned}\tag{6}$$

Figure 8 presents the results of the numerical simulation for the three injection energies, nominal HE-LHC intensity and number of bunches, two types of beam screens: LHC- and FCC-type. With the current LHC beam screen the growth rates remain small in the range of chromaticities $Q' = 5 - 20$ and for a damper gain higher than 1/50 to 1/100 inverse turns for all three cases. For these chromaticity and damper settings the octupole currents required to stabilize the beam remain relatively low: $I_{\text{oct}} < 10$ A for all scenarios.

A damper gain of 1/50 turns^{-1} or more is required in order to keep the instability growth rates at the same level for a tighter FCC-type beam screen, due to its higher impedance at low frequencies (Sec. 1.1.4). The most challenging option seems to be the lowest injection energy, where a feedback as fast as 25 turns is required. Provided sufficient damper gain and chromaticity in the range of 5 – 20, the octupole current required to stabilize the beam is small $I_{\text{oct}} < 10$ A.

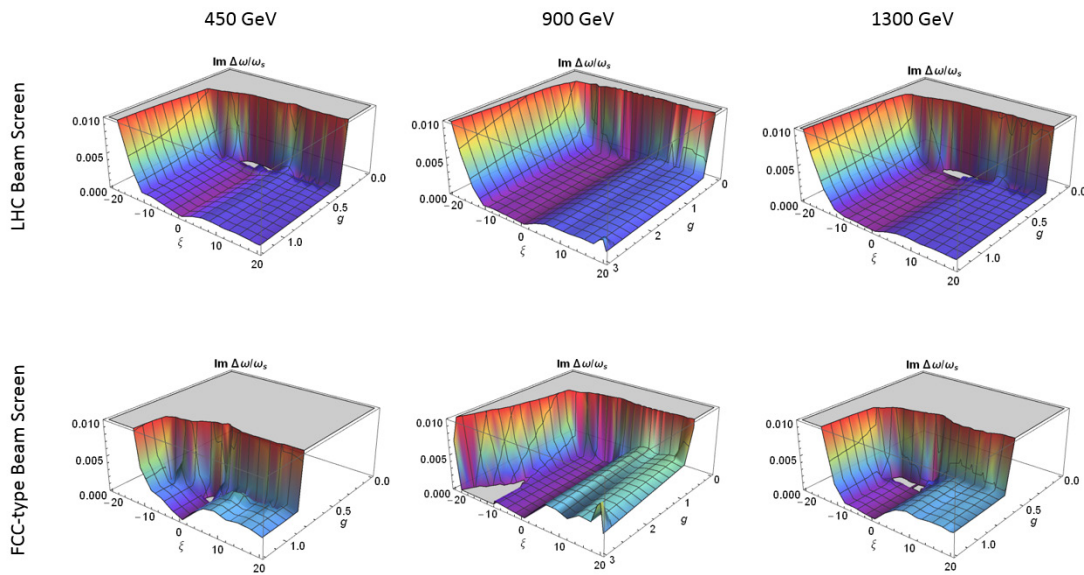


Figure 8: Growth rate of the most unstable couple-bunch mode for the LHC beam screen and FCC-type beam screen as a function of normalized gain (defined above) and chromaticity. 2748 bunches, 2.2×10^{11} ppb.

Apart from parameter scans for the nominal intensity, we also performed intensity scans to determine the safety margin with respect to couple-bunch TMCI and traditional head-tail instabilities. The mechanism and scaling estimates are discussed in detail in Sec. 1.1.3. We studied numerically the most critical case of $Q' = 0$ and several realistic damper gains. For a FCC-type beam screen there is no safety margin with a damper gain of 50 turns or below; a 25 turn gain is needed for a factor of two margin. The margin can be significantly improved with a bigger beam screen: for a LHC-type there is more than a factor of two margin for the nominal beam intensity (Fig. 9).

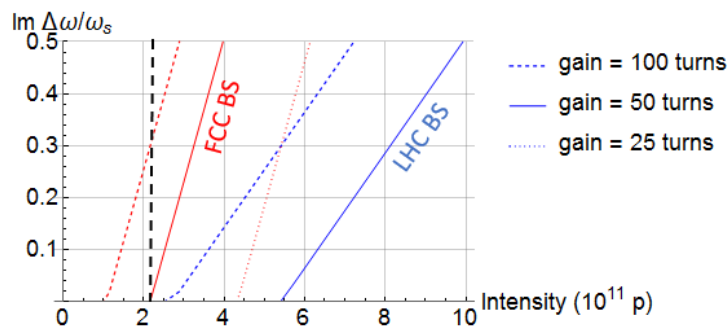


Figure 9: Stability thresholds as a function of damper gain. The safety margin in terms of beam intensity is small with a tighter beam screen and safe operation requires a higher damper gain. Growth rate for FCC beam screen are depicted in red, LHC – in blue; nominal intensity of 2.2×10^{11} ppb is shown by a black dashed line. $E = 1.3$ TeV, 2748 bunches, $Q' = 0$, no octupoles.

2.21.6.2 Flat top energy

The flat-top at 13.5 TeV is expected to be the most critical case from the machine impedance point of view. Since at the moment there is no solid baseline for HE-LHC collimator settings yet, we have assumed a collimator model similar to HL-LHC in order to create the impedance model. Based on the input from the collimation and machine protection [22] we put the primary collimators in IR-7 at 5σ and the secondary – at 6σ (Table 7). Note that these conservative estimates might be relaxed based on the outcome of machine protection studies.

Due to the increased beam rigidity at flat top energy ($E = 13.5$ TeV) the effectiveness of the octupole magnets is reduced. For a normalized beam emittance $\varepsilon = 2.5$ $\mu\text{m}\cdot\text{rad}$, in order to achieve a similar amount of tune spread as in the LHC with design beam parameters ($E = 7$ TeV and normalized beam emittance $\varepsilon = 3.75$ $\mu\text{m}\cdot\text{rad}$), an octupole current of 3080 A would be required considering the LHC octupole magnet technology and same averaged β -function at the octupoles. This can be easily evaluated rescaling linearly the octupole detuning with amplitude with respect to the LHC beam energy and emittance: $(\gamma^{\text{HE-LHC}}/\gamma^{\text{LHC}})^2 \times (\varepsilon^{\text{LHC}}/\varepsilon^{\text{HE-LHC}}) = 5.6$. With these assumptions, for HE-LHC collision energy, 940 Landau octupoles would provide the same amount of tune spread as in the LHC. This is shown in Fig. 10 where the LHC tune spread is represented by the black line and the HE-LHC footprint for 940 Landau octupoles is represented by the green line. As visible the tune spread expected for LHC is fully recovered. For completeness, the tune footprints for HE-LHC are also shown considering a current of ± 550 A for positive (red line) and negative (blue line) octupole polarity.

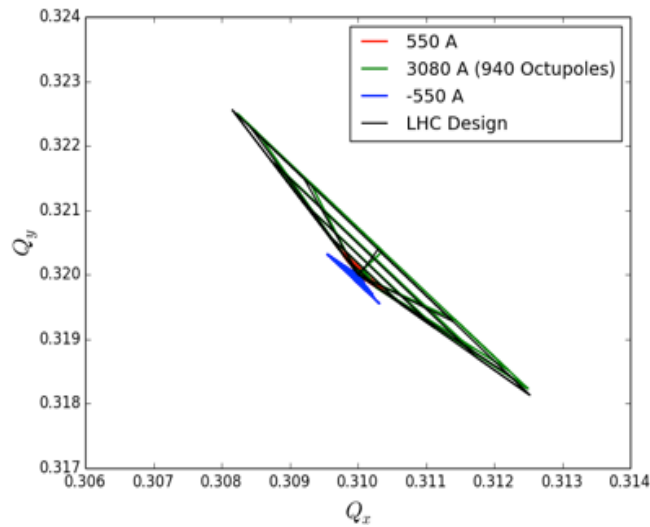


Figure 10: Tune footprints (till 6σ particle) at flat top energy (normalized beam emittance $\varepsilon=2.5$ $\mu\text{m}\cdot\text{rad}$) for positive (red line) and negative (blue line) octupole polarity compared to LHC tune footprint with design parameters (black line). The green line represents the HE-LHC tune footprint for a current of 3080 A.

The impedance of the machine at 13.5 TeV flat-top is dominated by its collimator contributions (Sec. 1.1.4) and is not affected significantly by the choice of the beam screen at the frequencies relevant for single-bunch motion (Fig. 5). Due to tighter

collimator gaps, which scale with the beam size, the coupled-bunch instability growth rate might be rather large at the top energy (Fig. 11). Still the growth rate remains below $10^{-2} \omega_s$ for $Q' > 5$ and damper gain higher than 100 turns. Even where the growth rate is relatively low, the octupole current required to stabilize the beam is large, since it increases as $1/\gamma^2$. It is estimated to reach at least 2000 A for $2 \mu\text{m}$ normalized emittance and $Q' \sim 10$ (Fig. 12), which is consistent with the current HL-LHC prediction of ~ 500 A where the top energy is 2 times lower (7 TeV).

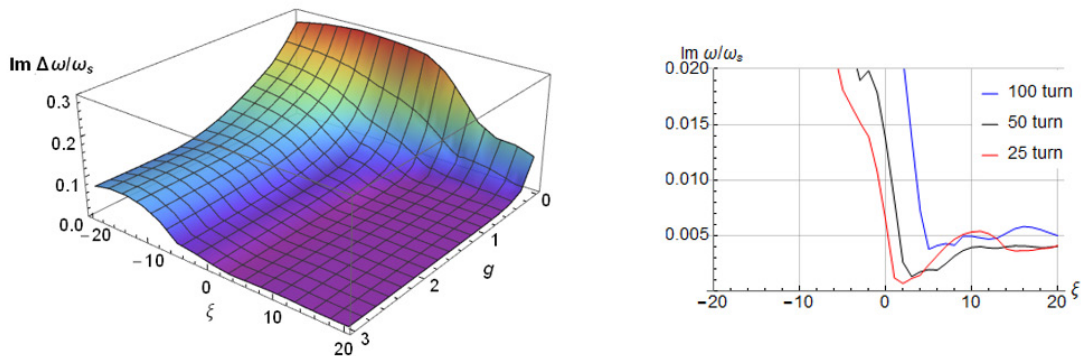


Figure 11: Growth rate of the most unstable coupled-bunch mode as a function of normalized gain and chromaticity. 13.5 TeV, 2748 bunches, 2.2×10^{11} ppb.

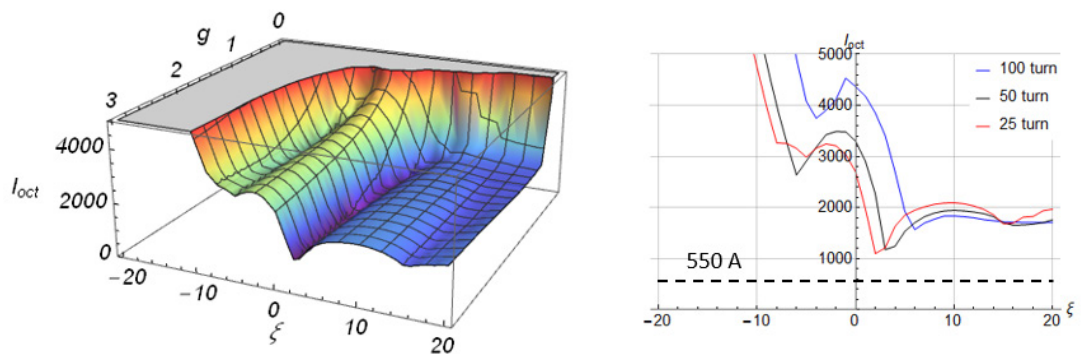


Figure 12: The octupole current required to stabilize the beam at flat-top exceeds the capabilities of the LHC octupoles. Left - octupole threshold as a function of normalized gain and chromaticity; right - cross-sections for several damper gains. The present octupole strength limit is shown by a black dashed line. 13.5 TeV, 2748 bunches, 2.2×10^{11} ppb, $\epsilon_n = 2.0 \mu\text{m}$, negative octupole polarity.

From the past operational experience at LHC, a factor of two safety margin in the octupole current is recommended to ensure smooth operation. The amount of octupole current available at LHC – 550 A – is clearly insufficient for that purpose, lacking nearly an order of magnitude. Several options can be considered to tackle this problem: first, one can think of further reducing the machine impedance. Since the main contribution at flat-top comes from the collimator system, it is the primary candidate for improvement. The restive wall contribution of collimators could be further improved by utilizing novel low-resistivity coatings and the geometric part – by optimizing the collimator geometry. This

approach allows acting on both the real and the imaginary parts of impedance, thus lowering both the instability growth rate and the tune shift of unstable modes and reducing the octupole threshold.

Second, one might consider installing additional octupole magnets or upgrading the existing ones in order to increase their current. Figure 13 shows the stability diagrams obtained by the PySSD code [16] along with the most unstable single-bunch modes, computed using BIM-BIM [18] using the wake fields extrapolated from the impedance model under the assumptions described in Sec. 1.1.4. For positive chromaticity an octupole current of ~ 1875 A (~ 570 Landau octupole magnets) would be sufficient to damp the expected single bunch and multi bunch mode (Fig. 12), while a current of ~ 3281 A (~ 1000 Landau octupole magnets) is required to damp the expected single bunch mode for $Q' \sim -5$ to -6 . Considering the maximum achievable current of 720 A for the HL-LHC octupole magnet technology, the number of required octupole magnets can be reduced to 440 and 770 in the two cases, respectively. Compared to the number of octupoles in the LHC, the two cases correspond to an increase of the octupole magnets by factor of 2.62 and 4.58 respectively.

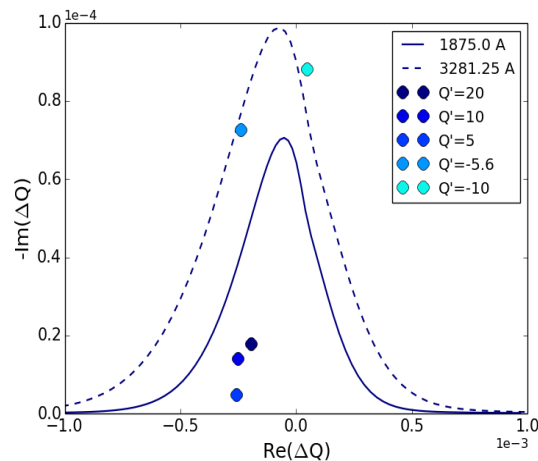


Figure 13: About 2000 A of octupole current is required to stabilize the beam at the top energy of 13.5 TeV. The most unstable single bunch modes were calculated by using the BIM-BIM code for different chromaticities. A normalized beam emittance of $2.0 \mu\text{m}\cdot\text{rad}$ has been considered with a transverse feedback gain of 50 turns.

Another possible option is to optimize the machine focusing optics. For example, a telescopic optics can increase β -functions in the octupoles, increasing Landau damping. In the HL-LHC the telescopic squeeze increases the octupole footprint by a factor of two. This procedure might significantly reduce the number of additional octupole magnets required for HE-LHC. In order to fully benefit from it one will need to implement the squeeze during the energy ramp. This ramp-and-squeeze procedure may be technically challenging, and its feasibility and reliability has to be studied in detail.

Finally, more effective alternatives for Landau damping for high energetic hadron beams, such as electron lens [23] or RF Quadrupoles [24, 25] should be explored and discussed also in terms of the impact of such devices on dynamic aperture. Compared to octupoles, an electron lens offers a more efficient way to stabilize at high energies, because the tune spread it creates decreases only linearly with energy: $1/\gamma$ vs $1/\gamma^2$ for

octupoles. According to tracking simulations, in a real accelerator lattice the dynamical aperture improves if the octupole are replaced with an electron lens producing the same tune spread [23]. Since the spread is created by the core of the beam distribution, the electron lens stability diagram is also more robust than the octupole one, with depends on the population of the tails [26].

Electron lenses have been used in the past to create large tune spreads up to 10^{-2} and improve beam stability in Tevatron [27] and RHIC [28]. Preliminary estimates show that using an electron lens of existing HL-LHC design [13] (planned for halo cleaning), one can attain a tune spread of up to 5×10^{-3} with moderate electron currents (Table 9). The resulting stability diagram significantly exceeds the octupole one, allowing damping of all unstable couple-bunch modes at flat-top with a large safety margin (Fig. 14).

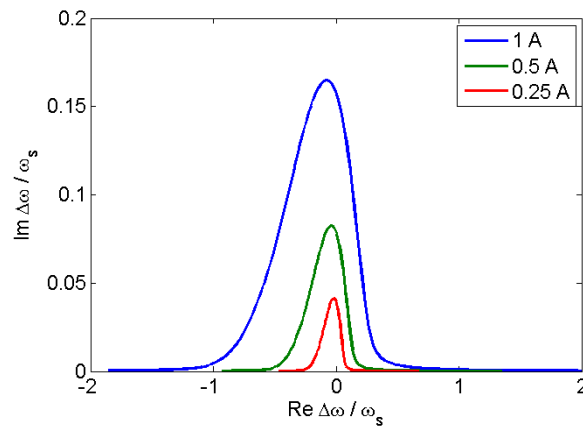


Figure 14: Stability diagrams for different currents in electron lens. $E = 13.5$ TeV, 2748 bunches, 2.2×10^{11} ppb, $\epsilon_n = 2.0$ μm .

Table 9: Parameters of a Gaussian electron lens for Landau damping in the HE-LHC at the top energy

<i>Parameter (Constraint)</i>	<i>Value</i>	<i>Comment</i>
Current density	$< 2\text{-}10$ A/cm ²	Present technology limit
Electron current	< 1 A	HL-LHC E-Lens: up to 5 A
Electron beam length	3 m	
Electron energy	10 kV	
Max field ratio	$B_m / B_g < 4.0$ T/0.2 T = 20	HL-LHC E-Lens design
Electron beam size	0.4 – 2.0 mm	
Beta-function	240 m	40 m downstream IP-4
Proton beam energy	13.5 TeV	
Norm. emittance	2.0 μm	
Proton beam size	0.18 mm	
Transverse distribution	Gaussian	

2.21.6.3 *Electron Cloud effects*

The build-up of electron clouds may lead to coherent beam instabilities, through the interaction between the beam and the electrons. In order to assess the risk of electron

cloud induced instabilities, simulation studies identifying the conditions for electron cloud build-up have been performed.

2.21.6.4 *Effect of beam screen design*

The effect of two proposed beam screen options on electron cloud build-up has been studied in the arc dipoles with a field of 16 T. The beam screen designs that have been considered are an LHC-type beam screen with a saw-tooth structure in the impact area of the synchrotron radiation for reduced photon reflection [29] with the half apertures scaled to 14 and 19 mm in the vertical and horizontal plane respectively, and the FCC beam screen with ante-chambers for the synchrotron radiation and shielding of the pumping slots [30,31].

Photoelectrons produced by the impacting synchrotron radiation can play an important role in seeding the build-up, as is believed to be the case e.g. in the LHC [32]. Their effect could be even more important in the HE-LHC, where the number of synchrotron photons produced would be nearly double that of the current LHC, similar to the HL-LHC, and, due to the increased beam energy, a larger fraction of the photons would have an energy above the copper work function and could potentially produce photoelectrons.

In the HE-LHC dipoles, where the magnetic field lines confine the electron cloud build-up to vertical stripes around the beam, mainly photoelectrons produced at the top and bottom of the beam screen can contribute to the build-up. The transverse distributions of absorbed photons in the HE-LHC arcs have been estimated through simulations with the SynRad3D code [33] for the two beam screen options [34]. The amount of photons absorbed respectively on the top and bottom of the beam screen make up less than a percent of the total number of absorbed photons for both beam screen options, and for the FCC beam screen is roughly a factor of ten smaller than for the LHC type beam screen. The number of photoelectrons depends in addition on the photoelectron yield of the absorbed photons, which is not well known for the case in question. In the absence of an experimental estimate of the yield, the number of absorbed photons can be used as an upper limit for the number of photoelectrons.

Electron cloud build-up simulations have been set up with photoelectron seeding considering the results of the photon absorption studies to evaluate the effect of the beam screen design. Central electron densities as a function of the secondary electron yield (SEY) of the chamber surface have been estimated from the simulations, as shown in Figure 15. The threshold electron density for inducing single-bunch instabilities has been evaluated with analytical calculations [35] and beam dynamics simulations to around 10^{12} m^{-3} at flat top energy [36]. The electron density lies below the instability threshold at typical values of the SEY for both chamber options, however the FCC beam screen gives rise to a lower density, reflecting the smaller amount of photoelectron seeding. Also the heat load produced by the electron cloud, shown on the left in Figure 15, which has to be counteracted by the cryogenic system, is lower for the FCC beam screen, which is hence overall the more favourable beam screen option.

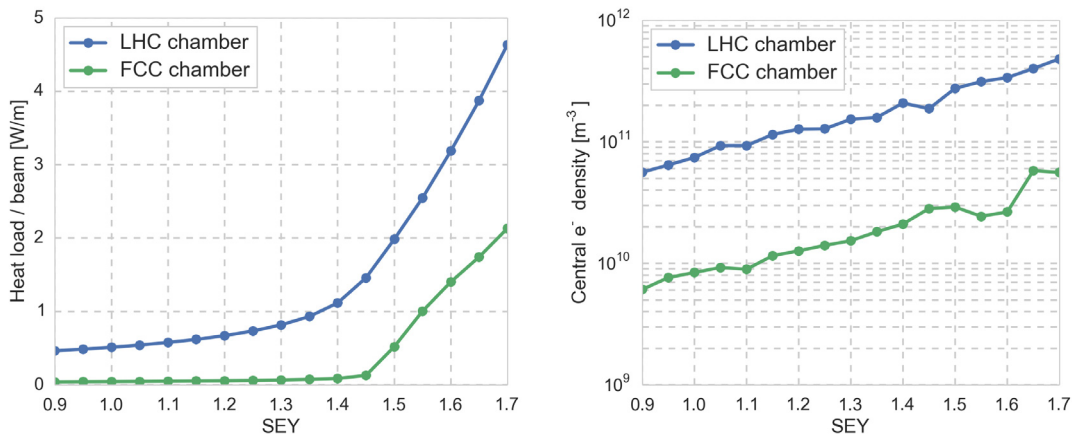


Figure 15: Comparison of the heat load and central electron density for the scaled LHC and the FCC beam screens for the nominal beam option.

2.21.6.5 *Effect of beam configuration*

Electron cloud build-up has been studied for the FCC beam screen in two main arc components: dipoles with a 16 T field and quadrupoles with a 220 T/m gradient, at injection (1.3 TeV) and at flat top energy. In addition to the nominal beam described in Table 1, two alternative beam options with the same total current as for the nominal beam have been considered: a beam with 12.5 ns bunch spacing, a bunch intensity of 1.1×10^{11} protons and normalized transverse emittances of 1.25×10^{-6} m, and a beam with 5 ns bunch spacing, bunch intensity 0.5×10^{11} and normalized transverse emittances of 0.5×10^{-6} m.

The estimated central densities for the three considered beam options at injection are displayed in Figure 16 for dipoles and quadrupoles respectively. The beam is more prone to instabilities at injection, where the threshold electron density for single-bunch instability has been estimated to around 10^{11} m⁻³ [36]. Taking into account that dipoles and quadrupoles cover around 80% and less than 10%, respectively, of the machine circumference, the nominal beam option could be prone to electron cloud induced instabilities if the SEY of the surface is above 1.4. Suppressing the electron cloud build-up with a low-SEY surface treatment, such as an amorphous carbon coating, would efficiently mitigate the occurrence of such instabilities. Also for the 12.5 ns beam option, electron densities above the threshold can be avoided by keeping the SEY at 1.1 or below. With the 5 ns beam option densities above the threshold can build up even for lower values of the SEY – this beam can be a viable option for the machine only with a surface treatment that guarantees a SEY no larger than unity.

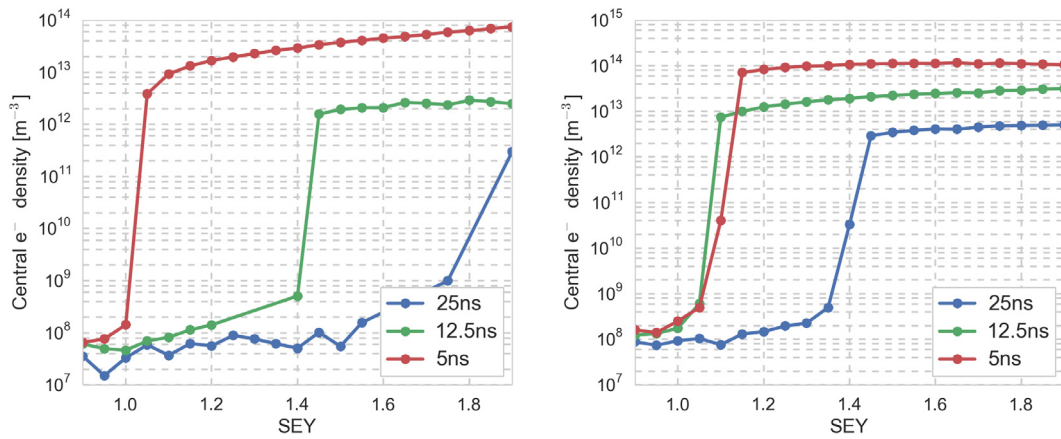


Figure 16: Central electron density as a function of SEY at injection energy for three different beam options in arc dipoles, on the left, and arc quadrupoles, on the right.

2.21.6.6 Evolution during a fill

Since electron cloud effects do not necessarily scale linearly with the bunch intensity, their evolution can change with the burn-off during a fill with luminosity production. This effect has been estimated with build-up studies, with decreasing bunch intensity and emittance. The central densities for the corresponding bunch intensities in dipoles and quadrupoles are shown in Figure 17. In dipoles only a mild dependence with intensity can be seen, whereas in the quadrupoles the multipacting threshold is seen to decrease and the central density increase with decreasing bunch intensity. In the absence of a surface treatment instabilities during fills could occur due to this effect, however a low-SEY surface treatment would be sufficient to prevent the build-up also for lower bunch intensities.

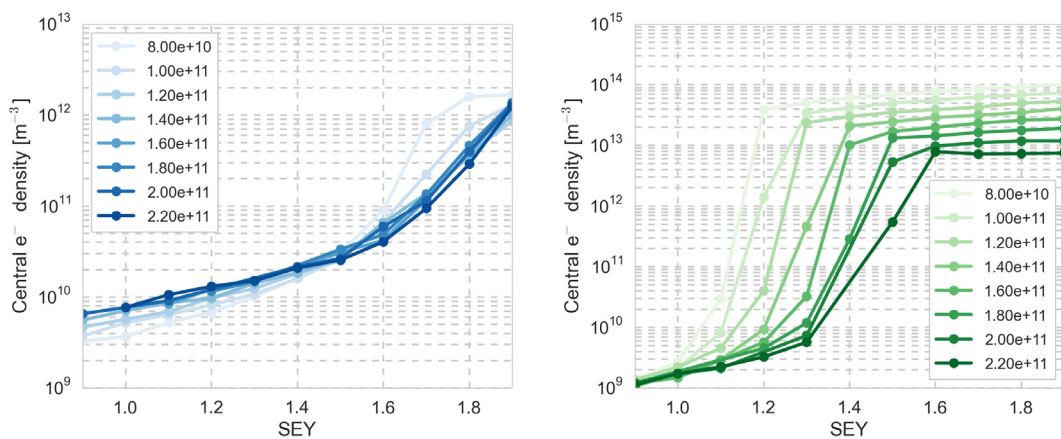


Figure 17: Central electron densities as a function of the SEY for the nominal beam with decreasing bunch intensity and emittance in arc dipoles, on the left, and arc quadrupoles, on the right.

2.21.7 Conclusion

Based on a set of preliminary parameters known at the time of writing this contribution, the impact of single beam transverse collective effects was addressed for HE-LHC and clear challenges identified in the design and baseline parameters have been identified: the instability thresholds are predicted to be low with an impedance model that accounts for the beam screens and the collimators and all available means to damp instabilities will need to be investigated to keep sufficient stability margin at both injection and flat top energies. A low SEY coating would be important to mitigate electron cloud related issues.

2.21.8 Acknowledgements

Work supported by the Swiss State Secretariat for Education Research and Innovation SERI.

We would like to thank the CERN collimation team for providing us with the collimator settings, in particular Roderik Bruce, Matthew Crouch and Stefano Pieloni.

2.21.9 References

1. E. Todesco, F. Zimmermann et al, "The High-Energy Large Hadron Collider", proceedings of the 2010 EuCARD-AccNet-EuroLumi Workshop, Malta (2010).
2. F. Ruggiero, in Ch. 5, collective effects section, LHC Design Report, report CERN-2004-003-V-1 (2004).
3. F. Ruggiero and F. Zimmermann. "Consequences of the direct space charge effect for dynamic aperture and beam tail formation in the LHC." *Particle Accelerator Conference, 1999. Proceedings of the 1999*. Vol. 4. IEEE, 1999.
4. A. Oeftiger. "Single-Bunch Stability With Direct Space Charge." *ICFA mini-workshop on Impedances and Beam Instabilities in Particle Accelerators*, Benevento, Italy (2017). Poster contribution, <https://cds.cern.ch/record/2290575>.
5. M. Benedikt et al, "FCC-hh Hadron Collider – Parameter Scenarios and Staging Options", proceedings of IPAC 2015, Richmond, VA, USA (2015).
6. "High-Luminosity Large Hadron Collider (HL-LHC): Technical Design Report V. 0.1", report CERN-2017-007-M (2017).
7. "LHC Design Report", report CERN-2004-003-V-1, p. 98-100.
8. N. Mounet, "The LHC Transverse Coupled-Bunch Instability", PhD thesis, Ecole Polytechnique, Lausanne (2012).
9. N. Biancacci et al., "The HL-LHC Impedance Model and Aspects of Beam Stability", proceedings of IPAC 2016, Busan, South Korea (2016).
10. M. Crouch, private communication, 11/10/2017
11. E. Quaranta et al., "Towards Optimum Material Choices for HL-LHC Collimator Upgrade", proceedings of IPAC 2016, Busan, South Korea (2016).
12. S. Arsenyev and S. Antipov, "Impedance/stability/feedback consideration for FCC-hh and HE-LHC", FCC-hh and HE LHC injector considerations meeting, CERN, Switzerland, 21/10/2017, <https://indico.cern.ch/event/667297/> (2017).
13. G. Stancari, et al., Conceptual design of hollow electron lenses for beam halo control in the Large Hadron Collider, CERN-ACC-2014-0248 (2014).
14. S. Berg, F. Ruggiero, "Landau Damping with two-dimensional betatron tune spread", CERN, Geneva, Switzerland, CERN- SL (AP) 71, Dec. 1996.

15. J. Gareyte *et al.*, "Landau Damping, Dynamic Aperture and Octupoles in LHC", CERN, Geneva, Switzerland, LHC Project Report 91, Apr. 1997.
16. X. Buffat *et al.*, "Stability Diagrams of colliding beams", Phys. Rev. ST Accel. Beams 17 111002, 2014.
17. T. Pieloni, EPFL Thesis 4211 (2008).
18. X. Buffat, EPFL Thesis 6321 (2015).
19. A. Burov, Nested Head-Tail Vlasov Solver, Phys.Rev.ST Accel. Beams 17 (2014) 021007
20. N. Mounet. DELPHI: an analytic Vlasov solver for impedance-driven modes. HSC Meeting, CERN, Apr. 2014
21. R. Tomas, L. Medina, Parameter update for the nominal HL-LHC: Standard, BCMS, and 8b+4e, HL-LHC TC, CERN, Mar. 2017 (2017)
22. R. Bruce, M. Crouch, private communication
23. V. Shiltsev, *et al.*, Landau Damping of Beam Instabilities by Electron Lenses, Phys.Rev.Lett. 119 (2017)
24. A. Grudiev, Radio frequency quadrupole for Landau damping in accelerators, Phys. Rev. Spec. Top. Accel. Beams 17 (2014).
25. M. Schenk *et al.*, "Analysis of transverse beam stabilization with radio frequency quadrupoles", PRSTAB 20, 104402 (2017).
26. N. Biancacci, E. Metral, C. Tambasco, Effect of tail cut and tail population on octupole stability threshold in the HL-LHC, HSC Meeting, CERN, Nov. 2015 (2015)
27. K. Bishofberger, Successful Beam-Beam Tuneshift Compensation, FERMILAB-THESIS-2005-105 (2005)
28. X. Gu, *et al.*, Phys. Rev. Accel. Beams 20, 023501 (2017).
29. O. Brüning *et al.*, "LHC Design Report, Volume v.1: the LHC Main Ring", CERN-2004-003-V-1 (2004).
30. C. Garion, "FCC-hh beam screen studies and beam screen cooling scenarios," FCC Week 2016, Rome (2016).
31. I. Bellafont "Studies on the beam induced effects in the FCC-hh", EuroCirCol meeting, CERN, Oct. 2017 (2017).
32. P. Dijkstal *et al.*, "Simulation studies on the electron cloud build-up in the elements of the LHC Arcs at 6.5 TeV", CERN-ACC-NOTE-2017-0057 (2017).
33. G. Dugan, D. Sagan, "Synrad3D photon propagation and scattering simulations", Proc. Joint INFN-CERN-EuCARD-AccNet Workshop on Electron-Cloud Effects, La Biodola, Isola d'Elba, Italy, 5–9 June 2012, pp. 117–129, CERN-2013-002.
34. G. Guillermo *et al.*, "Simulating proton synchrotron radiation in the arcs of the HE-LHC", HE LHC design meeting 07, CERN, Nov. 2016 (2016).
35. K. Ohmi, F. Zimmermann, E. Perevedentsev, "Wake-field and fast head-tail instability caused by an electron cloud", Phys. Rev. E65, 016502 (2001)
36. K. Ohmi, "Electron cloud thresholds in HE-LHC", HE LHC design meeting 08, CERN, Dec. 2016 (2016).

3 Workshop and Conference Reports

3.1 ICFA Mini-Workshop on Impedances and Beam Instabilities in Particle Accelerators 2017

M.R. Masullo¹⁾, S. Petracca²⁾, G. Rumolo³⁾

¹⁾ INFN Sezione di Napoli, Via Cinthia, 80126 Napoli, Italy

²⁾ University of Sannio, Piazza Roma, Pal. Bosco Lucarelli, 82100 Benevento Italy

³⁾ CERN, BE Department, 1211 Geneva 23, Switzerland

The ICFA Mini-Workshop on Impedances and Beam Instabilities in Particle Accelerators, was held in Benevento, Italy, from September 19 to September 22, 2017. The workshop was backed by a well assorted International Advisory Committee. The conference venue, the San Vittorino complex, is at the heart of the old town of Benevento. The workshop was supported and sponsored by several projects and networks (High Luminosity LHC, LHC Injectors Upgrade, LHC Collimation, ARIES), INFN (Napoli) and University of Sannio, and it was held under the auspices of the Italian Physical Society (SIF).

The main goal was to review relevant material in the field of impedances and beam instabilities and address recent advancements and breakthroughs. The workshop was attended by 84 participants from different laboratories all around the world, and more than a half were young accelerator physicists at the beginning of their careers. To best suit the young audience as well as the academic environment of the University of Sannio, speakers were requested to present their work providing an educational background of the subject, before highlighting also the novelties and challenges.

Given the timing, the workshop also provided an excellent setting to mark the occasion of two round anniversaries:

- 50 years of the Beam Coupling Impedance concept, introduced by Prof. Vittorio Vaccaro to describe the electromagnetic interaction of a particle beam with the external environment. Prof. Vaccaro entertained the audience with a historical talk describing the birth of the concepts of beam coupling impedance and stability charts. He was warmly thanked by the workshop participants and awarded a memorial plaque for his important achievements;
- 10 years of Francesco Ruggiero's passing away. F. Ruggiero was an outstanding accelerator physicist, who gave enormous contributions to the fields of impedances and instabilities, in particular by fostering the necessity of building detailed impedance models of machines and by working on the improvement of the models to describe beam instabilities. Applied to LHC, his vision led to the implementation of a strict impedance budget control during the phase of LHC design and the recognition of the relevance of electron cloud in the LHC beam parameter range. His foresight was instrumental to the design strategy of all future machines with challenging beam parameters.

The workshop featured plenary sessions with 48 talks and 5 final summary reports. A Poster Session was also organised, during which 22 posters were displayed in the Santa Sofia Cloister.

The general impression was that, although the subjects of beam coupling impedance and instabilities are 50 years old, they remain fashionable and up-to-date, because

- Old concepts need to be adapted and extended to new types of accelerators (e.g. FELs, plasma wake-field accelerators);
- Observations (or diagnostics) of new phenomena are made in running machines and need to be interpreted;
- Exploring new parameter regimes for upgrades or future machines requires original approaches and studies;
- Modeling and understanding of the phenomena related to impedance and instabilities are still making a steady progress benefiting from the advancement of technology;
- Open theoretical questions are still being intensively studied and widely debated.

In the field of beam coupling impedance, a few main points emerged from the various discussions:

- When a new device for either old or new accelerators is designed to its performance specifications, it is crucial to include impedance reduction at the design stage, possibly also including all considerations coming from multi-physics simulations associated to the impedance effects;
- The evaluation of beam coupling impedances of accelerator devices becomes increasingly challenging due to several factors:
 - Devices become more and more complicated and require accurate electromagnetic descriptions;
 - Accelerators have more and more demanding performance requirements, which requires special attention to their impedance budgets. This leads to the necessity of enacting a strictly low impedance design policy;
 - New regimes are being explored (e.g. frequencies beyond 100 GHz, small structures);
- Electromagnetic codes to calculate numerically beam coupling impedances and wake functions are becoming ever more powerful and new ones are being produced using more advanced computational techniques (e.g. the moving window). This allows the detailed analysis of structures that could not be efficiently simulated before.
- Beam based measurements of beam coupling impedances are of fundamental importance to understand and pinpoint the limitations of running machines, in particular to identify:
 - Missing impedances in the global impedance model of a certain machine;
 - Non-conformities or aging equipment leading to a degradation of impedance and possibly undesired effects on the beam;
 - Main contributors to the global impedance and relative mitigation techniques in view of upgrades.



Figure 1: Participants at the ICFA Mini-Workshop on impedances and beam instabilities in Benevento.

Establishing detailed impedance models of machines would be useless if this information could not be fed in beam dynamics calculations capable of assessing beam stability under the effect of the impedance.

Therefore, the techniques of modeling of beam instabilities were discussed at length and reviewed in detail:

- Two-particle models are still being used and extended to new cases (to include space charge, feedback systems, chromaticity). They are fairly simple, didactic and capable of unveiling the basic physics mechanisms behind coherent instabilities. An interesting generalization of these models is the circulant matrix formalism, which is based on a radial slicing of the longitudinal phase space making it effectively an N-particle model that takes into account the full complexity of the longitudinal structure of the beam in the study of the transverse stability;
- Vlasov solvers are widely used (e.g. MOSES, NHTS, DELPHI) to explore stability areas of complex machines in multi-dimensional parameter spaces. Their advantages and disadvantages were highlighted. They are:
 - Fast and suited to wide parameter scans;
 - Able to reveal the existence of slow growing modes;
 - Usually based on approximations/simplifications, necessary to find analytical solutions but which need to be kept in mind before drawing strong conclusions from their results.
- Macroparticle simulation codes are also widely used (e.g. PyHEADTAIL, Elegant, BLongD) and benefit from the increasing computing power that makes this approach more and more attractive. They:
 - Are relatively simple to implement and to be extended when additional effects need to be included (e.g. non-linearities, new driving terms, active loops, feedforward);
 - Provide full 6D monitoring of the beam evolution and their outputs can be used for building the signals that can be directly compared with beam

measurements (e.g. pick up signals, emittance evolution, Schottky analyses, BTF);

- Need an appropriate choice of the numerical parameters (based on physics as well as numerical considerations) and convergence studies;
- Are limited by hardware and computational time (e.g., memory, CPU time) and have a limited observation window, which may conceal slow growing modes.

It was underlined how, while the main driver of coherent instability is usually the machine beam coupling impedance, many other mechanisms then come into play and affect instability thresholds:

- Space charge: Models suggest it acts against the onset of Transverse Mode Coupling Instability, although some machine observations do not confirm this (e.g. the SPS TMCI thresholds). Besides, its influence on the loss of decoherence could play a detrimental role by helping coherent signals to remain long-lived;
- Beam-beam, electron cloud, ions: They can clearly be exciters of coherent motion coupling not only different bunches but also head and tail of single bunches. On the other hand they also introduce betatron tune spreads that should counteract the onset of beam instabilities.
- The study of the effect on the beam from the electron cloud in different regions of an accelerator has reached an unprecedented maturity. The combined effect of electrons and ions seems to be of relevance for machines like LHC and is being attacked by developing new ad-hoc simulation tools including multiple particle species.

Finally, several mechanisms to suppress beam instabilities and potentially extend the performance reach of present and future machines were reviewed and illustrated, in particular:

- Use the machine optics to reduce sensitivity to coherent motion (e.g. impact of tunes and chromaticities, effect of nonlinear chromaticity Q'' , change of the transition energy);
- Rely on Landau damping by using conventional methods like octupole detuning or by exploring the efficiency of novel sources of betatron tune spread like Radio Frequency Quadrupole (RFQ) or electron lenses, which have not been yet used for this purpose in running machines but hold promise for upgrades and future machines;
- Employ feedback systems to damp coherent instabilities. In their most cutting edge development, these systems have been demonstrated to be capable of damping transverse intra-bunch modes for short bunches (which requires high bandwidth and a complex electronics chain) or quadrupolar type oscillations in the longitudinal plane (which requires special tweaking of the hardware and could be of utmost interest for machines like the CERN PS).

To conclude, the workshop was very useful to summarise and debate all the scientific questions above, while at the same time it gave the participants a chance to enjoy the atmosphere and the sense of community fostered by the intense social program, which included a tour of the archeological site of Pompeii and a concert performed by Trio Pragma, at the Museum of Sannio.

More info can be found on the [web site](#) and [Indico page](#) of the workshop. The proceedings will be published at the beginning of 2018.

3.2 LHeC/FCC-eh Workshop at CERN, September 2017

Oliver Brüning, CERN, and Max Klein, University of Liverpool
Mail to: max.klein@cern.ch

The primary goal of this workshop [1] was to review the update and progress on various developments, which have taken place following the previous LHeC workshop in 2015. The LHeC is a proposed upgrade of the LHC to enable luminous electron-proton and electron-ion collisions to take place in the final phase of LHC operation. Its design is based on a high current, multi-turn, energy recovery, 60 GeV energy electron linac, arranged tangentially to the LHC. A smaller 400 MeV facility, termed PERLE [2], is under design to possibly be built at LAL and IPN Orsay with the aim to study and demonstrate efficient ERL operation under conditions resembling those at the LHeC and to develop the required technologies and operational procedures. The 60 GeV ERL is considered to serve also as the baseline for electron-hadron collisions at HE LHC should that follow the HL LHC, and for the future circular collider, the FCC-eh. The workshop discussed the developments and new studies related to the physics potential, test facility scope and requirements, the detector and accelerator developments, much in view of the forthcoming European and global strategy debates that are foreseen for the next years. It took place at CERN, in a three-day plenary session format, combining invited overview talks with shorter, topical contributions of which altogether 50 were made.

Strong activities and considerable progress were reported on the four essential areas of the study:

- **Physics:** many new results were shown, especially on the question of how ep (and eA) complement pp and AA physics. For the LHC, owing to the possible concurrent eh and hh operation, the prospect emerges to establish “a joint LHC facility” or “experiment” the search and precision measurement potential of which surpasses considerably that of the then existing HL-LHC alone. The addition of the LHeC can transform the LHC into a high precision Higgs facility at modest cost and effort as compared to e^+e^- colliders, which the LHC then would complement. This ep - pp symbiosis regards also a new level of precision tests of the Standard Model, it extends to empowering the LHC search programme by lifting the QCD uncertainties at high mass and, for ep itself, it comprises the exotic Higgs programme and new developments such as on top physics or heavy neutrino searches. Naturally the FCC-eh opens a most far reaching horizon for the discovery of new physics in ep . A strong interest has been formulated in electron-ion physics in kinematic ranges which extend orders of magnitude further than fixed target lepton-hadron scattering experiments or could be covered at the US EICs now under scrutiny.

- **PERLE:** major progress was reported in a dedicated session on the ERL development facility with highlights including the final fabrication of the first 802 MHz SC Niobium cavity, by Jlab in collaboration with CERN, new designs on the Orsay PERLE lattice and the return arc magnets. The intention was confirmed by BINP Novosibirsk, CERN,

Daresbury with Liverpool University, and Jefferson Laboratory to develop and possibly build PERLE in collaboration with INP and LAL at Orsay, while being open for further collaborators to join.

- **Detector:** new designs were presented on a high acceptance, high precision, high technology detector concept for FCC-eh and also the LHeC combined with HE LHC. A first study was presented on installation issues for an ep detector in IP2 (for HL and HE LHC) and a new detector for FCC-eh.

- **Accelerator:** the key parameters for ep and eA were presented as had been developed recently with the result that a luminosity of the order of $10^{34}\text{cm}^{-2}\text{s}^{-1}$ was achievable in all 3 configurations being considered, in which the electron ERL of up to 20mA current would be combined with the protons at 7 TeV at the LHC, 13 TeV at HE LHC or 50 TeV at FCC [3]. Progress was reported on the design of the interaction region and tunnel and infrastructure issues were presented in a novel civil engineering study of the arc and linac tunnels and the utilisation of point “L” at the FCC for electron-hadron collisions.

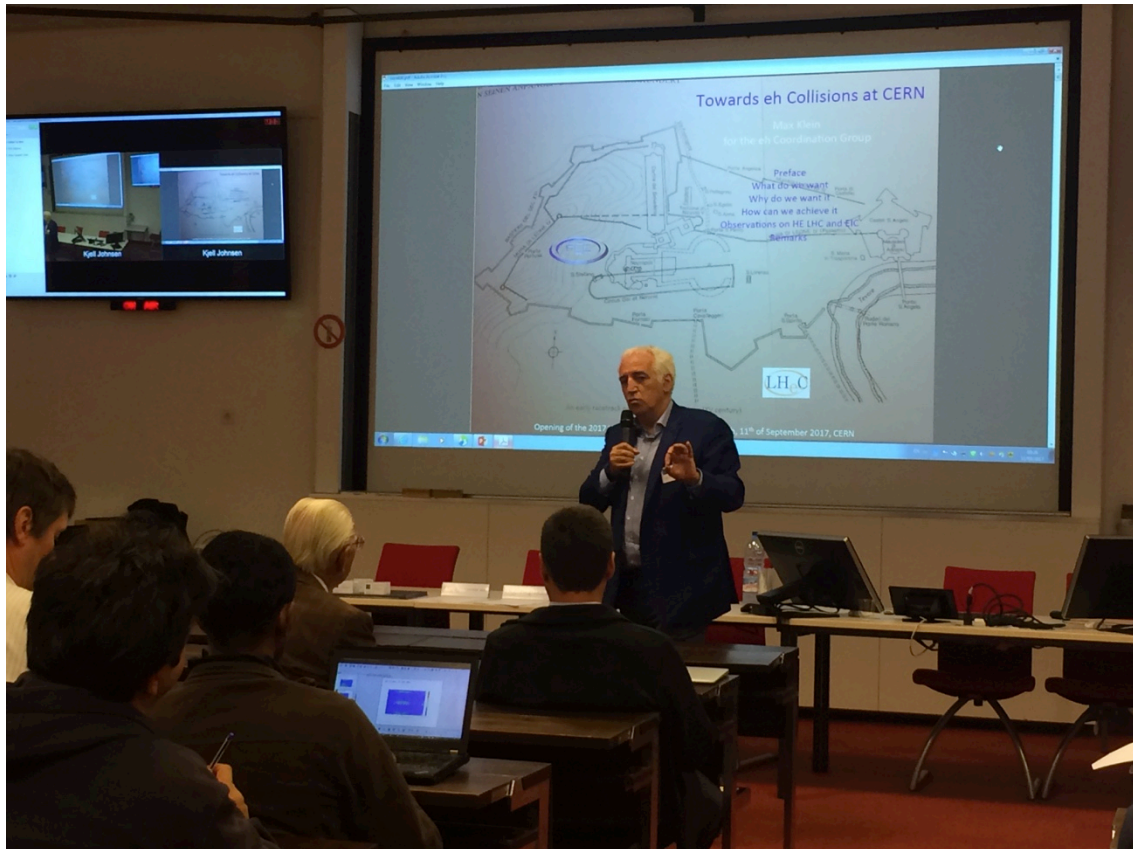


Figure 1: Opening of the 2017 Workshop on the LHeC and FCC-eh by CERN’s Director for Accelerators Frédérick Bordry.

During the workshop there was a session held with the referees nominated by CERN and the International Advisory Committee, chaired by Herwig Schopper, former DG of CERN, in which the status and next steps were discussed with certain emphasis on options, conditions and timeline for a possible realisation of the LHeC. It was stressed that ep could form a 5th grand experiment at the LHC, in the thirties with the support of the particle and nuclear physics communities, including the ones that are already engaged at the LHC. From today's point of view, it is conceivable that the HL LHC will be followed by the HE LHC. Therefore, a presentation on the possible use of the ERL as a photon-photon collider (SAPHIRE) or laser or fixed target physics facility was met with particular interest as it concerned the no-collider phase following the HL LHC, about a decade which it would take to replace the LHC by its high-energy successor. Should that happen with some certainty, the LHeC detector would be designed such that it could stay in the LHC when the higher proton energy was available. One may also imagine a staging scenario such that the highest electron energy may only be reached when the 13 TeV p beam becomes available, after an initial and affordable LHeC phase with possibly lower electron beam energy.

All in all, the workshop was extremely encouraging for progressing with the development of the LHeC and the FCC-eh. The physics in ep and eA was shown to be much richer than conventionally thought, and is now being scrutinized in the on-going physics workshops on the HL LHC and the FCC. The PERLE design is making much progress. It thus was decided to prepare for a possibly larger, next workshop, which will be held in June 27-29 at LAL Orsay in Paris, following the FCC annual overview week at Amsterdam on April 9-13, 2017.

3.2.1 References

13. LHeC/FCC_ah Study Group, Annual Workshop 2017, <https://indico.cern.ch/event/639067>
14. D. Angal-Kalinin et al., "PERLE Powerful Energy Recovery Linac for Experiments – Conceptual Design Report", J. Phys. G, to appear, arXiv:1705.08783 (2017).
15. O. Brüning, J. Jowett, M. Klein, D. Pellegrini, D. Schulte and F. Zimmermann, "FCC Study, FCC-eh Baseline Parameters", FCC-ACC-RPT-0012 (2017).

3.3 300 Scientists Discussed Novel Accelerators at the 3rd European Advanced Accelerator Concept Workshop

Edda Gschwendtner (CERN), Chair of Program Committee,
Ralph Aßmann (DESY) and Massimo Ferrario (INFN), Chairmen of EAAC 2017

The European Advanced Accelerator Concept Workshop (EAAC) 2017 took place for the third time on the Island of Elba in Italy from 24 to 30 September 2017.

Founded by the European Network for Novel Accelerators (EuroNNAc) in 2013, the EAAC has become a central workshop with worldwide visibility to discuss ideas and directions towards the new generation of ultra compact and cost effective accelerators with ground-breaking applications in science, medicine and industry.

At the EAAC workshop senior scientists from various specialities in the field of accelerator physics, RF technology, plasma physics, instrumentation and the laser field mix with junior experts and a large community of young students, attracted by the promise and success of compact particle accelerators. In 2017 about 70 PhD students presented their work at the EAAC. Besides the reports on scientific achievements the large diversity in age distribution, gender and nationalities made the EAAC 2017 a special event and a great success for the accelerator field.

More than three hundred scientists from all over the world followed the latest results and achievements in plasma wakefield acceleration, dielectric structures, high-gradient metallic structures, laser technology, simulation developments, advanced beam diagnostics and novel schemes using advanced technologies. In addition challenges, suitable concepts, future R&D and innovation for advanced and novel accelerators for high-energy physics at the TeV range were discussed.

Among the many outstanding presentations at EAAC2017 were reports on laser-driven kHz generation of MeV beams at LOA/TU Vienna, on dielectric acceleration results from PSI/DESY/Cockcroft, on first results from AWAKE the proton driven plasma wakefield experiment at CERN, on 7 GeV electron beams in laser plasma acceleration from LLNL, on 0.5 nC electron bunches from HZDR, on new R&D directions towards high power lasers at LLNL, on controllable electron beams from Osaka and LLNL, on measured undulator X ray generation after laser plasma accelerators from DESY/University Hamburg/SOLEIL/LOA, on important progress in hadron beams from plasma accelerators from Belfast/HZDR/GSI and on future collider plans from CERN.

A special session was devoted to the Horizon2020 Design Study EuPRAXIA (European Plasma Research Accelerator with eXcellence In Applications). EuPRAXIA designs a highly compact and cost-effective European facility with multi-GeV electron beams using plasmas as the acceleration medium and used for FEL applications, medical imaging, table top test beams for high energy physics and other applications.

The EAAC2017 workshop was supported by the EuroNNac3 network through the EU project ARIES, INFN as the host organization, DESY and the Helmholtz association, CERN and the industrial sponsors Amplitude, Vacuum_Fab and Laser_Optronic.

The combination of gathering scientists from the fast evolving field of advanced accelerator concepts with an ideal location that fosters the scientific exchange during the entire week makes the EAAC workshop a unique and inspiring experience.



Figure 1: Group photo of the EAAC 2017 attendants

3.4 The ICFA mini-workshop Space Charge 2017

Oliver Boine-Frankenheim*, Giuliano Franchetti
*Technische Universitaet Darmstadt,
GSI Helmholtzzentrum für Schwerionenforschung GmbH
Mail to: g.franchetti@gsi.de

The workshop Space Charge 2017, took place at the Wilhelm-Koehler-Saal of Technische Universitaet Darmstadt on 4th – 6th October 2017. Following the success of Space Charge 2013 (CERN), of Space Charge 2015 (Oxford UK), and based on a community demand, GSI and Technische Universitaet Darmstadt organised the 2017 edition of the workshop. The workshop has addressed actual topics of high interest in the accelerator community, and provided a forum for discussing between experts, which is synergetic to the well-established series of the HB workshops. Space Charge 2017 was organised under the auspices of ICFA and is an event of APEC/ARIES, the successor of XRING/XBEAM/EuCARD2, which jointly with ACCELENCE cover the majority of the cost for the workshop. (Figure. 1 workshop poster).

The workshop was attended by 52 international participants (Europe, America, Asia) from more than 17 different institutions (Figure 2 the seminar room, and the workshop dinner). The scientific program has been prepared with the supervision of an International Advisory Committee formed by 12 International accelerator physicists. The meeting has been divided in the following sessions: Machine study and performances; Diagnostics theory/experiments; New techniques, mitigations / applications; Collective effects, instabilities and modes; Longitudinal & transverse studies; Beam diagnostics, new developments & synergies; Codes, PIC and space charge; Special topics. The overall atmosphere was very positive, with several discussions facilitated by the several slots distributed along the workshop.

The meeting has hosted 37 talks presented during 2.5 days. Given the substantial number of talks, it was agreed that each speaker had to deliver his/her main message in 15 minutes. This format has found a very positive response from the speakers who perfectly kept the schedule. In the opening session P. Spiller has presented the status of the FAIR project at GSI, pointing out that the main challenge for SIS18 as injector is the beam loss, which significantly influence the dynamic vacuum. The present schedule foresees the first beam in SIS100 for 2023. Following F. Schmidt overviewed the space charge studies for the LHC pre-injector upgrade at CERN, and the strategy of code development and synergies. A new development for measuring the 6D phase space of intense beam has been reported by Sara Cousineau: at SNS it is planned in 2018 to carry out the first 5D/6D phase space reconstruction. Shinji Machida discussed the space charge effects in a new configuration of neutron/muon source FFAG. For this machine tuned near the diagonal the issues are how the beams respond to space charge driven resonances and nonlinearities in magnets, and the effect of the Montague resonance. All the other talks and details of the program and talks are available via the workshop website: <https://indico.gsi.de/event/5600/>



Figure 1: Poster of the Space Charge2017 workshop.



Figure 2: Participants of the workshop in the seminar room (left), and a moment of the workshop dinner (right).

3.5 The 2nd Workshop on Slow Extraction, 9-11 November 2017

Brennan Goddard, CERN
Mail to: brennan.goddard@cern.ch

Slow extraction is a complex beam delivery process relevant for many circular accelerators, ranging from medical machines to those serving high-energy physics (HEP) Fixed Target facilities. Although the requirements of the various users differ greatly in the specifics, there are many common features that underpin the observed performance limitations. This commonality and the challenges of controlling the non-linear beam dynamics coupled with sensitivity to technological imperfections make the topic a rich one for the community.

Following on from the success of the 2016 Slow Extraction Workshop held in GSI, Germany, a second workshop <https://indico.cern.ch/event/639766/> was held at CERN, Geneva, Switzerland from November 9 to 11, 2017, under the auspices of ICFA and ARIES (the successor of EuCARD2), and also supported by the CERN Physics Beyond Colliders study. The workshop was attended by 56 participants representing institutions from Asia, Europe and USA, with 15 (past, present and future) machines performing slow extraction directly represented.

The workshop was convened to address topical issues associated with Slow Extraction, as well as providing a forum for discussion between experts across this specialised domain. With new fixed target proposals like SHiP on the horizon the focus in 2017 was twofold: investigating new methods of beamloss reduction from the accelerator physics and technology side; and also on improving the structure of the slow extraction spill. The strong overlap between the requirements, problems and approaches from the provided fertile ground for debate and discussion, and highlighted the benefits to be gained from assembling the different experts together for this event.

The scientific program of the workshop was set up by the International Organizing Committee, which was chaired by B. Goddard (CERN) and comprised M. Bai (GSI), K. Brown (BNL), G. Franchetti (GSI), M. Fraser (CERN), L. Gatignon (CERN), V. Kain (CERN), S. Ivanov (IHEP), R. Jacobsson (CERN), V. Nagaslaev (FNAL), H. Stockhorst (FZJ), M. Tomizawa (KEK) and F. Zimmermann (CERN). Efficient Local Organization was provided by L. Mainoli (CERN) and M. Fraser (CERN).

A total of 35 talks were presented during the first four sessions, divided into Setting the Scene, Beamloss Control, Spill Control and Hardware. For each session, a general introduction talk was framed to recall the limitations and requirements from the community, while the remaining talks delved into the details.

In the first session, after an overview by R. Jacobsson (CERN) motivating the need for slow extraction for future HEP experiments, very complete overviews were given of the operational challenges facing both the high energy HEP machines and lower energy medical machines, and a common language was agreed for the different extraction techniques – an important step to aligning measurement and performance data to understand the differences and advantages of the multitude of approaches. In this session, the presenters were asked to pull no punches in describing problems and limitations, and they followed the instructions admirably, since some of the most instructive discussions were on the different dramatic failures and mishaps that invariably drive improvement in procedure and beam control.

In the second session, the existing and speculative methods for beamloss control were developed, with a fascinating array of proposals aired for comparison and discussed for applicability. Despite the very different objectives for high- and low-energy machines regarding beamloss control, many ideas flowed between the experts from the different machines, ranging from the use of passive or active pre-scatterers to phase-space manipulation of separatrices and a comparison of computational tools for particle tracking. The session concluded with a detailed comparison by S. Ivanov (IHEP) of the merits of translation- versus diffusion-driven 3rd integer extraction, which stimulated so much interest that a complementary presentation on the topic was held on the Saturday morning during the discussion session.

The third session on spill structure was perhaps the one where the different communities came together to the greatest extent. The relevance to the HEP and medical machines was underlined, with the clear request to the HEP experimentalists to define the allowable deviations from a perfect spill up to frequencies of 10 GHz. The common issues of wrestling with mains harmonics were illustrated several times, and the innovative solutions and mitigations described in detail, with presentations on stochastic noise diffusion, magnetic stability, feedback, feedforward, power converters and accurate instrumentation. It was evident that this topic is the main operational issue facing most machines, with continued efforts everywhere to improve the effective duty factor.

The final presentation session focussed more on extraction hardware, with the emphasis shifting back to beamloss, activation and radiation dose reduction. Promising new ideas for low-Z septum materials were discussed along with remote handling, activation modelling, improved alignment methods and instrumentation, including the very exciting method for performing tomography on the extracted beam separatrix, presented on behalf of A. Wastl by M. Pivi (MedAustron).

The Workshop then moved into a dedicated discussion phase, with three separate sessions clarifying some of the unresolved questions and defining the extraction types, establishing the common remaining topics and exploring the possibilities for collaborative follow-up and, last but not least, looking forward to a possible 3rd Workshop in 2019. These lively sessions were co-animated by the Workshop chair, G. Franchetti and V. Nagaslaev.

After the discussions, there was time for a short visit to the laboratory of the CERN septum team, where J. Borburgh (CERN) could show some of the technologies used in the different devices, and to the CERN Control Centre where V. Kain (CERN) could provide a hands-on demonstration of the regulation of the slow extraction of Xe ions from the SPS.

As concrete output, and resource for the future, the Workshop generated a collection of impressive presentations and ideas that are all available on the Indico pages. In addition, a catalogue of slow extraction types at the different facilities was drafted, with the objective of unifying the language and comparing the basic parameters for the machine setups. A sharepoint site has been setup to allow easy upload of reference lists and precious scanned publications and documents, and an update on the 2016 Workshop spill structure data was made. Finally, a list was established of topics of common interest for further study and collaboration between labs.

Overall, and after an intense few days, it was abundantly clear that Slow Extraction continues as an active field, with a compact but dedicated and highly creative expert community. The Workshop generated a lot of precious information and stimulated collaborative exchange between most, if not all, of the laboratories involved. The

opportunities for new or strengthened collaboration are important, since many of the more flexible lower energy machines have great facilities for testing, benchmarking and developing new Slow Extraction methods, which can find applicability across the range of energies and spill structures discussed. In addition, with the long CERN 2019-2020 shutdown approaching, the possibility of continuing and even expanding experimental slow extraction tests for the next generation of Fixed Target experiments is extremely important.

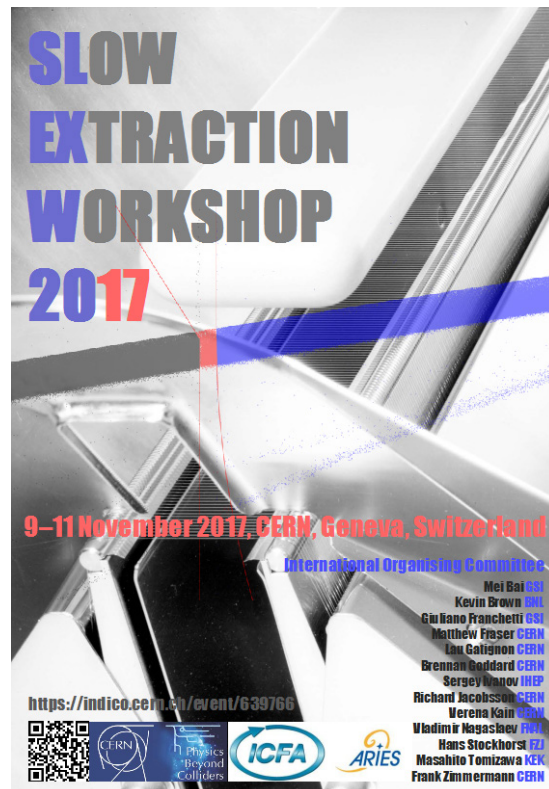


Figure 1. Slow Extraction Workshop 2017 poster.



Figure 2: Workshop social dinner, where lively discussion continued late into Thursday night.

One of the objectives set by the Organisers before the Workshop was to “further the educational and institutional knowledge retention concerning slow extraction techniques, technologies and limitations” – and this was achieved, in spades!



Figure 3. Workshop visit to CERN septa laboratory on Saturday morning.

4 Recent Doctoral Theses

4.1 Beam Diagnostics and Dynamics in Nonlinear Fields

Jim Ögren

Mail to: jim.ogren@physics.uu.se

Graduation date: December 8, 2017
Institutions: Uppsala University, Sweden
Supervisors: Dr. Roger Ruber, Dr. Volker Ziemann, Prof. Klaus Leifer
 (Uppsala University)

Abstract

To complement the beam diagnostics system of the Compact linear Collider (CLIC) we investigated methods utilizing the nonlinear fields arising from the octupolar component of the radio-frequency fields present in the CLIC accelerating structures. Steering the beam transversely it receives a nonlinear kick from the octupole-like field and we use this information to deduce the strength of the field, as well as the alignment of the structure. Moreover, by transversely scanning the beam we observe a change in the beam size on a downstream beam profile monitor. From the data we can determine the fully coupled transverse beam matrix.

In circular accelerators, nonlinear fields result in nonlinear beam dynamics, which often becomes the limiting factor for long-term stability. In theoretical studies using Lie-algebraic tools together with simulations we investigate optimum configurations for octupole magnets that compensate amplitude-dependent tune-shifts but avoid driving

fourth-order resonances and setups of sextupole magnets to control individual resonance driving terms in an optimal way.

4.2 Luminosity Performance Limitations due to the Beam-Beam Interaction in the Large Hadron Collider

Matthew Paul Crouch
Mail to: mrcrouch@cern.ch

Institutions: University of Manchester and the Cockcroft Institute, UK
Supervisors: Dr. Bruno Muratori (ASTeC and the Cockcroft Institute, UK),
Dr. Robert Appleby (University of Manchester, UK)

Abstract

In the Large Hadron Collider (LHC), particle physics events are created by colliding high-energy proton beams at a number of interaction points around the ring. One of the main performance indicating parameters of the LHC is the luminosity. The luminosity is limited, by amongst other things, the strength of the beam-beam interaction. In this thesis, the effect of the beam-beam interaction on the luminosity performance of the LHC and the proposed High Luminosity Large Hadron Collider (HL-LHC) is investigated. Results from a number of dedicated, long-range beam-beam machine studies are presented and analysed. In these studies, the minimum beam-beam separation for two different β^* optics are identified. This separation defines the minimum operational crossing angle in the LHC. The data from these studies are then compared to simulation of the dynamic aperture and the results are discussed. In addition to studies of the LHC, an analytical approach is derived in order to describe the hourglass effect, which may become a contributing factor in limiting the luminosity performance of the HL-LHC.

4.3 Applications of Neural Networks to Modeling and Control of Particle Accelerators

Auralee Edelen
auralee.l.morin@gmail.com

Institution: Colorado State University
Defense date: Nov. 29, 2017
Supervisors: Sandra Biedron and Stephen Milton

Abstract

Particle accelerators are host to myriad challenges for modeling and control: they involve a multitude of interacting systems, are often subject to tight performance demands, in many cases exhibit nonlinear behavior, sometimes are not well-characterized due to practical and/or fundamental limitations, and should be able to run for extended periods of time with minimal interruption. One avenue toward improving the way these systems are modeled and controlled is to incorporate techniques from machine learning. Within

machine learning, neural networks in particular are appealing because they are highly flexible and they are well-suited learning adaptive models and control policies for many-parameter systems with nonlinear behavior. Here, some of the challenges of particle accelerator control are described, recent advances in neural network techniques for modeling and control are highlighted (along with some of their remaining limitations), and some proposed avenues for applying neural networks to particle accelerators are discussed. This dissertation also highlights several pioneering efforts in this area that were focused on exploring neural network-based approaches for modeling and control of accelerator systems, through a combination of both simulation and experimental studies. By virtue of those examples, it also shows how neural networks can be used to create fast-executing surrogates of a priori simulations, combine physics-based knowledge and observed machine behavior, incorporate image-based diagnostics directly into models and control policies, and mimic/adapt upon existing control policies. The specific applications covered as examples include resonant frequency control of the radio frequency quadrupole for Fermilab's Proton Improvement Plan (PIP-II) Injector Test, fast switching between beam parameters for a compact THz free electron laser, modeling of the Fermilab Accelerator Science and Technology Facility (FAST) low energy beamline at Fermilab, temperature control for the FAST RF gun, and trajectory control for the Jefferson Laboratory free electron laser.

5 Forthcoming Beam Dynamics Events

5.1 7th Low Emittance Rings Workshop, 15-17 January 2018

Yannis Papaphilippou, CERN, Geneva, Switzerland

Mail to: ioannis.papaphilippou@cern.ch

The 7th Low Emittance Rings Workshop will take place at CERN, from Monday 15th to Wednesday 17th of January 2018 – <https://indico.cern.ch/event/671745/>.

The goal of the workshop is to bring together experts from the scientific communities working on low emittance e^+/e^- rings. It is sponsored by the RULE network (<http://aries.web.cern.ch/content/wp7>) under the ARIES European project (<https://aries.web.cern.ch/>) and includes light source storage rings, linear collider damping rings and future e^+/e^- circular colliders.

The workshop will treat beam dynamics and technology challenges for producing and controlling ultra-low emittance beams. Participants will benefit from the experience of colleagues who have designed, commissioned and operated such rings.

5.2 ARIES Topical Workshop on "Emittance Measurements for Light Sources and FELs", 29-30 January 2018

Ubaldo Iriso, ALBA-CELLS, Barcelona, Spain
Mail to: uiriso@cells.es

The Topical Workshop on “Emittance Measurements for Light Sources and FELs”, which will be held at ALBA Synchrotron from January 29 - 30, 2018 – <https://indico.cells.es/indico/event/128> .

This is the first of a sub-series of workshops on “Advanced Diagnostics for Accelerators” (ADA) within the newly EU funded ARIES programme (Accelerator Research and Innovation for European Science and Society).

Experts from the scientific community working on emittance measurements for electron machines (including light sources, damping rings, FELs and future e+/e- circular colliders), will gather with the aim to present the status of the different beam size measurement techniques, discuss the challenges that the community faces for the next generation of ultra-low emittance machines, and enhance synergies between the different communities.

5.3 ICFA Mini-Workshop on Beam-Beam Effects in Circular Colliders, 5-7 February 2018

Ji Qiang and Jean-Luc Vay, LBNL, Berkeley, U.S.A.
Mail to: jqiang@lbl.gov and/or jlvey@lbl.gov

The ICFA Mini-Workshop on Beam-Beam Effects in Circular Colliders will be held in Berkeley, CA, USA – <https://indico.physics.lbl.gov/indico/event/586/> . This workshop is a successor and follows up to similar workshops held at CERN in April 1999, at Fermilab in June 2001, in Montauk 2003, and at CERN in March 2013.

A lot of progress has been made since the last workshop at CERN in the study of the beam-beam effects in colliders such as the LHC. Meanwhile, there are also beam-beam challenges in future colliders such as the next generation nuclear physics electron ion collider (EIC). The purpose of this workshop is to bring experts in this field to review progress in beam-beam studies of the current and past colliders and to discuss potential beam-beam issues and solutions in the future colliders.

5.4 TIARA, ARIES and AMICI joint Accelerator-Industry Co-innovation Workshop

Roy Aleksan, CEA, France
Mail to: roy.aleksan@cea.fr
Maurizio Vretenar, CERN, Switzerland
Mail to: Maurizio.Vretenar@cern.ch

TIARA, ARIES and AMICI (*) are jointly organising an Accelerator-Industry Co-innovation Workshop, which will take place on 6th and 7th February 2018 at the Crowne Plaza Hotel in Brussels.

The Workshop will be of interest to executives from European industry and to researchers and directors of research in European universities and laboratories engaged in R&D on particle accelerator technologies. With the contribution of officials from the European Commission, we aim to discuss and identify present and future tools, strategies and funding schemes to enhance industry-academia cooperation in the particle accelerator community.

Further information, including objectives and expected impact of the Workshop are available on the web site: <https://indico.cern.ch/event/682411/>.

The Workshop is open to all actors of the particle accelerator R&D but attendance is limited and prior registration is necessary. If you plan to attend, please register as soon as possible and in any case before January 10th on the web page <https://indico.cern.ch/event/682411/registrations>. A limited number of rooms has been pre-reserved at the Crowne Plaza; details are given on the Accommodation page of the web site.

(*) TIARA is the consortium of European research institutions in the Particle Accelerator Research Area; ARIES and AMICI are collaborative projects supported by the European Commission to develop accelerator R&D and to support accelerator and magnet technological infrastructures.

5.5 ICFA Mini-Workshop on Machine Learning Applications in Accelerator Physics, February 28 - March 2, 2018

Daniel Ratner, SLAC National Accelerator Laboratory, Menlo Park, U.S.A.
Mail to: dratner@slac.stanford.edu

The ICFA Mini-Workshop on Machine Learning Applications in Accelerator Physics, February 28 - March 2, 2018 will be held at SLAC, California, USA
<https://conf.slac.stanford.edu/icfa-ml-2018/>.

The goal of this workshop is to help build a world-wide community of researchers interested in applying machine learning techniques to particle accelerators. The workshop will be split into four sequential topics:

- Tuning/optimization/control
- Prognostics/alarm handling/anomaly-breakout detection
- Data analysis

- Simulations/modeling

Talks will include both accelerator physicists and computer scientists. This workshop has the following goals:

- Collect and unify the community's understanding of the relevant state-of-the-art ML techniques.
- Provide a simple tutorial of machine learning for accelerator physicists and engineers.
- Seed collaborations between laboratories, academia, and industry.
- Author a whitepaper explaining the current opportunities for ML techniques in particle accelerators, with a few illustrative examples. This whitepaper should explain why now is the time for the community to fully embrace ML alongside optimization as the modern way to aid particle accelerator design and operation.

Given the early state of machine learning at accelerator facilities, a heavy emphasis will be placed on discussions, collaboration planning, and poster sessions, with only a few general talks. This workshop is by invitation only. Those interested to attend should contact Daniel Ratner at dratner@slac.stanford.edu.

5.6 ARIES APEC Topical Workshop on Ion Sources and Low Energy Beam Transport into RF Linacs, February 28 - March 2, 2018

Ulrich Ratzinger, University of Frankfurt, Germany

Mail to: U.Ratzinger@iap.uni-frankfurt.de

Florian Hug, University of Mainz, Germany

Mail to: flohug@uni-mainz.de

The ARIES APEC Topical Workshop on “Ion Sources and Low Energy Beam Transport into RF Linacs”, February 28 - March 2, 2018 will be held at the University of Frankfurt, University - Campus Riedberg.

The workshop will address the following topics:

- beam emittance after source extraction (2D and 4D)
- emittance increase along focusing elements and/or electrically charged LEBT components
- beam compensation topics: influence of beam current ripple, chopped beam cases etc.
- experience and simulations on relevant beam diagnostics (accuracy, band width, technical layout)
- beam injection into the first RF linac cavity (usually an RFQ): elements for an efficient matching into the RFQ acceptance, better understanding of the beam charge decompensation process.

5.7 60th ICFA Advanced Beam Dynamics Workshop on Future Light Sources, FLS2018, March 4-9, 2018, SINAP

Yong Ho Chin, KEK, Japan
 Mail to: yongho.chin@gmail.com
 Zhentang Zhao, SINAP, China
 Mail to: zhaozhentang@sinap.ac.cn

The 60th ICFA Advanced Beam Dynamics Workshop on Future Light Sources (FLS2018) will take place in Shanghai, from 5 to 9 March, 2018. FLS2018 is hosted by the Shanghai Institute of Applied Physics, CAS – <http://indico.sinap.ac.cn/event/4/>.

The Future Light Source Workshop has a long history, dating back to the 1990s. The first FLS workshop was held in Grenoble, hosted by ESRF in 1996. It was followed by FLS 1999 in Argonne, FLS 2002 in Hyogo, FLS 2006 in Hamburg, FLS 2010 in Menlo Park, and FLS 2012 in Newport News.

In the spirit of the FLS workshop series, FLS2018 will bring together worldwide scientists to exchange ideas and best practices about accelerator based light sources, their new development trend and related key technologies. The workshop program will consist of plenary talks and working group sessions. The working groups will include Linac-based light sources, Ring-based light sources, Compact light sources, and Key technologies.

Shanghai is the financial center in China and a famous international metropolis. It is also a popular tourist destination renowned for its historical landmarks such as the Bund, City God Temple and Yu Garden as well as the financial district of Lujiazui with its extensive skyline. In its metropolis, one finds a unique blend of oriental and occidental cultures, which makes the visit to Shanghai a memorable experience.

5.8 ARIES-APEC Pulse Power for Kicker Systems (PULPOKS) Workshop, 12-13 March 2018, CERN

Mike Barnes, CERN, Switzerland
 Mail to: Mike.Barnes@cern.ch

The workshop (PULPOKS) is scheduled at CERN for 12 & 13 March 2018 – <https://indico.cern.ch/event/682148/>

The scope is:

- Valve switches (probably mainly thyratrons, but may include other switches)
- HV cables
- Solid state switches and modulators
- Triggering
- Pulsed measurements and online monitoring and analysis
- Magnetic materials
- Modelling software and simulation
- Impedance shielding

Registration for the workshop is open. There is limited accommodation available at the CERN hostel: hence you are encouraged to register for the workshop very soon and book your accommodation.

5.9 ALEGRO 2018 workshop, Oxford, 26-29 March 2018

Andrei Seryi, U. Oxford, United Kingdom
Mail to: Andrei.Seryi@adams-institute.ac.uk

The ALEGRO 2018 workshop will be organized at the University of Oxford on 26-29 March 2018 - www.physics.ox.ac.uk/confs/alegro2018.

Following the ANAR 2017 workshop, a study group towards advanced linear colliders, named ALEGRO for Advanced LinEar collider study GROup, has been set up to co-ordinate the preparation of a proposal for an Advanced Linear Collider in the multi-TeV energy range.

The objective of this first ALEGRO workshop is to prepare and deliver, by the end of 2018, a document detailing the international roadmap and strategy of advanced novel accelerators (ANAs) with clear priorities as input for the European Strategy Group, as well as input to ICFA.

5.10 Future Circular Collider Week 2018, 9-13 April 2018

Michael Benedikt and Frank Zimmermann, CERN, Geneva, Switzerland
Mail to: Michael.Benedikt@cern.ch and Frank.Zimmermann@cern.ch

The **Future Circular Collider Collaboration Week 2018** will take place in Amsterdam, the Netherlands (**9-13 April 2018**) at the Beurs van Berlage conference centre.

The FCC worldwide community now stands at 116 institutes and 25 companies in 32 countries and the EC. The aim of the 2018 collaboration week is to bring together this community to share results, to solidify the vision of a circular post-LHC particle-collider research infrastructure, and, in particular, to critically review the conceptual design baselines for all collider scenarios towards the completion and delivery of the FCC Conceptual Design Report.

The programme will follow the same format as in previous years with plenary and parallel sessions, a welcome reception and gala dinner, and a public event in Dutch, all organized with the support of the Dutch National Institute for Subatomic Physics (NIKHEF) and the University of Twente.

Registration and abstract submission through the conference website are [open](#). Participants are encouraged to apply for the [FCC Innovation Award](#) via a poster submission, and the FCC Accelerating Diversity Prize.

Further information can be found on the conference website:
<http://fccw2018.web.cern.ch/>

5.11 9th International Particle Accelerator Conference (IPAC'18), in Vancouver, from April 29 to May 4, 2018

Shane Koscielniak, TRIUMF, Vancouver, Canada

Mail to: shane@triumf.ca

Tor Raubenheimer, SLAC, Menlo Park, U.S.A.

Mail to: tor@slac.stanford.edu

The 9th International Particle Accelerator Conference (IPAC'18), will be held in Vancouver, British Columbia, Canada from April 29 to May 4, 2018 – <https://ipac18.org>

The venue will be the brand new JW Marriott parq Vancouver which features overlooking views of False Creek, Granville Island, and English Bay.

IPAC is the main international event for the worldwide accelerator community and industry. Attendees will be presented with cutting-edge accelerator research and development results and gain the latest insights into accelerator facilities across the globe. Over 1200 delegates and 70 industry exhibits are expected to be in attendance.

At IPAC'18, you will have the opportunity to meet and interact with accelerator scientists, engineers, students, and vendors while experiencing Canada's most culturally and geographically diverse city.

5.12 E-CLOUD'18, 3-7 June 2018

Roberto Cimino, INFN Frascati, Italy

Mail to: Roberto.Cimino@Inf.infn.it

Frank Zimmermann, CERN, Geneva, Switzerland

Mail to: Frank.Zimmermann@cern.ch

The sixth electron-cloud workshop, E-CLOUD'18, will take place from 3 to 7 June, 2018 at La Biodola (Isola d'Elba) Italy. The existence of the electron-cloud effects (ECE's) has been firmly established experimentally at essentially all modern positron and hadron storage rings, either via performance limitations or by deliberate provocation. The ECE is a consequence of the strong coupling between a positively charged particle beam and a cloud of electrons that inevitably develops inside the vacuum chamber. Resulting deleterious effects include beam instabilities, beam losses, emittance growth, increases in vacuum pressure, additional heat load on the vacuum chamber walls, and interference with certain types of beam diagnostics.

Electron-cloud effects remain dynamical phenomena which are only incompletely understood. While the fundamental mechanisms are well recognized and the qualitative picture is clear, the phenomena involve many surface properties and geometrical parameters of the vacuum chamber coupled in a nontrivial way with the beam characteristics. The ECE can also conspire with classical wake-field effects and/or the beam-beam interaction. In addition, the relevant time and energy scales span a wide range, and many of the essential parameters are not well known a priori. Hence the detailed prediction of ECE's at a given machine, not to mention the extrapolation from one machine to another, are subject to great uncertainty.

High-power microwave applications in modern satellites are perturbed by phenomena of multipacting and RF breakdown, which are governed by the same surface parameters

as ECE in accelerators. Especially for multi-carrier signals, they exhibit very similar characteristics and electron-cloud build-up time scales, and can be modelled by similar simulation tools. Since the last workshop ECLOUD' 12, which also took place in La Biodola, Italy (<https://agenda.infn.it/conferenceDisplay.py?ovw=True&confId=13351>), an intense R&D effort has been under way to further understand the physics of the electron cloud and to investigate new methods for the mitigation of its adverse consequences.

Electron cloud remains a major concern for the High Luminosity LHC and even for the actual LHC run 2. At CERN and worldwide a significant effort is also dedicated to the study of Future Circular Collider (FCC) options – involving both proton and electron-positron colliders which may suffer from electron cloud. As a consequence of the high synchrotron radiation, large bunch charge, and close bunch spacing in several of the FCC machines, the ECE's are expected to be significant. It is urgent to better quantify and understand the associated phenomena to ascertain the feasibility of the performance goals. ECE's have been noticeable during the first commissioning run of SuperKEKB in 2016. The next commissioning run from early 2018 onward will further raise the beam intensity.

The ECLOUD'18 workshop will be a timely meeting at which to present, discuss, and compare many recent and new electron-cloud observations at the LHC, SuperKEKB, CESR-TA and DAFNE, electron cloud predictions for FAIR and for the FCC. The ECLOUD'18 workshop will also showcase and examine electron-cloud mitigation measures, such as clearing electrodes, graphite/carbon coatings, and chemically or laser treated surfaces, along with the modeling of incoherent electron-cloud effects, self-consistent simulations, synergies with other communities like the Valencia Space Consortium and the European Space Agency.

The ECLOUD'18 program will focus on: a review of EC observations at existing machines; recent experimental efforts to characterize the EC (including EC diagnostics, experimental techniques, characterization of mitigation methods, and characterization of beam instabilities and emittance growth); the status of EC physics models and simulation codes and their comparison with recently acquired experimental data; and the mitigation requirements and potential performance limitations imposed by the EC on existing, upgraded and future machines.

ECLOUD'18 will be held at the Hermitage Hotel in La Biodola, Isola d'Elba. We are looking forward to an exceptional gathering where we can enjoy the beautiful location, have interesting scientific discussions about the state of the art, and initiate stimulating collaborations among electron-cloud key experts as well as with students and other scientists from neighbouring fields.

Up to date information about ECLOUD'18 is available on the workshop web site <https://agenda.infn.it/conferenceDisplay.py?confId=13351>.

5.13 2018 LHeC/FCC-eh/PERLE Workshop

Max Klein, University of Liverpool, U.K.
Mail to: mklein@hep.ph.liv.ac.uk

The 2018 workshop on the LHeC and FCC-eh, co-supported by ARIES APEC, will be held at LAL Orsay (France) from June 27-29 (Wednesday until Friday), 2018. The June 2018 workshop takes place prior to the submission of the documents for consideration in the European strategy process, which gives it a special role. The intention

is to update the Conceptual Design Report on the LHeC by fall 2018, and to also deliver the contributions characterising the FCC-eh option of the FCC.

The workshop will discuss i) high energy ep and eA physics and its special relation to the hadron colliders LHC (HL and HE) and FCC, ii) the detector and IR designs, iii) the high energy ERL accelerator configuration, and iv) the status of the low energy Orsay ERL facility which is under development by the PERLE Collaboration.

Further information can be obtained from the LHeC website: <http://lhec.web.cern.ch>. The Orsay 2018 workshop follows a series of previous meetings, as in 2015 at Chavannes-de-Bogis (<https://indico.cern.ch/event/356714>) and in 2017 at CERN (<https://indico.cern.ch/event/639067>). The LHeC CDR was published J Phys G, in 2012, <https://arxiv.org/abs/1206.2913>. The PERLE CDR was published in 2017, J Phys G to appear, <https://arxiv.org/abs/1705.08783>.

5.14 High-Brightness Hadron Beams 2018 (HB2018)

Dong-O Jeon, IBS, Korea

Mail to: jeond@ibs.re.kr

Yong Ho Chin, KEK, Japan

Mail to: yongho.chin@gmail.com

The 61st ICFA Advanced Beam Dynamics Workshop on High-Intensity and High-Brightness Hadron Beams (HB2018) will be held in Daejeon, Korea, from June 18 to 22, 2018 – <http://hb2018.ibs.re.kr>.

This workshop is a continuation of the successful biennial HB workshop series started about fifteen years ago (2002 at FNAL, 2004 at GSI, 2006 at KEK, 2008 at ORNL, 2010 at PSI and 2012 at IHEP, 2014 at MSU and 2016 at ESS). HB workshop series is a platform for presenting and discussing new progresses, status and future developments of high intensity, high brightness, and high power hadron beams, including beam physics, linear and circular hadron machines, technical systems and accelerator projects (under construction or in design) around the world.

The Scientific Program for HB2018 will consist of invited orals, contributed orals and poster presentations. The abstract submission is open via JACoW's Scientific Program Management System (SPMS) at <https://spms.kek.jp/pls/hb2018/profile.html>.

5.15 29th Linear Accelerator Conference (LINAC18)

The 29th Linear Accelerator Conference (LINAC18), will be held on September 17-21, in Beijing, China.

6 Announcements of the Beam Dynamics Panel

6.1 ICFA Beam Dynamics Newsletter

6.1.1 Aim of the Newsletter

The ICFA Beam Dynamics Newsletter is intended as a channel for describing unsolved problems and highlighting important ongoing works, and not as a substitute for journal articles and conference proceedings that usually describe completed work. It is published by the ICFA Beam Dynamics Panel, one of whose missions is to encourage international collaboration in beam dynamics.

Normally it is published every April, August and December. The deadlines are 15 March, 15 July and 15 November, respectively.

6.1.2 Categories of Articles

The categories of articles in the newsletter are the following:

1. Announcements from the panel.
2. Reports of beam dynamics activity of a group.
3. Reports on workshops, meetings and other events related to beam dynamics.
4. Announcements of future beam dynamics-related international workshops and meetings.
5. Those who want to use newsletter to announce their workshops are welcome to do so. Articles should typically fit within half a page and include descriptions of the subject, date, place, Web site and other contact information.
6. Review of beam dynamics problems: This is a place to bring attention to unsolved problems and should not be used to report completed work. Clear and short highlights on the problem are encouraged.
7. Letters to the editor: a forum open to everyone. Anybody can express his/her opinion on the beam dynamics and related activities, by sending it to one of the editors. The editors reserve the right to reject contributions they judge to be inappropriate, although they have rarely had cause to do so.

The editors may request an article following a recommendation by panel members. However anyone who wishes to submit an article is strongly encouraged to contact any Beam Dynamics Panel member before starting to write.

6.1.3 How to Prepare a Manuscript

Before starting to write, authors should download the template in Microsoft Word format from the Beam Dynamics Panel web site:

<http://icfa-bd.kek.jp/icfabd/news.html>

It will be much easier to guarantee acceptance of the article if the template is used and

the instructions included in it are respected. The template and instructions are expected to evolve with time so please make sure always to use the latest versions.

The final Microsoft Word file should be sent to one of the editors, preferably the issue editor, by email.

The editors regret that LaTeX files can no longer be accepted: a majority of contributors now prefer Word and we simply do not have the resources to make the conversions that would be needed. Contributions received in LaTeX will now be returned to the authors for re-formatting.

In cases where an article is composed entirely of straightforward prose (no equations, figures, tables, special symbols, etc.) contributions received in the form of plain text files may be accepted at the discretion of the issue editor.

Each article should include the title, authors' names, affiliations and e-mail addresses.

6.1.4 Distribution

A complete archive of issues of this newsletter from 1995 to the latest issue is available at

<http://icfa-usa.jlab.org/archive/newsletter.shtml>.

Readers are encouraged to sign-up for electronic mailing list to ensure that they will hear immediately when a new issue is published.

The Panel's Web site provides access to the Newsletters, information about future and past workshops, and other information useful to accelerator physicists. There are links to pages of information of local interest for each of the three ICFA areas.

Printed copies of the ICFA Beam Dynamics Newsletters are also distributed (generally some time after the Web edition appears) through the following distributors:

John Byrd	jmbyrd@lbl.gov	North and South Americas
Rainer Wanzenberg	rainer.wanzenberg@desy.de	Europe++ and Africa
Toshiyuki Okugi	toshiyuki.okugi@kek.jp	Asia**and Pacific

++ Including former Soviet Union.

** For Mainland China, Jiu-Qing Wang (wangjq@mail.ihep.ac.cn) takes care of the distribution with Ms. Su Ping, Secretariat of PASC, P.O. Box 918, Beijing 100039, China.

To keep costs down (remember that the Panel has no budget of its own) readers are encouraged to use the Web as much as possible. In particular, if you receive a paper copy that you no longer require, please inform the appropriate distributor.

6.1.5 Regular Correspondents

The Beam Dynamics Newsletter particularly encourages contributions from smaller institutions and countries where the accelerator physics community is small. Since it is impossible for the editors and panel members to survey all beam dynamics activity worldwide, we have some Regular Correspondents. They are expected to find interesting activities and appropriate persons to report them and/or report them by themselves. We hope that we will have a "compact and complete" list covering all over the world eventually. The present Regular Correspondents are as follows:

<i>Liu Lin</i>	Liu@ns.lnl.br	<i>LNLS Brazil</i>
Sameen Ahmed Khan	Rohelakan@yahoo.com	SCOT, Middle East and Africa

We are calling for more volunteers as Regular Correspondents.

6.2 ICFA Beam Dynamics Panel Members

Name	eMail	Institution
Rick Baartman	baartman@lin12.triumf.ca	TRIUMF, 4004 Wesbrook Mall, Vancouver, BC, V6T 2A3, Canada
Marica Biagini	marica.biagini@lnf.infn.it	INFN-LNF, Via E. Fermi 40, C.P. 13, Frascati, Italy
John Byrd	jmbyrd@lbl.gov	Center for Beam Physics, LBL, 1 Cyclotron Road, Berkeley, CA 94720-8211, U.S.A.
Yunhai Cai	yunhai@slac.stanford.edu	SLAC, 2575 Sand Hill Road, MS 26 Menlo Park, CA 94025, U.S.A.
Swapan Chattopadhyay	swapan@fnal.gov	Northern Illinois University, Dept. of Physics, DeKalb, Illinois, 60115, U.S.A.
Yong Ho Chin	yongho.chin@kek.jp	KEK, 1-1 Oho, Tsukuba-shi, Ibaraki-ken, 305-0801, Japan
Jie Gao	gaoj@ihep.ac.cn	Institute for High Energy Physics, P.O. Box 918, Beijing 100049, China
Ajay Ghodke	ghodke@cat.ernet.in	RRCAT, ADL Bldg. Indore, Madhya Pradesh, 452 013, India
Eliana Gianfelice-Wendt	eliana@fnal.gov	Fermilab, Mail Station 312, PO Box 500, Batavia IL 60510-5011, U.S.A.
Ingo Hofmann	i.hofmann@gsi.de	High Current Beam Physics, GSI Darmstadt, Planckstr. 1, 64291 Darmstadt, Germany
Sergei Ivanov	sergey.ivanov@ihep.ru	Institute for High Energy Physics, Protvino, Moscow Region, 142281 Russia
In Soo Ko	isko@postech.ac.kr	Pohang Accelerator Lab, San 31, Hyoja-Dong, Pohang 790-784, South Korea
Elias Metral	elias.metral@cern.ch	CERN, CH-1211, Geneva 23, Switzerland
Toshiyuki Okugi	toshiyuki.okugi@kek.jp	KEK, 1-1 Oho, Tsukuba-shi, Ibaraki-ken, 305-0801, Japan
Peter Ostroumov	Ostroumov@frib.msu.edu	FRIB, National Superconducting Cyclotron Laboratory, Michigan State University, 640 S. Shaw Lane East Lansing, Michigan 48824, U.S.A.
Mark Palmer	mpalmer@bnl.gov	Brookhaven National Lab, Upton, NY 11973, U.S.A.
Chris Prior	chris.prior@stfc.ac.uk	ASTeC Intense Beams Group, STFC RAL, Chilton, Didcot, Oxon OX11 0QX, U.K.
Yuri Shatunov	Yu.M.Shatunov@inp.nsk.su	Acad. Lavrentiev, Prospect 11, 630090 Novosibirsk, Russia
Jiu-Qing Wang	wangjq@ihep.ac.cn	Institute for High Energy Physics, P.O. Box 918, 9-1, Beijing 100039, China
Rainer Wanzenberg	rainer.wanzenberg@desy.de	DESY, Notkestrasse 85, 22603 Hamburg, Germany
Zhentang Zhao	zhaozhentang@sinap.ac.cn	SINAP, Jiading campus: 2019 Jia Luo Road, Jiading district, Shanghai 201800, P. R. China Zhangjiang campus: 239 Zhang Heng Road, Pudong New District, Shanghai 201203, P. R. China

*The views expressed in this newsletter do not necessarily coincide with those of the editors.
The individual authors are responsible for their text.*